Title
HIGH-ENERGY NUCLEAR COLLISIONS

Authors
Nagamiya, S.
Gyulassy, M.

Publication Date
1982-02-01

Lawrence Berkeley Laboratory
UNIVERSITY OF CALIFORNIA

To be published as a chapter in Advances in Nuclear Physics, Plenum Pub. Corp., New York, NY

HIGH-ENERGY NUCLEAR COLLISIONS

S. Nagamiya and M. Gyulassy

February 1982

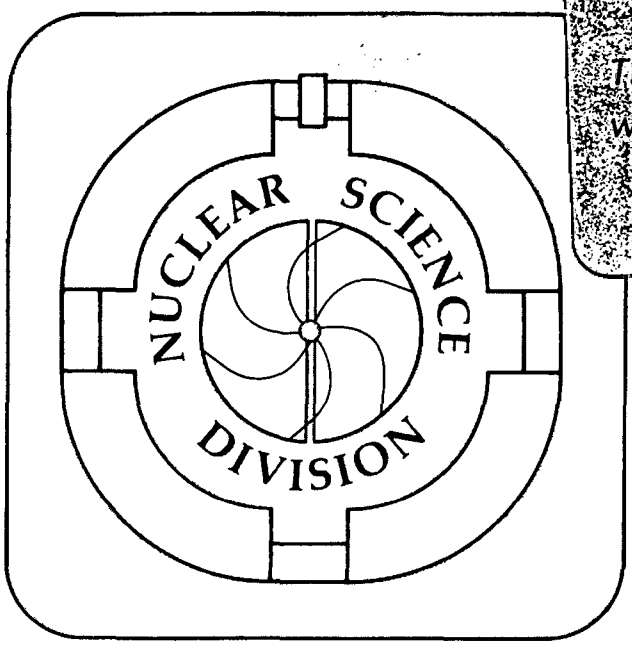

Prepared for the U.S. Department of Energy under Contract DE-AC03-76SF00098

DISCLAIMER

LBL-14035

HIGH–ENERGY NUCLEAR COLLISIONS

S. Nagamiya[†] and M. Gyulassy

Nuclear Science Division, Lawrence Berkeley Laboratory,

University of California, Berkeley, CA 94720

[†] Also, Department of Physics, Faculty of Science, University of Tokyo, Hongo, Bunkyo-ku, Tokyo, Japan.

CONTENTS

1. INTRODUCTION

1.1. Motivation

Until recently the properties of nuclear matter at high densities $\rho > \rho_0 = 0.15$ fm^{-3} and/or temperatures $T > B_0 = 16$ MeV have been inaccessible for study experimentally. This is because normal nuclei saturate at one density, $\rho \approx \rho_0$, with a unique volume energy per nucleon, $-B_0$. In the past, nuclear properties have been studied either with elementary probes such as electrons, pions, and protons, or with low energy nuclear probes. Such probes, however, cannot compress entire nuclei nor heat them up to $T > B_0$. Thus these probes have been unable to shed light on this aspect of nuclear matter. In nature, gravity can crush nuclear matter to high densities in the hearts of neutron stars. Also, supernova collapse may involve high densities and temperatures before exploding. However, it is clear that the properties of dense nuclear matter are very difficult to extract from the limited observations of such objects.

From the theoretical point of view, the properties of dense nuclear matter are rather uncertain. Since only one measured point, $(\rho,-B) = (\rho_0,-B_0)$, exists to constrain theories, it is not surprising that almost anything is possible theoretically at high densities. For example, speculations on phase transitions to abnormal nuclear states, pion condensates, and quark-gluon plasmas have been advanced.[TA1]-[TA7],[TA9]-[TA11] Even in "standard" many body calculations the form of the high density equation of state varies by large factors depending on the particular nuclear potential or approximation scheme employed. Clearly, the measurement of the equation of state away from saturation density would be invaluable in constraining competing nuclear many body theories.

With heavy-ion accelerators we have at last the opportunity to probe the properties of dense, highly excited nuclear matter in the laboratory. What nuclear

beams offer that cannot be duplicated with elementary particle beams is the ability to alter drastically the nuclear state over a space-time volume, $V \cdot c\tau_c \approx R^4 \approx A^{4/3}$ fm^4, that is much larger than typical hadronic scales (≈ 1 fm^4). Elementary particle beams can deposit energy and momentum only into a small fraction of the nuclear volume. They are therefore ideal for studying the response of ground state nuclei to localized disturbances. High-energy nuclear beams test, on the other hand, the response to a major global change in baryon and energy density.

As shown in Fig. 1, that response is often the complete disintegration of both projectile and target nuclei. Fig. 1 shows a streamer chamber photograph[EJ16] of a Ca + Pb collision at E_{Lab} = 2.1 GeV per nucleon (or, hereafter called A·GeV). Of course, we see only the shattered remains (nucleons and pions) of the hot, compressed nuclear state. From the distributions of particles and momenta our task is to reconstruct, if possible, the properties of that state. Clearly, the necessary first step must be understanding the basic reaction mechanism of compression, equilibration, expansion, and final state interactions. In addition, non-equilibrium processes such as direct knock-out must be separated out from any equilibrated components. This ambitious program has been now under way since 1974. A vast arsenal of data as well as increasingly sophisticated theoretical tools have become available. While further decisive (for example, 4π exclusive) experiments are still to be performed, it is appropriate to take perspective at this time of the progress made thus far.

In this report we discuss current interpretations of the available data. Qualitatively, inclusive data involving light nuclear beams ($A \leq 40$) can be understood in terms of multiple nucleon-nucleon collisions. The role of nuclear geometry, finite mean free paths, available phase space, initial Fermi motion, final composite formation, and Coulomb distortions have been clarified by those data. Theoretical methods now exist to incorporate all these effects in a semi-quantitative way. However, there are also several observations that have not been "explained" up to now. It may be these observations that hold the key to the physics of hot, dense nuclear matter.

Those observations include, for example, (1) non-statistical one- and two-particle angular distributions of light fragments in high multiplicity events, (2) small deuteron-to-proton ratios, and (3) anomalously short mean free paths of some secondary nuclei produced in nuclear collisions. The first observation addressed the fundamental question of whether nuclei behave as a fluid or a cascading nucleon gas. In other words, do nuclei flow? If they do, then we may be able to examine the nuclear equation of state. The second observation raises interesting questions about the entropy, the degrees of freedom of the excited nuclear system. Are nucleon degrees of freedom sufficient or must collective excitations such as pion condensates be invoked to explain the apparent high entropy? Finally, the third observation addresses the question of whether long-lived novel or exotic states of nuclei can be formed under the conditions of high baryon and excitation energy densities. Definitely, more data and theoretical work are needed in resolving these questions.

It should also be emphasized that up to now the heaviest nuclear beams available have been ^{40}Ar and low intensity ^{54}Fe ions. Within a year truely heavy nuclei, ^{207}Pb or ^{238}U, should become available at the Bevalac. These heavy nuclear beams are expected to provide more insight into the current puzzles. With 4π exclusive experiments with ^{238}U + ^{238}U, we may finally know whether "all the king's horses and all the king's men can put *dense nuclei* together again". In any case, the enlarged domain of A dependence provided by heavy nuclei will be essential in sorting out the many complex elements of the reaction mechanism. Also, the fragmentation of such nuclei will certainly extend the current study of neutron-rich nuclei far from stability. In the following sections, our aim is to point out the key unsolved questions and the directions of needed theoretical and experimental work.

1.2. High–Energy Heavy–Ion Accelerators in the World

In 1974, a high-energy heavy-ion accelerator, the Bevalac, was completed in Berkeley. This machine is a combination of the Hilac and the Bevatron accelerators, as shown in Fig. 2. Nuclear beams are accelerated to 8 A·MeV with the Hilac, then injected into the Bevatron, and finally accelerated to energies of 50-2100 A·MeV. In the winter, 1981, a new vacuum system was installed inside the Bevatron ring. With an improved vacuum down to 10^{-10} Torr it is expected that ^{207}Pb ions will be available in the summer of 1982.

Another working accelerator in the world is the Synchrophasotron in Dubna, U.S.S.R. It supplies nuclear beams up to ^{20}Ne with energies up to 4 A·GeV. The beam energy there is higher than in Berkeley, but the beam intensity as well as the duty factor of the machine are substantially lower. These two accelerators are currently the only machines available in the field of high-energy nuclear collisions.

If we extend the beam energy and projectile mass into a wider region, then three other machines should be cited. In the energy region of $\approx$ 100 A·MeV the CERN SC machine has been supplying ^{12}C and ^{20}Ne beams at high intensities ($\leq 10^{12}$ ions/sec) since 1979. Light ions such as d, ^{3}He and α at about 1 A·GeV are available at Saclay in France. In addition, α-α colliding-beam experiments at 10 A·GeV became possible at CERN ISR in the summer, 1980.

In several countries there are active plans for future machines. At the Saturne II in Saclay, France, an improved ion source is being constructed to accelerate Ne or C beams. Here, the duty factor as well as the beam intensity are comparable to those of the present Bevalac. In the immediate future, GANIL in France and the Michigan State University in the U.S.A. will complete the construction of intermediate-energy machines up to 100 A·MeV. Furthermore, in the energy region of 1-10 A·GeV three accelerators may be completed in 4-7 years; SIS in Darmstadt, Germany, the Numatron in Tokyo (or Nagoya), Japan, and TIS in Moskow, U.S.S.R. These plans are very

ambitious, and beam qualities from these machines are expected to be much better than those obtainable now. In the planning stage are even more ambitious proposals for much higher energies. At CERN modifications of the ion source and linac are under discussions. If these modifications are carried out, then heavy ions beams up to Ar with beam energies ≈ 100 A·GeV in the laboratory frame (SPS), or 10 A·GeV + 10 A·GeV in the CM (ISR) would become available. In Berkeley a proposal to construct VENUS (Variable-Energy Nuclear Synchrotron) is being formulated. This colliding beam facility would cover an incredible three decade range of energies, 20 A·MeV to 20 A·GeV in the center-of-mass frame, and be able to accelerate projectiles from protons to ^{238}U.

1.3. The High Density–Temperature Nuclear Domain

Fig. 3 illustrates some theoretical speculations on novel phases of nuclear matter that could arise at high density (ρ) and temperature (T). It is important to emphasize again that experimentally we know only one point on this figure: (ρ, T) = (ρ_0, 0). First consider what may happen to nuclear matter as it is compressed to densities $\rho \geq 2\rho_0$ at $T = 0$. Nucleons move well within the one pion exchange range allowing virtual pions to propagate over longer distances in the medium. The enhanced amplitude for pion propagation in the medium can result in long range correlations. Because the pion is a pseudoscalar-isovector particle, the spin-isospin density correlations would be expected to be most affected. At a high enough density it is in fact possible that a phase transition to a spin-isospin lattice takes place. Detailed calculations[TA4]–[TA7] indicate that the critical density may be $\rho_c \approx 2\rho_0$. As the compression is increased, the attractive two pion exchange potential (σ exchange) may lead to a further phase transition. In non-linear σ-models[TA1]–[TA3] that phase transition results a drastic change of the properties of the nucleus. The effective nucleon mass vanishes $m^* \to 0$ in that abnormal nuclear state! Ultimately at some very high density $\rho > 10\rho_0$, it is believed that the quark structure of nucleons comes into play and nuclear matter

melts into a quark-gluon plasma state.[RA6]

If on the other hand, the density is fixed and the matter is heated to high temperatures, then as $T \rightarrow m_\pi c^2$ the nucleons are excited into isobar states (Δ_{33}, N^*, $\cdots$) and mesons appear in the system (π, ρ, $\cdots$). This qualitative change in the constituents of the system can be called a transition from nuclear matter to a hadronic gas.[TJ7] Above $T \geq m_\pi c^2$, so many hadrons are produced that their quark wavefunctions overlap significantly. At that point it is believed that hadronic matter melts into a quark-gluon plasma state. Therefore, both the very high ρ and high T limit of nuclear matter is thought to dissolve into a plasma state.

Also indicated in Fig. 3 are the estimated densities and temperatures that may be reached in nuclear collisions at different energies. For the Bevalac energy range, we can in principle explore up to $T \approx 100$ MeV and $\rho \approx 4\rho_0$. To see the quark-gluon plasma transition would require much higher energies as VENUS or ISR would provide.

An important question is how long nuclei can remain compressed during nuclear collisions. Fig. 4 shows the results of an intranuclear calculation[TB3] for the time evolution of the maximum density and temperature in typical reactions. Observe that the total time spent in the high (ρ, T) domain is only $\Delta t \approx 10$ fm/c. Because causality limits the maximum growth rate of any collective phenomena to $\Gamma < \hbar c / R \approx \hbar / \Delta t$, where R is the dimension of the system, no phase transition can develop fully in nuclear collisions. At best we can expect to see only the onset of critical phenomena[TA11],[RA13] associated with new phases of nuclear matter. We can look also for indirect evidence of phase transitions such as increased entropy associated with softening of pion modes.[TN1],[TN2] However, we cannot expect chunks of pion condensed matter to emerge from the reaction.

There are several additional factors that complicate the deduction of bulk nuclear properties from nuclear collisions. First, even local thermal equilibrium may not be reached in a significant fraction of the nuclear volume. Thus, transient phenomena

associated non-equilibrium properties may be important. Second, the expansion phase of the collision could distort the signals we expect to see from the high (ρ,T) region due to final state interactions. Finally, we must necessarily deal with finite systems. For such systems collective modes with $\omega < \hbar/$ (collision time) and $k < \hbar/R$ are suppressed. Furthermore, surface curvature and thickness are not negligible. Thus, bulk, transient, and surface properties of nuclear matter are all intermingled. Clearly to have any hope to unravel these effects, careful and systematic studies must be undertaken. No one experiment can possibly provide all the necessary information. However, with the leverage arm provided by variations of the projectile and target nuclei and the beam energy, we can hope that enough circumstantial evidence can be accumulated eventually to deduce at least qualitative picture of the high (ρ,T) nuclear domain.

1.4. The Experimental View

Before we begin the detailed interpretation of data, it is useful to illustrate what actual nuclear collisions look like in the laboratory. In Figs. 1, 5 (a), and 5 (b) three "typical" events were recorded by streamer-chamber photographs.[EJ16),(EP3)] The reactions shown involve 2.1 A·GeV Ca + Pb. Thus, 40 nucleons, each with 2.1 GeV kinetic energy, are scattering from 207 nucleons in the target. Comparing these figures, qualitatively different phenomena are obvious. Fig. 5 (a) shows mainly one forward jet of fragments. Such an event is expected to occur at a large-impact-parameter ("peripheral") collision at which the projectile and target nuclei barely touch each other. The energy-momentum transfer between these two nuclei are relatively small, so that the projectile nucleus breaks up into a few fragments with velocities close to the initial beam velocity. The second picture, Fig. 5 (b), shows a larger number of tracks; about 30 charged particles. In this picture a forward jet still exists, but at the same time nearly half the tracks are observed at large angles. Also,

negative charges due to π^- show up. It suggests that two types of reaction mechanisms can operate in one event; one in which a part of the projectile nucleus interacts weakly with target (creating the forward jet) and the other in which the remainder part of the projectile interacts strongly with the target (creating the large-angle spray). The third picture, Fig. 1, illustrates a much more violent collision. Almost all particles are emitted over a wide range of angles and no forward jets remain. Such an event originates from a small-impact-parameter ("central") collision in which all nucleons of the projectile interact strongly with the target nucleons. In such events the available energy is shared among all participating nucleons and pions.

Counter experiments revealed these different features quantitatively. Fig. 6 (a) displays the proton spectra measured at 0° [Ref. (EA14)] and 180° [Ref. (EL12)] in C + C collisions at E_{Lab} = 1.05 A·GeV. The spectra show two peaks, one at the beam momentum per nucleon (at the beam velocity) and the other at zero momentum (at the target velocity). The former peak corresponds to forward jets in the previous photographs and arises as a result of projectile fragmentation. Similarly, the latter peak arises from target fragmentation. In Fig. 6 (b) these fragmentation peaks can be seen clearly also in the neutron spectra for 390 A·MeV Ne + U.[ED3] Fig. 7 shows the proton spectra measured at large angles[EC7] in 0.8 A·GeV Ar + KCl collisions. The spectra are now very smooth as a function of proton momentum and extend over a wide region of momenta. These protons correspond to large-angle sprays observed in Fig. 5 (b) and Fig. 1. The large angle neutron spectra are also smooth as seen in Fig. 6 (b).

These observations suggest that nucleons can be separated into two groups, participants and spectators.[TW2] Participants suffer large momentum transfer collisions, while spectators suffer at most small momentum transfer collisions. Qualitatively, the Fermi momentum, $p_F \approx 250$ MeV/c, sets the scale for large and small momentum transfers. Of course, such a classification is somewhat arbitrary, but it helps us to define the kinematic domain into which particles are emitted, as illustrated

schematically in Fig. 8. In the plane of rapidity (y) [see Appendix] and transverse momentum (p_T/mc) of an emitted particle, the projectile and target fragments, which are mainly from spectator nucleons, are clustered at (y, p_T/mc) = (y_P,0) and (y_T,0), respectively, where y_P and y_T are the projectile and target rapidities. On the other hand, particles emitted from the overlap region between the projectile and target are mostly participants and observed over a wide region of rapidity and transverse momentum. The data shown in Fig. 7 are mainly from the participant nucleons. Because the available phase space for participants is much larger than for spectators, the differential cross sections in Fig. 7 are much smaller than those in the fragment at the regions of Fig. 6. In addition, particles emitted at large angles are expected to be mainly elementary particles such as protons and pions, since the energy transfer in each nucleon-nucleon collision is expected to be much larger than typical nucleon binding energies.

In contrast to reactions at high energies (Fig. 1), nuclear collisions at low energies $E_{Lab} \leq 30$ A·MeV are far less dramatic.[RA12] The multiplicity of fragments is smaller and the momentum distributions fall off much more rapidly. No clean separation can be made between participant and spectator nucleons. The projectile and target nuclei can even fuse occasionally. This qualitative change at low energies is due not only to the smaller accessible phase space but also a rapid increase of the nucleon mean free path with decreasing energies. At low energies the Pauli principle becomes very effective in suppressing two-body collisions. Hence the dynamics is controlled by the time-dependent nuclear mean field, and the momentum transfers are much smaller. Only at high energies, $E_{Lab} > 200$ A·MeV, does the mean free path approach the geometrical value, $\lambda = 1/(\sigma_{NN}\rho)$. At intermediate energies, $E_{Lab} \approx 100$ A·MeV, λ is still substantially larger than $1/(\sigma_{NN}\rho)$ as a result of non-local interactions due to exchange force.[MB5] To take advantage of the small mean free path at high energies it is also important that the de Broglie wavelength $\hbar/k$ of incident nucleons is much smaller than the nuclear radius, R. As we discuss in the next section the story is not quite so

simple. However, qualitatively, the violence of high-energy nuclear collisions and the separation between participant and spectator nucleons follow from the smallness of $\hbar/k$ in comparison to R and the ability of some nucleons (participants) to suffer large momentum transfer collisions ($\lambda < R$).

2. THEORETICAL TOOLS

2.1. Quantal and Classical Aspects

Ideally, the theory of high-energy nuclear collisions should be based on a complete quantum theory of strong interactions. It is currently believed that Quantum Chromodynamics (QCD) is, in fact, that theory. In terms of QCD, nuclear collisions involve a complex cascade of correlated clusters of quarks and gluons. It may be possible to perform such a QCD calculation when Monte Carlo lattice formulations of QCD became sufficiently sophisticated. However, until that time an effective theory of strong interactions must be employed. Unfortunately, even the non-relativistic N-body Schrödinger equation with static potentials is too complicated to solve for nuclear collisions. Approximation schemes such as the time-dependent Hartree-Fock method are not applicable because of the short mean free paths at high energies. The Eikonal-Glauber approach is not applicable, because large momentum transfers are involved. We are therefore forced to devise phenomenological theories and models of nuclear collisions. Such a limitation on theory is of course not new to many body physics and does not detract from the usefulness of a phenomenological approach. For example, if a hydrodynamical model could fit the data with unique equation of state and transport coefficients, then that phenomenological equation of state could provide valuable constraints of more fundamental theories of nuclear matter.

Accepting the phenomenological approach, we can ask whether a classical or quantal description is most appropriate. At the classical level, there exist many well-explored methods to calculate non-equilibrium transport of matter and energy. Newton's classical equation of motion can be directly integrated in some cases. The Boltzmann-Vlasov equation provides a general framework for describing transport properties of macroscopic systems. Monte-Carlo cascade calculations could be used to describe finite mean free path systems. The Navier-Stokes equation could describe

linear departures from local equilibrium. Thus, at the classical level there is an arsenal of theoretical tools with which nuclear collisions could be analyzed.

At the quantum level, there are on the other hand very few practical tools at our disposal. Therefore, it is not surprising that most of the models developed thus far are based on classical considerations. Before applying the classical arsenal though, we must consider the importance of quantum effects. Whether classical concepts apply or not depend sensitively on the specific observables and kinematic domain we wish to describe. For example, diffractive elastic scattering, which accounts for nearly one half of the total cross section, is a pure wave phenomenon. However, we generally observe only the reaction cross section, σ_r. Because the total angular momentum in the nucleus-nucleus center-of-mass can reach large values

$$L_{max} \approx Ak \times 2R \approx 10A^{4/3}\left(\frac{k}{1\ \mathrm{GeV/c}}\right)\hbar \gg \hbar, \tag{2.1}$$

where k is the c.m. momentum per nucleon and A is the number of nucleons in the projectile, the partial wave sum can be replaced by an integration over impact parameters b. Nuclei are furthermore highly absorbtive, i.e. there are very many inelastic channels open for each impact parameter. Therefore, the reaction cross section reduces to the classical geometrical value

$$\sigma_r \simeq \pi(R_P + R_T)^2, \tag{2.2}$$

where R_P and R_T are the projectile and target radii, respectively. Finite surface effects can be estimated by integrating over a realistic density profiles as in the Glauber theory.[TW1]

A more interesting question is whether classical concepts can be applied to inclusive or exclusive differential cross sections. In general, there are distinct interference effects between different partial wave amplitudes in differential cross section. However, with nuclei such interference effects can be expected to be far less important because of the enormous number of orthogonal final channels accessible.

Specifically, two different impact parameters (or partial waves) most often lead to orthogonal final states. An obvious example is that peripheral collisions lead to two slightly excited nuclei in the final states while more central collisions lead most often to states containing many free protons, deuterons, pions, etc. Therefore, the amplitudes for these two processes cannot interfere. In fact, changing the impact parameter by ≈ 1 fm will result in additional NN scatterings that must leave the nuclear fragments in higher excited and hence orthogonal states. Because small changes in the initial impact parameter lead to large changes in the final channels populated, the amplitudes to scatter at different impact parameters are not likely to interfere. Thus, even though the projectile center-of-mass wavefunction is a plane wave (and not a localized packet!), it makes sense to sum over the probabilities to scatter at different impact parameters.

For a given impact parameter we can ask next how quantum phenomena affect the dynamical path. Consider the scattering of two nucleons at these energies. While the total nuclear angular momentum is large in Eq. (2.1), the relative angular momentum in each nucleon-nucleon collision is not. Taking the force range as $\hbar/m_\pi c \approx 1.4$ fm, the relative angular momentum is only

$$l_{\rm rel} = \left[\frac{k}{m_\pi c}\right]\hbar . \tag{2.3}$$

For an incident laboratory momentum $k_{\rm Lab} < 1$ GeV/c, $l_{\rm rel} < 3\hbar$ cannot be regarded as large even initially. After only one NN collision subsequent NN collisions will have a relative angular momentum $\approx \hbar$. This implies that a quantum mechanical treatment of individual nucleon-nucleon collisions is necessary. This is also true if during the collision a fireball were formed with a temperature $T = (2/3)E_{\rm c.m.}$, with $E_{\rm c.m.}$ being the c.m. energy per nucleon ($E_{\rm c.m.} \approx E_{\rm Lab}/4$ in equal-mass collisions). In a fireball, the thermal momenta $k_T \approx \sqrt{2mT}$ is generally so small (e.g. $k_T \approx 300$ MeV/c for Ar + Ar collisions at 400 MeV per nucleon) that S- and P-waves dominate the NN scattering

process. Thus at least on the nucleon-nucleon level a quantum treatment of the scattering is necessary.

How does quantum mechanics affect two successive *NN* collisions? Two *NN* collisions occur on the average every mean free path λ:

$$\lambda = \frac{1}{\sigma_{NN}\rho} \approx \frac{\hbar}{m_\pi c}\left(\frac{\rho_0}{\rho}\right). \tag{2.4}$$

Note that mean free path is on the same order of the force range if $\rho \simeq \rho_0$. The time interval between two successive collisions is $\delta t \approx \lambda m_N / 2k$. The uncertainty in energy $\delta\varepsilon \approx \hbar/\delta t$ compared to the c.m. kinetic energy $\varepsilon_k \approx k^2/(2m_N)$ is thus given by

$$\frac{\delta\varepsilon}{\varepsilon_k} \approx \frac{4\hbar}{k\lambda} \approx 4\hbar\left(\frac{m_\pi c}{k}\right)\left(\frac{\rho}{\rho_0}\right). \tag{2.5}$$

By using Eq. (2.3) we also have $\delta\varepsilon/\varepsilon_k \approx 4\hbar/l_{\rm rel}$ for $\rho \simeq \rho_0$. Therefore, the higher the nuclear density the more uncertainty is there in the *kinematics* of each succeeding *NN* collisions! This uncertainty in the kinematics of the multiple collision sequence may have profound implications for the evolution of the system. Studies of such effects have only just begun[TY3] and call for much further theoretical investigation. Eqs. (2.3) and (2.5) thus serve as a warning that even though the de Broglie wavelength of each nucleon, $\hbar/k$, is much smaller than the nuclear radii, $\hbar/k$ cannot be regarded as small compared to the force range, $\hbar/m_\pi c$ and mean free path λ.

The coincidence of $\hbar/m_\pi c$ and λ also leads to another difficulty. Subsequent *NN* collisions may not be treated as independent. The amplitudes to scatter off two successive nucleons could interfere with one another. In other words, the scattering wave generated by the first target nucleon may not have reached its asymptotic form by the time it reachs the second target nucleon. Thus, near-zone effects may come into play. The assessment of the magnitude of such effects remains an open theoretical problem.

Usually, application of classical methods to heavy-ion collisions has been motivated by noting

$$kR \gg \hbar . \tag{2.6}$$

While Eq. (2.6) is certainly necessary, it is by no means obvious that it is sufficient. There are many length scales in the problem besides R including $\hbar / m_\pi c$, λ, $\hbar / p_F$, $\hbar / m_N c$, $\hbar c / U_{opt}$. It would seem that we need only to go to higher energies. However, higher energies actually makes things worse! That is because beyond $E_{Lab} \gtrsim 300$ A·MeV pion production can reduce the momentum of the incident nucleon. For example, at $E_{Lab} \approx 600$ A·MeV, $NN \rightarrow N\Delta$ leads to Δ essentially at rest in the c.m. frame. In this case the propagation of the Δ and the resulting $N\pi$ system should certainly be described quantum mechanically.

Up to this time a full list of necessary and sufficient conditions for the validity of a classical description of nuclear collisions has not been given. The more difficult problem of estimating the magnitudes of quantum corrections to specific observables has not even been formulated yet. These are important theoretical problems for the future. If classical methods can eventually be justified, it is likely to be due to the immense complexity of the nuclear systems. It could be that relatively few dynamical paths can lead to the same *exclusive* final state and hence interfere.

Thus far, we have considered the possible role of quantum effects on the dynamical path during what can be regarded as the intermediate stage of the reaction. In addition, there are initial and final state interactions. The initial state interactions result obviously in Fermi motion. This internal motion is naturally a quantum property of ground state nuclei. Its effect will be to broaden the momentum distributions of the final fragments. Thus, at the very least some prescription will have to be invented to incorporate this internal motion in any classical framework. In the final state, there are often many nucleons emerging with small relative momentum, $q_{ij} = |\vec{p}_i - \vec{p}_j|$. For $q_{ij} \lesssim p_F$ such nucleons can coalesce into nuclear fragments such as d, t, α, $\cdots$. The state

of these fragments must certainly be described quantum mechanically. The abundance of nuclear fragments emerging from nuclear collisions implies that we cannot neglect such final state interactions. Therefore, it will be necessary to supplement any classical approach with information on the ground state wavefunctions of nuclei.

Another way in which quantum effects enter is through the indistinguishability of identical particles such as two protons or two π^-. Many particle wavefunctions describing such particles must be (anti) symmetrized. This symmetrization can result in constructive or destructive interference when the relative momentum $q_{ij} \leq \hbar / R$. As we will see later in Sec. 3.5.4. such interference effects can in fact be observed in two-particle correlation functions.

We can only conclude that the nature and importance of quantum effects needs much more study. There are obvious examples such as initial and final state interactions where these are important. There are suspicious signs, Eqs. (2.3) and (2.5), that indicate that quantum effects are not negligible in the intermediate state either. Therefore, when applying classical concepts, we should always keep in mind the reservations expressed above. On the other hand, progress can be made at this point only if we devise phenomenological classical models. With these reservations, we proceed therefore to exploit our calssical arsenal.

2.2. Classical Tools

Given a static spin-independent nucleon-nucleon force, the Classical Equation of Motion (CEM) could in principle be integrated directly.[TC1]-[TC5] Aside from the above reservations, in order to apply CEM the energy should be low enough so that particle (π) production can be neglected. This implies that the beam energy per nucleon is $E_{\text{Beam}} \ll 1$ A·GeV. The energy region between 200 - 500 A·MeV is probably the most suitable with respect to the use of CEM. At these energies, pion production, relativistic

kinematics, simultaneity, and retardation effects can also be neglected to a first order approximation. Therefore, we could attempt to use the non-relativistic Newton's CEM.

Depending on the time and length scales in the problem, CEM can sometimes be reduced to an approximate dynamical framework such as hydrodynamics or intranuclear cascade. The relevant length scales are again the force range, $\hbar/m_\pi c$, the mean free path, λ, and the nuclear radius, $R \approx 1.2\, A^{1/3}$ fm. These scales satisfy the inequality

$$\hbar/m_\pi c \lesssim \lambda \lesssim R\,. \tag{2.7}$$

(Quantum mechanics introduces the additional scale, $\hbar/k$, the de Broglie wavelength) Various approximation schemes to CEM could be justified[TC1] if any of the "$\lesssim$" signs in Eq. (2.7) would be replaced by "$\ll$" signs.

Consider the following possibilities:

$$\text{(A)}\quad \hbar/m_\pi c \ll \lambda \longrightarrow \rho/\rho_0 \ll 1, \tag{2.8}$$

$$\text{(B)}\quad \lambda \ll R \longrightarrow \rho/\rho_0 \gg A^{-1/3}, \tag{2.9}$$

$$\text{(C)}\quad \hbar/m_\pi c \ll \lambda \ll R \longrightarrow A^{-1/3} \ll \rho/\rho_0 \ll 1, \tag{2.10}$$

In these three cases, CEM reduces to (A) Intranuclear cascade, (B) Hydrodynamics, and (C) Ideal gas hydrodynamics, respectively.

In case (A), isolated two-body collisions occur. Potential energy effects are negligible between NN scatterings and the nucleons propagate as free particles. This is the dilute gas limit. In this case CEM reduces to the Boltzmann equation or to intranuclear cascade (INC). In both methods the free space NN cross section is the main dynamical input. Intranuclear cascade is the more general of the two methods in that it provides information on the full A-body density matrix, $\rho_A(x_1,\cdots,x_A,p_1,\cdots,p_A,t)$. On the other hand, the Boltzmann equation assumes that $\rho_A \approx \rho_1(x_1,p_1,t)\cdots\rho_1(x_A,p_A,t)$, and thus it provides information on only the one-body density matrix ρ_1. Clearly, correlations should be negligible if the Boltzmann equation is to provide a reasonable

approximation to INC. For nuclear collisions, Eq. (2.8) is not satisfied well, especially since densities up to $(2 - 4)\rho_0$ are expected at these energies.[TJ1),(RA8),(RA15)]

It is important to note that conditions (A) - (C) can only be regarded as sufficiency conditions. Under special circumstances, each method may yield reasonable results even when these conditions are violated. For example, just because the force range is $\hbar/m_\pi c \approx \lambda$, it does not imply necessarily that the corrections due to potential effects be large. The large momentum transfer *NN* collisions ($q > m_\pi c$) most likely occur as a result of hard core interactions at a radius

$$r_c \approx 0.5 \text{ fm} \approx \hbar/3m_\pi c. \tag{2.11}$$

The tails of the one pion exchange potential lead on the other hand to low momentum transfer scatterings ($q < m_\pi c$). Therefore, the condition $r_c \ll \lambda$ insures that at least the hard core scattering can be treated via cascade calculations. The longer range parts of the *NN* potential could contribute to an effective optical potential or mean field. In terms of the Boltzmann equation this potential could be included via a Vlasov term. The effect of hard core collisions ($\sigma_{\text{core}} < \sigma_{NN}$) could be included in the usual collision integral. Such a separation of hard core and potential effects has been advocated by Remler.[TE7]

It remains an open theoretical problem to evaluate the importance of potential effects. In CEM studies[TC1)-(TC5)] a substantial fraction of the available kinetic energy was found to be converted into potential energy during the maximum compression phase of the reaction. However, that potential energy is associated with the short-range, hard-core repulsive interaction which might be well approximated by INC. The question of the effect of the longer range attractive forces which are not well approximated by INC has yet to be investigated.

In case (B), $\lambda \ll R$, the mean free path is so short compared to size of the system that local thermal equilibrium could be reached. In this case CEM reduces to *viscous hydrodynamics*. Potential energy effects can be included readily via the equation of

state, $P(\rho,T)$, for nuclear matter. In addition, transport coefficients such as viscosity and thermal conductivity can be included to estimate first order $O(\lambda)$ corrections to ideal Euler hydrodynamics. Those corrections are described by the Navier-Stokes equation. The requirement for the validity of Navier-Stokes equation is that the gradients of the density and temperature should be small in both space and time, e.g. $|\partial_\mu \rho| \ll \rho/\lambda$. This follows from the fact that the transport coefficients are related to the static, long wavelength ($\omega = kc = 0$) form of basic correlation functions of the system. See for example the Kubo formulae.[TT4] In general, frequency and wavelength dependent transport functions are necessary.

Another important consideration in applications of hydrodynamics is that $\lambda \ll R$ applies only for nucleons traversing the central region of the target. For finite nuclei approximately half ($3\lambda/R$) of the nucleons lie within *one* mean free path of the surface. These "surface" nucleons cannot be expected to reach local thermal equilibrium. Therefore, only a fraction of the nucleons can be considered to behave hydrodynamically even in a $^{238}U + ^{238}U$ collisions! Consequently, hydrodynamics should always be supplemented with a model to handle the non-equilibrium components of the spectrum.

Case (C) provides the simplest limit of CEM. Potential energy may be neglected as compared to kinetic energies. Furthermore, sufficient number of NN scatterings occur in order to equilibrate the kinetic degree of freedom. In this ideal gas limit the dynamics is likely to be the least sensitive to the details of the NN interaction. The geometry and available phase space can be expected to dominate gross features of the inclusive distributions. The geometry gives the number of nucleons that scatter with any incoming nucleon. The available phase space becomes uniformly populated (equilibrated) after sufficiently many collisions. In this case, thermodynamics or phase space models may apply. Of course, as in case (B), $\lambda \ll R$ is likely to hold only for a fraction of the nucleons at any give impact parameter.

While non of the limiting conditions (A) - (C) are obviously satisfied for nuclear collisions, Eq. (2.7) indicates that neither are they grossly violated. Therefore, many approximations to CEM may give qualitatively similar and reasonable results. Since all approximations to CEM have energy-momentum conservation and the correct nuclear geometry built in, their results must be similar to the extent that detailed dynamics are not relevant as, for example, when equilibrium is reached. Furthermore, the sensitivity to dynamics is diminished by the fact that inclusive cross sections necessarily average over a wide spectrum of unobserved multiparticle configurations. Unfortunately, there is no way to estimate the intrinsic errors introduced by any approximation scheme when the basic inequality [Eq. (2.7)] contains "$\lesssim$" rather than "$\ll$" signs. Only by confrontation with data can that accuracy be determined empirically.

Since no rigorous and calculable theoretical framework exists at present to calculate nuclear collisions, the only way to proceed is to turn to model calculations that incorporate as many "realistic" effects as possible. By varying the parameters and assumptions within each model, we can hope to isolate at least the most essential elements of the reaction mechanism. As we shall see, the cross comparison of results of many models and their confrontation with data have already provided much insight into the problem. Nuclear collisions have certainly not been "solved", but some order is beginning to emerge out of the chaos. In the subsequent subsections, we describe some of the models developed and the lessons they have provided. The list of models is by no means exhaustive but is sufficient to introduce various important concepts.

2.3. Statistical Models

In both quantal and classical domains energy-momentum conservation and the nuclear geometry are automatically included. An important question is to what extent these basic features control the form and magnitude of inclusive cross sections. To answer this question we turn to statistical models[TG1–TG7] of nuclear collisions.

The starting point is the decomposition of inclusive cross sections into a sum of cluster-cluster collisions:[TD1)–(TD5),(TB11),(TG4),(TG5]

$$\varepsilon \frac{d^3\sigma}{d^3p} \equiv \sigma_{AB}(\vec{p}) = \sum_{m,n} \sigma_{AB}(m,n) \cdot F^{(1)}_{m,n}(\vec{p}), \tag{2.12}$$

$$\varepsilon\varepsilon' \frac{d^6\sigma}{d^3p\, d^3p'} \equiv \sigma_{AB}(\vec{p},\vec{p}') = \sum_{m,n} \sigma_{AB}(m,n) \cdot F^{(2)}_{m,n}(\vec{p},\vec{p}') + \sum_{m,n,m',n'} \sigma_{AB}(m,n,m',n') \cdot F^{(1)}_{m,n}(\vec{p}) F^{(1)}_{m',n'}(\vec{p}'). \tag{2.13}$$

In these equations m nucleons from the projectile A interact with n nucleons from the target B. The geometrical weights $\sigma_{AB}(m,n)$ are the cross sections for a $m \times n$ cluster interaction. The distribution $F^{(1)}_{m,n}$ describes the one particle distribution arising from such a cluster collision. Similarly, $F^{(2)}_{m,n}$ describes the two particle distribution from that cluster. The two and higher particle inclusive cross sections involve additional terms as in Eq. (2.13) to account for the contribution of different clusters to a given many body final state. Thus, for example $\sigma_{AB}(m,n,m',n')$ is the cross section for producing two independent cluster collisions.

With the cluster decomposition, nuclear collisions are reduced to a superposition of cluster collisions. Next we have to specify σ_{AB} and $F_{m,n}$. The simplest choice for the dynamical path is one that is so complicated that the available momentum space is uniformly populated. In that case, $F^{(i)}_{m,n}$ can be expressed in terms of phase space integrals,

$$\varphi_N(P) = \int \frac{d^3p_1}{\varepsilon_1} \cdots \frac{d^3p_N}{\varepsilon_N}\, \delta^4(\sum_1^N p_i - P), \tag{2.14}$$

where $\varepsilon_i = \sqrt{p_i^2c^2 + m_i^2c^4}$ and m_i is the mass of the i^{th} particle. The i particle distribution $F^{(i)}_{m,n}$ is given by

$$F^{(i)}_{m,n}(\vec{p}_1, \cdots, \vec{p}_i) = \frac{(m+n)!}{(m+n-i)!} \frac{\varphi_{m+n-i}(P_{mn} - \sum_{j=1}^{i} p_j)}{\varphi_{m+n}(P_{mn})}, \tag{2.15}$$

where $P_{mn} = mp_A + np_B$ is the incident four momentum of the cluster in terms of the ~~four momentum per nucleon p_A (p_B) of the projectile~~ (target). ~~For large cluster sizes~~, $m+n \gg 1$, Eq. (2.15) reduces in the non relativistic limit ($\varepsilon_i = mc^2 + p_i^2/2m$) to the familiar Boltzmann thermodynamic form

$$F^{(i)}_{m,n}(\vec{p}_1, \cdots, \vec{p}_i) \simeq \frac{(m+n)!}{(m+n-i)!} \frac{\exp[-\sum(\vec{p}_i - \vec{p}(mn))^2/2mT_{mn}]}{(2\pi m T_{mn})^{3i/2}}, \tag{2.16}$$

where $\vec{p}(mn)$ and $(3/2)T_{mn}$ are the momentum per nucleon of the cluster and the energy per nucleon in the c.m. of the cluster, respectively. Eq. (2.15) is of course more general, because it incorporates the suppression of low and high energy regions of phase space due to finite number effects. However, as shown in Fig. 9, finite size effects are negligible as soon as the cluster size exceeds a relatively small value, $m+n \geq 4$. Also, it is clear that the knock out or direct contribution,[(TF1)-(TF9)] $m+n = 2$, is a rather special case. For the knock out component, $F^{(1)}_{1,1}(\vec{p})$, it is important to improve the statistical model by using the experimental elastic NN cross section directly [see e.g. Refs. (TD5),(TL1),(TL2)]. A further improvement of the model is to evaluate $F^{(i)}_{m,n}$ assuming a one dimensional cascade.[(TD1)-(TD5)]

Having specified the $F^{(i)}_{m,n}$, we turn to the geometrical weights σ_{AB}. At high energies ($E_{Lab} > 1$ A·GeV) the NN cross sections are forward peaked. This observation forms the basis of the Eikonal-Glauber approximation, that treats all nucleons as moving in straight line trajectories along the beam direction. With this straight line assumption, the average number of collisions that an incident nucleon will suffer in a

target B at impact parameter $\vec{s}$ is[TW1),(TD1)-(TD5)]

$$\langle N_B(\vec{s})\rangle = \int dz\ \rho_B(z,\vec{s})\sigma_{NN}, \tag{2.17}$$

where ρ_B is the target density distribution. Furthermore, the distribution of the number of collisions is approximately a Poisson,

$$P_B(n,\vec{s}) \simeq e^{-\langle N_B(\vec{s})\rangle}\ (\langle N_B(\vec{s})\rangle)^n / n!\ . \tag{2.18}$$

In terms of this distribution the geometrical weights are given in this straight line approximation by[TD5]

$$\sigma_{AB}(m,n) = \int d^2b\ B(\vec{b}) \int \frac{d^2s_A d^2s_B}{\sigma_{NN}}\ \delta(\vec{b}-\vec{s}_A-\vec{s}_B) P_A(m,\vec{s}_A) P_B(n,\vec{s}_B)\ , \tag{2.19}$$

where $B(\vec{b})$ is the distribution of nucleus-nucleus impact parameters (B = 1 for impact parameter average reactions).

At lower energies, the straight line geometrical assumption breaks down[TE2] and Eq. (2.19) can be expected to underestimate considerably the contribution for large clusters. A detailed study based on a three dimensional intranuclear cascade model[TB11] has shown in fact that the finite perpendicular range of nuclear forces and large angle scattering leads to a much broader distribution from $\sigma_{AB}(m,n)$ than given by Eq. (2.19) even at 800 A·MeV. Nevertheless, the final inclusive cross sections, Eq. (2.12), were found insensitive to the detailed form of $\sigma_{AB}(m,n)$. This insensitivity to the detailed geometry can be traced to Eqs. (2.15) and (2.16). Beyond some relatively small cluster size, $m+n \geq 4$, the spectra approach the thermodynamic limit. Energy and momentum conservation then controls the form of the inclusive distributions. Thus, we only need to know the cross section for producing large clusters of *any* size $m+n \geq 4$. This integral property of $\sigma_{AB}(m,n)$ is not sensitive to the detailed form of σ_{AB}.

The cascade theory[TB11] also shows that the moments of cluster inclusive distributions are rather insensitive to $m+n$ even for small $m+n$. This is a

confirmation of many studies[TD1]-[TD5] that also show that inclusive distributions are remarkably insensitive to dynamical details. The main lesson here is that in analyzing data the first step should always be to compare them with the results of statistical model. The regions of phase space showing the strongest deviation are likely to posses the most dynamical information. Conversely, those regions where the statistical model works well contain little dynamical information. Of course, in those regions more elaborate models are also guaranteed to fit the data as well. An example of a reaction where phase space dominates is the high momentum spectrum from Ar + KCl at 800 A·MeV shown in Fig. 10. In this region dynamical effects, as measured by the discrepancy between the solid curves and data, result in less than a factor of two variations over four decades of inclusive cross sections. The physics is in that factor of two discrepancy not in the overall trend of the angular and energy spectrum. We will return often to this theme: Statistical considerations often lead to an agreement with data within a factor of 2. A more detailed dynamical model must agree with data much better in order that its dynamical content be tested. Log plots such as in Fig. 10 are very forgiving in that factor of two discrepancies are barely resolved by the human eye.

The statistical model is clearly not limited to treating nucleons only. Pion production and light nuclear fragment yield may also be calculated with the additional assumption of *chemical equilibrium*. As in Fermi's statistical theory, the probability for any multiparticle configuration can be estimated from the total number of accessible states for that configuration. If V is the interaction volume, then the total number of accessible states for a configuration of n particles consisting of n_1 nucleons plus n_2 pions plus other fragments is,[TG5]

$$\Lambda_n = \left[\frac{V}{(2\pi\hbar)^3}\right]^{n-1} \varphi_n(P) \prod_i [(2s_i+1)(2\tau_i+1)m_i], \qquad (2.20)$$

where (s_i,τ_i) is the spin-isospin of particle i and P is the total four momentum of the particles. The statistical assumption implies that the probability for a particular

configuration $n = \{n_1, n_2, \cdots\}$ is simply

$$P_n = \frac{\Lambda_n}{\sum_i \Lambda_i}, \tag{2.21}$$

where the sum runs over all configurations that conserve baryon number and charge (and by construction energy and momentum) of a given cluster. Note that the creation of one pion introduces an additional factor of the interaction volume V while the coalescence of two nucleons into a composite state (deuteron) removes one factor of the interaction volume. Therefore, P_n depends on the volume explicitly if the final configuration differs from all free nucleons. Such a volume dependence is to be expected since in the limit of $n \to \infty$, $V \to \infty$, it must be possible to recover the law of mass action formulas for chemical equilibrium. These formulas state for example that the average number of pions and deuterons in chemical equilibrium are[RA14]

$$\langle n_\pi \rangle = 3V \int \frac{d^3p}{(2\pi\hbar)^3} (e^{\varepsilon_\pi / T} - 1)^{-1} \simeq 0.1 \left[\frac{V}{\mathrm{fm}^3}\right] \left[\frac{T}{m_\pi c^2}\right]^4, \tag{2.22}$$

$$\langle n_d \rangle = \langle n_p \rangle \langle n_n \rangle \frac{3}{4} \left[\frac{2\pi\hbar^2}{m_p T}\right]^{3/2} \frac{1}{V}, \tag{2.23}$$

where the $\simeq$ sign in Eq. (2.22) is valid for temperatures $50 \leq T \leq 150$ MeV. The volume should be taken such that the mean free path λ_i for particle i becomes comparable with the size of the system $\approx V^{1/3}$. As the system expands beyond that point, interactions cease and the concentration and momentum distributions of the particles cease to vary with time. This "freeze-out" volume depends in general on the particle species since λ_i for π, p, d vary considerably. Qualitatively through, the freeze-out volume V can be expected to satisfy $A/V \leq \rho_0$. These formulas will be compared with data in subsequent sections. Extensive comparisons of thermal models with data are given in Ref. (RA14).

We conclude this section by emphasizing that statistical[TG1]-[TG7] and thermodynamic[RA14],[TJ1]-[TJ10] models provide valuable insight into the constraints

imposed by conservation laws and geometry. They should not be expected, however, to yield quantitative results as their conditions for applicability (absence of non-equilibrium dynamical effects) are not satisfied in nuclear collisions. As we shall see, these models agree with the overall trend of the data within a factor of two or so. Therefore, the dynamical information is buried typically in that factor of two discrepancy with data.

2.4. Hydrodynamics

One of the prime motivations for studying nuclear collisions has been the expectation that during the course of the collision nuclear matter will be highly compressed and heated. This expectation has been based on the assumption that at high energies a nuclear shockwave is formed as two supersonic nuclei interpenetrate. The shock compression and heating can be estimated from the Rankine-Hugoniot equation[RA15),(TA8)-(TA10),(TJ1),(TK23)]

$$(W^2 - W_0^2) + P(W/\rho - W_0/\rho_0) = 0, \tag{2.24}$$

which follows from the continuity of baryon, momentum, and energy fluxes across the shock front. Eq. (2.24) applies to the rest frame of the compressed matter (nucleon-nucleon c.m. frame). In Eq. (2.24), $W_0 = m_N c^2 - B \simeq 931$ MeV and $\rho_0 \simeq 0.15$ fm^{-3} are the energy per nucleon and the saturation density, respectively, of ground state nuclei. The density, temperature, energy per nucleon, and pressure in the shock zone are, ρ, T, $W = W(\rho,T)$, and $P = P(\rho,T)$, respectively. The total pressure P is related to W via

$$P(\rho,T) = \rho^2 \, \partial W(\rho,T)/\partial\rho \, |_{S(\rho,T) = \text{const.}}, \tag{2.25}$$

where $S(\rho,T)$ is the entropy per nucleon in the shock zone. The energy per nucleon, W, is, however, fixed by the incident laboratory kinetic energy, E, to be

$$W = \gamma_{c.m.}(E) \, W_0, \tag{2.26}$$

with $\gamma_{c.m.}(E) = \sqrt{1+E/2W_0}$. For a given $W(\rho,S)$ Eqs. (2.24)-(2.26) can be solved for

$\rho(E)$, $S(E)$, and, hence, $P(E)$. In particular, the pressure in the shock zone is simply related to the compression $\rho(E)$ via[TK23]

$$P(E) = \frac{1}{2}E\rho_0[1 - \gamma_{c.m.}(E)\rho_0/\rho(E)]^{-1}. \tag{2.27}$$

The dependence of $\rho(E)$ on E of course depends on the specific form of $W(\rho,S)$. For an ideal nuclear gas we have

$$P = \frac{2}{3}\rho W,$$

$$\rho(E) = \rho_0\left(\frac{5}{2}\gamma_{c.m.}(E) + \frac{3}{2}\right). \tag{2.28}$$

In Fig. 11 the range of compressions, pressures, and entropies that can be expected in nuclear collisions is illustrated.[TK23] As we can see, in this energy range, high compressions [$\rho \approx (2-6)\rho_0$] and high entropies per baryon ($S \approx$ 1-4) are expected for $T \approx$ 20-200 MeV due to shockwaves.

To describe the full three dimensional evolution of shock formation the hydrodynamical equations must be integrated numerically. The equations that include first order deviations from local equilibrium are the Navier-Stokes equations[TK24],[RA15]

$$\partial_t\rho + \partial_i(\rho v_i) = 0\,, \tag{2.29}$$

$$\partial_t(\rho v_i) + \partial_j(\rho v_i v_j) = -\frac{1}{m}\partial_i P + \frac{1}{m}\partial_j \prod_{ij}, \tag{2.30}$$

$$\partial_t(\rho W_T) + \partial_j(\rho W_T v_j) = -\partial_j(v_j P_T) + \partial_i(v_j \prod_{ij}) + \kappa\partial_j\partial_j T\,, \tag{2.31}$$

where the viscosity tensor is

$$\prod_{ij} = \eta(\partial_i v_j + \partial_j v_i - \frac{2}{3}\delta_{ij}\partial_k v_k) + \xi\delta_{ij}\partial_k v_k. \tag{2.32}$$

In these equations $\vec{v}(\vec{x},t)$ is the flow velocity field of the fluid, $\rho(\vec{x},t)$ is the baryon density, $W_T = W(\rho,T) - W(\rho,0)$ is the thermal energy per nucleon, P is the total pressure, P_T is the thermal pressure, T is the temperature field, and (η,ξ,κ) are transport coefficients. When the transport coefficients are set to zero, Eqs. (2.29) - (2.31) reduce to the Euler equations.[RA8] With an assumed form of $W(\rho,T)$ and $S(\rho,T)$,

Eqs. (2.29) - (2.31) specify five equations for five unknowns $\rho(\vec{x},t)$, $\vec{v}(\vec{x},t)$, and $T(\vec{x},t)$. In general, the dependence of the transport coefficients on ρ and T must also be specified.

Unfortunately, even with the great complexity of these equations, they are not sufficient for comparison with the data. A model needs to be specified to describe the breakup of the nuclear fluid into the nuclear fragments which are ultimately detected. As the fluid expands, the density reaches such a low value that the mean free path, $\lambda \approx (\sigma\rho)^{-1}$, becomes comparable to the dimension of the system. Beyond that point local thermal equilibrium certainly cannot be maintained.

The most simple model[RA8] for fluid breakup is terminating the hydrodynamical calculation at some late time where the average density falls below ρ_0. The inclusive baryon spectra are thus determined by the momentum distribution of the fluid at that breakup time. A more realistic model, that has been used,[TN4] is to "freeze-out" fluid cells one at a time when the cell density falls below a freeze-out density, $\rho \approx (0.3\text{-}1)\rho_0$. Different fluid cells therefore freeze out at different times. Both models of breakup can be supplemented by assuming that chemical equilibrium is reached by the freeze-out time. Thus, the average number of pions, deuterons, tritons, etc. can be estimated in each fluid cell using Eqs. (2.22) and (2.23), with V, T, N replaced by the volume, temperature, and baryon number in each cell. Another model that has been used to describe breakup is the evaporation model.[RA15],[TK24] In this model the number of unbound nucleons (protons, neutrons) is estimated by assuming a mean potential energy, V_0, in each fluid cell. Only those nucleons with kinetic energy greater than V_0 are allowed to escape the cell as unbound nucleons. The rest are assumed to emerge as bound fragments. In practice, calculations with this model for 400 A·MeV Ne + U collisions have shown that only $\approx$ 20 % of the matter in each cell ends up free nucleons.

It is clear that any model of fluid breakup must involve assumptions and parameters beyond those leading to Eqs. (2.29) - (2.31). It is therefore vital to vary

those parameters by a wide margin to assess which feature of the spectra reveal true hydrodynamic behavior and which are dictated by the breakup mechanism. Calculations[TK19),(TK24] show that the spectra of individual fragments, p, d, α, $\cdots$ are indeed sensitive to the breakup mechanism. However, the inclusive charged or neutral baryon cross sections,

$$d\sigma_{ch} = \sum_{Z,N} Z\ d\sigma(Z,N), \tag{2.33}$$

$$d\sigma_{nt} = \sum_{Z,N} N\ d\sigma(Z,N), \tag{2.34}$$

show far less sensitivity to that mechanism. In these equations $d\sigma(Z,N)$ is the inclusive cross section for a nuclear fragment of charge Z, neutron number N, and a fixed momentum per nucleon. These cross sections ($d\sigma_{ch}$, $d\sigma_{nt}$) measure the matter flow. Therefore, it is most appropriate to compare fluid calculations with summed charge data, Eq. (2.33), or with $d\sigma_{nt}$ when more neutron data become available.[ED1)-(ED3]

Fig. 12 illustrates the results of a hydrodynamic calculation where the transport coefficients were set to zero. In practice, finite numerical cell size effects introduce "numerical" velocity effects.[RA8),(RA15] On a qualitative level, hydrodynamics accounts for the general trend of the energy and angular distributions well. However, the large numerical uncertainties make a quantitative comparison difficult. Those large numerical uncertainties also conceal the variation of the results on the assumed nuclear equation of state. The discrepancy at low energies ($E \leq 20$ MeV) may be due to the absence of fragments heavier than α particles in the experimental points. At low energies, higher mass fragments will increase the experimenta $d\sigma_{ch}$ considerably.

Thus far, the full Navier-Stokes equation could be solved only in the two-dimensional approximation.[TK14),(TK24] Results for the reaction in Fig. 12 are not available. However, estimates[TK22),(TN4] for the effect of viscosity show that the entropy increase is only $\approx$ 20 %. Such effects are not likely to be observable on top of large numerical uncertainties in solving Eqs. (2.29) - (2.31).

We now address the question of the level at which variations of the equation of state can affect the final spectra. In a one dimensional model[TK25] a high precision numerical study showed that the final spectra are remarkably insensitive to the equation of state. Those results can be understood readily from Eq. (2.27). The main driving force for hydrodynamical flow is the pressure in shock zones. However, energy, momentum, and baryon conservations constrain P to be given by Eq. (2.27). All the dependence of P on $W(\rho,T)$ occurs through the dependence of ρ on $W(\rho,T)$ and E. Unfortunately, what Eq. (2.27) shows is that the higher the compression achieved, the less sensitive P is to ρ. Numerical estimates[TK23] have shown that $P(E)$ varies by only $\approx$ 30 % when the compressibility is varied by a factor of 10. Even this modest sensitivity is reduced at higher energies ($E \geq$ 400 A·MeV) as the compression increases. This is then the level at which variations in the equation of state can be expected to show up in hydrodynamical calculations. Clearly it will be necessary to reduce the numerical uncertainties below 10 % and compare to data of the same accuracy if the equation of state is ever to be deduced from nuclear collisions.

Given all the input quantities, S, η, ρ_I, $\cdots$ that also need to be specified in addition to $W(\rho,T)$, it is a highly non-trivial task to pin down $W(\rho,T)$ from data. This situation is aggravated by the contribution to the spectra from non-equilibrium processes (single and double collision terms from surface scattering). Perhaps, multi-component hydrodynamical models[RA8],[TK7] need to be used to handle such non-equilibrium effects. While determining $W(\rho,T)$ from data remains far out of reach at present, we can still look for qualitative features such as collective matter flow predicted by hydrodynamics. The search for signatures of collective flow is one of the "hot" topics of current research as discussed in Sec. 4.1.

2.5. Intranuclear Cascade

In contrast to hydrodynamic models where the dynamics is controlled by the equation of state of bulk nuclear matter, the assumption underlying a cascade model is that the nuclear collision can be described simply as a superposition of elementary nucleon-nucleon collisions. The dynamical input is therefore the free space elastic and inelastic *NN* cross section. In its simplest form[TD1)-(TD5] the cascading of nucleons is assumed to occur along straight line trajectories. These linear or one dimensional cascade models are then used to obtain more realistic distribution functions, $F^{(i)}_{m,n}$ in Eqs. (2.12) and (2.13), than provided by statistical models alone. In practice, though, such models have applicability only for the higher energy ($\geq$ 1 A·GeV) collisions and do not result in substantially better agreement with data than statistical models[RA14),(TG1)-(TG7] alone. However, they have provided insight as to rate of approach to thermal equilibrium. A rule of thumb that has emerged from such studies is that after only 3 collisions the form of the distribution, $F^{(1)}_{m,n}$, becomes insensitive to the detailed form of the *NN* cross section. It is, however, essential to include the direct component ($m = n = 1$) through a Fermi momentum averaged free space *NN* cross section.[TL1),(TL2]

At lower energies ($\leq$ 1 A·GeV), the straight line geometrical assumption is certainly not valid[TB11),(TE2] and the full complication of three-dimensional trajectories has to be treated. The simplest three-dimensional cascade model[TB1),(TB12] can be called literally a "billiard ball" model. Each nucleus is represented by a collection of balls of radius $R = \sqrt{\sigma_{tot}/\pi}$. The cascade then follows the deterministic classical path of multiple billiard ball collisions. Such an approach neglects several important properties of nuclei such as Fermi motion, binding, and the Pauli principle. It has the great virtue, however, of having no parameters, and in this sense it is the cleanest and least ambiguous of the cascade models. A comparison of such a billiard ball calculations[TB12] with inclusive data is presented in Fig. 13. Comparing Fig. 13 with Fig.

12, we see that billiard balls dynamics can reproduce the qualitative trend of the data as well as hydrodynamics. The sensitivity of the inclusive distribution to various assumptions about the scattering properties of the billiard balls was also tested.[TB12] For example, hard sphere scattering was replaced by soft sphere scattering, which involved a random scattering angle at the point of closest approach. The conclusion reached from that study was that within the statistical uncertainties (≈ factor 2) no significant sensitivity of the results on the form of the *NN* cross section was found. This observation confirms the results of statistical models and hydrodynamical models that all the interesting physics (that which depends on the dynamics rather than phase space and geometry alone) is confined to ≈ 50 % modifications of the overall energy and angular distributions.

The most elaborate intranuclear cascade models[TB2]-[TB11] involve Monte-Carlo sampling of the free space *NN* cross sections and include a variety of "realistic" effects such as Fermi motion, etc. Thus, the quantum mechanics of isolated *NN* collisions is incorporated through the use of experimental cross sections, although interference and off-shell effects discussed in Sec. 2.1. are neglected. The most important "realistic" effect which is simulated is Fermi motion. This is included usually by assigning initially each nucleon in the target a random momentum in the Fermi sphere $\Theta(p_F-|\vec{p}|)$. Similarly, each nucleon in the projectile is assigned a random Fermi momentum in addition to the beam momentum per nucleon. The main problem with this prescription is that an artificial energy $\approx \frac{3}{5}(A_P+A_T)\cdot E_F$, with $E_F \approx 35$ MeV, is introduced. For some aspects of the data, such as the yield of high energy ($E \gg E_F$) nucleons, this additional energy is not expected to modify the results significantly. However, for other aspects, such as threshold production, this prescription is likely to yield an overestimate of the pion yield. Furthermore, the low energy fragment ($E \leq E_F$) distribution cannot be correct in this model. On the other hand, for the high energy fragments we have learned that phase space and geometry controlled the gross

features of the data. Therefore, good qualitative agreement is expected and found[TB9] in those cases as shown in Fig. 14.

To correct for the artificial Fermi energy introduced by the above procedure, an effective potential energy V_0 can be included[TB6] such that $\frac{3}{5}E_F + V_0 \approx -8$ MeV. While saturation of nuclear matter cannot be simulated by such a potential, energy conservation is thus insured. The simplest way to include such a potential is to assume that nuclear scattering occurs as in the previous model,[TB4] but that after the collision all nucleons are slowed down according to $\vec{p} \rightarrow \vec{p}\sqrt{1+2mV_0/p^2}$, as they climb out of the nuclear well. A more sophisticated prescription including refraction at the nuclear surface has also been formulated.[TB6] However, none of these prescriptions is satisfactory from a theoretical point of view. Fermi motion and nuclear binding arise from quantum properties of ground state nuclei. Only in the case when the impulse approximation is valid could they be treated as above.

In Fig. 15 the large discrepancy at forward angles and low energies between data and calculation[TB6] is most likely associated with the model of Fermi motion and binding employed. Notice that the results of pure billiard ball calculations[TB12] that include none of these effects (Fig. 13) differ by a factor of ten in that region from those[TB6] in Fig. 15. Not surprisingly, it is possible to construct binding prescriptions[TB4],[TM9],[TP2] that lead to closer agreement with data. We emphasize, however, that the cascade results are rather sensitive to the procedure used to handle Fermi motion and binding. Therefore, intranuclear cascade models are not in fact free of (implicit) parameters. The results depend on many technical details that go beyond the simple billiard ball multiple collision picture for the dynamics.

An example of another technical detail on which the results are sensitive is the method used to suppress multiple collisions with the same pair of nucleons. In Ref. (TB6) two methods were considered: "fast" and "slow" rearrangement. In fast rearrangement, immediately after the projectile scatters with a nucleon in the target,

the whole target density is depleted by one nucleon ($\delta\rho = \rho/A$). In slow rearrangement, only the density within a small radius around the interaction point is depleted. These two technical possibilities lead to a factor ≈ 2 variation in the results. The model in Ref. (TB9) does not suffer from this problem, but in this model the results are sensitive to how nucleons with Fermi motion are assumed to propagate before they interact.

Having emphasized the main loophole in cascade models, it is important to recognize the tremendous versatility of such models. A cascade model automatically provides an approximation to the full A body density matrix, $\rho_A(\vec{x}_1,\vec{p}_1,\cdots\vec{x}_A,\vec{p}_A,t)$. In fact, it is the only dynamical model capable of producing an approximation for ρ_A including multiparticle correlations. As such, cascade models provide the most powerful theoretical laboratory to study[TB10),(TB11] the validity of various simplifying assumptions. In addition, cascade models can be easily generalized to incorporate pion production, rescattering and absorption. This is achieved through Monte Carlo sampling the inelastic $NN \to NN\pi$ cross sections. Furthermore, Remler has developed[TM8)-(TM10] a rigorous framework to calculate composite fragment yields from the cascade data.

The cascade provides the positions and momenta, $\{\vec{x}_i^p(t),\vec{p}_i^p(t);\ i=1,Z\}$ and $\{\vec{x}_i^n(t),\vec{p}_i^n(t);\ i=1,N\}$, for all protons and neutrons as a function of time. Also for each particle the final collision time $\{t_i^p,\ t_i^n\}$ can be recorded. In terms of this cascade "data", the charged and neutral inclusive distributions, Eqs. (2.33) and (2.34), are given by

$$\sigma_{ch}(\vec{p}) = \sigma_r < \sum_{i=1}^{Z} \delta^3(\vec{p} - \vec{p}_i^p(t_i^p)) >, \tag{2.35}$$

$$\sigma_{nt}(\vec{p}) = \sigma_r < \sum_{i=1}^{N} \delta^3(\vec{p} - \vec{p}_i^n(t_i^n)) >, \tag{2.36}$$

where $<\cdots>$ denotes an average over many cascade runs. Recall that σ_{ch} includes all protons whether bound in clusters or not. In this sense σ_{ch} and σ_{nt} can be called the

primordial proton and neutron distributions. From Remler's theory,[TM8]-[TM10] the primordial deuteron distribution $\sigma_{"d"}(\vec{p})$ can also be calculated from the $\{\vec{p}_i^{\,p}, \vec{p}_j^{\,n}\}$ as

$$\sigma_{"d"}(\vec{p}) = \sigma_r < \frac{3}{4}\sum_{i=1}^{Z}\sum_{j=1}^{N} \delta^3(\vec{p} - \vec{p}_i^{\,p}(t_{ij}^*) - \vec{p}_j^{\,n}(t_{ij}^*)) \cdot W_d(r_{ij}, q_{ij}) >, \qquad (2.37)$$

where $t_{ij}^* = \max(t_i^p, t_j^n)$, $r_{ij} = x_i^p(t_{ij}^*) - x_j^n(t_{ij}^*)$, $q_{ij} = p_i^p(t_{ij}^*) - p_j^n(t_{ij}^*)$, and $W_d(r,q)$ is the quantum mechanical Wigner density of the deuteron. Eq. (2.37) measures the total number of deuteron like correlated (n,p) pairs including those bound in heavier fragments.[TM8]-[TM10] Therefore, Eq. (2.37) should be compared to the primordial deuteron distribution

$$d\sigma_{"d"} = d\sigma(1,1) + P_{d/t}\,d\sigma(1,2) + P_{d/He^3}d\sigma(2,1) + P_{d/\alpha}d\sigma(2,2) + \cdots, \qquad (2.38)$$

where $P_{d/A}$ is the *a priori* probability of finding a deuteron in a heavy fragment A, and $d\sigma(Z,N)$ is the inclusive cross section for a final fragment with Z protons and N neutrons for a given energy per nucleon. Simple estimates[TN5] for $P_{d/A}$ yield $P_{d/t} \simeq P_{d/He^3} \simeq 1.5$ and $P_{d/\alpha} \simeq 3$.

The results of cascade calculations[TM9] using the Cugnon code[TB9] and Eq. (2.37) are shown in Fig. 16. A binding potential ($V_0 \approx$ -46 MeV) in each nucleus was used in this calculation to correct the final momentum distribution. It is seen that both the primordial charge and deuteron yields are qualitatively reproduced to within 50 % accuracy. It was found, however, that the deuteron yields are not sensitive to the detailed form of $W_d(r,q)$. Therefore, it appears that phase space and geometry strongly constrain the composite yields as well. A sort of generalized chemical equilibrium seems to be reached. In Sec. 4.2. we will return to the question of deuteron production with regard to question of entropy production.

Pion production was found to be more sensitive to dynamical assumptions. The early calculations[TB6],[TB9] tended to overestimate considerably the pion yield at all energies and angles. Subsequently, more refined calculations including the rescattering have approached the data. However, the pion yield as a function of beam

energy is still predicted to be higher by ≈ 50 % as compared with experiment. As shown in Ref. (TG5), phase space considerations alone lead to the expectation of more pions than actualy observed.[RA14] The origin of this discrepancy is not completely understood yet. However, it should be kept in mind that the pion yield peaks at low momentum in the c.m. frame. For low c.m. momentum pions, $p_\pi \leq 100$ MeV/c, a pion wave packet must overlap a few nucleons at a time especially at high densities. It is thus possible that quantum many body effects become important for production of low energy pions. These could in principle suppress pion production. For further discussion on pion production see Sec. 3.5.

2.6. Non–Equilibrium Quantum Scattering

In addition to the classical models described in the previous section, a new attempt has been made in Ref. (TY3) to formulate a quantum theory for nuclear scattering. The theory is based on the non-equilibrium Green's function diagrammatic technique initiated by Kadanoff and Baym[TY1]. This technique has been proposed already to extend time dependent Hartree Fock methods for low-energy nuclear collisions.[TY2]

In this approach the equations of motion for the one-particle Green's functions

$$G^<(x,y) = i\langle\varphi^\dagger(x)\varphi(y)\rangle \tag{2.40}$$

$$G^>(x,y) = -i\langle\varphi(y)\varphi^\dagger(x)\rangle \tag{2.41}$$

are derived in terms of the proper self energies $\Sigma^{>(<)}$. Here $\varphi(x)$ is the Heisenberg nucleon field operator at space time position $x = (\vec{x},t)$. The expectation value is with respect to some non-equilibrium state, such as two separated Fermi spheres that are prepared at a time t_0. The Kadanoff-Baym equations of motion are [see Eqs. (8) - (27) of Ref. (TY1)]

$$\left(i\frac{\partial}{\partial t_1}+\frac{\nabla_1^2}{2m}\right)G^{\alpha}(x_1,x_1') = \int d^3x_2\,\Sigma_{HF}(\vec{x}_1t_1,\vec{x}_2t_1)\;G^{\alpha}(\vec{x}_2t_1,\vec{x}_1't_1')$$
$$+\int_{t_0}^{t_1} d^4x_2\,(\Sigma^{>}-\Sigma^{<})(x_1,x_2)\;G^{\alpha}(x_2,x_1')$$
$$-\int_{t_0}^{t_1'} d^4x_2\,\Sigma^{\alpha}(x_1,x_2)\;(G^{>}-G^{<})(x_2,x_1') \qquad (2.42)$$

where $\alpha = >$ or $<$. In practice, Σ_{HF}, $\Sigma^{>}$, and $\Sigma^{<}$ are calculated in terms of $G^{>}$ and $G^{<}$ via diagrammatic technique similar to those used in ordinary $T = 0$ many body theory. In the study undertaken in Ref. (TY3), the second order diagrams, corresponding to direct-Born scattering, were included. In this case

$$\Sigma^{>}(x_1,x_1') = \int d^3\vec{x}_2 d^3\vec{x}_2'\;V(\vec{x}_1-\vec{x}_2)V(\vec{x}_1'-\vec{x}_2')G^{>}(x_1,x_1')G^{>}(x_2,x_2')G^{<}(x_2',x_2) \qquad (2.43)$$

where V is the two-body potential. Even with this simplifying approximation, Eq. (2.42) poses a formidable non-linear integro-differential problem. However, in Ref. (TY3) a numerical procedure was devised to solve Eqs. (2.42), (2.43).

In addition to solving Eq. (2.42) directly, an approximate Boltzmann kinetic equation can be derived for the Wigner density $f(\vec{x},\vec{p},t)$ from Eq. (2.42). The necessary assumption is that the gradients in space and time of f are small compared to the characteristic energies and momenta in the problem. Furthermore, it is necessary to assume that the evolution of the system can be approximated by the evolution of a spacially uniform one. In this case f satisfies the Boltzmann equation

$$\left[\frac{\partial}{\partial t}+\frac{\vec{p}}{m}\vec{\nabla}_x\right]f(\vec{x},\vec{p},t) = \Sigma^{<}(\vec{p}\,\omega_p,\vec{x}t)(1-f(\vec{x},\vec{p},t)) - \Sigma^{>}(\vec{p}\,\omega_p,\vec{x}t)f(\vec{x},\vec{p},t), \qquad (2.44)$$

where $\vec{p}$, $\omega_p = p^2/2m$ in the self energies are the Fourier transforms in the relative variables. From Eq. (2.44) $\Sigma^{>}$ and $\Sigma^{<}$ are seen to correspond to the scattering out and in rates.

The question posed in Ref. (TY3) was whether the assumption leading to a kinetic equation (Eq. (2.44)) are in fact satisfied in nuclear collision at energies $200 \leq E_{Lab}/A \leq$

800 MeV. Comparing the numerical results from the quantal equation (2.42) with those from (2.44) considerable differences were found in the final momentum distributions. Instead of reaching rapidly thermal equilibrium as with Eq. (2.44), the quantal evolution was about 50 % slower and non-thermal momentum distributions resulted. The quantal evolution is slowed down because the typical frequencies $\omega \approx 50$ - 100 MeV are comparable to the scattering rates $\sigma\rho v \approx 50$ - 100 MeV in this energy range. Therefore, not as many binary collisions can occur in the quantal case. Based on these calculations Danielewicz claims that quantal dynamics cannot be ignored even at high energies.

These techniques offer the exciting possibility of providing a unified description of both low and high energy nuclear collisions. Clearly, more work is be needed in this area before the results can be applied to experimental data.

3. ELEMENTS OF THE REACTION MECHANISM

3.1. Collision Geometry

Suppose that the projectile nucleus consists of Z_P protons and N_P neutrons ($A_P = Z_P + N_P$) and that the target nucleus consists of A_T nucleons. Then the geometrical cross section, σ_G, is approximately expressed as

$$\sigma_G = \pi r_0^2 \, (A_P^{1/3} + A_T^{1/3})^2, \tag{3.1}$$

with $r_0 \simeq 1.0$-1.2 fm. If a proton inside the projectile hits the target, it is classified as a participant, otherwise it remains as a spectator. An estimate of the average number of participants and spectators can be obtained from Glauber theory.[TW1),(TD1),(TD2),(RA11] The average number of participant protons from the projectile nucleus is approximately given by Z_P multiplied by the ratio of the target cross section to σ_G:

$$<Z_{Proj}^{Parti}> \approx Z_P \cdot \frac{\pi r_0^2 A_T^{2/3}}{\sigma_G} = \frac{Z_P A_T^{2/3}}{(A_P^{1/3} + A_T^{1/3})^2}. \tag{3.2}$$

Similarly we have

$$<Z_{Targ}^{Parti}> \approx \frac{Z_T A_P^{2/3}}{(A_P^{1/3} + A_T^{1/3})^2}. \tag{3.3}$$

The total number of protons assigned to the participant, $Z_{eff}^{(Parti)}$, is thus given by

$$\begin{aligned} Z_{eff}^{(Parti)} &= <Z_{Proj}^{Parti}> + <Z_{Targ}^{Parti}> \\ &\approx \frac{Z_P A_T^{2/3} + Z_T A_P^{2/3}}{(A_P^{1/3} + A_T^{1/3})^2}. \end{aligned} \tag{3.4}$$

Similarly the total numbers of protons assigned to the projectile spectator and target spectator are, respectively, given by

$$\begin{aligned} Z_{eff}^{(Proj\ Spec)} &= Z_P - <Z_{Proj}^{Parti}> \\ &\approx \frac{Z_P \cdot (A_P^{2/3} + 2A_P^{1/3} A_T^{1/3})}{(A_P^{1/3} + A_T^{1/3})^2}, \end{aligned} \tag{3.5}$$

and

$$Z_{\rm eff}^{\rm (Targ\ Spec)} \approx \frac{Z_T\cdot(A_T^{2/3} + 2A_p^{1/3}A_T^{1/3})}{(A_p^{1/3} + A_T^{1/3})^2}. \tag{3.6}$$

The total integrated inclusive cross section of nuclear charge for each of these three regions is, therefore, expressed as

$$\sigma_{\rm tot}^{\rm charge}(i) = Z_{\rm eff}^{(i)} \times \sigma_G. \tag{3.7}$$

In Figs. 17 (a) and (b) the above formula is compared with the data. The observed projectile- and target-mass dependences are reproduced very well by Eq. (3.7). With regard to absolute cross sections, however, the data at large angles fit with Eq. (3.7) at r_0 = 1.2 fm, whereas the data of projectile fragments require r_0 = 0.95 fm which is somewhat smaller than expected. Why do we have a smaller value of r_0 for projectile fragments than for the data at large angles? The participant-spectator model with straight-line trajectories is only an approximation. Because of finite scattering angles, the boundary between spectators and participants is not sharp. The nucleons in the boundary region are more likely to contribute to the large angle yield, thereby depleting the yield near the projectile rapidity. Noticing this fact a more detailed analysis on $\sigma_{\rm tot}^{\rm charge}(i)$ has recently been done in Ref. (TW3). There it is pointed out that, for nearly equal-mass collisions, $Z_{\rm eff}$ for the projectile spectator (or target spectator) is almost equal to $Z_{\rm eff}$ for the participant, contrary to the predictions by Eqs. (3.5)-(3.7) which yield the ratio of $Z_{\rm eff}$ between these two regions to 3/2 for these collisions.

3.2. Evidence for Multiple Collisions

From this section through Sec. 3.6. we study the dynamics for the participant region. The spectator physics will be discussed separately in Sec. 3.9.

We start with the question of what experimental evidence is there for the occurrence of multiple *NN* collisions. The cleanest evidence has been obtained in the measurements of large-angle two-proton correlations.[EC3),(EC4),(EJ9)] In this experiment

four sets of detectors were prepared, as shown in Fig. 18. They were placed at $\vartheta = 40°$ with respect to the beam direction. The azimuthal angular separation between two neighboring counters $\Delta\varphi$ was 90°. Here, the U (up), D (down), and R (right) telescopes were plastic scintillator telescopes and S is a magnetic spectrometer. Proton energies were measured with the spectrometer in coincidence with these telescopes. Consider the ratio, C, defined by

$$C \equiv \frac{2 \times S \cdot R}{S \cdot U + S \cdot D}, \tag{3.8}$$

where $S \cdot R$ indicates the coincidence counts between the spectrometer and the R telescope. If $C > 1$, then two protons tend to be emitted on the opposite side but within the same reaction plane. This ratio may thus be called the ***degree of coplanarity***. If multiple NN collisions are dominant, the ratio C would be close to one, because the particle emission tends in that case to be statistical. On the other hand, if only the first NN collisions are important, this ratio would be larger than one, because pp quasi-elastic scatterings induce two-proton emission in the same reaction plane. In 800 A·MeV C + C collisions the observed ratio, C, is larger than one and has a peak at the exact momentum which is expected from pp quasi-elastic scatterings, as shown in Fig. 18. Therefore, this experiment clearly demonstrates the importance of single-NN-collision processes.

However, the data of Fig. 18 also show the existence of multiple NN collisions. If all protons suffered only one NN collision, without subsequent second or third collisions, then the calculated peak height of $(C\text{-}1)$ would be about six times larger than the observed one. This fact implies that the coplanar two-proton correlation is diluted by the presence of multiple NN collisions. The coplanar correlation seen in Fig. 18 originates from the process in which both protons after the first collision are not rescattered thereafter. If one of a pair of protons in a pp quasi-elastic scattering is rescattered, then the coplanar correlation decreases. Therefore, the probability that a nucleon experiences only one NN collision is given approximately by $\sqrt{1/6} \simeq 0.4$, where

1/6 is the dilution factor of (C-1). In other words, the probability for each nucleon to experience multiple NN collisions is about 0.6 in 800 A·MeV C + C collisions. This number is consistent with several recent theoretical calculations from cascade,[TB9] linear-cascade,[TD2] transport,[TE4] and phase-space[TG4] models.

The probability that a nucleon does not suffer an additional collision after the first one is given approximately by $\exp(-R/\lambda)$, where λ is the mean free path of nucleons inside the nucleus and R is the radius of the interaction region. Recent measurements of two-proton correlations in proton-nucleus collisions[EJ12] have determined the value of λ to about 2.4 fm at 800 MeV based on such considerations.[EJ12] Values of R for various nuclear collisions have been determined to 2-4 fm by a large number of experiments; two-pion interferometry,[EJ3],[EJ6],[EJ13],[EJ15] two-proton interferometry,[EJ14] composite spectra,[EE2],[EC7] and pion spectra.[TH4] These values are consistent with a simple expectation from the participant-spectator model in which R is given by $r_0[P\cdot(\rho_0/\rho)]^{1/3}$, where P is the nucleon number involved in the participant region and ρ is the density. $R \simeq 2$ fm is estimated for C + C. Therefore, we have $\lambda \simeq R$ for this system implying that $\exp(-R/\lambda) \approx 0.4$. This value is consistent with that obtained from the study of two-proton correlations discussed above.

It is expected that the probability of multiple NN collisions increases as projectile and target masses increase. Reflecting this expectation, the evidence of pp quasi-elastic scatterings is observed only for light-mass nuclei (up to Ar + Ar). Two-proton correlations in heavier-mass combinations such as Ar + Pb exhibit a completely different feature, as we will describe it later in Sec. 4.1. In the presence of frequent multiple collisions global collective flow phenomena might occur. Such global flow aspect is discussed later in this article. In this section we concentrate on the *microscopic* aspect of multiple NN collisions from the spectra of protons, composite fragments, pions and strange particles.

3.3. Inclusive Proton Spectra

Much proton data has become available in the past few years.[EC1)-(EC7)] In Fig. 19 the proton energy spectra at c.m. 90° from three sets of nearly equal-mass nuclear collisions, C + C, Ne + NaF, and Ar + KCl are shown.[EC4),(EC7)] Invariant cross sections, defined by Eq. (A.13), are plotted as a function of the kinetic energy, $E_p^{c.m.}$. The nominal beam energy was 800 A·MeV for all cases. These data tend to reflect the dynamics of the participant region, because at $\vartheta_{c.m.} = 90°$ the influence from the spectator is the smallest.

Three features are observed in the data. First, the spectrum shape is nearly identical for all cases. This fact suggests that the beam energy per nucleon, rather than the total beam energy, determines the major feature of a proton emission. This is consistent with an expectation that the nuclear collision at high energies is, to a first order approximation, a superposition of individual *NN* collisions. Secondly, a copious production of high-energy protons is observed, which now cannot be explained as a superposition of single *NN* collisions. If we ignore the Fermi motion, the maximum proton energy is 182 MeV in this case. Even if we include a Gaussian-type Fermi momentum distribution, the emission of these high-energy protons cannot be explained,[TG6)] as shown in Fig. 19. Thirdly, in this high-energy domain the spectrum shape approaches an exponential, although it deviates substantially from it at low energies.

The observed cross sections shown in Fig. 19 can be parameterized,[EC7)] to a good approximation, as

$$E \frac{d^3\sigma}{d^3p} \propto A^{\alpha}, \tag{3.9}$$

where A is the projectile (and target) mass. Observed values of $\alpha = \alpha(E_p^{c.m.})$ are displayed in Fig. 20 for various c.m. kinetic energies, $E_p^{c.m.}$. For low-energy protons the value of α is very close to the geometrical limit of 5/3. In this limit the cross section is

proportional to the product of the participating nucleon number ($\propto A$) times the geometrical cross section ($\propto A^{2/3}$) [see also Eq. (3.7)]. However, in the high energy region the power α exceeds 2 and finally reaches the value of 2.6 or 2.7 at the highest energy observed in this experiment. Such a large value of α strongly suggests that multiple *NN* collisions are important for the production of high-energy (in this case high-p_T) protons.

An extreme limit of multiple collisions is the thermal process. In this case the spectrum shape is of a Boltzmann type [Eq. (2.16)]. Therefore, the exponential behavior for high-energy protons seems consistent with the thermal-model expectation. However, in the thermal limit the power α is predicted to coincide with the geometrical limit of 5/3.[TE6] Therefore, the observed power dependence indicates that high-energy protons are produced through several but not too many *NN* collisions. Then, how many nucleons are involved? This question has been studied by several groups.[TD3],[TG4],[TE6] According to a recent calculation by Schürmann and Macoc-Borstnik,[TE6] the average number of *NN* collisions, $<n>$, monotonically increases as the observed proton energy increases. The value of $<n>$ evaluated from this calculation is $\approx$ 3 for $E_p^{c.m.} \approx$ 200 MeV and $\approx$ 4-5 for $E_p^{c.m.} \approx$ 800 MeV for the Ar + KCl system.

3.4. Composite Formation

In certain regions of momentum space a significant fraction of nucleons emerge by composite fragments such as d, t, ^{3}He etc.[EC6] We consider in this section how these composite fragments are created. An additional implication of composite fragments, which is related to entropy, will be discussed separately in Sec. 4.2.

According to a simple phase space consideration, we expect that the probability of forming a deuteron at a velocity $\vec{v}_d$ is proportional to the product of the probabilities of finding a proton and a neutron at the same velocity:

$$P_d(v = v_d) \propto P_p(v = v_d) \cdot P_n(v = v_d). \tag{3.10}$$

For relatively high energy fragments ($E/A \geq 50$ MeV) the neutron spectra can be replaced by the proton spectra.[ED3] Then, the cross section of a composite fragment with mass number A would be given by

$$E_A \frac{d^3\sigma_A}{d^3p_A} = C_A \cdot \left[E_p \frac{d^3\sigma_p}{d^3p_p} \right]^A \qquad \text{for } p_A = A \cdot p_p, \tag{3.11}$$

where C_A is a constant. The validity of the above power law was first tested with 250 and 400 A·MeV Ne beams,[EE1] as shown in Fig. 21. Eq. (3.11) holds remarkably well with one normalization constant C_A. Recently it was demonstrated for light-mass composite fragments[EE2),(EE3),(EC7] that this power law holds very well over a much wider kinematic domain than reported in Ref. (EE1), although a slight deviation from Eq. (3.11) is observed for heavy-mass composite fragments.[EF4]

In order to study this power law in more detail the ratios of *observed* deuteron cross sections to the squares of *observed* proton cross sections are displayed in Fig. 22 for Ne + NaF collisions at three bombarding energies, 0.4, 0.8, and 2.1 A·GeV.[EC7] The value of C_A is about 15×10^{-6} in units of $[(\text{mb} \cdot \text{GeV})/(\text{sr} \cdot (\text{GeV}/c)^3)]^{-1}$, and it is almost independent of deuteron momentum as well as deuteron emission angle. In addition, the value of C_A is almost independent of the projectile energy.

To what extent does the power law of Eq. (3.11) hold in different theoretical models? Assume that the particle density per unit phase space volume is given by $f(\vec{p})$ such that

$$\frac{1}{V} \frac{d^3n}{d^3p} = f(\vec{p}), \tag{3.12}$$

where V is the phase space volume. Then, the ratio C_A is given by

$$C_A = \left[\frac{1}{\gamma V} \right]^{A-1} \frac{f(\vec{p}_A)}{[f(\vec{p}_p)]^A} \qquad \text{for } \vec{p}_A = A \cdot \vec{p}_p, \tag{3.13}$$

where γ is the Lorentz factor of a particle measured in the frame at which Eq. (3.12) is

defined. In the simple fireball model,[EC1]

$$f(\vec{p}) \propto e^{-E/T}, \tag{3.14}$$

where E is the kinetic energy of an emitted particle and T is the temperature. Consequently, C_A is given by[TM4]

$$C_A = \frac{\text{const.}}{(\gamma V)^{A-1}}. \tag{3.15}$$

The range of γ is 1 - 2 for the data shown in Fig. 22. Therefore, within a factor two this fireball model seems to agree with the observed fact the C_A is almost constant.

However, it is now known that the simple fireball model needs to be modified substantially in order to explain the observed large angular anisotropy of various light fragments.[EC7] For this purpose the firestreak model[TJ4],[TJ5] was proposed and it has been used often to fit the experimental data.[RA14] In this model the nucleus is divided into several tubes with each tube-tube collision leading to a contribution as in Eq. (2.16). Therefore, the temperature is different from tube to tube, and $f(\vec{p})$ is now given by a superposition of firestreaks as

$$f(\vec{p}) = \sum_i a_i e^{-E/T_i}. \tag{3.16}$$

In this case C_A is no longer constant and has a strong fragment-energy dependence, as shown in Fig. 22. For example, the predicted value[TJ5] of C_A in the case of 400 A·MeV at 30° (left upper corner in Fig. 22) varies from 5 to 20, depending on the fragment energy, and this clearly disagrees with the data. This fact implies that composite fragments are unlikely to be produced from a macroscopic chemical equilibrium.

Another model is the coalescence model.[TM1],[TM2] According to this model the power law follows because nucleons located within a radius of p_0 in the momentum space are assumed to stick together to form a composite fragment. In this case C_A is given by[EE1],[EE2]

$$C_A = \frac{(N_S/Z_S)^y}{x!y!A^2}\left[\frac{4\pi p_0^3}{3m\sigma_0}\right]^{A-1}, \tag{3.17}$$

where p_0 is called the coalescence radius. Here, x and y are, respectively, the proton and neutron numbers in the composite particle ($A = x + y$); Z_S and N_S are, respectively, the proton and neutron numbers of the projectile plus target system ($Z_S = Z_P + Z_T$ and $N_S = N_P + N_T$), m is the nucleon mass, and σ_0 is the nucleus-nucleus reaction cross section which is given by Eq. (A.14). In this model the cross section of composite fragment A is expected to be proportional to the A^{th} power of the primordial nucleon cross section, since the *a priori* probability of finding A nucleons within a momentum radius p_0 of $\vec{p}$:

$$\sigma_A \propto [p_0^3 \sigma_{ch}(\vec{p})]^A. \tag{3.18}$$

However, the experimental fact is that the power law holds using the *observed* proton cross sections. Of course, if the cross section for protons is much larger than that for composite fragments, there is no significant difference between σ_{ch} and σ_p. But, in certain kinematic regions the ratio of protons to composite fragments is close to one. Still, the power law holds empirically using the *observed* proton cross sections.

It is very hard to reconcile the constancy of C_A with angle, momentum, and beam energy in Fig. 22 with chemical equilibrium models.[RA14] For the very light nuclear system such as Ne + NaF, however, a macroscopic thermodynamic description is least likely to hold. In this case a microscopic approach such as described in Sec. 2.5 is more appropriate. Up to now such detailed comparison with data for heavy system has not been made. Thus, it is not known whether chemical equilibrium is indeed reached for large A.

Assuming chemical equilibrium Mekjian[TJ3] showed that an estimate of the interaction volume V can be obtained from Eq. (3.13), in the limit that the intrinsic radius of a composite particle is negligibly small compared to the source radius $R = (3V/4\pi)^{1/3}$. A generalization of this idea was proposed in Ref. (TM5).

Empirically,[EK2),(EE2)] the interaction radii obtained in this way are reasonable (a few Fermis), but the quantitative accuracy of these radii cannot be assessed at this time.

3.5. Pion Production

For beam energies of ≈ 1 A·GeV the dominant secondary particles created in collisions are pions. At these energies the pion production proceeds mainly from Δ_{33} excitation of nucleons. Some of pions are then absorbed inside the media through $\pi NN \rightarrow NN$, or they are rescattered through $\pi N \rightarrow \pi N$. Since a typical cross section of $\sigma_{tot}(\pi N)$ is 100-200 mb which is much larger than $\sigma_{tot}(NN)$ (≈ 40 mb), pion spectra tend to freeze out at a later stage than nucleons.[TA9),(TA10)]

In this section we describe the excitation function, multiplicity, energy and angular distributions, subthreshold pion production, pion interferometry, and a test of coherent pion production. Some of pion data at forward and backward angles will be discussed separately in Sec. 3.8. in connection with scaling.

3.5.1. Excitation function and multiplicity distribution

Using a streamer chamber, multiplicities of both negatively and positively charged tracks have been measured.[EG3),(EJ10),(EJ13)] Negative charges are mostly from π^- while positive charges contain both π^+ and charged nuclear fragments. For nearly equal-mass collisions with $Z \simeq A/2$ we expect $m(\pi^-) \simeq m(\pi^+)$, where m is the multiplicity. Therefore, to a good approximation, the difference in numbers between positive- and negative-charge tracks is almost equal to the multiplicity of charged nuclear fragments, m_Z.

The average multiplicities, $<m_\pi>$ and $<m_Z>$, have also been measured from inclusive spectra with a magnetic spectrometer.[EC7)] These quantities are related to the total integrated inclusive cross section through Eq. (A.16). We discuss in this section (1) the beam-energy dependence of $<m_\pi>/<m_Z>$, (2) distribution of m_π at a

fixed value of m_Z, (3) correlation between m_π and m_Z, and (4) the projectile- and target-mass dependence of $\langle m_\pi \rangle$ and $\langle m_Z \rangle$.

We expect that the production rate of pions increases as the beam energy increases, whereas the number of participant nucleons is almost independent of the beam energy, as shown in Fig. 17 (b). In Fig. 23 the observed ratios, $\langle m_\pi \rangle / \langle m_Z \rangle$, for almost equal-mass collisions are displayed. The streamer-chamber data agree well with the data obtained from inclusive spectra. The ratio smoothly increases as the beam energy increases. No sudden increase in the pion yield at a certain beam energy is observed. Theoretical predictions[TK18),(TG5),(TJ5),(TF4),(EC7)] generally agree with these data to within a factor of two.

According to the participant-spectator model the value of m_Z is directly related to the impact parameter, since once the impact parameter is fixed, the number of participant nucleons is almost uniquely determined by the geometry. Correlations between m_π and m_Z provide information on the impact parameter dependence of the pion yields. Fig. 24 shows the pion multiplicity distribution for events with $m_Z \geq 30$ for Ar + KCl collisions in a streamer chamber.[EJ10] Since the maximum value of m_Z is $Z_P + Z_T = 36$ in this case, the collision is almost head-on; the corresponding maximum impact parameter, b_{max}, is about 2.2 fm. The observed distribution is of a Poisson type which has been expected on very general theoretical grounds.[TG2] In this Poisson distribution the square of dispersion, D^2, must be proportional to the average multiplicity, $\langle m_\pi \rangle$. The linear relation between D^2 and $\langle m_\pi \rangle$ was confirmed for various values of m_Z in Ar + KCl collisions,[EJ10] although a certain deviation from the Poisson type is reported in Ref. (EJ13) for Ar + Pb collisions.

In Fig. 25 the correlations between m_π and m_Z are shown. For Ar + KCl an almost linear correlation between these two quantities is observed.[EJ10] In the data for non-equal-mass collisions, such as Ar + Pb,[EJ13] however, a deviation from the linear correlation is observed. In this case, the value of $m(\pi^-)$ is not equal to that of $m(\pi^+)$,

since $N \neq Z$. Therefore, plotted in Fig. 25 (right) is the multiplicity correlation between π^- and the total charged particles (which include both positively and negatively charged particles). The unusual features of the correlations for Ar + Pb have not been explained up to now.

Finally we describe the projectile- and target-mass dependence of $<m_\pi>$. Plotted in Fig. 26 (a) are the observed values of $<m_\pi>$[EC7] as a function of the average participant nucleon number, P, for various projectile and target combinations at E_{Beam} = 800 A·MeV. Here the value of P was evaluated from Eq. (3.4). The multiplicity is parametererized roughly as[EK1),(EK2)]

$$<m_\pi> = a \cdot P^x, \tag{3.19}$$

with $x \simeq 2/3$. This suggests that the pions are emitted from the surface of the participant region and not from the deep inside of this region. We observe in Fig. 26 (b) that $<m_Z> \propto P_Z$, where P_Z is the average nuclear charge involved in the participant region evaluated from Eq. (3.4). Therefore, the $P^{2/3}$ dependence of $<m_\pi>$ suggests the importance of pion absorption process.

On the other hand, in Fig. 25 there was a linear dependence of $m_\pi \propto m_Z$ for Ar + KCl. To reconcile the $P^{2/3}$ dependence suggested in Fig. 26 and the P^1 dependence in Fig. 25, we note that several asymmetric reactions ($A_P \neq A_T$) have been included in Fig. 26. Omitting those reactions leave only three data points which are consistent with a P^1 dependence for symmetric system. A possible explanation of this effect is that for asymmetric collisions a larger piece of cold spectator matter remains to absorb pions. The bigger the asymmetry, A_P/A_T, a higher fraction of the produced pions can be therefore reabsorbed. While pions are produced only by participants, the absorption process is considerably complicated by the presence of spectators. What Fig. 26 clearly demonstrates is that pion absorption cannot be neglected in theoretical models.

3.5.2. Energy and angular distributions

Next we consider the energy and angular distributions of pions.[EA3),(EB1)-(EB8),(EC3),(EC7),(EG2)-(EG9),(EM1)-(EM5)] In Fig. 27 the energy distributions of negative pions at 0° [Ref. (EB6)], 180° [Ref. (EM5)], and at 90° [Ref. (EC7)] are compared in the c.m. frame at E_{Beam} = 2.1 A·GeV. Although no direct comparison is possible for the same projectile and target combination, we observe that the energy distribution is almost of exponential at any emission angle. It has been known that for projectiles heavier than α particles the spectrum shape approaches exponential.[EK2),(EB6),(EA3)]

In Fig. 28 the energy spectra at c.m. 90° in Ne + NaF collisions are plotted for beam energies from 0.2 to 2.1 A·GeV.[EC7),(EG9)] At any beam energy the spectrum shape is approximately exponential:

$$E\,\frac{\mathrm{d}^3\sigma}{\mathrm{d}^3p} \propto \exp(-E_\pi^{\mathrm{c.m.}} / E_0). \tag{3.20}$$

In Fig. 29 the observed values of the slope factor E_0 are plotted as a function of the beam energy per nucleon in the c.m. frame. E_0 increases monotonically as the beam energy increases. In addition, we notice that the value of E_0 for pions is consistently smaller than that for high-energy protons (see Fig. 19 for the definition of E_0).

Several ideas have been proposed to explain the observation of $E_0(\pi) < E_0(p)$, in terms of (1) finite mean free path effects, (2) radially exploding flow[TK12], and (3) phase space[TG4),(TG5)]. In nuclear matter, the mean free path of protons (≈ 2 fm) is generally longer than that of pions (> 0.5 fm). Therefore, pions may be more sensitive to the late colder stage of the collision than protons [possibility (1)]. The radially exploding flow possibility will be discussed in Sec. 4.1. A third possibility is related to the *NN* kinematics. In order to create pions the 140 MeV rest-mass energy has to be supplied. Then, the average kinetic energy available for pions is less than that for protons. From the comparison between the protons and pions alone, it is hard to prove which of these

mechanisms is the most important. With the aid of K^+ spectra, a partial answer is obtained, as we will discuss in Sec. 3.6.

A typical angular distribution is shown in Fig. 30. Here the ratios of the π^- cross sections between 30° and 90° in the c.m. frame for 800 A·MeV Ar + KCl collisions[EC7] are plotted as a function of the pion energy in that frame. The ratio has a peak at $E_\pi^{c.m.} \simeq 100$ - 200 MeV. This feature is consistent with the expectation that most pions arise from Δ_{33} resonances, which are observed in $NN \rightarrow NN\pi$ reactions to produce pions anisotropically with a c.m. energy of ≈ 200 MeV.

Much attention has focused recently on the detailed structure for low-energy pions. Wolf *et al.*[EG5] and Nakai *et al.*[EG7] reported a broad 90° peak for π^+ at $E_\pi^{c.m.} \simeq$ 10-20 MeV in Ar + Ca and Ne + NaF collisions at beam energies of 0.8-1.0 A·GeV. The peak is about 20-30 % above the smooth backgrounds. Theoretically, it has been suggested that Coulomb effects might be responsible for creating such a broad peak.[TR1],[TR2] Therefore, Frankel *et al.*[EG8] have recently measured both π^+ and π^- with a magnetic spectrometer in 1.05 A·GeV Ar + Ca collisions, the same projectile and target combinations used by Wolf *et al.* They have observed larger yields for π^- than for π^+, most likely due to Coulomb effects. However, these data show less evidence of the peaking for π^+. Further experiments are necessary to clarify this situation.

3.5.3. Subthreshold pion production

In nuclear collisions at laboratory beam energies below 290 A·MeV (which is the pion production threshold energy in free NN collisions), the pion production is due either to the nucleon Fermi motion or to an accumulation of available energy greater than $m_\pi c^2$ through successive NN collisions. Benenson *et al.*[EB3] have measured both π^- and π^+ at 0° in Ne + NaF collisions and showed that pions are produced even at a beam energy of 80 A·MeV, as seen in Fig. 31. At c.m. 90° the subthreshold pion production has been studied in 183 A·MeV Ne + NaF collisions,[EG9] as shown in Fig. 28. The kinetic energy of the observed pion extends up to 250 MeV in this frame, and the

spectrum shape is nearly exponential over the entire energy region. If we ignored the Fermi motion, a large number of nucleons (up to 9) would have to share their kinetic energies in order to create these pions. In terms of single NN collisions a large Fermi momentum has to be assumed; in this case, if both projectile and target nucleons carry the same Fermi momentum in opposite directions, then a virtual momentum ≈ 350 MeV/c for both nucleons has to be assumed.

Previous thermal[TJ2),(TJ5)] and hard-scattering[TF3)] models underestimate the cross section at 0°. However, recently it was pointed out[TF9)] that, if we use the experimental data of $pp \rightarrow \pi$ and $pn \rightarrow \pi$, together with a realistic Fermi-momentum shape that fits the (e,e') data, then the hard-scattering model explains reasonably well the observed data at 0°. The exponential shape at 90°, on the other hand, cannot be explained by hard scatterings alone. It is reproduced only when πN rescatterings after the creation of pions are taken into account,[EG9)] as shown in Fig. 28. The phase-space model[TG7),(EG9)] also explains qualitatively the exponential shape at 90°. In this model, kinematic and chemical equilibrium are assumed (see Sec. 2.3.). For the creation of 250 MeV pions at 183 A·MeV in Fig. 28 about eight nucleons have to be involved. The qualitative agreement of the data with both of these approaches suggests that the microscopic rescattering and absorption effects are effectively replaced by the statistical behavior of a rather large number of nucleons.

3.5.4. Pion interferometry

As Fig. 24 shows, there is a large probability of producing two or more π^- in nuclear reactions at high energies. Because pions are bosons, the wavefunction of the multipion system must be symmetrized. This symmetrization leads to interference phenomena at small relative momenta. In astronomy such ($\gamma\gamma$) interference effects were first used by Hanbury-Brown and Twiss[TQ1)] to measure stellar radii. Later Goldhaber *et al.*[TQ2)] used $\pi^-\pi^-$ correlations to determine the size of $\bar{p}p$ interactions. Analogously, it has been proposed that pion interferometry could provide information

on the space-time history of nuclear collisions.[TQ5]-[TQ8]

The basis for pion interferometry is the observation that the amplitude Ψ_{12} to measure two pions with four momenta (k_1,k_2), given that they were produced at space-time points (x_1,x_2), is

$$\Psi_{12} \approx \frac{1}{\sqrt{2}}[e^{-ik_1x_1}e^{-ik_2x_2} + e^{-ik_1x_2}e^{-ik_2x_1}]. \tag{3.21}$$

Therefore, the probability of observing (k_1,k_2) is

$$P(k_1,k_2) \propto \int |\Psi_{12}(x_1,x_2)|^2\rho(x_1,x_2)\, d^4x_1 d^4x_2, \tag{3.22}$$

where $\rho(x_1,x_2)$ is the probability density that two pions were created at points (x_1,x_2). Assuming uncorrelated production, $\rho(x_1,x_2) = \rho(x_1)\rho(x_2)$, Eq. (3.22) reduces to

$$P(k_1,k_2) \propto 1 + |\rho(k_1-k_2)|^2, \tag{3.23}$$

where $\rho(q)$ is the space-time Fourier transform of the source distribution $\rho(x)$. For a Gaussian source with radii R_i and lifetime τ we have[TQ6]

$$P(k_1,k_2) \propto 1 + \exp[-(q_x^2R_x^2 + q_y^2R_x^2 + q_z^2R_z^2 + \omega^2\tau^2)/2]. \tag{3.24}$$

where

$$\vec{q} = \vec{k}_1 - \vec{k}_2, \tag{3.25}$$

and

$$\omega = \sqrt{k_1^2 + m_\pi^2} - \sqrt{k_2^2 + m_\pi^2}\ . \tag{3.26}$$

Therefore, measurements of $P(k_1,k_2)$ can in principle reveal the three dimensional spatial structure and the lifetime of the pion source. In practice, final state interactions especially Coulomb interactions must be treated carefully to eliminate optical distortions.[TQ7]

In addition, Eq. (3.24) holds only if the pions are produced uncorrelated. Dynamical correlations can be induced in many ways. In Ref. (TQ8) it was shown that absorption of pions by the spectator fragments could alter significantly the form of P. Also, if collective phenomena such as pion condensation would occur in nuclear

collisions, the form of P would be very different. Therefore, pion interferometry is not only a tool to study reaction geometry but also a tool to uncover novel dynamic phenomena.

Experimentally the following ratio, $C_2(\text{exp})$, is usually measured:

$$C_2(\text{exp}) \equiv \sigma_0 \frac{d^2\sigma/d\vec{k}_1 d\vec{k}_2}{(d\sigma/d\vec{k}_1)\cdot(d\sigma/d\vec{k}_2)} \qquad (3.27)$$

where the denominator, $d\sigma/d\vec{k}$, is the single-particle inclusive cross section. This quantity, $C_2(\text{exp})$, is directly related to Eq. (3.24). The measurement of $C_2(\text{exp})$ was first performed in a streamer chamber with 1.8 A·GeV Ar beams.[EJ4] Here, the numerator in Eq. (3.27) was replaced by the coincidence counts between two negative pions and the denominator by the product of inclusive counts of π^+ and π^-. From the best fits to the data the reaction time of $\tau \approx 5 \times 10^{-24}$ s and the reaction size of $R \simeq$ 3-4 fm were obtained. This value of R is consistent with what we expect from the participant-spectator model with normal nucleon density. It is also consistent with the value obtained from composite fragments[EC7],[EE3],[EK2] In addition, $C_2(\text{exp}) \simeq 2$ at $|\vec{q}| \simeq 0$ is evidence against coherence effect.

After this experiment a large amount of data of pion interferometry have been collected. Lu *et al.*[EJ13] have continued their streamer chamber analysis and reported recently that the radius R increases as the event multiplicity increases. This is consistent with a naive expectation, since more nucleons are involved in collisions for higher event multiplicities. The Dubna streamer chamber[EJ6] also demonstrated results which give reasonable values of the collision size. Zajc *et al.*[EJ15] have performed extensive measurements using a magnetic spectrometer and obtained the results with much higher statistics. Their typical result is shown in Fig. 32, which leads to $R = 3.0 \pm 0.3$ fm for 1.8 A·GeV Ar + KCl system. Whether $C_2 = 2$ at $|\vec{q}| \simeq 0$ depends on the normalization of the data of Eq. (3.27). They have tried various possibilities on the value of σ_0. At present, however, there is no indication for a deviation of C_2 from 2.

In the analysis of the data shown in Fig. 32 it was pointed out that actual two-pion spectra are affected significantly by final state interactions. These interactions originate both from Coulomb and strong interactions, and especially from the former because $\pi^-\pi^-$ (T = 2) strong interactions at small relative momentum are very small. Therefore, the observed widths do not immediately reflect R and τ. Coulomb corrections of the two-pion spectra change significantly the shape of the correlation function.

It is also worthwhile to mention here the data on two-proton interferometry. In this case the correlation function, C_2, becomes 0 at $|\vec{q}| = 0$, because fermion wavefunctions must be antisymmetrized. Zarbakhsh *et al.*[EJ14] have recently measured C_2 for two protons in 1.8 A·GeV Ar + KCl collisions, as shown in Fig. 33. The observed correlation function does not show a simple interference pattern. Instead, it shows a peak at $|\vec{q}| \simeq 20$ MeV/c, most likely due to the strong final state interactions between two protons.[TQ5] In this case both repulsive Coulomb and attractive strong interactions are important. The strong interaction induces a positive correlation while the Coulomb interaction induces a negative correlation, resulting in a peak at a certain momentum.[TQ5] In this experiment, a smaller source radius is observed for proton emission at $y = (y_P+y_T)/2$ than at $y = y_P$, where y_P and y_T are the projectile and target rapidities, respectively. In addition, a much smaller radius is obtained for higher event multiplicity. The last statement is not consistent with the result of two-pion interferometry.[EJ13] However, the great differences in in final state interactions between pp and $\pi^-\pi^-$ makes it difficult to evaluate the significance of this latter result.

3.5.5. Test for coherent pion production

Since the early work on pion condensation[TA4],[TA5] many attempts have been made to look for exotic phenomena in nuclear collisions. In this section we review a new test for possible pion field instabilities in such reactions.

If a spin-isospin instability occurred under the extreme conditions generated in nuclear collisions, then the nuclear axial (spin-isospin) current $\vec{J}_{\mu 5}(\vec{x},t)$ would acquire a non vanishing expectation value. This current is coupled to the pion field through the field equation

$$(\Box + m_\pi^2)\,\vec{\pi}(x) = g_\pi \partial^\mu \vec{J}_{\mu 5}(\vec{x},t). \qquad (3.28)$$

Therefore a time varying $\vec{J}_{\mu 5}$ will act as an antenna radiating pions. Such a radiation is furthermore characterized by a coherent state. In Ref. (RA13) the unusual properties of such a pion field were discussed. An estimate of the number of such pions per baryon showed that $n_{\pi^-}/A \approx 10^{-4}$, which is much smaller than the number $n_{\pi^-}/A \approx 10^{-2}$ expected from the usual incoherent processes ($NN \rightarrow NN\pi$). Thus, contrary to naive expectation pion condensation is not expected to lead to copious pion production.

To detect such a small signal requires that the background incoherent component be reduced. As seen in Fig. 28, this can be achieved by reducing the beam energy. At $E_\pi^{c.m.} \approx 200$ MeV at $\vartheta_{c.m.} = 90°$ the pion cross section falls by five orders of magnitude as the beam energy is lowered from 2.1 A·GeV to 183 A·MeV. The tiny signal due to coherent pions should be visible as a bump at $E_\pi^{c.m.} \approx 200$ MeV at $E_{Beam} = 183$ A·MeV. As seen in Fig. 28, only a smooth exponential spectrum is observed consistent with incoherent phase-space models. Although no bumps are observed in Ne + Pb collisions as well,[EC9] an interesting experiment that has not yet been performed is to look at this subthreshold π^- spectra with much heavier nuclei such as U + U. It is possible that collective phenomena could occur for such a heavy system. In any case, Fig. 28 shows a method to search for a needle in a haystack. In this case there is only hay.

3.6. Strange Particle Production

In Fig. 34 threshold energies for particle production in nucleon-nucleon collisions are displayed. As the beam energy increases, the production of strange particles becomes possible. At beam energies of around 2 A·GeV the production of K^+ [Ref. (EH1)], Λ [Ref. (EH2)], and K^- [Ref. (EH3)] have been now measured. We discuss these data below.

The motivation of measuring K^+ is as follows: Since the cross section of $K^+ + N$ [$\sigma(K^+N) \simeq 10$ mb] is much smaller than that of $N + N$ [$\sigma(NN) \simeq 40$ mb] or $\pi + N$ [$\sigma(\pi N) \simeq 100$ mb],[MB1] K^+ is less likely to be rescattered by surrounding nucleons in contrast to π or N. In other words, the spectrum of K^+ may be a useful messenger of the violent initial, and perhaps, very compressed and hot stage in the nuclear collision.

Schnetzer *et al.*[EH1] have measured K^+ spectra with a magnetic spectrometer. In Fig. 35 an example of energy spectra in the c.m. frame is plotted for 2.1 A·GeV Ne + NaF collisions. The spectrum shape is almost exponential with inverse exponential slope, $E_0 \simeq 142$ MeV. This value of E_0 is larger than E_0 for protons or pions (see Fig. 29), suggesting that K^+'s seem to be created at a more violent stage than pions or protons. The exponential behavior of the spectrum is a general feature found for any projectile (even p or d) on nuclear targets. In addition, the angular distribution of K^+ is almost isotropic in the NN c.m. frame, again for any projectile on nuclear targets.

It is interesting to compare the value E_0 for K^+ with E_0 for pions and protons (see Sec. 3.5.2.). If the slope E_0 is determined mainly by the mean free path of product particle, then we expect

$$E_0(\pi) < E_0(p) < E_0(K^+), \tag{3.29}$$

since $\lambda(\pi) < \lambda(p) < \lambda(K^+)$. This relation Eq. (3.29) agrees with the experiment. On the other hand, in a phase space model we may expect

$$E_0(K^+) < E_0(\pi) < E_0(p), \tag{3.30}$$

since the threshold energy of K^+ production is much higher than that of π production. Thus, when K's are produced less energy is available for kinetic energy. The observation that Eq. (3.29) is satisfied suggests that the pions and nucleons are "cooled" down more in the expansion phase because of their shorter mean free paths. We also note that Eq. (3.29) is not consistent with the model of radial explosive flow,[TK12] since in that case $E_0(\pi) < E_0(K^+) < E_0(p)$ because $m_\pi < m_K < m_p$ (see Sec. 4.1.).

According to Randrup and Ko,[TU1] high energy tails can be explained neither by Fermi motion nor by the multiple NN collisions during the compression stage. It is explained only if we allow at most one rescattering of K^+ by surrounding nucleons after the creation of K^+ (the average number of rescattering is estimated to be 0.68).[TU2] However, this calculation fails to reproduce the angular distribution, especially for the case of proton + nucleus collisions. Therefore, this point still remain an open question.

An interesting aspect of K^+ data is seen in the A dependence. If the cross section is parameterized as a power of A_T ($\propto A_T^\alpha$), then the value of α is consistently larger for Ne projectiles than for d projectiles, as seen in Fig. 36. From a simple geometrical consideration we expect the opposite trend, since with a heavier-mass projectile the increase of target size must be less affected on the yield (in fact, we expect $\propto A_T^{2/3}$ for heavy-mass projectiles and $\propto A_T$ for light-mass projectiles from Eq. (3.7). Perhaps this experiment indicates that the compressed hot region is created easier with heavier-mass projectiles. Such a feature is not (or only slightly) observed for pion production, as seen in Fig. 36.

The Λ production has been studied recently by Harris *et al.*[EH2] with a streamer chamber in 1.8 A·GeV Ar + KCl collisions. In this measurement the decay of Λ,

$$\Lambda \rightarrow p + \pi^- \quad (64\ \%\ \text{branching}), \tag{3.31}$$

was used for the identification. Although statistics of the data are low, a large number

This is consistent with the previous data of K^+.

It is well known that the decay of Λ shown in Eq. (3.31) is through weak interactions. Therefore, if Λ has a polarization, P, the angular distribution of the decay products, p and π^-, is expressed as

$$W(\vartheta) = 1 + \alpha P \cos\vartheta, \tag{3.32}$$

where ϑ is the emission angle of protons with respect to the polarization axis and α = -0.64 in this case. By defining the reaction plane such that the beam and the emitted Λ form this plane, the value of P has been determined to $P = -0.10 \pm 0.05$.[EH2] In terms of the quark model Λ is described as (uds) in which spins of u and d are coupled to zero.[MB3] Therefore, the polarization of Λ measures the polarization of s-quark. Measurements of Λ polarization may thus shed light on the role of quarks in high-energy nuclear collisions.

The K^- yield has been measured recently with a magnetic spectrometer.[EH3] In this case, the yield is extremely low, since the Bevalac maximum energy is 2.1 GeV per nucleon while the threshold energy of K^- in NN collision is 2.6 GeV. Although these data were compared with various model calculations, meaningful physics can be extracted only when more data become available.

3.7. Coulomb Final State Interactions

Because the nucleus carries a positive charge, Coulomb interactions may distort fragment spectra. These interactions are important especially in the kinematic regions in which nuclear charges are highly clustered, namely for velocities close to those of projectile and target fragments.

The importance of Coulomb effects in high-energy nuclear collisions was first pointed out by Heckman and Lindstrom[EA4] from the study of target-mass dependence of the cross section for projectile fragments. As shown in Fig. 37, the target-mass (A_T) dependence of one-nucleon removal reactions, such as $^{16}O \rightarrow {}^{15}N$ or $^{12}C \rightarrow {}^{11}C$, is much stronger than that observed for ordinary projectile fragments. Such an yield increase was interpreted as due to the Coulomb excitation of a giant E1 resonance of a projectile nucleus[EA4],[EA9] followed by its dissociation into a nucleus of mass number (A_P-1) plus a nucleon.

In the fragmentation of ^{16}O at 90-120 A·MeV beam energies, Van Bibber *et al.*[EA10] found that the transverse momentum distribution of the projectile fragment is much wider than the longitudinal momentum distribution. They interpreted that this as due mainly to the orbital deflection of a projectile via Coulomb interactions.

Recently an obvious effect of Coulomb interactions was seen in the data of π^- to π^+ ratio.[EB3],[EB5] In these experiments both π^- and π^+ have been measured at 0° in Ne + NaF collisions. To a first order approximation, we expect that the yield of π^- is the same as that of π^+, since both Ne and NaF contain almost equal numbers of protons and neutrons. However, as seen from Fig. 38, the π^- yield is much higher than that of π^+. In addition, the spectrum of π^- has a sharp peak at a certain momentum, whereas that of π^+ has a valley there. The pion velocity at this peak (or valley) is very close to the beam velocity which is indicated by arrows in Fig. 38. There the π^- to π^+ ratio reaches about 20-30. These results immediately suggest the importance of Coulomb interactions, since π^- will be attracted by the projectile fragment whereas π^+ will be

repelled by it. In fact, theoretical calculations of Coulomb interactions[EB3),(TR1),(TR2)] have explained reasonably well these observations.

Detailed study of Coulomb effects may tell us about the charge distribution and its evolution in time. If the nucleus is completely transparent, then both projectile and target pass through each other, and consequently, most of the nuclear charge will be clustered at $(y,p_T) = (y_P,0)$ and $(y_T,0)$. On the other hand, if the nucleus is completely black, then the projectile and target will stop each other completely in the c.m. frame. For Ar + KCl collisions (at around 1 A·GeV) a theoretical value of the π^- to π^+ ratio at $p_T = 0$ at c.m. 90° is 2.8 for the complete black case and 1.6 for the complete transparent case.[TR2] From large angle data of the π^- to π^+ ratio[EC7),(EG8)] we obtain the ratio to be about 2 which is just in between these two extreme values.

If π^- to π^+ ratios show Coulomb effects, we expect also that neutron-to-proton (n/p) as well as triton-to-^{3}He ratios might be affected by Coulomb interactions. In 300-400 A·MeV Ne + (Pb,U) collisions it has been reported[ED1),(ED2)] that the observed n/p ratio is larger than the neutron-to-proton (N/Z) ratio of the system especially for small fragment energies. A similar tendency is observed for the $t/^3$He ratios in 800 A·MeV Ar + KCl and Pb collisions.[EC7]

With regard to the n/p and $t/^3$He ratios, however, a different mechanism might be involved other than the Coulomb effect. We consider the case of $N/Z > 1$. Naively one would expect that the n/p ratio for the initial system is almost equal to the N/Z ratio of the whole system. However, some of these nucleons are combined together to form composite fragments due to final state interactions. Among these fragments the formation of dueterons would be the largest. Since deuterons carry equal numbers of protons and neutrons, the final system after the formation of deuterons contains much more neutrons than protons than expected from the n/p ratio of the initial system. Such an effect is especially important in the small momentum region, because deuterons are more easily created there. Therefore, we might expect a n/p or $t/^3$He

ratio larger than N/Z in the small momentum region. Theoretically, this mechanism has been formulated by Randrup and Koonin[TP1] and also by Stevenson.[TP2] Especially, Stevenson showed that this isospin equilibration explains very well the observed n/p ratio reported in Ref. (ED1).

3.8. Forward and Backward Spectra

In nuclear collisions the phase space accessible to any single particle is much greater than that in free NN collisions. The maximum momentum in the c.m. frame, $p_{\rm max}^{\rm c.m.}$, allowed by the kinematics is given, for example, by Eq. (A.8). In Fig. 39 values of $p_{\rm max}^{\rm c.m.}$ for the production of pions and nucleons are plotted for C + C and p + p collisions. The value of $p_{\rm max}^{\rm c.m.}$ is much larger for C + C than for p + p at the same beam energy per nucleon. Thus far, the particle emission near the absolute kinematical limit has been measured extensively at forward[EB1],[EB2],[EB4],[EB6] and backward[EM1]–[EM5] angles. In this section we review these data.

Schmidt and Blankenbecler[TF2] estimated single-particle inclusive cross sections at 0° and 180° using a structure function of the nucleus. By using the Feynman scaling variable, x defined by Eq. (A.7), the cross section is approximately expressed as

$$E\,\frac{{\rm d}^3\sigma}{{\rm d}^3p} \propto (1-x)^g, \tag{3.33}$$

where

$$g = 2T\cdot(A-1) + H. \tag{3.34}$$

In the case of forward pion spectra, A is the projectile mass, H is an adjustable parameter which is normally 3 except for the hydrogen target for which H = 1. The parameter T describes the type of NN interactions. If NN interactions are due to vector meson exchange plus monopole form factors, then T = 3. Fig. 40 shows the π^- spectra measured at 2.5° from p, d, and α beams at several bombarding energies.[EB2] Observed cross sections fall almost precisely on the curves predicted by Eq. (3.33) with

$T = 3$. Recently it was pointed out[EB6] that this scaling law holds also for the π^- spectra at 0° from C + C collisions at 1-2 A·GeV beam energies. A noticeable exception to the $T = 3$ power law occurs in the case of 2.1 A·GeV α + hydrogen collisions.[EB6] There the data show a less steeper fall-off as a function of x than predicted by Eq. (3.33). If $A_P > A_T$, the target nucleus interacts with a part of projectile nucleus, and consequently, the forward pion production may not reflect the structure function of the entire projectile.

A similar deviation from Eq. (3.33) is observed for the backward pion production in the case of $A_P < A_T$.[EM4] Again, the projectile nucleus will interact with a part of the target nucleus, and the data will not reflect the structure function of the entire target. Landau and Gyulassy[TF5] therefore applied Eq. (3.33) to cluster-cluster collisions and found that the apparent non-scaling could be accounted for if only small clusters are involved.

Aslanides *et al.*[EB4] have measured pion spectra at 0° in 303 A·MeV ^{3}He + ^{6}Li collisions over a wide kinematic region of pions up to almost the absolute kinematical limit. The data are shown in Fig. 41. It is claimed in this paper that the prediction by Eq. (3.33) deviates largely from the data especially in the region of $0.9 < x < 1.0$. Also, it is stated that a small bump is observed at $x \simeq 1$, which may show an evidence of a coherent enhancement of pion production. The data are certainly interesting, but the statistical significance of the bump is not great. It is important to test for this bump in higher statistics measurements. Also, it is not so surprising that the data deviate from Eq. (3.33), since the theory of Schmidt and Blankenbecler has been formulated for the limit of high beam energies.

High-energy proton spectra have also been measured at forward[EA3],[EA5],[EA14] and backward[EL1]–[EL12] angles. Compared to the pion spectra, the proton spectra cover smaller region in x. In addition, the spectra contain both fragmentation and hard-collision effects, which makes the comparison between the data and theories not so

straightforward. Nevertheless, much theoretical work on the backward proton emission has been performed during the last few years,[TS1]-[TS7] especially for proton + nucleus collisions. These theoretical models are classified into two types; one based on the single *NN* collisions with a large nucleon Fermi momentum inside the target, and the other based on the projectile proton scattered by a cluster of nucleons inside the target nucleus. These two types of mechanisms might be strongly related, because the cluster formation requires short-range correlations between nucleons, and these correlations may introduce high-momentum tails for nucleons in the momentum space.[TT2] In addition, multiple collisions can lead to high-energy tails in the spectra.[TG4]-[TG6] Thus far, it has not been possible to disentangle the different reaction mechanism responsible for the high energy tails. Very recently experimental efforts to separate these mechanisms have just begun from measurements of backward-forward two-proton correlations.[EL8],[EL13]

3.9. Spectator Physics

From the viewpoint of collision mechanism the spectator region seems less interesting, because it is the region where no strong nucleon-nucleon collisions take place. However, several interesting phenomena can be found in this region that need further investigation. Since much of the basic data of projectile fragments has been reviewed already in Ref. (RA7), we concentrate here on two current topics.

3.9.1. Nucleon momentum distribution inside the nucleus

In the study of ^{16}O and ^{12}C fragmentations[EA1] it was found that the distribution of parallel momenta ($p_{\parallel}$) of projectile fragments in the projectile rest frame is expressed, to a first order approximation, by a Gaussian form;

$$\frac{d\sigma}{dp_{\parallel}} \propto \exp\left(\frac{-p_{\parallel}^2}{2\sigma^2}\right). \tag{3.35}$$

The width σ is the largest for a fragment whose mass number is nearly equal to half the projectile mass, as shown in Fig. 42. Goldhaber[TV2] proposed a simple explanation of this observed systematics. Since the projectile fragment is formed mainly from the spectator region which has not experienced any strong interaction, it tends to keep various static properties that the projectile nucleus had before the collision. He assumed that the above distribution, Eq. (3.35), reflects the momentum distribution of the equivalent cluster inside the static nucleus. In the rest frame of the projectile (with mass number A) the sum of individual nucleon momenta, $\vec{p}_i$, must be zero:

$$\sum_{i=1}^{A} \vec{p}_i = 0. \tag{3.36}$$

Therefore, the squared average of the above quantity is expressed as

$$\sum_{i=1}^{A} \langle p_i^2 \rangle + \sum_{i \neq j}^{A} \langle p_i p_j \rangle$$
$$\approx A \cdot \langle p_i^2 \rangle + A(A-1) \cdot \langle p_i p_j \rangle = 0. \tag{3.37}$$

Here the value of $\langle p_i p_j \rangle$ is assumed to be independent of i and j. Now, if we pick up a subset of F nucleons from the projectile nucleus, then the squared average of the momentum of this subset is given by

$$\langle (\sum_{i=1}^{F} p_i)^2 \rangle \approx F \cdot \langle p_i^2 \rangle + F(F-1) \cdot \langle p_i p_j \rangle. \tag{3.38}$$

Using the relation of Eq. (3.37) we have

$$\langle (\sum_{i=1}^{F} p_i)^2 \rangle^{1/2} \approx \sqrt{F(A-F)/(A-1)} \sqrt{\langle p_i^2 \rangle}. \tag{3.39}$$

According to the Fermi gas model $\langle p_i^2 \rangle = (3/5) \cdot p_F^2$, where p_F is the Fermi momentum. Therefore, the relation between σ in Eq. (3.35) and p_F is given by

$$\sigma \approx \sqrt{3/5} \sqrt{F(A-F)/(A-1)} \cdot p_F. \tag{3.40}$$

If one uses p_F = 221 MeV/c, then the gross structure of experimental values of σ is well explained by Eq. (3.40), as seen in Fig. 43. This analysis further suggests that the

projectile fragments are useful to determine the momentum distribution of a nuclear cluster inside the static nucleus.

Even in a gentle collision, the projectile spectator will feel a certain force $\vec{F}(t)$ from the target. In the projectile rest frame the direction of the time-integrated force, $\int \vec{F}(t)dt$, will be perpendicular to the beam direction. Since this integral, called the impulse, is equal to the momentum change $\vec{q}$, the projectile spectator receives a momentum change into the transverse direction of the beam. Roughly speaking, $|\vec{F}| \approx$ 50 MeV/fm and the interaction time $\Delta t \approx$ (a few fm)/c. Thus, $|\vec{q}| \simeq$ a few 100 MeV/c. This magnitude of $|\vec{q}|$ was confirmed in the elastic and inelastic proton-nucleus collisions[MB4] as well as from the Doppler broadening of nuclear γ rays from excited nuclei.[EF9] Therefore, we expect that the experimental momentum spread of a projectile fragment, $(\Delta\vec{p})_{exp}$, is related to the intrinsic momentum spread of the corresponding cluster inside the nucleus, $(\Delta\vec{p})_{intr}$, by the following relations:

$$(\Delta p_{\parallel})_{exp} \approx (\Delta p_{\parallel})_{intr}$$
$$(\Delta p_{\perp})_{exp} \approx \sqrt{(\Delta p_{\perp})^2_{intr} + q^2}\,. \qquad (3.41)$$

In other words, the transverse momentum distribution of a fragment reflect both nuclear reaction and internal motion effects, whereas the longitudinal momentum distribution reflects only the internal motion effect.

Noticing the above feature, Fujita, Hüfner, and Nemes[TT1),(TT3] pointed out that the parallel momentum distribution in the fragmentation process of one-nucleon removal reaction, such as $\alpha \rightarrow {}^3\mathrm{He}$ or ${}^{16}\mathrm{O} \rightarrow {}^{15}\mathrm{O}$, will directly reflect the internal momentum distribution of a nucleon inside the nucleus. In this reaction the longitudinal momentum distribution of the observed $(A\text{-}1)$ cluster in the projectile rest frame must be equal to the momentum distribution of a single nucleon (which was scraped out by the target) inside the projectile, because of the momentum conservation. Fig. 43 shows the analysis for ${}^{16}\mathrm{O} \rightarrow {}^{15}\mathrm{O}$.[TT3] A simple Gaussian momentum distribution does not explain the data and an appropriate modification to nuclear wavefunction is

required in the high momentum region. In this analysis multi-step processes which might be involved in the creation of ^{15}O are neglected, and perhaps a more careful consideration is needed. Nevertheless, it is very interesting to extend such measurements and analyses into the region of much higher momenta. In the region above 0.3 GeV/c it is not feasible to extract the nucleon momentum distribution by (e,e') or (e,e'p) reactions with electron accelerators. Thus, high-energy nuclear beams might offer a unique opportunity for the study of internal structure of the nucleus.

3.9.2. Production of neutron-rich isotopes

The second area under intense study is the production of neutron-rich isotopes. Qualitatively, the neutron-to-proton ratio of the projectile spectator is nearly equal to the neutron-to-proton (N/Z) ratio of the projectile nucleus, since the former is a part of the latter. For example, if we use ^{238}U as a projectile, then $N/Z \simeq 1.6$. It is well known, on the other hand, that the stability line of nuclei extends along $N \approx Z$ for light nuclei. Thus projectile spectators from ^{238}U beams tend to fill the unstable neutron-rich-isotope region.

Symons *et al.*[EA12] and Westfall *et al.*[EA13] have accelerated ^{40}Ar ($N/Z \simeq 1.2$) and ^{48}Ca ($N/Z \simeq 1.4$) beams and discovered 16 new isotopes in projectile fragments especially from the latter, as shown in Fig. 44. It is almost certain that many more new isotopes will be created with ^{238}U beams. The lifetimes and even the spectroscopy of isotopes far from the line of stability could be studied with these fragments. These new isotopes can eventually provide stringent tests for theories of nuclear structure.

Another application of neutron-rich isotopes is their use as secondary beams. Because projectile fragments generally emerge with a velocity close to the projectile velocity, we may obtain high-quality secondary beams. So far, only stable nuclei have been used as projectiles. If these new isotopes were used, we would have unstable nuclei as projectiles. For example, when ^{238}U beams become available, it may be possible to use ^{52}Ca as projectiles.

The production mechanism of isotopes consists of the fast process (abrasion) in which the projectile nucleus is scraped by the target nucleus, followed by the slow process (ablation) in which particles are evaporated from the projectile spectator.[TV3]-[TV6] In fact, the observed isotope distribution is substantially different from what is expected from the abrasion process alone. If one uses an evaporation model for the ablation process with $T \simeq 8$ MeV, and in addition, if one further takes into account the isospin equilibration mechanism, then the experimental isotope distribution can be reproduced reasonably well by this abrasion-ablation model.[TV4]

Currently the dynamics for both abrasion and ablation processes is widely studied. In the abrasion process a frictional force may be involved which could heat the spectator matter. Thus, the temperature may be increased higher than 8 MeV. An example of such studies is found in Ref. (TV7). Whether one can theoretically justify a clear separation between these abrasion and ablation processes is an open question.

4. TOWARD THE PHYSICS OF DENSE NUCLEAR MATTER

Thus far, we have concentrated on data which can be explained in terms of a combination of conventional reaction mechanisms. However, there are some data that have not as yet been explained in terms of such mechanisms. Perhaps, it is these data that contain clues on the physics of dense nuclear matter. We review these data in this section.

4.1. Do Nuclei Flow?

4.1.1. Hints of collective flow from existing data

Comparing Fig. 12 and 16 we could not decide whether nuclei behave as a fluid or as a dilute gas at high energies. In this section we address a more general question of whether there is any evidence for collective matter flow in nuclear collisions. Collective flow would occur if hydrodynamics were valid for such reactions. However, as described in Sec. 3.2., the necessary condition ($\lambda \ll R$) is not well satisfied, especially for light ($A < 40$) nuclei. In addition, impact parameter averaged data include peripheral reactions where that condition is obviously violated. Therefore, to have any hope of seeing nuclear flow we should not only look at reaction involving heavy nuclei (Pb or U) but also select small impact parameter collisions. The later can be achieved by selecting high associated multiplicity events.

So far, two methods have been used to select high-multiplicity events. The most straightforward one is the detection of as many particles as possible using a large number of counter arrays which surrounded the target.[EJ7),(EJ8)] The other method, which is suitable for low-intensity beams of $\leq 10^{(5-6)}$ projectiles/s, is the selection of events with no high-Z fragments near 0°,[EG3),(EJ10)] where Z is the charge of the fragment. This second method is equivalent to the first because high-multiplicity events tend to spray nuclear charge over a wide range of angles leaving only a small

fraction of charge at 0°.

The first data on high-multiplicity reactions were taken with nuclear emulsions. Baumgardt *et al.* [EN1] found that the angular distribution, $d\sigma/d\vartheta$, of α particles showed a sidewards peak, suggesting the existence of nuclear shockwaves.[TAB] A similar experiment was repeated later by Heckman *et al.* [EJ2] who found, however, less evidence for this peak.

The first high statistics counter experiment on high-multiplicity events was reported in Ref. (EJ7). Stock *et al.* measured the proton spectra for 393 A·MeV Ne + U collisions in coincidence with a multiplicity counter system. The associated multiplicity distribution for a 90° proton was first measured. High-multiplicity events were defined such that the associated multiplicity was in the highest 15 % of that distributions. Theoretical estimates[TL1],[TL2] for the range of impact parameters probed by this trigger indicate that $b < 2$ fm. Low-multiplicity events were defined as those events belonging to the lowest 15 % of that associated multiplicity distribution. As Fig. 45 shows, the measured spectra differ considerably between the low (peripheral) and high (central) multiplicity events. For low multiplicities the angular distribution is peaked at $\vartheta_{Lab} = 0°$ for all energies. However, for high multiplicities the forward yield is reduced significantly. A similar tendency toward forward suppression in high-multiplicity events was reported in Ref. (EJ8) for 800 A·MeV Ar + Pb. Qualitatively this forward suppression can be attributed to the non-transparency of heavy nuclei to small projectiles (forward shadowing).

In Fig. 45 there is also a hint that the low-energy fragments tend to emerge at finite angles (for $E_p \approx 12$ MeV, $\vartheta_{Lab} \approx 80°$). This suggests that some collective flow away from the beam direction may be occurring. In terms of hydrodynamics, a sidewards splash[TK15] of the nuclear fluid is expected in central collisions as illustrated in Fig. 46 (a). To test quantitatively whether the observed forward suppression can be attributed to hydrodynamics, Fig. 47 shows a comparison of several model calculations[TK19] with

the data. Both cascade models[TB4),(TB6)] predict only a $\vartheta_{Lab} = 0°$ peak and thus cannot account for the data. Similarly firestreak[TJ5)] and transport[TL1),(TL2)] models lead to only a forward peak. In contrast the hydrodynamical model[TK17)] with no thermal breakups (Fluid 1) leads to very pronounced sidewards peaking, much narrower than the data. In a modified hydrodynamical model (Fluid 2) including an evaporation model of the fluid to simulate composite formation (see Sec. 2.4.), the qualitative trend of the data is reproduced.

Fig. 47 (a) emphasizes the difference between hydrodynamic and cascade model predictions. The former always lead to conspicuous sidewards collective flow, while the latter do not.[TB9),(TB10)] Unfortunately, the proton data[EJ7)] are not sufficient to let us draw the conclusion that nuclei flow. First, the statistical uncertainties in the data are rather large ($\approx$ 30 %) and systematic errors at forward angles are not well understood. This problem can be overcome only in the next generation of experiments with the plastic ball-wall system.[EP1)] Second, the cascade models used thus far do not yield the proton spectrum but the charged inclusive spectrum given by Eq. (2.33). As seen comparing Fluid 1 and Fluid 2 calculations, when composite formation is included, the proton spectrum can differ markedly from the charged inclusive spectrum. Indeed it was emphasized in Ref. (TM9) that the high phase space density in the forward direction implies that most protons emerge in composite nuclear fragments rather than as free protons. Thus the free proton spectrum can be depleted in the forward direction due to composite formation. It is thus crucial to measure the d, t, α, $\cdots$ angular distributions at high multiplicities. If these also show a sidewards peak as in Ref. (TA8), then a cascade picture can be ruled out. Preliminary data [Fig. 24 on page 127 in Ref. (RA4)] on d and t spectra seem to support a sidewards emission of at least light fragments. The spectrum of heavier mass fragments, especially α, has yet to be measured.

Fig. 47 (b) shows a detailed comparison of one-fluid,[TK17)] two fluid,[TK7)] and a cascade[TB6)] calculations with the same charge inclusive spectra (including p, d, t only)

selected on high multiplicity. Quantitatively none of these models reproduce the data (note the compressed log scale). However, the numerical uncertainties are also great. At low energies, $E \leq 50$ MeV per nucleon, the discrepancy with data is particularly severe. It is in this region where binding, composite formation, and Coulomb distortions are most important. Furthermore, the precise relationship between the range of impact parameters selected by this particular high multiplicity trigger is not clear. The calculated spectra are sensitive to variations in the assumed impact parameter cutoff. In Fig. 47 (c), this same reaction is compared to calculations,[TM9] based on Cugnon's cascade model[TB9] with an impact parameter cutoff, $b_{max} = 2.1$ fm, adjusted to obtain the best fit. Both the high energy sum charge and the primordial deuteron specta are well reproduced. However, the spectra below 25 MeV per nucleon are overestimated and do not show forward suppression, in agreement with Cascade 1 and 2 results in Fig. 47 (a). Comparing Figs. 47 (a) - (c), we see that the high energy spectra are consistent with cascade but not with hydrodynamics, whereas the low energy spectra are inconsistent with cascade models and can be reproduced with a modified hydrodynamic model.[TK24] From this comparison it appeas that at most only a fraction of the nucleons involved in Ne + U collisions exhibit collective flow and there is probably a substantial mixture of both cascade and hydrodynamical behabior for this reaction.

Further circumstantial evidence for collective flow can be seen in the two-proton correlation function in 800 A·MeV C + Pb and Ar + Pb collisions.[EC4],[EJ9],[EJ11] The experimental layout is illustrated in Fig. 48. The ratio C defined as

$$C \equiv \frac{2 \times S(\vartheta,E)\cdot R}{S(\vartheta,E)\cdot U + S(\vartheta,E)\cdot D}, \tag{4.1}$$

was measured, where $S(\vartheta,E)\cdot R$ indicates the coincidence counts between S and R, similar to Eq. (3.8). As seen in Fig. 48, U, D, and R refer to plastic-scintillator telescopes and S to a magnetic spectrometer. These three telescopes, which were placed at $\vartheta_{Lab} = 40°$, selected relatively high-energy protons with $E_p \geq 200$ MeV

(namely, *fast* particles). The spectrometer, on the other hand, was rotated at angles from 15° to 110° and detected both low- and high-energy protons above 50 MeV. If $C > 1$, then two protons tend to be emitted on the opposite sides in azimuth, while if $C < 1$, then they tend to be emitted on the same side.

Contour lines of the observed C are plotted in Fig. 49. At $(\vartheta, E) \simeq (40°, 1\ \text{GeV})$ we see $C < 1$. This implies that, once the first *fast* proton was detected by one of the telescopes at 40°, then the second *fast* proton tends to be emitted on the same side at $\vartheta \simeq 40°$, as illustrated in Fig. 48 (lower-left). On the other hand, at $(\vartheta, E) \simeq (90°, 30$ MeV) we observe $C > 1$. In this case, if the first *fast* proton was detected at 40°, the second *slow* proton is emitted on the opposite side at 90°, as shown in Fig. 48 (lower-right). These features are exactly what we expect from the bounce-off effect of the hydrodynamical flow,[TK15),(TK16),(TK20] as schematically illustrated in Fig. 46 (b).

A third indication of possible collective flow is seen in the energy spectra of protons and pions for high-multiplicity events reported in Ref. (EJ8). Data are shown in Fig. 50. The energy spectra at 90° in the c.m. frame are plotted for 800 A·MeV Ar + KCl collisions. Typical features are (1) the non-exponential shape for protons, (2) the exponential shape for pions, and (3) the steeper slope for pions than for protons. Although the "shoulder-arm" type energy distribution for protons is already observed in the inclusive spectra, as shown in Fig. 19, the flattening of the shape in the low-energy region as well as the difference in exponential slopes between protons and pions are more pronounced in high-multiplicity events. In the phase-space model the "shoulder-arm" feature has been thought of as due to the existence of NN quasi-elastic scatterings, since these scatterings increase the proton yield at $E_p^{\text{c.m.}} \simeq E_{\text{Beam}}^{\text{c.m.}}/A$ (= 182 MeV in this case). However, in high-multiplicity events these NN quasi-elastic components are expected to be suppressed. Still, the "shoulder-arm" shape is pronounced there. In order to solve this puzzle, Siemens and Rasmussen[TK12] interpreted these data as evidence for a radially exploding nuclear flow. At a fixed kinetic energy the velocity of a proton is much smaller than that of a pion. Therefore,

if there is an explosive flow, then the addition of that flow velocity will tend to broaden the proton distribution more than the pion distribution The best fit to the data by this model is shown in Fig. 50. The observed shapes for both protons and pions are reasonably well reproduced by this model. There are, however, two shortcomings of this model. First, the absolute yields of pions are underestimated by more than a factor of two in this model.[TN4] Second, this model assumes that all particles are emitted from a thermal bath on which a explosive flow is superposed. Therefore, the mass difference between the proton and pion solely determines the difference in the slope. However, the largest value of E_0 among p, K^+, and π, is observed for K^+, as described in Sec. 3.6. This fact cannot be explained by this model without further dynamical assumptions.

4.1.2. Global analysis

The data above provide some hints that collective flow may occur in nuclear collisions. However, it is clear that the evidence is weak and ambiguous. In order to test for hydrodynamic flow more directly in the future, several proposals have been made to study global variables.

The simplest example of global variable is the longitudinal energy fraction[TK8]

$$f_z = \left(\sum_\nu p_z^2(\nu)/2m_\nu \right) / \left(\sum_\nu |\vec{p}(\nu)|^2/2m_\nu \right) , \tag{4.2}$$

where $\vec{p}(\nu)$ and m_ν are the momentum and mass, respectively, of fragment ν. A thermal equilibrated system yields $f_z = 1/3$, while in central collisions (Fluid 1) hydrodynamics[TK8] yields $f_z \simeq 1/6$. More complete global variables are thrust[TX3] and sphericity[TX4],[TX7],[TX8] given by

$$T(\hat{n}) = \sum_\nu |\hat{n}\cdot\vec{p}(\nu)| / \left(\sum_\nu |\vec{p}(\nu)| \right) , \tag{4.3}$$

$$S_{ij} = \sum_\nu p_i(\nu)\, p_j(\nu) . \tag{4.4}$$

Maximizing $T(\hat{n})$ with respect to $\hat{n}$ gives the direction, $\hat{n}$, of maximum momentum flow. Thrust does not provide, however, three dimensional event shape analysis. For that purpose the sphericity tensor can be used to extract the three principal axes specifying the "shape" of the event.[TX7] However, usual sphericity is not suitable for nuclear collisions, because many fragments are produced.[TX3] Thus, α particles are weighed more than four nucleons at the same energy per nucleon. Note that using the momentum per nucleon of fragment ν underestimates the contribution of composites to the matter flow. Correct weighting of composites can be achieved by dividing $p_i p_j$ by the fragment mass m_ν. This leads to the kinetic flow tensor,[TX6]

$$F_{ij} = \sum_\nu p_i(\nu)\, p_j(\nu) \,/\, 2m_\nu \,. \tag{4.5}$$

In terms of F_{ij}, $f_z = F_{zz}/\mathrm{Tr}(F)$ in Eq. (4.2). Note that F and S are equivalent if only free nucleons were present. The eigenvalues of F specify the kinetic energy flowing along three principal axes. Simple analytic formulas exist for the three eigenvalues λ_i and principal axes, $\hat{e}_i$. The sphericity or flow tensors characterize an event as a three dimensional ellipsoid in momentum space with principal axes oriented along $\hat{e}_i$ and radii $\propto \sqrt{\lambda_i}$. Of course, all global variables must be evaluated in the *nucleus-nucleus* center-of-mass system. In Fig. 51 a typical charge exclusive event for 400 A MeV Ca + Ca is shown as measured by the plastic ball-wall system.[EP1] The momenta of all particles are projected on the plane spanned by the beam axis ($\hat{p}_z$) and the principal axis $\hat{e}_1$ corresponding to maximum kinetic flow. The oriented ellipse that is determined by the flow analysis is also shown. This event shows a finite deflection angle $\vartheta_{\mathrm{Flow}} \approx 19°$ and corresponds to an ellipse with aspect ratio $a/b = 3$.

Global analysis is done on an event by event basis. Sphericity or flow analysis produces six independent numbers per event (λ_1, λ_2, λ_3, $\vartheta_{\mathrm{Flow}}$, φ_{Flow}, ϑ_2). It is important to plot these quantities in pairs to display the correlations. For example, $\lambda_1/\lambda_3 \gg 1$ is expected to be correlated with $\vartheta_{\mathrm{Flow}} \approx 0°$ corresponding to peripheral collision. A flow diagram[TX6], where $\vartheta_{\mathrm{Flow}}$ is plotted vs. λ_1/λ_3, is shown in Fig. 51. The flow

characteristics arising from hydrodynamics[TX9] are compared to those calculated[TX6] using Cugnon's cascade code[TB9]. The reaction considered is $^{238}U + ^{238}U$ at 400 A·MeV. For such heavy system the fluctuations (shaded area) are small. Fig. 51 shows the dramatic difference between a fluid and cascade behavior. There is some flow with cascade, but far less than predicted by non-viscous fluid calculations. It should be noted that the triple differential inclusive yield,[TK18],[TK24] $d\sigma/dE d\vartheta d\varphi$, where φ is measured with respect to the reaction plane, φ^*, would provide even more detailed information on central collisions. Of course, a measurement of $\varphi^* = \varphi_{Flow}$ requires first a global analysis to determine the reaction plane.

What are the main features we can expect from such global analysis? For "light" nuclei, $A < 100$, it was shown in Ref. (TX6) that the finite number fluctuations lead to large fluctuations of ϑ_{Flow} and λ_1/λ_3. Second, for energies $E_{Lab} > 400$ A·MeV the flow angles become more and more confined to small angles. The optimal beam energy for collective flow analysis is therefore $E_{Lab} \approx 100$ - 400 A·MeV, where as noted in Sec. 2.4. the internal pressures are also most sensitive to dynamical assumptions. In the coming year, truely heavy nuclear beams, Pb and U, will become available at the Bevalac. The streamer chamber and the plastic ball-wall system are in operation and have the capability of measuring all charged fragments necessary for global analysis. Only after that analysis will we be able to conclude if nuclei flow at high energies.

4.2. Entropy Puzzle

Siemens and Kapusta[TW1] pointed out that the yield ratios of composite-fragments-to-protons may provide information on "entropy" created in nuclear collisions. Assuming chemical and thermal equilibrium and isentropic expansion, the entropy per nucleon in the compressed stage is approximately given by[TW1],[RA14]

$$S = 3.95 - \ln(\sigma_d/\sigma_p), \tag{4.6}$$

where σ_d and σ_p are, respectively, the deuteron and proton production cross sections.

Furthermore, they pointed out that the value of S obtained using Eq. (4.6) is larger, $S_{exp} \approx 5.5 \pm 0.5$, than expected in a thermal model ($S_{th} \approx 4$) for E_{Beam} = 800 A·MeV. Therefore, they suggested that a new degree of freedom may be involved in high-energy nuclear collisions.

If entropy, S, is constant throughout the disassembly stage of the system, then the study of S may provide us with a tool to probe highly compressed matter. In a recent cascade calculation by Bertsch and Cugnon,[TN5] it was shown that after most particles have collided, the value of S stays almost constant, as shown in Fig. 52. The same conclusion is obtained in macroscopic theories,[TN4],[TN3],[TK18] although the frictional force in the viscous fluid introduces a slight increase in the value of S by up to 0.6 in units of S. These calculations suggest that the "entropy" may indeed be a useful concept for the study of highly compressed phase.

In thermal models[TM3],[TN1] and in the intranuclear cascade study[TN5] the ratio of the integrated yield of deuterons and protons (d/p) exceed the data by as much as a factor of 2 - 3, as shown in Fig. 53, leading via Eq. (4.6) to a prediction of S that is smaller than S_{exp}. By invoking new degrees of freedom such as pion condensation, models have been constructed that can account in part for this missing entropy.[TN2] However, before any conclusion on the existence of such novel degree of freedom can be accepted, several points must be clarified.

First, Stöcker *et al.*[TK18] pointed out that the d/p ratio could be significantly smaller than the equilibrium value if excited nuclear states also come into chemical equilibrium. In that case, after the freeze-out point of the fireball, excited nuclear fragments (d^*, α^*, $\cdots$) could decay into $p + X$ much easier than into $d + X$. Consequently, the observed proton concentration after the decay of those fragments could be larger than the equilibrium proton concentration. Thus, the observed d/p ratio does not necessarily reflect on the equilibrium concentration.

Concerning cascade estimates[TN5),(TM9] for d/p ratio it should be kept in mind that the spectra of nucleons with momenta close (within one Fermi momenta, $\Delta p \approx p_F$) to the target or projectile momenta per nucleon are strongly affected by the model used to treat binding. As noted in Sec. 2.5., the large momentum transfer nucleons are insensitive to binding prescriptions, but the low energy nucleons are very sensitive to those prescriptions. Therefore, the integrated deuteron and proton yields are intrinsically less accurate than the high momentum differential yields. In Fig. 16 that differential yields of high momentum fragments could be reproduced well,[TM9] although the integrated d/p ratio was found to be too large as in Ref. (TN5).

Thirdly, it should be noted that the integrated ratios in Fig. 53 exclude fragments near the beam and target velocities. Those fragments are mostly composites. The high momentum spectra were extrapolated to low momenta in order to obtain the experimental integrated yields. Therefore, deuterons in the projectile and target fragmentation regions are not included in the extraporated yields. Theoretical estimates,[TN5),(TM9] on the other hand, include some deuterons in the fragmentation region.

Finally, we should note the observed mass dependence. As pointed out in Ref. (EC7), the projectile and target mass dependence of the d/p ratio for 800 A·MeV beams is empirically expressed as $(A_P + A_T)^{0.36}$. This tendency can be expected because as the mass of the system increases, the event multiplicity increases so that it becomes easier for one nucleon to pick up another nucleon to form a deuteron. The thermal model,[TM3),(TN1] however, does not predict this mass dependence (it predicts no projectile and target mass dependences at least for equal-mass nuclear collisions with $N = Z$), as seen in Refs. (TM3) and (RA14). Furthermore, it is difficult to reconcile thermal models with observations in Fig. 22. Obviously, some important mechanisms, such as the effect of finite nucleon number, are missing in the current thermal model.

These issues must be resolved before quantitative information on the nuclear entropy function can be extracted from d/p, α/p, etc. ratios. This remains an important topic for research in the near future.

4.3. Novel States of Nuclei

4.3.1. Anomalon

Since early cosmic ray studies, there have been recurring observations[EN4] in emulsions on anomalous projectile fragments with cross sections much larger than expected from conventional nuclear collision geometry. With regard to the reaction mean free paths of nuclei with charge $2 \leq Z \leq 26$ and energy between 0.2 and 2 A·GeV, the mean free paths for primary beams are consistent with simple geometrical cross sections given by Eq. (A.14). However, the secondary fragments produced in a nuclear collision seem to have a component with a much smaller mean free path.

In a recent experiment by Friedlander *et al.* [EN5] the subsequent interactions of secondaries and even tertiaries in sequential interactions have been studied in nuclear emulsions. Fig. 54 shows a "typical" (interesting) event-chain in this study.[EN6] An incident Fe beam (Z = 26) at 1.88 A·GeV interacts with an emulsion nucleus (AgBr) by loosing two charges. The Cr (Z = 24) fragment continues in the emulsion until it too interacts, this time by loosing four charges. This tertiary Ca (Z = 20) fragment then suffers yet another collision leaving a fourth generation projectile fragment with Z = 11 to interact once more before leaving the emulsion as an α particle. Such multi-chain events are rare, but seem to occur more frequently than we would expect from normal geometrical mean free paths.

Quantitatively, the reduced mean free paths of the secondary fragments were measured as a function of D:

$$\Lambda^* = \Lambda^*(D), \tag{4.7}$$

where D is the distance from the primary interaction-vertex point (at which the secondary fragment was created), where the mean free paths were determined. The reduced mean free path in Eq. (4.7) is used to parameterize the mean free path of secondary fragments of charge Z according to

$$\lambda(Z) = \Lambda^* Z^{-b}. \tag{4.8}$$

Using Eq. (4.8) allows data for different Z fragments to be combined, increasing the statistics.

In practice each secondary track in the emulsion within a 6° cone of the beam direction is followed for a length l_i. The charge of the fragment Z_i is recorded. The number $N(D)$ of secondary tracks that propagate freely for a least distance D and interact at a distance $l_i > D$ from the primary vertex is recorded. With Eq. (4.8) [$b \approx 0.44$[EN4]] one obtains

$$\Lambda^*(D) = \sum_i (l_i - D) Z_i^b \Theta(l_i - D) / N(D), \tag{4.9}$$

as an estimate for $\Lambda^*(D)$, where $\Theta(x) = 1$ for $x > 0$ and $= 0$ for $x < 1$.

For primary fragments $\Lambda^* = 30.4 \pm 1.6$ cm does not depend on D (in this case the distance into the emulsion). However, Fig. 55 shows that $\Lambda^*(D)$ varies significantly as a function of D for secondaries. For $D > 10$ cm $\Lambda^*(D)$ approaches the value expected from normal geometrical cross sections. However, it appears that for $D < 5$ cm a component with much shorter mean free path is mixed in. Assuming that some fraction of the secondaries had an anomalously large cross section, then the data can be fit if 6 % of the secondaries have 10 times the geometrical cross section. Acceptable fits could also be obtained assuming 20 % of the secondaries had 4 times the geometrical cross section. Such a large cross section cannot be expected within the framework of current knowledge of nuclear physics. This anomalous component was named the anomalon. Two other emulsion groups[EN6],[EN7] seem to see the same phenomena.

One of the difficulties associated with the interpretation of the data on Λ^* is that only a fraction, f = 50-70 %, of the total reaction cross section is measured in emulsions. The fraction depends on the criteria used to define interactions and on the efficiency E for detecting such interactions. Thus, Λ^* varies by 10 % between experimental groups even for primaries. It is also possible that the efficiency to detect secondaries, E_2, is greater than for detecting primary interactions E_1.[EN8] Also the efficiency is in general Z dependent[EN8] with $E(Z>20) < E(Z<20)$. Estimating these efficiencies and their effect on the analysis of such data is still in progress. Nevertheless, the results thus far are certainly provocative.

If the effect is real, then it is anomalous in the extreme. While the mean free path for anomalons is much smaller than for nuclei, there seems to be no difference in the characteristics of their interactions in emulsions from those of primary nuclei. Thus, the distribution of "black" fragments, N_h, in an anomalon interaction cannot be differentiated from the distribution due to primary interactions.[EN5],[EN7] In particular, no enhancement of "white star" events with $N_h = 0$ is seen. Adding to the mystery, no decays in flight have been observed either in the target or projectile fragmentation region. Therefore, if anomalons decay at all, they must have virtually no branching ratio to charged fragment channels. Even more mysterious is the great abundance of anomalons produced. At least 6 % if not more of all secondaries in the forward direction must be anomalons. This is no needle in a haystack - it is an everyday phenomena.

The above observations rule out virtually any conventional explanation (hyper-fragments, pionic atoms, isotope effects, etc.). Therefore, it is either an artifact of the emulsion technique or a new state of nuclear matter.[TA12] If it is the later, then it could revolutionize nuclear physics. If it is the former, then we must continue the hunt for novel states elsewhere.

Decisive experiments on anomalons must await high statistics counter experiments. Already experiments have been proposed to study invariant mass spectra of projectile fragments to look for unusual bumps. In addition, transmission experiments using several targets at variable distances are being proposed. The current data are so provocative that a major effect must be mounted to either prove or disprove the existence of anomalons.

4.3.2. Search for super–heavy compounds

Since the proposal of meta-stable nuclear matter at high density (called abnormal nuclear matter)[TA1]–[TA3], several searches have been made.[EN2],[EN3],[EN9] These experiments searched for primarily super-heavy compounds, since if a high-density matter exists, it could show up in these compounds. No evidence of the creation of fragments with mass number substantially larger than the target mass has been discovered.

4.3.3. Multi–baryonic excited states

Another area in which unusual nuclear states could show up is in multi-baryonic excited states. No experimental data are currently available in this topic. However, we discuss it, because future experiments on this subject are being contemplated.

When research on high-energy nuclear collisions was started, one goal was to see if new exotic phases associated with high-density nuclear matter exist. For the creation of such new phases, however, two difficulties may exist. The first one is related to the time dependence. As pointed out in Sec. 1.3. (see Fig. 4) the high-density phase is created only for the time period of (2-3) $\times 10^{-23}$ sec. However, exotic phases are usually predicted only for *static* high-density nuclear matter.[TA1]–[TA7] In order for the system to change into such new phases a certain relaxation time is required. The minimum relaxation time is of the order of 10^{-23} sec which is already comparable to the time period during which the system is at its high-density phase. Thus, the system

may not have enough time to undergo the phase transition into exotic phases.

The second difficulty is related to the dynamical path. In order to create high-density nuclear matter, a large fraction of available energies must be converted into compression energy. However, in nuclear collisions, the energy could be used for exciting nucleons into baryonic excited states such as Δ, N^*, or Λ, without compressing nuclear matter. In this case we would create highly excited yet non compressed matter.

It may be possible that in such matter "multi-baryonic excited states" could be formed. For example, a multi Δ system is a particularly interesting system. At beam energies of around 700 A·MeV where the production cross section of Δ reaches its maximum, each NN collision creates Δ at a probability of about 50 %. In a nuclear collision, therefore, up to 1/2 of projectile nucleons could turn into Δ's. In Xe + Xe collisions, $\approx$ 10-50 Δ's may be created. Since at this beam energy these Δ-particles are almost at rest in the NN c.m. frame, and in addition, since they are created within a radius of a few fm, they have a greater chance to interact with each other to form a Δ-soup. Could a meta-stable $^{16}\Delta$ exist? All 16 Δ's could sit in the $1s$ orbit, because $S = T = 3/2$ for Δ. Of course, some mechanism must be invoked to prevent its decay in 10^{-23} s, but it is fun to speculate.[MA10],[MA11]

If we use light nuclei as projectiles, the study of dibaryons may also be interesting. Nucleon-nucleon interactions have been studied for long time with proton (and occasionally neutron) beams. However, very little is known on the interactions between Δ and N, Δ and Δ, or Δ and N^*. With respect to Δ–Δ interactions, several calculations, from phenomenological to six-quark models,[MA1],[MA2],[MA5],[MA6] predicted that perhaps a Δ-Δ pair is deeply bound with mutual binding energy up to 100 MeV. At much higher beam energies a dihyperon matastable state (with lifetime longer than 10^{-4} s) might be created.[MA4] Experimental searches for such dibaryons have been done mostly with elementary-particle beams such as γ, p, K, etc.[MA8] Nuclear beams,

however, may offer a unique opportunity for this study.

Discussions described above are mainly related to the creation of the multi-baryonic excited states in the participant region. In the spectator region one can also expect to create two or more baryonic excited states. For example, the excitation of the deuteron projectile into $\Delta-\Delta$ state has been proposed.[MA12] Also, three-neutron projectile spectator that absorbs π^- to form a negatively charged nucleus (triton-like) has been proposed.[MA13] In addition, a possibility of creating a hypernucleus which contains two or more hyperons is also interesting. These unusual nuclear states could be looked for in future experiments.

5. SUMMARY AND OUTLOOK

Form the foregoing discussion it is clear that the field of high-energy nuclear collisions is still in a state of rapid development and flux. In the past five years a tremendous body of experimental and theoretical work has been completed. On the experimental side, single particle (p, d, t, α, π, K, Λ) and two-particle (pp, $\pi\pi$) inclusive distributions have been measured for a wide variety of projectile and target combinations. Systematic studies on the beam energy dependence of these yield between 200 A·MeV and 2 A·GeV have been completed. Recently, central collision events were studied using high multiplicity triggers. On the theoretical side, many phenomenological models have been developed and applied to the above data. It is a major achievement to have reached the point where nine competing models could be compared to the new central collision data as in Figs. 47 (a) - (c), and cross correlated in Figs. 12 - 16.

Before these new data become available it was difficult to get a handle on the reaction mechanism, because so many models with contradictory assumptions could reproduce the qualitative trend of the data. The new data provided on the other hand a severe test for models. As seen in Figs. 47 (a) - (c) most models fail the test. Part of the reason is that different combinations of reaction mechanisms seem to operate in different kinematical domains. The high-energy fragments can be understood as due to a few ($\approx$ 3 - 4) but not too many NN collisions, as seen in Sec. 3.3. Therefore, for such fragments finite number effects are crucial and call for an intranuclear cascade description. For low-energy fragments, there is some indication of collective flow possibly reflecting hydrodynamic effects. However, the data clearly show that composite formation is very important in that region. Thus, no model can succeed in reproducing low-energy proton spectra without getting the composite yields right at the same time. Composite yields at high energies ($\geq$ 50 MeV per nucleon) can be accounted for in a cascade theory, but the low-energy composites, especially the

deuterons, have defied explanation. This later problem [Fig. 53] has led to the so called entropy puzzle and may also be related to the forward suppression of protons in central collisions.

From the theoretical side the solution of these problems may necessitate a new approach - quantum scattering - heretofore neglected in all models. As indicated in Sec. 2.1., and emphasized in Ref. (TY3), there is no obvious justification for neglecting quantum effects. In fact they may be especially important in the low fragment energy regions where most difficulties are encountered by classical models when confronting data. Formulating and solving a quantal theory of non-equilibrium processes as outlined, for example, in Sec. 2.6. is one of the exciting theoretical challenges in the near future.

From the experimental side it will be vital to carry out the program of global event analysis. With the charge exclusive experiments in preparation it should be possible to pin down whether nuclei behave in any way as a fluid and exhibit collective flow patterns at high energies. It will be also exciting and crucial to utilize the truly heavy nuclear beams that will soon be available at the Bevalac. Reactions such as Pb + Pb and U + U may exhibit qualitatively different features than light nuclear ($A < 100$) reactions. In particular, many finite number effects can be expected to be less important and collective phenomena phenomena could be easier to detect.

In searches for phase transitions, several sensitive experiments have been performed, all with negative findings. The pion multiplicity distribution was found to be accurately Poisson. The excitation function for pions is smooth and linear in E_{Lab}. The $\pi^-\pi^-$ correlation data are consistent with chaotic pion source. Finally, the subthreshold pion spectra show no anomaly at high p_T. Pion field instabilities are thus ruled out for systems as light as Ar. It remains an open question of whether Pb + Pb collisions can generate coherent pion fields. In any case, the study of the pion yield with increasing A will help to clarify the role of pion production and absorption in

nuclear collisions.

The most provocative result obtained thus far is the observation of secondary fragments with an apparently enormous cross sections. These anomalons are so weird that much effort has been spent thus far in trying to find faults with the experiments. An important experimental challenge is to devise a high statistics counter experiment to prove or disprove the existence of these objects. If they are real, they may open the door to the study a completely new class of nuclear phenomena.

In addition to the provocative experiments, it is important to recognize the vast body of experimental work that has clarified the basic reaction mechanism. The differential yields [Figs. 6 and 7] integrated in different kinematical domains [Figs. 17 (a) and (b)] have established the usefulness of the participant-spectator classification. Thus, the role of nuclear geometry is understood reasonably well. Two-proton correlation experiments [Figs. 18 and 49] have revealed quantitatively finite mean free path effects and the increasing importance of multiple *NN* scattering with increasing *A*. The *A* dependence of the high transverse momentum particles [Fig. 20] shows that such nucleons suffer several but not many *NN* collisions. The role of final state interactions due to strong interactions has been demonstrated through the abundance of nuclear composites [Figs. 21 and 53] and through two-proton interferometry [Fig. 33]. The importance of Coulomb final state interactions was seen in pion spectra [Figs. 31 and 38], pion interferometry [Fig. 32] and projectile fragmentation [Fig. 37]. The role of initial state interactions has been demonstrated in particle spectra far beyond the *NN* kinematical domain [Fig. 40], projectile fragmentation [Fig. 42], and stripping reactions [Fig. 43]. Finally, kaon production [Fig. 35] has provided a glimpse at the initial violent phase of the reaction, showing the largest inverse exponential slope ($E_0 \approx$ 142 MeV) observed thus far.

In the future several additional areas need attention.

(1) *Measurements of extremely small cross sections*

The smallest cross section measured so far in high-energy nuclear collisions is of the order of 1 $(\mu b \cdot GeV)/(sr \cdot (GeV/c)^3)$. However, new phenomena may be hiding in much smaller cross sections. With current accelerator and detector technology, it is possible to measure cross sections down to 1 $(nb \cdot GeV)/(sr \cdot (GeV/c)^3)$ and perhaps down to 1 $(pb \cdot GeV)/(sr \cdot (GeV/c)^3)$. Obviously, a special experimental device is needed to measure such low cross sections. The large magnet system called the HISS[EP4] could be useful, for example, for such measurements.

(2) *γ and lepton yields*

Measurement of γ spectra provides a tool for searching for highly excited nuclear matter. It also provides a tool for hunting for long-lived excited states. Especially, delayed coincidence measurement is useful. For example, since no charge decays of anomalons have been seen, it is possible that the γ yield could be used clarifying the anomalon puzzle. Also, further thought should be given to e^+e^- or $\mu^+\mu^-$ measurements as a probe of the highly excited phase of nuclear collisions. Lepton yields have been suggested as a tool to search for the quark-gluon plasma phase transition in very hot nuclei.

(3) *Neutron-rich isotopes*

As we mentioned in Sec. 3.9., the production and systematic study of neutron-rich isotopes far from stability is an important and basic research program. It is in this area that nuclear collisions at high energies have immediate impact on conventional nuclear physics.

(4) *Multi-baryonic excited states*

The high energy density generated in nuclear collisions can in principle produce multi Δ, multi Λ systems, as discussed in Sec. 4.3.3. Up to now such excitations have not been searched for systematically and surprises are possible.

(5) *Higher and lower beam energies*

We expect a transient region where the basic reaction mechanism changes from mean-field interactions to microscopic nucleon-nucleon interactions at beam

energies between 20 and 200 A·MeV. At beam energies at around 10 A·GeV there is another turning point where the basic reaction mechanism changes from nucleon-nucleon interactions to quark-quark or quark-gluon interactions. In order to understand more in depth the physics of nuclear collisions at $E_{\rm Lab} \approx 1$ A·GeV, it is important and useful to extend the study into these lower and higher beam energies.

There is clearly much work ahead in this frontier area of nuclear science. The systematic study of high energy nuclear collisions has yielded a wealth of new data around which theory must now be molded. Already much progress has been made in unraveling the many complex elements of the reaction mechanism. However, it remains a formidable challenge to uncover novel states of nuclei, if they exist, and to replace the "gedanken" (ρ, T) landscape in Fig. 3 with empirical facts.

ACKNOWLEDGMENTS

This article includes several unpublished data and calculations. First of all, the authors would like to express their sincere thanks to L. Anderson, B. Jakobsson, R. Madey, H. Ritter, A. Sandoval, S. Schnetzer, L. Schroeder, and W. Zajc for permission to use their data prior to publications. Stimulated discussions with G. Bertsch, J. Boguta, M. Faessler, K. Frankel, J. Knoll, M.-C. Lemaire, Y. Miake, E. Moeller, H. Pugh, J. Randrup, H. Ryde, D. Scott, R. Stock, and H. Stöcker are gratefully acknowledged. We thank P. Danielewicz for contributing material used in Secs. 2.1. and 2.6. We are also grateful to R. Nix, E. Remler, and H. Stöcker for making unpublished calculations available to us. Both of us especially thank one of the editors, J. Negele, for his patience and persistence needed to complete this work. The work was supported by the Director, Office of Energy Research, Division of Nuclear Physics of the Office of High Energy and Nuclear Physics of the U.S. Department of Energy under Contract DE-AC03-76SF00098. One of us (S.N.) also acknowledges the support from the INS-LBL Collaboration Program.

Appendix: DEFINITION OF COMMON VARIABLES

The single-particle inclusive process is defined as

$$A + B \rightarrow C + X, \tag{A.1}$$

where A is the projectile, B the target, C the particle which is actually detected, and X is anything else. Similarly we can define the two-particle inclusive process as

$$A + B \rightarrow C + D + X, \tag{A.2}$$

where particles C and D are now detected.

In high-energy nuclear collisions it is convenient to introduce Lorentz-invariant kinematical variables to describe the phase space domain into which particles are emitted. The relativistic invariant quantity which describes the motion parallel to the beam direction is called the rapidity, y. Suppose the beam direction is along the z-axis, the rapidity is expressed as

$$y = \frac{1}{2}\ln\frac{E + p_z c}{E - p_z c} = \tanh^{-1}(v_z / c), \tag{A.3}$$

where $v_z / c = p_z c / E$. In non-relativistic case ($v_z / c \ll 1$), the rapidity is nearly equal to the velocity v_z / c. The advantage of the use of y is that a longitudinal boost of the velocity v_0 along the z direction simply adds a constant $y_0 = \tanh^{-1}(v_0 / c)$ to y. For example, in the collision of $A + B \rightarrow C + X$ the velocity v_0 of the center-of-mass frame of the total system (relative to the laboratory frame) is given by

$$\frac{v_0}{c} = \beta = \frac{p_A c}{E_A + m_B c^2}, \tag{A.4}$$

where p_A and E_A are the momentum and total energy of particle A, respectively, and m_B is the mass of particle B. The rapidity of particle C as viewed in the laboratory frame is related to the rapidity as viewed in this center-of-mass frame by

$$y_C^{\text{Lab}} = y_C^{\text{c.m.}} + y_0. \tag{A.5}$$

The variable complementary to the rapidity is the transverse momentum p_T. We normally use the dimensionless transverse momentum,

$$p_T/mc = \sqrt{p_x^2 + p_y^2}/mc, \tag{A.6}$$

which is nearly equal to the transverse velocity (v_T/c) if $p_T \ll mc$.

In order to describe the longitudinal motion, the following variable, called the Feynman scaling variable, is also used:

$$x = p_z^{c.m.}/p_{max}^{c.m.}. \tag{A.7}$$

Here, $p_{max}^{c.m.}$ is the maximum c.m. momentum of particle C allowed by the kinematics For example, if particle C is a boson with zero baryon number, then $p_{max}^{c.m.}$ in the collision of $A + B \rightarrow C + X$ is given by

$$p_{max}^{c.m.} = \frac{\sqrt{(s - m_C^2c^4 - M^2c^4) - 4m_C^2c^4 \cdot M^2c^4}}{2\sqrt{s}}, \tag{A.8}$$

where

$$s = m_A^2c^4 + m_B^2c^4 + 2E_A m_A c^2, \tag{A.9}$$

$$M^2 = (m_A + m_B)^2. \tag{A.10}$$

For the case that

$$\sqrt{s} \gg Mc^2, \tag{A.11}$$

we have

$$p_{max}^{c.m.} \simeq \sqrt{s}/2. \tag{A.12}$$

The Lorentz-invariant single-particle inclusive cross section, σ_{inv}^{incl} for particle C is written as

$$\sigma_{inv}^{incl}(C) = E_C \frac{d^3\sigma}{d^3p_C} = \frac{1}{\pi} \frac{d^2\sigma}{dy dp_T^2}. \tag{A.13}$$

By integrating this cross section over the phase space d^3p_C/E_C we have the *total integrated inclusive* cross section, $\sigma_{tot}^{incl}(C)$. This cross section should be distinguished from the *total* cross section, σ_0, which is approximately given by[RA7]

$$\sigma_0 = \pi r_0^2 \cdot (A_P^{1/3} + A_T^{1/3} - \delta)^2, \quad \text{with } r_0 = 1.29 \text{ fm}, \tag{A.14}$$

where

$$\begin{aligned} \delta &= 1.0 - 0.028\, A_{min} && \text{for } A_{min} < 30 \\ &= 0 && \text{for } A_{min} \geq 30\,, \end{aligned} \tag{A.15}$$

with $A_{min} = \text{Min}(A_P, A_T)$. Here, A_P and A_T are the projectile and target mass numbers, respectively. The quantity $\sigma_{tot}^{incl}(C)$ is related to σ_0 by the relation,

$$\sigma_{tot}^{incl}(C) = \langle m_C \rangle\, \sigma_0, \tag{A.16}$$

where $\langle m_C \rangle$ is the average multiplicity of the detected particle C. For two-particle inclusive processes we can define the invariant cross section as

$$E_C E_D \frac{d^6\sigma}{d^3p_C d^3p_D}, \tag{A.17}$$

and the total integrated cross section of the above quantity is related to the total cross section by

$$\begin{aligned} \sigma_{tot}^{incl}(C,D) &= \langle m_C m_D \rangle\, \sigma_0 && \text{for } C \neq D \\ &= \langle m_C(m_C - 1) \rangle\, \sigma_0 && \text{for } C = D. \end{aligned} \tag{A.18}$$

Finally, we define associated multiplicity, M, as the number of charged fragments registered in a particular counter array in coincidence with one or two particles for which energy, angle, and charge measurements are performed.

REFERENCES

(Not intended as an exhaustive list)

I. CONFERENCE PROCEEDINGS AND REVIEW ARTICLES

RA1. Proceedings of Symposium on Relativistic Heavy Ion Research, GSI Report GSI-P-5-78, Darmstadt, March, 1978.

RA2. Proceedings of Fourth High Energy Heavy Ion Summer Study, Lawrence Berkeley Laboratory Report LBL-7766, Conf-780766, Berkeley, July, 1978.

RA3. Proceedings of Symposium on Heavy Ion Physics from 10 to 200 MeV/AMU, Brookhaven National Laboratory Report BNL-51115, Brookhaven, July, 1979.

RA4. Proceedings of the Hakone Seminar on High-Energy Nuclear Interactions and Properties of Dense Nuclear Matter, Hakone, Japan, July, 1980, ed. by K. Nakai and A. S. Goldhaber.

RA5. Proceedings of Symposium on Future Relativistic Heavy Ion Experiments, GSI Report GSI-81-6, Darmstadt, October, 1980, ed. by R. Bock and R. Stock.

RA6. Proceedings of Fifth High Energy Heavy Ion Summer Study, Lawrence Berkeley Laboratory Report LBL-12652, Conf-8105104, Berkeley, May, 1981.

RA7. A. S. Goldhaber and H. H. Heckman, Ann. Rev. Nucl. Sci. 28, 161 (1979).

RA8. J. R. Nix, Prog. Part. Nucl. Phys. 2, 237 (1979).

RA9. D. K. Scott, Prog. Part. Nucl. Phys. 4, 5 (1980).

RA10. P. J. Siemens, Nucl. Phys. A335, 491 (1980).

RA11. S. Nagamiya, Nucl. Phys. A335, 517 (1980).

RA12. D. K. Scott, Nucl. Phys. A354, 375 (1981).

RA13. M. Gyulassy, Nucl. Phys. A354, 395 (1981).

RA14. S. Das Gupta and A. Z. Mekjian, Phys. Reports 72, 131 (1981).

RA15. H. Stöcker, J. Hofmann, J. A. Maruhn, and W. Greiner, Prog. Part. Nucl. Phys. 4, 133 (1980).

II. EXPERIMENTAL DATA AND EQUIPMENTS

II–1 Data at Forward Angles (< 10°)

(Protons and Nuclear Freagments)

EA1. D. E. Greiner, P. J. Lindstrom, H. H. Heckman, B. Cork, and F. S. Bieser, Phys. Rev. Lett. 35, 152 (1974).

EA2. P. J. Lindstrom, D. E. Greiner, H. Heckman, B. Cork, and F. S. Bieser, Lawrence Berkeley Laboratory Report LBL-3650 (1975), unpublished.

EA3. J. Papp, Thesis, Lawrence Berkeley Laboratory Report LBL-3633 (1975), unpublished.

EA4. H. H. Heckman and P. J. Lindstrom, Phys. Rev. Lett. 37, 56 (1976).

EA5. L. Anderson, Thesis, Lawrence Berkeley Laboratory Report LBL-6767 (1977), unpublished.

EA6. M. M. Gazzaly, J. B. Carroll, J. V. Geaga, G. Igo, J. B. McClelland, M. A. Nasse, H. Spinka, A. L. Sagle, V. Perez-Mendez, R. Talaga, E. T. B. Whipple, and F. Zarbakhsh, Phys. Lett. 79B, 325 (1978).

EA7. H. H. Heckman, D. E. Greiner, P. J. Lindstrom, and H. Shwe, Phys. Rev. C17, 1735 (1978).

EA8. J. Jaros, A. Wagner, L. Anderson, O. Chamberlain, R. Z. Fuzesy, J. Gallup, W. Gorn, L. Schroeder, S. Shannon, G. Shapiro, and H. Steiner, Phys. Rev. C18, 2273 (1978).

EA9. G. D. Westfall, L. W. Wilson, P. J. Lindstrom, H. J. Crawford, D. E. Greiner, and H. H. Heckman, Phys. Rev. C19, 1309 (1979).
EA10. K. Van Bibber, D. L. Hendrie, D. K. Scott, H. H. Wieman, L. S. Schroeder, J. V. Geaga, S. A. Chessin, R. Treuhaft, Y. J. Grossiord, and J. O. Rasmussen, Phys. Rev. Lett. 43, 840 (1979).
EA11. Y. P. Viyogi, T. J. M. Symons, P. Doll, D. E. Greiner, H. H. Heckman, D. L. Hendrie, P. J. Lindstrom, J. Mahoney, D. K. Scott, K. Van Bibber, G. D. Westfall, H. Wieman, and H. J. Crawford, C. MacParland, and C. K. Gelbke, Phys. Rev. Lett. 42, 33 (1979).
EA12. T. J. M. Symons, V. P. Viyogi, G. D. Westfall, P. Doll, D. E. Greiner, H. Faraggi, P. J. Lindstrom, D. K. Scott, H. J. Crawford, and C. McParland, Phys. Rev. Lett. 42, 40 (1979).
EA13. G. D. Westfall, T. J. M. Symons, D. E. Greiner, H. H. Heckman, P. J. Lindstrom, J. Mahoney, A. C. Shotter, D. K. Scott, H. J. Crawford, C. McParland, T. C. Awes, C. K. Gelbke, and J. M. Kidd, Phys. Rev. Lett. 43, 1859 (1979).
EA14. L. Anderson, W. Brückner, E. Moeller, S. Nagamiya, S. Nissen-Meyer, L. Schroeder, G. Shapiro, and H. Steiner, preprint (1982).

(Pions)

EB1. A. M. Baldin, S. B. Gerasimov, M. Guiordenescu, V. N. Zubarev, L. K. Ivanova, A. D. Kirillov, N. S. Moroz, V. D. Radomanov, V. N. Ramzhin, V. S. Stavinskii, and M. Yatsuta, Yad. Fiz. 18, 79 (1973) [Sov. J. Nucl. Phys. 18, 41 (1974)].
EB2. J. Papp, J. Jaros, L. Schroeder, J. Staples, H. Steiner, A. Wagner, and J. Wiss, Phys. Rev. Lett. 34, 601 (1975).
EB3. W. Benenson, G. Bertsch, G. M. Crawley, E. Kashy, J. A. Nolen, Jr., H. Bowman, J. G. Ingersoll, J. O. Rasmussen, J. Sullivan, M. Koike, J. Peter, and T. E. Ward, Phys. Rev. Lett. 43, 683 (1979); Phys. Rev. Lett. 44, 54 (1980) (E).
EB4. E. Aslanides, P. Fassnacht, F. Hibou, E. Chiavassa,G. Dellacasa, M. Gallio, A. Musso, T. Bressani, and G. Puddu, Phys. Rev. Lett. 43, 1466 (1979).
EB5. J. P. Sullivan, J. A. Bistirlich, H. R. Bowman, R. Bossingham, T. Buttke, K. M. Crowe, K. A. Frankel, C. J. Martoff, J. Miller, D. L. Murphy, J. O. Rasmussen, W. A. Zajc, O. Hashimoto, M. Koike, J. Peter, W. Benenson, G. M. Crawley, E. Kashy, and J. A. Nolen, Jr., Phys. Rev. C (in press).
EB6. E. Moeller, L. Anderson, W. Brückner, S. Nagamiya, S. Nissen-Meyer, L. Schroeder, G. Shapiro, and H. Steiner, preprint (1982).
See also Ref. EA3.

II–2 Data at Large Angles ($10° \leq \vartheta \leq 170°$)

(Inclusive Protons)

EC1. G. D. Westfall, J. Gosset, P. J. Johansen, A. M. Poskanzer, W. G. Meyer, H. H. Gutbrod, A. Sandoval, and R. Stock, Phys. Rev. Lett. 37, 1202 (1976).
EC2. J. Gosset, H. H. Gutbrod, W. G. Meyer, A. M. Poskanzer, A. Sandoval, R. Stock, and G. D. Westfall, Phys. Rev. C16, 629 (1977).
EC3. S. Nagamiya, I. Tanihata, S. Schnetzer, L. Anderson, W. Brückner, O. Chamberlain, S. Schnetzer, G. Shapiro, and H. Steiner, J. Phys. Soc. Japan Suppl. 44, 378 (1978).
EC4. S. Nagamiya, L. Anderson, W. Brückner, O. Chamberlain, M.-C. Lemaire, S. Schnetzer, G. Shapiro, H. Steiner, and I. Tanihata, Phys. Lett. 81B, 147 (1979).
EC5. V. G. Antonenko, V. M. Galitskij, Yu. I. Grigor'yan, M. S. Ippolitov, K. V. Karadjev, E. A. Kuz'min, V. I. Manko, A. A. Ogloblin, V. V. Paramonov, A. A. Tsvetkov, and A. A. Vinogradov, Institute of Atomic Energy Preprint, IAE-3220 (1979).
EC6. A. Sandoval, H. H. Gutbrod, W. G. Meyer, R. Stock, Ch. Lukner, A. M. Poskanzer,

J. Gosset, J.-C. Jourdain, C. H. King, G. King, Nguyen Van Sen, G. D. Westfall, and K. L. Wolf, Phys. Rev. C21, 1321 (1980).
EC7. S. Nagamiya, M.-C. Lemaire, E. Moeller, S. Schnetzer, G. Shapiro, H. Steiner, and I. Tanihata, Phys. Rev. C24, 971 (1981).

(Inclusive Neutrons)
ED1. W. Schimmerling, J. Kast, D. Ortehdahl, R. Madey, R. A. Cecil, B. D. Anderson, and A. R. Baldwin, Phys. Rev. Lett. 43, 1985 (1979).
ED2. R. A. Cecil, B. D. Anderson, A. R. Baldwin, R. Madey, W. Schimmerling, J. W. Kast, and D. Ortendahl, Phys. Rev. C24, 2013 (1981).
ED3. R. Madey, private communication (1982).

(Inclusive Light–Composite Fragments)
EE1. H. H. Gutbrod, A. Sandoval, P. J. Johansen, A. M. Poskanzer, J. Gosset, W. G. Meyer, G. D. Westfall, and R. Stock, Phys. Rev. Lett. 37, 667 (1976).
EE2. M.-C. Lemaire, S. Nagamiya, S. Schnetzer, H. Steiner, and I. Tanihata, Phys. Lett. 85B, 38 (1979).
EE3. M.-C. Lemaire, in: Proceedings of the 2nd French-Japanese Colliqium on Nuclear Physics with Heavy Ions, IN2P3 Publication, p. 139, Gif-sur-Yvette, France, October, 1979 [Preprint: Lawrence Berkeley Laboratory Report LBL-10555 (1979)].
EE4. B. Jakobsson et al., private communication (1981).
See also Refs. EC2, EC6, and EC7.

(Inclusive Heavy–Composite Fragments)
EF1. W. Loveland, R. J. Otto, D. J. Morrissey, and G. T. Seaborg, Phys. Rev. Lett. 35, 152 (1975); Phys. Lett. 69B, 284 (1977).
EF2. S. B. Kaufman, M. W. Weisfield, E. P. Steinberg, B. D. Wilkins and D. Hederson, Phys. Rev. C14, 1121 (1976).
EF3. J. Stevenson, P. B. Price and K. Frankel, Phys. Rev. Lett. 38, 1125 (1977).
EF4. P. B. Price, J. Stevenson, and K. Frankel, Phys. Rev. Lett. 39, 177 (1977).
EF5. D. J. Morrissey, W. Loveland, and G. T. Seaborg, Z. Physik A289, 123 (1978).
EF7. D. J. Morrissey, W. R. Marsh, R. J. Otto, W. Loveland, and G. T. Seaborg, Phys. Rev. C18, 1267 (1978).
EF8. P. B. Price and J. Stevenson, Phys. Lett. 78B, 197 (1978).
EF9. T. Shibata, H. Ejiri, J. Chiba, S. Nagamiya, K. Nakai, A. Anholt, H. Bowman, J. G. Ingersoll, E. A. Rauscher, and J. O. Rasmussen, Nucl. Phys. A308, 513 (1978).
EF10. D. R. Fortney and N. T. Porile, Phys. Lett. 76B, 553 (1979).
EF11. D. J. Morrissey, W. Loveland, M. de Saint Simon and G. T. Seaborg, Phys. Rev. C21, 1783 (1980).
EF12. W. G. Meyer, H. H. Gutbrod, Ch. Luckner, and A. Sandoval, Phys. Rev. C22, 179 (1980).
EF13. S. B. Kaufman, E. P. Steinberg, B. D. Wilkins, and D. J. Henderson, Phys. Rev. C22, 1897 (1980).
EF14. W. Loveland, D. J. Morrissey, K. Aleklett, G. T. Seaborg, S. B. Kaufman, E. P. Steinberg, B. D. Wilkins, J. B. Cumming, P. E. Haustein, and H. C. Hseuh, Phys. Rev. C23, 253 (1981).
EF15. K. Aleklett, D. J. Morrissey, W. Loveland, P. L. McGaughey, and G. T. Seaborg, Phys. Rev. C23, 1044 (1981).
EF16. K. A. Frankel and J. D. Stevenson, Phys. Rev. C23, 1511 (1981).

(Inclusive Pions)
EG1. D. R. F. Cochran, P. N. Dean, P. A. M. Gram, E. A. Knapp, E. R. Martin, D. E. Nagle,

P. B. Perkins, W. J. Shlaer, H. A. Thiessen, and E. D. Theriot, Phys. Rev. D6, 3085 (1972).
EG2. W. Schimmerling, K. G. Vosburgh, K. Koepke, and W. Wales, Phys. Rev. Lett. 34, 601 (1975).
EG3. S. Y. Fung, W. Gorn, G. P. Kiernan, F. F. Liu, J. J. Lu, Y. T. Oh, J. Ozawa, R. T. Poe, L. S. Schroeder, and H. Steiner, Phys. Rev. Lett. 40, 292 (1978).
EG4. I. Tanihata, S. Nagamiya, O. Chamberlain, M.-C. Lemaire, S. Schnetzer, G. Shapiro, and H. Steiner, Phys. Lett. 87B, 349 (1979).
EG5. K. L. Wolf, H. H. Gutbrod, W. G. Meyer, A. M. Poskanzer, A. Sandoval, R. Stock, J. Gosset, C. H. King, G. King, Nguyen Van Sen, and G. D. Westfall, Phys. Rev. Lett. 42, 1448 (1979).
EG6. J. Chiba, K. Nakai, I. Tanihata, S. Nagamiya, H. Bowman, J. Ingersoll, and J. O. Rasmussen, Phys. Rev. C20, 1332 (1979).
EG7. K. Nakai, J. Chiba, I. Tanihata, M. Sasao, H. Bowman, S. Nagamiya, and J. O. Rasmussen, Phys. Rev. C20, 2210 (1979).
EG8. K. Frankel, J. Bistirlich, H. Bowman, K. M. Crowe, C. J. Martoff, J. Miller, D. Murphy, J. O. Rasmussen, J. Sullivan, W. Zajc, O. Hashimoto, M. Koike, J. Peter, W. Benenson, G. M. Crawley, E. Kashy, J. A. Nolen, Jr., and J. Quebert, Phys. Rev. C (submitted) [Lawrence Berkeley Laboratory Report LBL-12585 (1981)].
EG9. S. Nagamiya, H. Hamagaki, P. Hecking, R. Lombard, Y. Miake, E. Moeller, S. Schnetzer, H. Steiner, S. Kadota, I. Tanihata, S. Bohrmann, and J. Knoll, Lawrence Berkeley Laboratory Report LBL-14033 (1982), to be published.
See also Refs. EC3 and EC7.

(Inclusive Strange Particles)
EH1. S. Schnetzer, Thesis, Lawrence Berkeley Laboratory Report LBL-13727 (1981), unpublished.
EH2. J. W. Harris, A. Sandoval, R. Stock, H. Stroebele, R. E. Renfordt, J. V. Geaga, H. G. Pugh, L. S. Schroeder, K. L. Wolf, and A. Dacal, Phys. Rev. Lett. 47, 229 (1981).
EH3. A. Shor, K. Ganezer, J. Carroll, G. Igo, J. Geaga, S. Abachi, A. Sagle, T. Mulera, V. Perez-Mendez, P. Lindstrom, F. Zarbakhsh, and D. Woodard, in: Proc. 5th High Energy Heavy Ion Summer Study, LBL-12652, Conf-8105104, Berkeley, May, 1981, p.470.

(Particle Correlations)
EJ1. G. M. Chernov, K. G. Gulamov, V. G. Gulyamov, S. Z. Nashyrov, and L. N. Svechnikova, Nucl. Phys. A280, 478 (1977).
EJ2. H. H. Heckman, H. J. Crawford, D. E. Greiner, P. J. Lindstrom, and Lance W. Wilson, Phys. Rev. C17, 1651 (1978).
EJ3. S. Y. Fung, W. Gorn, G. P. Kiernan, J. J. Lu, Y. T. Oh, and R. T. Poe, Phys. Rev. Lett. 41, 1592 (1978).
EJ4. B. Jakobsson, Physica Scripta 17, 491 (1978).
EJ5. K. B. Bhalla, S. Hertzman, A. Oskarsson, I. Otterlund, and B. Jakobsson, Phys. Lett. 82B, 216 (1979).
EJ6. J. Bartke, Nucl. Phys. A335, 481 (1980).
EJ7. R. Stock, H. H. Gutbrod, W. G. Meyer, A. M. Poskanzer, A. Sandoval, J. Gosset, C. H. King, G. King, Ch. Lucker, Nguyen Van Sen, G. D. Westfall, and K. L. Wolf, Phys. Rev. Lett. 44, 1243 (1980).
EJ8. S. Nagamiya, M.-C. Lemaire, S. Schnetzer, H. Steiner, and I. Tanihata, Phys. Rev. Lett. 45, 602 (1980).
EJ9. I. Tanihata, M.-C. Lemaire, S. Nagamiya, and S. Schnetzer, Phys. Lett. 97B, 363 (1980).
EJ10. A. Sandoval, R. Stock, H. E. Stelzer, R. E. Renfordt, J. W. Harris, J. P.

Branniggan, J. V. Geaga, L. J. Rosenberg, L. S. Schroeder, and K. L. Wolf, Phys. Rev. Lett. 45, 874 (1980).
EJ11. I. Tanihata, in: Proceedings of Hakone Seminar on High-Energy Nuclear Interactions and Properties of Dense Nuclear Matter (K. Nakai and A. S. Goldhaber, ed.), p.382, Hakone, Japan, July, 1980.
EJ12. I. Tanihata, S. Nagamiya, S. Schnetzer, and H. Steiner, Phys. Lett. 100B, 121 (1981).
EJ13. J. J. Lu, D. Beavis, S. Y. Fung, W. Gorn, A. Huie, G. P. Kiernan, R. T. Poe, and G. VanDalen, Phys. Rev. Lett. 46, 898 (1981).
EJ14. Z. Zarbakhsh, A. L. Sagle, F. Brochard, T. A. Mulera, V. Perez-Mendez, I. Tanihata, J. B. Carroll, K. S. Ganezer, G. Igo, J. Oostens, D. Woodard, and R. Sutter, Phys. Rev. Lett. 46, 1268 (1981).
EJ15. W. A. Zajc, J. A. Bistirlich, R. R. Bossingham, H. R. Bowman, C. W. Clawson, K. M. Crowe, K. A. Frankel, O. Hashimoto, J. G. Ingersoll, M. Koike, J. P. Kurck, C. J. Martoff, W. J. McDonald, J. P. Miller, D. Murphy, J. O. Rasmussen, J. P. Sullivin, P. Truol, and E. Yoo, in: Proc. 5th High Energy Heavy Ion Summer Study, LBL-12652, Conf-8105104, Berkeley, May, 1981, p.350; also private communication (1981).
EJ16. A. Sandoval, private communication (1981).
See also Refs. EC3, EC4, EC6, EE3, EF12, and EG3.

(Miscellaneous Cited)

EK1. I. Otterlund, in: Proc. of the Workshop on Future Relativistic Heavy Ion Experiments, GSI, Darmstadt, 1980, p. 185.
EK2. S. Nagamiya, in: Proceedings of the 5th High Energy Heavy Ion Summer Study, LBL-12652, Conf-8105104, Berkeley, May, 1981, p.141.

II–3 Data at Backward Angles (> 170°)

(Protons)

EL1. S. Frankel, W. Frati, O. Van Dyck, R. Werbeck, and V. Highland, Phys. Rev. Lett. 36, 642 (1976).
EL2. V. I. Komarov, G. E. Kosarev, H. Muller, D. Netzband, and T. Stiehler, Phys. Lett. 69B, 37 (1977).
EL3. S. Frankel, Phys. Rev. Lett. 38, 1338 (1977); Phys. Rev. C17, 697 (1978).
EL4. V. I. Komarov, G. E. Kosarev, H. Muller, D. Netzband, T. Stiehler, and S. Tesch, Phys. Lett. 80B, 30 (1978).
EL5. S. Frankel, W. Frati, G. Blanpied, G. W. Hoffmann, T. Kozlowski, C. Morris, H. A. Thiessen, O. Van Dyck, R. Ridge, and C. Whitten, Phys. Rev. C18, 1375 (1978).
EL6. S. Frankel, W. Frati, R. M. Woloshyn, and D. Yang, Phys. Rev. C18, 1379 (1978).
EL7. S. Frankel, W. Frati, M. Gazzaly, G. W. Hoffman, O. Van Dyck, and R. M. Woloshyn, Phys. Rev. Lett. 41, 148 (1978).
EL8. V. I. Komarov, G. E. Kosarev, H. Muller, D. Netzband, V. D. Toneev, T. Stiehler, S. Tesch, K. K. Gudima, and S. G. Mashnik, Nucl. Phys. A326, 297 (1979).
EL9. J. R. Wu, C. C. Chang, and H. D. Holmgren, Phys. Rev. C19, 698 (1979).
EL10. Y. D. Bayukov, V. I. Efremenko, S. Frankel, W. Frati, M. Gazzaly, G. A. Leksin, N. A. Nikiforov, C. F. Perdrisat, V. I. Tchistilin, and Y. M. Zaitsev, Phys. Rev. C20, 764 (1979).
EL11. S. Frankel, W. Frati, M. Gazzaly, Y. D. Bayukov, V. I. Efremenko, G. A. Leksin, N. A. Nikiforov, V. I. Tchistilin, Y. M. Zaitsev, and C. F. Perdrisat, Phys. Rev. C20, 2257 (1979).
EL12. J. V. Geaga, S. A. Chessin, J. Y. Grossiord, J. W. Harris, D. L. Hendrie, L. S. Schroeder, R. N. Treuhaft, and K. Van Bibber, Phys. Rev. Lett. 45, 1993 (1981).

EL13. I. Tanihata, Y. Miake, H. Hamagaki, S. Kadota, Y. Shida, R. Lombard, E. Moeller, S. Nagamiya, S. Schnetzer, and H. Steiner, in Proceedings of the 5th High Energy Heavy Ion Summer Study, LBL-12652, Conf-8105104, Berkeley, May, 1981, p.365.

(Pions)

EM1. A. M. Baldin, AIP Conference Proceedings 26, 621 (1975) and references therein.
EM2. A. M. Baldin, M. Guiordenescu, V. N. Zubarev, N. S. Moroz, A. A. Povtoreiko, V. D. Radomanov, and V. S. Stavinskii, Yad. Fiz. 20, 1201 (1975) [Sov. J. Nucl. Phys. 20, 629 (1976)].
EM3. C. F. Perdrisat, S. Frankel, and W. Frati, Phys. Rev. C18, 1764 (1978).
EM4. L. S. Schroeder, S. A. Chessin, J. V. Geaga, J. Y. Grossiord, J. W. Harris, D. L. Hendrie, R. Treuhaft, and K. Van Bibber, Phys. Rev. Lett. 43, 1787 (1979).
EM5. S. A. Chessin et al., private communication (1981).

II–4 Exotic Hunting

EN1. H. G. Baumgardt, J. U. Schott, Y. Sakamoto, E. Schopper, H. Stöcker, J. Hofmann, W. Scheid, and W. Greiner, Z. Physik A273, 359 (1975).
EN2. P. B. Price and J. Stevenson, Phys. Rev. Lett. 34, 405 (1975).
EN3. R. L. Holt, J. P. Schiffer, J. Specht, L. M. Bollinger, and G. E. Thomas, Phys. Rev. Lett. 36, 183 (1976).
EN4. E. M. Friedlander, R. W. Gimpel, H. H. Heckman, Y. Karant, B. Judek, and E. Ganssauge, Phys. Rev. Lett. 45, 1084 (1980).
EN5. H. H. Heckman, in: Proc. of the Workshop on Future Relativistic Heavy Ion Experiments, GSI, Darmstadt, 1980, p. 80 [Preprint, Lawrence Berkeley Laboratory Report LBL-12120 (1981)].
EN6. P. L. Jain and G. Das, Phys. Rev. Lett. 48, 305 (1982).
EN7. H. B. Barber, P. S. Freier, and C. J. Waddington, private communication (1982).
EN8. P. Lindstrom, E. Greiner, and H. Crawford, private communication (1982).
EN9. K. Frankel and J. Stevenson, Phys. Rev. C14, 1455 (1976).
See also Refs. EJ2 and EJ10.

II–5 New Detectors

EP1. M. R. Maier, H. G. Ritter, and H. H. Gutbrod, IEEE Trans. on Nuclear Science NS-27, 42 (1980).
EP2. J. Gosset, in: Proc. 1981 INS International Symposium on Nuclear Radiation Detectors (to be published in Nucl. Instr. Meth.).
EP3. K. Van Bibber and A. Sandoval, to be published in: Heavy Ion Science, Plenum Press, New York, 1982.
EP4. HISS Conceptional Design Report, Lawrence Berkeley Laboratory Report LBL-5004 (1978).

III. THEORETICAL MODELS

III–1 Abnormal Nuclear Matter, Pion Condensation, Shockwave, Phase Transition

TA1. A. R. Bodmer, Phys. Rev. D4, 1601 (1974).
TA2. T. D. Lee and G. C. Wick, Phys. Rev. D9, 2291 (1974).
TA3. T. D. Lee, Rev. Mod. Phys. 47, 267 (1976) and references therein.
TA4. W. Weise and G. E. Brown, Phys. Reports 27C, 1 (1976) and references therein.
TA5. A. B. Migdal, Rev. Mod. Phys. 50, 107 (1978) and references therein.
TA6. V. Ruck, M. Gyulassy, and W. Greiner, Z. Phys. A277, 391 (1979).
TA7. G. G. Bunatjan, Yad. Fiz. 29, 258 (1979) [Sov. J. Nucl. Phys. 30, 131 (1979)].

TA8. W. Scheid, H. Muller, and W. Greiner, Phys. Rev. Lett. 32, 741 (1974).
TA9. C. F. Chapline, H. H. Johnson, E. Teller, and M. S. Weiss, Phys. Rev. D8, 4302 (1973).
TA10. H. Stöcker, J. Maruhn, and W. Greiner, Z. Physik A286, 121 (1978); Phys. Lett. 81B, 303 (1979).
TA11. M. Gyulassy and W. Greiner, Ann. Phys. 109, 485 (1977).
TA12. J. Boguta, Lawrence Berkeley Laboratory Reports LBL-13874 (1982), LBL-13885 (1982).

III–2 Cascade (Intranuclear)

TB1. J. P. Bondorf, H. T. Feldmeier, S. Garpman, E. C. Halbert, Phys. Lett. 65B, 217 (1976); Z. Phys. 279, 385 (1976).
TB2. R. K. Smith and M. Danos, private communication, 1978.
TB3. K. K. Gudima and V. D. Toneev, Yad. Fiz. 27, 658 (1978) [Sov. J. Nucl. Phys. 27, 351 (1978)].
TB4. J. D. Stevenson, Phys. Rev. Lett. 41, 1702 (1978).
TB5. K. K. Gudima, H. Iwe, and V. D. Toneev, J. Phys. G5, 229 (1979).
TB6. Y. Yariv and Z. Fraenkel, Phys. Rev. C20, 2227 (1979); Phys. Rev. C24, 488 (1981).
TB7. H. Iwe, J. Phys. G5, 1405 (1979).
TB8. K. K. Gudima and V. D. Toneev, Dubna Report E2-12644 (1979).
TB9. J. Cugnon, Phys. Rev. C22, 1885 (1980).
TB10. J. Cugnon, T. Mizutani, and J. Vandermeulen, Nucl. Phys. A352, 505 (1981).
TB11. J. Cugnon, J. Knoll, and J. Randrup, Nucl. Phys. A360, 444 (1981).
TB12. E. C. Halbert, Phys. Rev. C23, 295 (1981).
See also Refs. TN5, TK19, and TP2.

III–3 Classical Equation of Motion

TC1. A. R. Bodmer and A. D. MacKeller, Phys. Rev. C15, 1342 (1977).
TC2. L. Wilets, Y. Yariv, and R. Chestnut, Nucl. Phys. A301, 359 (1978).
TC3. D. J. E. Callaway, L. Wilets, and Y. Yariv, Nucl. Phys. A327, 250 (1979).
TC4. A. R. Bodmer, C. N. Panos, and A. D. MacKeller, Phys. Rev. C22, 1025 (1980).
TC5. A. R. Bodmer and C. N. Panos, Nucl. Phys. A356, 517 (1981).

III–4 Linear Cascade

TD1. J. Hüfner and J. Knoll, Nucl. Phys. A290, 460 (1977).
TD2. J. Hüfner, in: Proc. 4th High Energy Heavy Ion Summer Study, LBL-7766, Conf-780766, Berkeley, 1978, p.135.
TD3. J. Randrup, Phys. Lett. 76B, 547 (1978).
TD4. J. Knoll and J. Randrup, Nucl. Phys. A324, 445 (1979).
TD5. J. Knoll and J. Randrup, Phys. Lett 103B, 264 (1981).
See also Refs. TU1 and TU2.

III–5 Transport

TE1. H. J. Pirner and B. Schürmann, Nucl. Phys. A316, 461 (1979).
TE2. B. Schürmann, Phys. Rev. C20, 1607 (1979).
TE3. J. Randrup, Nucl. Phys. A316, 509 (1979).
TE4. P. Hecking and H. Pirner, Nucl. Phys. A333, 514 (1980).
TE5. R. Malfliet, Phys. Rev. Lett. 44, 864 (1980).
TE6. B. Schürmann and N. Macoc-Borstnik, preprint (1981).
TE7. E. A. Remler, preprint (1981).

III–6 Hard Scattering

TF1. S. E. Koonin, Phys. Rev. Lett. 39, 680 (1977).

TF2. I. A. Schmidt and R. Blankenbecler, Phys. Rev. D15, 3321 (1977); Phys. Rev. D16, 1318 (1977).
TF3. G. Bertsch, Phys. Rev. C15, 713 (1977).
TF4. R. L. Hatch and S. E. Koonin, Phys. Lett. 81B, 1 (1978).
TF5. R. H. Landau and M. Gyulassy, Phys. Rev. C19, 149 (1979).
TF6. M. Chemtob, Nucl. Phys. A314, 387 (1979); Nucl. Phys. A336, 299 (1979).
TF7. B. K. Jain, Phys. Rev. C22, 583 (1980).
TF8. C. Y. Wong and R. Blankenbecler, SLAC-PUB-2488 (1980), unpublished.
TF9. P. Hecking, Lawrence Berkeley Laboratory Report, LBL-12671 (1981), to be published.

III–7 Phase Space (Statistical)

TG1. E. Fermi, Prog. Theor. Phys. 5, 570 (1950).
TG2. M. Gyulassy and S. K. Kauffmann, Phys. Rev. Lett. 40, 298 (1978).
TG3. G. Mantzouranis, Phys. Rev. C18, 2227 (1978).
TG4. J. Knoll, Phys. Rev. C20, 773 (1979).
TG5. S. Bohrmann and J. Knoll, Nucl. Phys. A356, 498 (1981).
TG6. S. Bohrmann, private communication (1981).
TG7. A. H. Blin, S. Bohrmann, and J. Knoll, to be published in Z. Phys.

III–8 Collective Tube

TH1. J. Vary, Phys. Rev. Lett. 40, 294 (1978).
TH2. H. B. Mathis and Meng Ta-Chung, Phys. Rev. C18, 952 (1978).
TH3. Meng Ta-Chung and E. Moeller, Phys. Rev. Lett. 41, 1352 (1978).
TH4. Meng Ta-Chung, Phys. Rev. Lett. 42, 1331 (1979).

III–9 Thermal

TJ1. M. Sobel, P. J. Siemens, J. P. Bondorf, and H. A. Bethe, Nucl. Phys. A251, 502 (1975).
TJ2. J. I. Kapusta, Phys. Rev. C16, 1493 (1977).
TJ3. A. Z. Mekjian, Phys. Rev. Lett. 38, 640 (1977); Phys. Rev. C17, 1051 (1978); Nucl. Phys. A312, 491 (1978); Phys. Lett. 89B, 177 (1980).
TJ4. W. D. Myers, Nucl. Phys. A296, 177 (1978).
TJ5. J. Gosset, J. I. Kapusta, and G. D. Westfall, Phys. Rev. C18, 844 (1978).
TJ6. S. Das Gupta, Phys. Rev. Lett. 41, 1450 (1978).
TJ7. N. K. Glendenning and Y. Karant, Phys. Rev. Lett. 40, 374 (1978).
TJ8. I. Montvay and J. Zimanyi, Nucl. Phys. A316, 490 (1979).
TJ9. S. I. A. Garpman, N. K. Glendenning, and Y. J. Karant, Nucl. Phys. A322, 382 (1979).
TJ10. I. G. Bofatskaya, C. B. Chiu, M. I. Gorenstein, and G. M. Zinovjev, Phys. Rev. C22, 209 (1980).
See also Refs. RA14, EC1, EC2, TK19, TM3, TM6, TM7, TN1, TN2, and TU3.

III–10 Hydrodynamical

TK1. A. A. Amsden, G. F. Bertsch, F. H. Harlow, and J. R. Nix, Phys. Rev. Lett. 35, 905 (1975).
TK2. C. Y. Wong, J. A. Maruhn, and T. A. Welton, Nucl. Phys. A253, 469 (1975); Phys. Lett. 66B, 19 (1977).
TK3. Y. Kitazoe, K. Matsuoka, and M. Sano, Prog. Theor. Phys. 56, 860 (1976).
TK4. A. A. Amsden, F. H. Harlow, and J. R. Nix, Phys. Rev. C15, 1059 (1977).
TK5. A. A. Amsden, J. N. Ginocchio, F. H. Harlow, J. R. Nix, M. Danos, E. C. Halbert, and R. K. Smith, Phys. Rev. Lett. 38, 1055 (1977).
TK6. J. P. Bondorf, S. I. A. Garpman and J. Zimanyi, Nucl. Phys. A296, 320 (1978).

TK9. Y. Kitazoe and M. Sano, Nuovo Cimento Lett. 14, 400 (1975); Nuovo Cimento Lett. 14, 407 (1975); Nuovo Cimento Lett. 22, 153 (1978); Prog. Theor. Phys. 54, 922 (1975); Prog. Theor. Phys. 54, 1575 (1975).
TK10. H. Stöcker, J. A. Maruhn, and W. Greiner, Z. Physik A293, 173 (1979).
TK11. P. Danielewicz, Nucl. Phys. A314, 465 (1979).
TK12. P. J. Siemens and J. O. Rasmussen, Phys. Rev. Lett. 42, 844 (1979).
TK13. H. Stöcker, R. Y. Cusson, J. A. Maruhn, and W. Greiner, Z. Physik A294, 1 (1980).
TK14. H. H. K. Tang and C. Y. Wong, Phys. Rev. C21, 1846 (1980).
TK15. H. Stöcker, J. A. Maruhn, and W. Greiner, Phys. Rev. Lett. 44, 725 (1980).
TK16. L. P. Csernai and W. Greiner, Phys. Lett. 99B, 85 (1981).
TK17. J. R. Nix and D. Strottman, Phys. Rev. C23, 2548 (1981).
TK18. H. Stöcker, Lawrence Berkeley Laboratory Report LBL-12302 (1981).
TK19. H. Stöcker, C. Riedel, Y. Yariv, L. P. Csernai, G. Buchwald, G. Graebner, J. A. Maruhn, W. Greiner, K. Frankel, M. Gyulassy, B. Schürmann, G. Westfall, J. D. Stevenson, J. R. Nix, and D. Strottman, Phys. Rev. Lett. 47, 1807 (1981).
TK20. L. P. Csernai, W. Greiner, H. Stöcker, I. Tanihata, S. Nagamiya, and J. Knoll, Phys. Rev. C (in press) [Preprint Lawrence Berkeley Laboratory Report LBL-13944 (1981)].
TK21. L. P. Csernai, B. Lukacs, and J. Zymanyi, Nuovo Cimento Lett. 27, 111 (1980).
TK22. L. P. Csernai and H. W. Barz, Z. Phys. A296, 173 (1980).
TK23. H. Stöcker, M. Gyulassy, and J. Boguta, Phys. Lett. 103B, 269 (1981).
TK24. G. Buchwald, L. P. Csernai, J. A. Maruhn, and W. Greiner, Phys. Rev. C24, 135 (1981).
TK25. A. J. Sierk and J. R. Nix, Phys. Rev. C22, 1920 (1980).
TK26. J. R. Nix, D. Strottman, Y. Yariv, and Z. Fraenkel, LASL preprint LA-UR-81-3280 (1981).
See also Refs. TA8, TA10, TN3, TN4, and RA9.

III–11 Direct plus Thermal

TL1. M. Chemtob and B. Schürmann, Nucl. Phys. A336, 508 (1980).
TL2. B. Schürmann and M. Chemtob, Z. Physik A294, 371 (1980).

III–12 Formation of Composite Particles

(Formation Mechanism)

TM1. S. F. Butler and C. A. Pearson, Phys. Rev. 129, 836 (1963).
TM2. A. Schwarzschild and C. Zupancic, Phys. Rev. 229, 854 (1963).
TM3. R. Bond, P. J. Johansen, S. E. Koonin, and S. Garpman, Phys. Lett. 71B, 43 (1977).
TM4. J. I. Kapusta, Phys. Rev. C21, 1301 (1980).
TM5. H. Sato and K. Yazaki, Phys. Lett. 98B, 153 (1981).
TM6. B. K. Jennings, L. Satpathy, and S. Das Gupta, preprint (1981).
TM7. B. K. Jennings, S. Das Gupta, and N. Mobed, preprint (1981).
TM8. E. A. Remler, Ann. Phys. (N.Y.) 136, 293 (1981).
TM9. M. Gyulassy, E. A. Remler, and K. Frankel, Bull. Am. Phys. Soc. 26, 1113 (1981), to be published.
TM10. E. A. Remler, College of William and Mary Preprint, Dec. (1981), to be published.
See also Refs. TJ3, TJ5, TJ8, TK18, and RA9.

(Entropy)

TN1. P. J. Siemens and J. I. Kapusta, Phys. Rev. Lett. 43, 1486 (1979); 43, 1690 (1979) (E).

TN2. I. N. Mishustin, F. Myhrer, and P. J. Siemens, Phys. Lett. 95B, 361 (1980).
TN3. L. P. Csernai and H. W. Barz, Z. fur Physik A296, 173 (1980).
TN4. J. I. Kapusta and D. Strottman, Phys. Rev. C23, 1282 (1981).
TN5. G. Bertsch and J. Cugnon, preprint (1981), and p. 246 in Ref. (RA6).
See also Refs. TK18, and TJ9.

(Applications to n/p and t/ ^{3}He Ratios)

TP1. J. Randrup and S. E. Koonin, Nucl. Phys. A356, 223 (1981).
TP2. J. D. Stevenson, Phys. Rev. Lett. 45, 1773 (1980).

III–13 Pion Interferometry (Hanbury–Brown/ Twiss Effects)

TQ1. R. Hanbury-Brown and R. Q. Twiss, Nature 178, 1046 (1956).
TQ2. G. Goldhaber, S. Goldhaber, W. Lee, and A Pais, Phys. Rev. 120, 300 (1960).
TQ3. G. I. Kopylov, Phys. Lett. 50B, 572 (1974).
TQ4. G. Cocconi, Phys. Lett. 49B, 459 (1974).
TQ5. S. E. Koonin, Phys. Lett. 70B, 43 (1977).
TQ6. F. B. Yano and S. E. Koonin, Phys. Lett. 78B, 556 (1978).
TQ7. M. Gyulassy and S. K. Kauffmann, and L. W. Wilson, Phys. Rev. C20, 2267 (1979).
TQ8. M. Gyulassy, Phys. Rev. Lett. 48, 454 (1982).

III–14 Coulomb Effects

TR1. K. G. Libbrecht and S. E. Koonin, Phys. Rev. Lett. 43, 1581 (1979).
TR2. M. Gyulassy and S. K. Kauffmann, Nucl. Phys. A362, 503 (1981).

III–15 Backward Particle Production

TS1. R. D. Amado and R. M. Woloshyn, Phys. Rev. Lett. 36, 1435 (1976); Phys. Lett. 69B, 400 (1977).
TS2. S. Frankel and R. M. Woloshyn, Phys. Rev. C16, 1680 (1977).
TS3. V. V. Burov, V. K. Lukyanov, and A. I. Titov, Phys. Lett. 67B, 46 (1977).
TS4. T. Fujita, Phys. Rev. Lett. 39, 174 (1977); Nucl. Phys. A324, 409 (1979).
TS5. T. Fujita and J. Hüfner, Nucl. Phys. A314, 317 (1979).
TS6. L. L. Frankfurt and M. I. Strikman, Phys. Lett. 83B, 407 (1979).
TS7. T. Yukawa and S. Furui, Phys. Rev. C20, 2316 (1979).

III–16 Ground–State Correlations

TT1. T. Fujita and J. Hüfner, Nucl. Phys. A343, 493 (1980).
TT2. O. Bohigas and S. Stringari, Phys. Lett. 95B, 9 (1980).
TT3. J. Hüfner and M. C. Nemes, Phys. Rev. C23, 2538 (1981).
TT4. D. Forster, *Hydrodymamics*, *Fluctuations*, *Broken Symmetry*, *Correlation Functions*, Benjamin Press, Mass., 1975.

III–17 Strange Particle Production

TU1. J. Randrup and C. M. Ko, Nucl. Phys. A343, 519 (1980).
TU2. J. Randrup, Phys. Lett. 99B, 9 (1981).
TU3. F. Asai, H. Sato, and M. Sano, Phys. Lett. 98B, 19 (1981).
TU4. C. M. Ko, Phys. Rev. C23, 2760 (1981).
TU5. F. Asai, Nucl. Phys. A356, 519 (1981).

III–18 Spectator Dynamics

TV1. H. Feshbach and K. Huang, Phys. Lett. 47B, 300 (1973).
TV2. A. S. Goldhaber, Phys. Lett. 53B, 306 (1974).
TV3. J. Hüfner, K. Schafer, and B. Schürmann, Phys. Rev. C12, 1888 (1975).
TV4. J. P. Bondorf, G. Fai, and O. B. Nielsen, Phys. Rev. Lett. 41, 391 (1978).

TV2. A. S. Goldhaber, Phys. Lett. 53B, 306 (1974).
TV3. J. Hüfner, K. Schafer, and B. Schürmann, Phys. Rev. C12, 1888 (1975).
TV4. J. P. Bondorf, G. Fai, and O. B. Nielsen, Phys. Rev. Lett. 41, 391 (1978).
TV5. D. J. Morrissey, L. F. Oliviera, J. O. Rasmussen, G. T. Seaborg, Y. Yariv, and Z. Fraenkel, Phys. Rev. Lett. 43, 1139 (1979).
TV6. X. Campi and J. Hüfner, preprint (1981); submitted to Phys. Rev. C.
TV7. J. Bondorf, preprint (1981).

III–19 Geometrical and Kinamatical Analysis

TW1. R. J. Glauber and G. Matthiae, Nucl. Phys. B21, 135 (1970).
TW2. J. D. Bowman, W. J. Swiatecki, and C. F. Tsang, Lawrence Berkeley Laboratory Report LBL-2908 (1973), unpublished.
TW3. V. I. Manko and S. Nagamiya, Nucl. Phys. A (submitted), 1981.

III–20 Global Variables

TX1. B. Brandt and H. Dahman, Z. Phys. C1, 61 (1979).
TX2. H. Pirner, Phys. Rev. C22, 1962 (1980).
TX3. J. Kapusta and D. Strottman, Phys. Lett. 106B, 33 (1981).
TX4. S. L. Wu and G. Zoberning, Z. Phys. C2, 107 (1979).
TX5. C. Y. Wong, Phys. Lett. 88B, 39 (1979).
TX6. M. Gyulassy, K. A. Frankel, and H. Stöcker, Phys. Lett. (in press) [Preprint, Lawrence Berkeley Laboratory Preprint LBL-13379 (1981)].
TX7. J. Knoll, p. 210, Ref. (RA6).
TX8. J. Cugnon, J. Knoll, C. Riedel, and Y. Yariv, GSI preprint (1981).
TX9. H. Stöcker, G. Buchwald, L. P. Csernai, G. Graebner, J. A. Maruhn, and W. Greiner, to be published.

III–21 Quantum Scattering

TY1. L. P. Kandanoff and G. Baym, *Quantum Statistical Mechanics*, Benjamin Press, New York, 1962.
TY2. C. Y. Wong and H. H. K. Tang, Phys. Rev. C20, 1419 (1979).
TY3. P. Danielewicz, Ph. D. Thesis, University of Warsaw, 1981, and to be published.

IV. MISCELLANEOUS

IV–1 Multi Baryonic Excited States

MA1. F. J. Dyson and N.-H. Xuong, Phys. Rev. Lett. 13, 815 (1964).
MA2. T. Kamae and T. Fujita, Phys. Rev. Lett. 38, 471 (1977).
MA3. R. L. Jaffe, Phys. Rev. Lett. 38, 195 (1977).
MA4. S. A. Chin and A. K. Kerman, Phys. Rev. Lett. 43, 1292 (1979).
MA5. N. K. Glendenning, Phys. Rev. C23, 2527 (1981).
MA6. M. Oka and K. Yazaki, Phys. Lett. 90B, 41 (1980).
MA7. M. Cvetic, B. Golli, N. Mankoc-Borstnik, and M. Rosina, Phys. Lett. 93B, 489 (1980).
MA8. A review of the current status of dibaryon search is given by H. Spinka, in: Proceedings of the Workshop on Nuclear and Particle Physics up to 31 GeV, Los Alamos Scientific Laboratory Report LA-8775-C, Los Alamos, January, 1981, p. 220.
MA9. L. A. Kondratyuk and I. S. Shapiro, Yad. Fiz. 12, 401 (1970) [Soviet J. Nucl. Phys. 12, 220 (1971)]. (1971).
MA10. J. Boguta, Lawrence Berkeley Laboratory Report LBL-12333 (1981), to be published.

MA13. R. van Dantzig and J. M. van der Velden, private communication (1981).

IV–2 Others

MB1. Particle Data Group, Rev. Mod. Phys. 52, No. 2, Part II, S1 (1980).
MB2. B. Andersson, G. Gustafson, and G. Ingelman, Phys. Lett. 85B, 417 (1979), and references therein.
MB3. Recent review of proton-nucleus collisions is given by C. A. Whitten Jr., Nucl. Phys. A335, 419 (1980).
MB4. A. S. Goldhaber, Nature 275, 114 (1978).
MB5. J. W. Negele and K. Yazaki, Phys. Rev. Lett. 47, 71 (1981).

FIGURE CAPTIONS

Fig. 1 Streamer-chamber pictures in 2.1 A·GeV Ca + Pb collisions (I). Here a truely head-on collision is selected. See also Fig. 5. Pictures were taken by Sandoval *et al.* [Ref. (EJ16)] at the Bevalac. The bright blots are artifacts of the apparatus.

Fig. 2 Schematical illustration of the Bevalac.

Fig. 3 Possible phases of dense, highly excited nuclear matter. Dashed lines indicate the density and temperature domains that become accessible in nuclear collisions at different bombarding energies. Dynamical paths *A* and *b* illustrate different ways in which the available energy could be used wither for compression or internal excitation of hadrons.

Fig. 4 Time evolution of nuclear collisions calculated by cascade codes of Gudima and Toneev [Ref. (TB8)], in the plane of τ (temperature) and n (density). The time scale of t is in units of 10^{-23} s. Critical temperature $\tau(n)$ for pion condensation is also given by RGG [Ref. (TA6)] and B [Ref. (TA7)].

Fig. 5 Streamer-chamber pictures in 2.1 A·GeV Ca + Pb collisions (II). Here, a peripheral [see (a)] and a typical central but not head-on [see (b)] collisions are seen. See also Fig. 1. Pictures were taken by Sandoval *et al.* [Ref. (EJ16)] at the Bevalac.

Fig. 6 (a) The forward (0°) and backward (180°) spectra for proton production in 2.1 A·GeV C + C collisions. Data are taken from Refs. (EA14) and (EL12).
(b) Preliminary neutron spectra [Ref. (ED3)] in 390 A·MeV Ne + U collisions.

Fig. 7 Proton spectra at large laboratory angles in 800 A·MeV Ar + KCl collisions. Data are taken from Ref. (EC7).

Fig. 8 Diagram presentation of the participant-spectator model and the kinematical region into which particles are likely emitted. See Appendix for definition of kinematic variables.

Fig. 9 Single particle distribution in the statistical model [Ref. (TG4)]. $\varphi_{m,n} = F^{(1)}_{m,n}/(m+n)$, Eq. (2.15), as a function of center-of-mass kinetic energy, $\varepsilon_{c.m.}$, for different cluster sizes for an incident laboratory kinetic energy of 800 A·MeV.

Fig. 10 (a) Comparison of the statistical model predictions [Ref. (TG4)] with proton inclusive data [Refs. (EC4),(EC7)] at 800 A·MeV.

(b) Proton c.m. angular distributions for fixed kinetic energies [Ref. (EJ8)]. Solid and dashed curves are calculated with the statistical model [Ref. (TG4)] for non-triggered and high-multiplicity triggered events, respectively.

Fig. 11 The pressure, $P(E)$, entropy per baryon, $S(E)$, and compression, $\rho(E)/\rho_0$, as a function of the laboratory kinetic energy per nucleon are shown for a variety of possible nuclear equations of state [Ref. (TK23)]. Curve FG refers to the ideal Fermi gas case; 170, 270, 550 refer to relativistic mean field equations of state with different incompressibility moduli K in MeV.

Fig. 12 Comparison of charge inclusive data [Ref. (EC6)] (dots) with non-viscous hydrodynamical calculations [Ref. (TK17)] (histogram). Results for three equations of state are shown.

Fig. 13 Comparison of billiard ball cascade calculations [Ref. (TB12)] with the same data [Ref. (EC6)] as in Fig. 12. EMU = 1.63 MeV.

Fig. 14 Monte Carlo cascade results of Cugnon [Ref. (TB9)] (histogram) compared with proton inclusive data [Refs. (EC4),(EC7)] (dots).

Fig. 15 Monte Carlo cascade results of Yariv and Fraenkel [Ref. (TB6)] compared with the same reaction as in Figs. 12 and 13.

Fig. 16 Comparison of charge inclusive data [Ref. (EC6)] ((a) and (c)) with calculations [Ref. (TM9)] based on Cugnon's cascade code. In (b) and (d), the primordial deuteron distribution, Eq. (2.38), as calculated using Eq. (2.37) is compared to data (solid triangles) including (d, t, ^{3}He, α) fragments [Ref. (EC6)]. The free deuteron data are indicated by dots.

Fig. 17 (a) Total integrated cross sections of nuclear charge for projectile fragments, as compared with Eq. (3.7) with Z_{eff} given by Eq. (3.5). Data points were evaluated from the cross-section data listed in Ref. (EA2).

(b) Total integrated cross sections of nuclear charge for high energy particles emitted at large angles. Data are taken from Ref. (EC7), and they are compared with Eq. (3.7) with Z_{eff} given by Eq. (3.6).

Fig. 18 Experimental configuration and the data of large-angle two-proton correlations in 800 A·MeV C + C collisions. The observed values of the degree of coplanarity, C, defined by Eq. (3.8) are plotted as a function of the proton momentum. Namely, the momentum spectrum of one proton emitted at $\vartheta_{Lab} = 40°$ in coincidence with the other proton detected by an in-plane counter (which is normalized by the spectrum for out-of-plane coincidence) is plotted. Data are taken from Ref. (EJ9).

Fig. 19 Proton energy spectra at $\vartheta_{c.m.} = 90°$ in collisions of 800 A·MeV C + C, Ne + NaF, and Ar + KCl. The cross section for the high-energy tail is parametrized as $\exp(-E_p^{c.m.}/E_0)$ with an E_0 as indicated. Data are taken from Ref. (EC7). The dashed curve is calculated with a single NN collision model assuming a Gaussian-type Fermi momentum distribution [Ref. (TG6)].

Fig. 20 Projectile and target mass dependence of the proton emission in $A + A$ collisions. Data shown in Fig. 19 are parameterized to $\sigma \propto A^{\alpha}$, and this α is plotted as a function of the kinetic energy of protons ($E_K^* \equiv E_p^{c.m.}$). Data are taken from Ref. (EC7).

Fig. 21 Evidence of the power law of Eq. (3.11) for composite particle emission. Solid curves were calculated by Eq. (3.11) by using the observed proton spectra. Figure taken from Ref. (EE1).

Fig. 22 Observed d/p^2 ratios in cross sections at $\vec{p}_d = 2\vec{p}_p$ for Ne + NaF collisions. Figure taken from Ref. (EC7).

Fig. 23 Excitation function of $\langle m_\pi \rangle / \langle m_Z \rangle$ for almost equal-mass collisions. Black circles [Ref. (EJ10)] were obtained with a streamer chamber for high-multiplicity events in Ar + KCl collisions, whereas open circles and open squares [Ref. (EC7)] are obtained from single particle inclusive data. FB indicates the prediction of the fireball model while dashed curves show the calculations of the viscous fluid model, where η indicates the degree of viscosity. Figure taken from Ref. (TK18).

Fig. 24 Pion multiplicity distribution for central collisions. Here, events with $m_Z \geq 30$ are selected in 1.8 A·GeV Ar + KCl collisions. Data are taken from Ref. (EJ16).

Fig. 25 Multiplicity correlations between negative pions and nuclear fragments in 1.8 A·GeV Ar + KCl collisions (left), and those between negative pions and total charged particles in 1.8 A·GeV Ar + Pb collisions (right). Here, the total charged particles include nuclear fragments and positive and negative pions. Data are taken from Refs. (EJ10) and (EJ13).

Fig. 26 (a) Average multiplicity $\langle m_\pi \rangle$ for negative pions determined from the inclusive spectra, plotted as a function of P, where P is the average nucleon number involved in the participant region. Beam energies are 800 A·MeV. Data points were evaluated from the observed cross sections reported in Ref. (EC7).
(b) Average nuclear-charge multiplicity $\langle m_Z \rangle$ determined from the inclusive spectra, plotted as a function of P_Z, where P_Z is the average proton number involved in the participant region. Beam energies are also 800 A·MeV. Data points are from Ref. (EC7).

Fig. 27 Pion spectra at 0°, 180°, and 90° in the c.m. frame with 2.1 A·GeV beams. Since no direct comparison is possible for the same projectile and target combinations, the data from Ne + NaF collisions are multiplied by $(12/20)^{5/3}$ [see Eq. (3.7)] for comparison. Data are taken from Refs. (EB6), (EC7), and (EM5).

Fig. 28 Pion energy spectra at $\vartheta^{\text{c.m.}} = 90°$ in Ne + NaF collisions at four beam energies, 0.2, 0.4, 0.8, and 2.1 A·GeV. E_0 is the slope factor when the cross sections are

parametrized by $\exp(-E_\pi^{c.m.} / E_0)$. The dotted curve is the predicted cross section for pionic instability as calculated by Gyulassy [Ref. (RA13)]. The dashed line is the calculated result by a phase-space model, and the broken solid line is the result by a microscopic hard-collision model. Both data and calculated results are taken from Ref. (EG9).

Fig. 29 Values of E_0 for both pions and high-energy protons as a function of the beam energy per nucleon in the c.m. frame. For the definition of E_0 see also Figs. 19 and 28. Figure taken from Ref. (EC7).

Fig. 30 The 30°-to-90° yield ratio of π^- in the c.m. frame in 800 A·MeV Ar + KCl collisions, plotted as a function of the pion kinetic energy in that frame. Figure taken from Ref. (EC7).

Fig. 31 Pion spectra at 0° in low-energy Ne + NaF collisions. Data and figure are taken from Ref. (EB3) after the corrections for the beam energies cited in the errata.

Fig. 32 Recent two-pion interferometry results in 1.8 A·GeV Ar + KCl collisions. Raw data give broader shape than the Coulomb corrected data. Figure taken from Ref. (EJ15).

Fig. 33 Two-proton correlation function in 1.8 A·GeV Ar + KCl collisions, plotted as a function of relative momentum between two protons. Figure taken from Ref. (EJ4).

Fig. 34 Threshold energies for various particle production in nucleon-nucleon collisions.

Fig. 35 Measured K^+ spectra in the c.m. frame in 2.1 A·GeV Ne + NaF collisions. Data are taken from Ref. (EH1).

Fig. 36 Target-mass dependence of K^+ cross section. By parameterizing the cross section, σ, as $\sigma \propto A_T^{\alpha}$ for both deuteron and Ne projectiles, the value of α is plotted as a function of the K^+ energy in the c.m. frame. For comparison, the corresponding value for pions is also plotted. Figure taken from Ref. (EH2).

Fig. 37 Target mass dependence of the projectile fragments in one-nucleon removal reactions, as compared with that obtained from the the data systematics for normal fragmentation processes (solid line). Data are taken from Ref. (EA2).

Fig. 38 Spectra of π^- and π^+ measured at forward angles in 380 A·MeV Ne + NaF collisions. Arrows indicate the pion velocity which is equal to the beam velocity. Figure taken from Ref. (EB5).

Fig. 39 Maximum c.m. momenta for proton and pion emission in C + C and $p + p$ collisions.

Fig. 40 Negative pion production at 2.5° from p, d, and α beams at various bombarding energies. Cross sections are plotted as a function of the Feynman scaling variable, x, defined by Eq. (A.7). Also the predictions by Schmidt and Blankenbecler [Ref. (TF2)], given by Eq. (3.30), are plotted. Data are taken from Ref. (EB2), and figure taken from Ref. (TF2).

Fig. 41 Negative pion production at 0° in 303 A·MeV ^{3}He + ^{6}Li collisions. Inset shows the detailed structure of the pion spectrum near $x = 1$. Figure taken from Ref. (EB4).

Fig. 42 Widths of parallel momentum distributions of projectile fragments measured in the projectile rest frame. The fit to the data by Eq. (3.37) is shown by a solid curve. Data are taken from Ref. (EA1).

Fig. 43 Parallel momentum distribution of ^{15}O measured at 0° in 2.1 A·GeV ^{16}O + ^{12}C collisions. Data are plotted in the projectile rest frame. Figure taken from Ref. (TT3).

Fig. 44 New isotopes produced with ^{40}Ar and ^{48}Ca beams. See Refs. (EA12) and (EA13).

Fig. 45 Angular distributions of low-energy protons for both low- and high-multiplicity events in 393 A·MeV Ne + U collisions. Figure taken from Ref. (EJ7).

Fig. 46 (a) Hydrodynamical side-splash effect expected at small impact parameters, and (b) bounce-off effect at large impact parameters. Figure taken from Ref.

(TK15).

Fig. 47 (a) The angular distribution of protons with different laboratory kinetic energies emitted from high-multiplicity Ne (393 A·MeV) + U. Data (middle left from Ref. (TK15)) are compared to Cascade 1 [Ref. (TB4)], Cascade 2 [Ref. (TB6)], two-component [Refs. (TL1),(TL2)] (dashed line), firestreak [Ref. (TJ5)] (solid), Fluid 1 [Ref. (TK17)], and Fluid 2 [Ref. (TK24)] with thermal break-up. Figure taken from Ref. (TK19).

(b) The energy distribution of charged fragments including p, d, and t for the same reaction [Ref. (TK15)] as in Fig. 47 (a). Fluid 1,[Ref. (TK17)], Two-fluids model [Ref. (TK7)], and Cascade 2 [Ref. (TB6)] predictions are shown. Figure taken from Ref. (TK26).

(c) As in Fig. 47 (b), compared to Cugnon's cascade model [Ref. (TB9)] supplemented with Remler's composite production theory [Ref. (TM9)]. The primordial deuteron spectrum including d and t and the sum charge spectra are calculated by integrating over impact parameters $b \leq 2.1$ fm. The unrestricted impact-parameter integration yields Fig. 16.

Fig. 48 Experimental layout for two-proton measurements in Ar + Pb collisions (above), and intuitive explanation for the data shown in Fig. 49 (below).

Fig. 49 Contour plot of the degree of coplanarity, C, defined by Eq. (4.1) for two-proton emission in 800 A·MeV Ar + Pb collisions, plotted in the (ϑ,E) plane in the laboratory frame. The kinematical domain covered by the R telescope is indicated by a hatched region. Data are taken from Refs. (EJ11) and (TK20).

Fig. 50 Proton and pion energy spectra for high-multiplicity events in 800 A·MeV Ar + KCl collisions. Fits to the data are based on the radial explosion model [Ref. (TK12)]. Figure taken from Ref. (EJ8).

Fig. 51 Calculated flow diagram [Ref. (TX6)] for U + U at 400 A·MeV. Insert shows one Ca + Ca (400 A·MeV) event measured in the plastic ball [Ref. (EP1)] where the

observed charge multiplicity for $y_{c.m.} < 0$ was 22. The dots represent measures and reflected (about $p_{c.m.} = 0$) momenta projected in the plane spanned by the beam axis and the principle axis, $\vec{a}$, of the kinetic flow tensor. The angle between $\vec{a}$ and p_z is the flow angle and the kinetic flow ratio is $(a/b)^2$, where b is the radius of the minor axis. For the event a/b =3, a = 1 GeV/c, ϑ_{Flow} = 19°. The solid curve shows the flow characteristics of non-viscous hydrodynamics [Ref. (TX9)]. The shaded region shows the results [Ref. (TX6)] using intranuclear cascade [Ref. (TB9)]. The numbers along the curve indicate the impact parameter b in units of $b_{max}/10$.

Fig. 52 Time evolution of entropy per nucleon (black circles) and the number of participant nucleons (triangles) for 800 A·MeV Ca + Ca collisions. Calculations have been done by a Monte Carlo cascade code of Ref. (TB10). Figure taken from Ref. (TN5).

Fig. 53 Observed d/p ratios and entropy. Data for equal-mass collisions are compared with various theoretical predictions by Siemens and Kapusta (thermal) [Ref. (TN1)], Bertsch and Cugnon (cascade) [Ref. (TN5)] and Stö cker (hydrodynamics + thermal break-up) [Ref. (TK18)]. The C + C data are taken from Ref. (EE4) while others are from Ref. (EC7).

Fig. 54 An example of multi-chain events in emulsions for Fe projectile-fragments. Beam energy is 1.88 A·GeV. Figure taken from Ref. (EN5).

Fig. 55 Evidence of short mean free path for projectile fragments. With 1.88 A·GeV Fe beams the mean free paths of secondary fragments, Λ^*, were measured as a function of D, where D is the distance between the primary interaction-vertex point (at which the secondary fragment of interest was created) and the starting point (from which the mean free path of this secondary fragment was actually measured). Figure taken from Ref. (EN4).

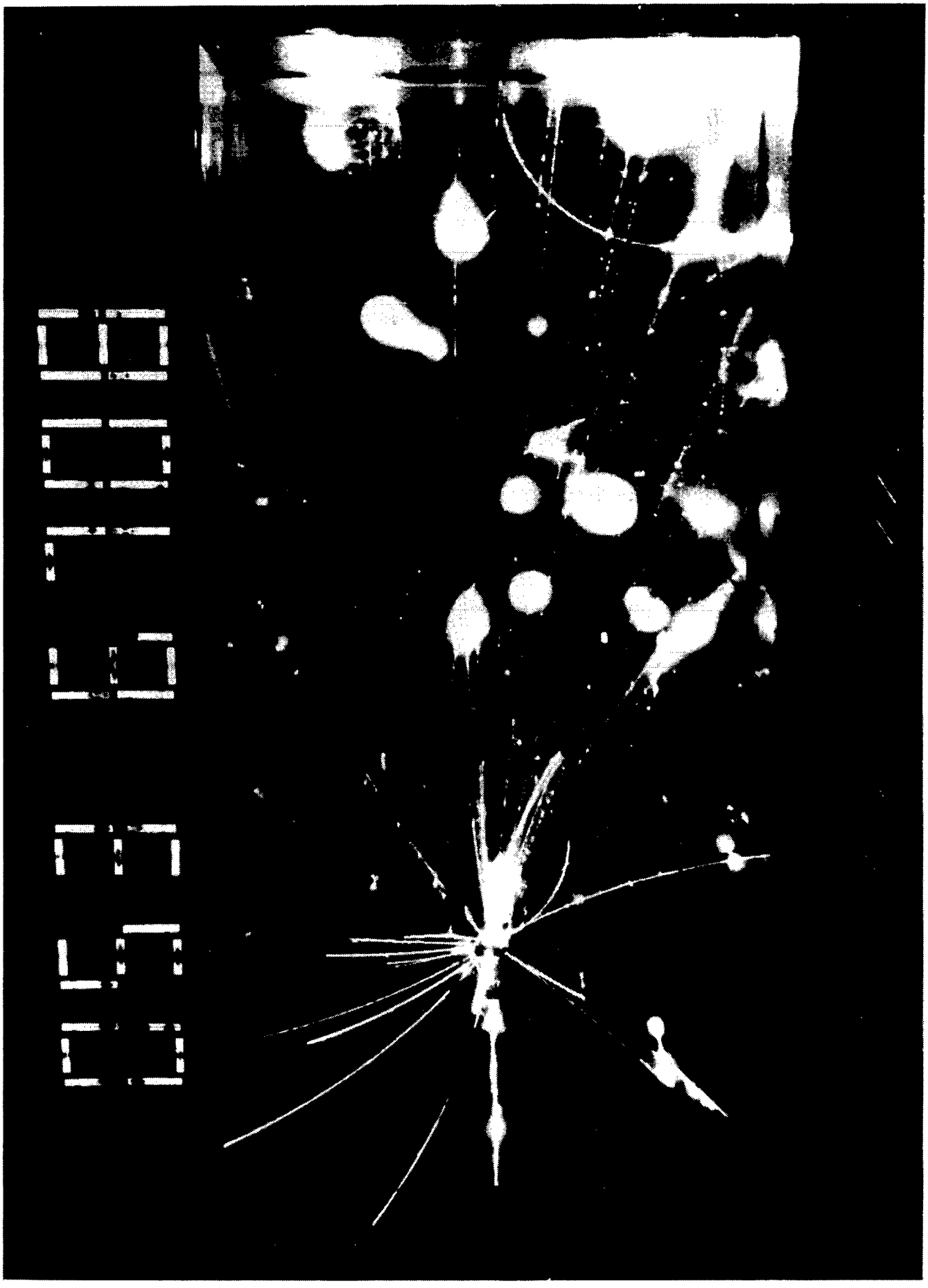

XBB 815-4408

Fig. 1

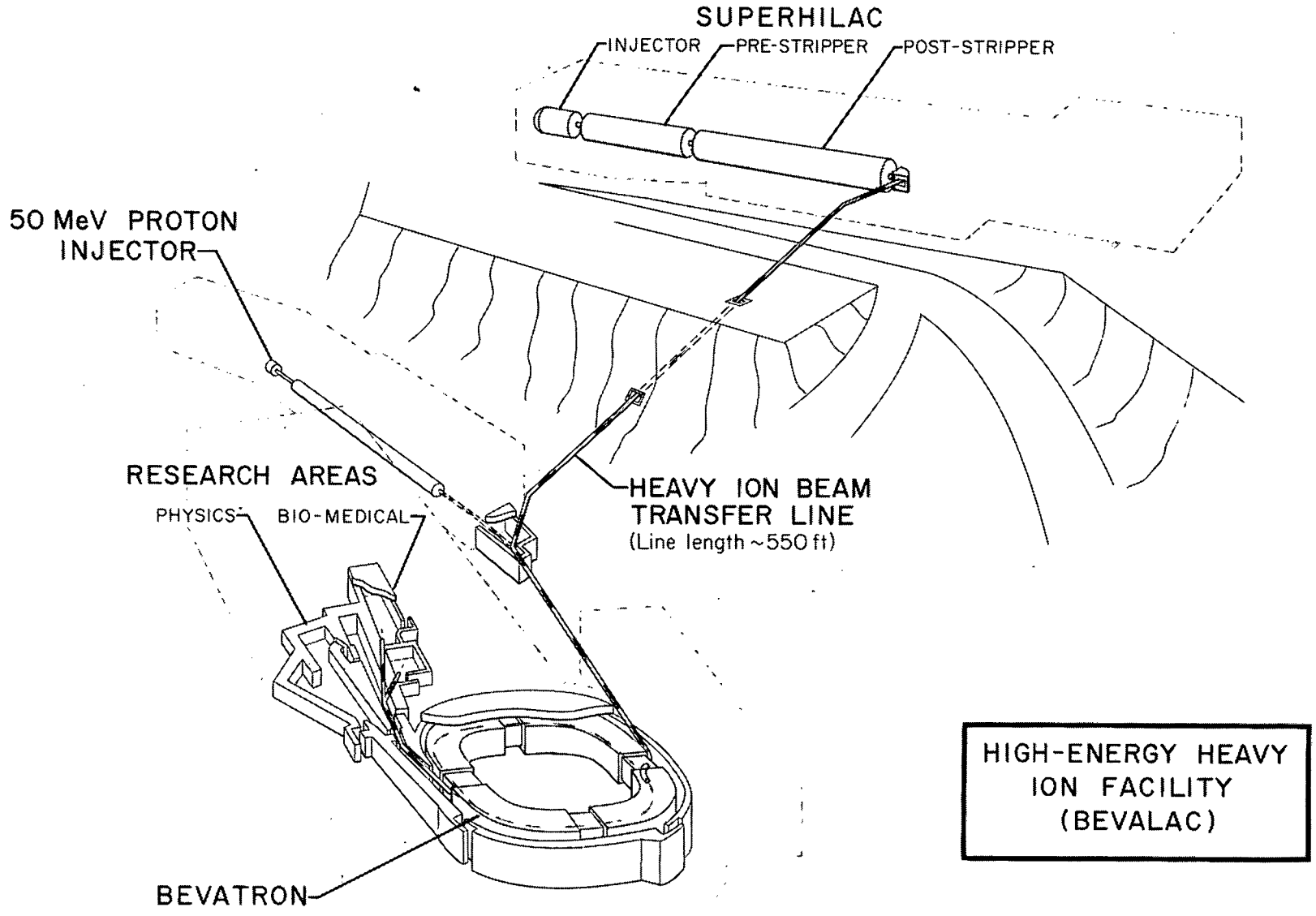

Fig. 2

CBB 729-4520

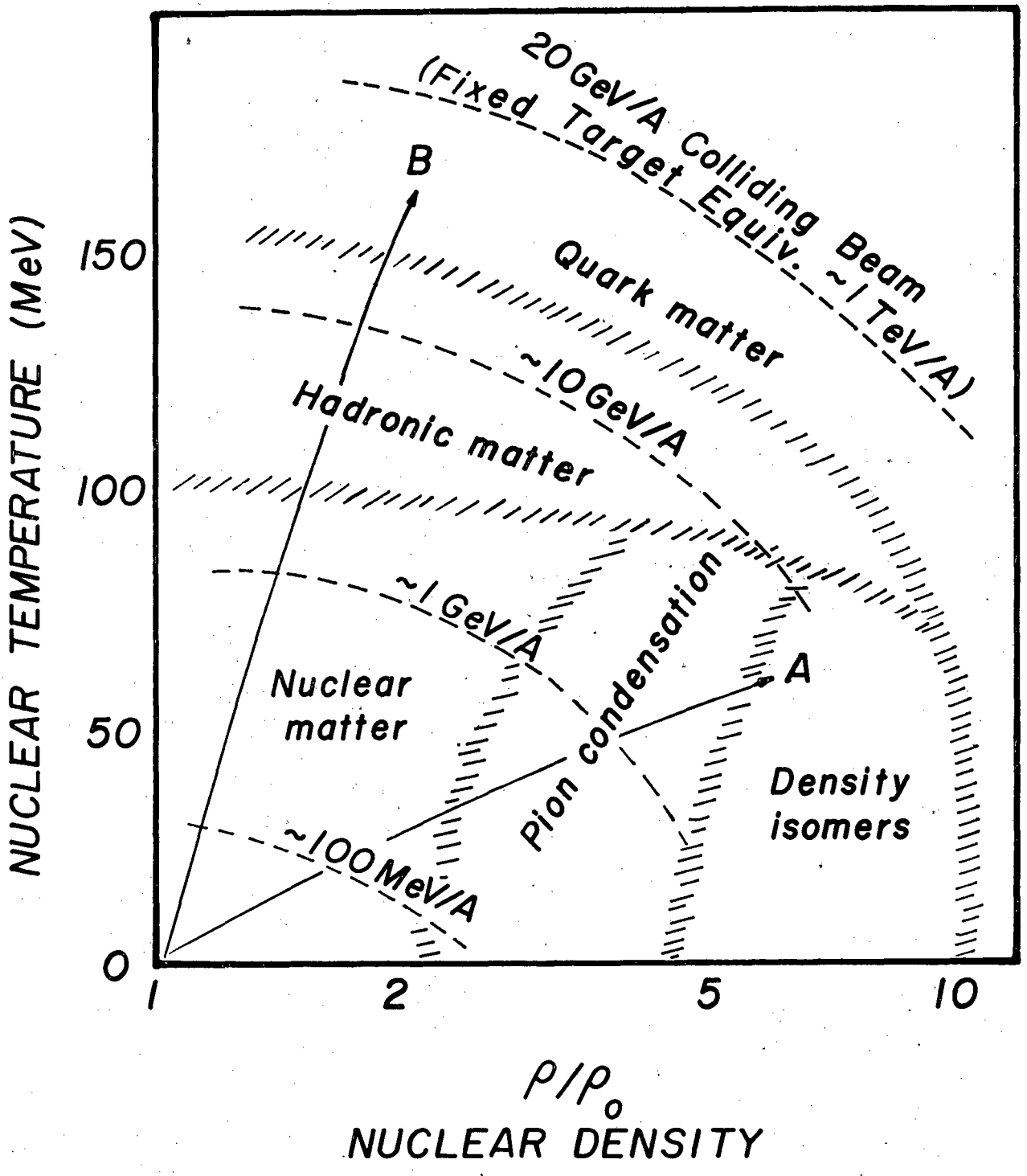

XBL 7910-12108

Fig. 3

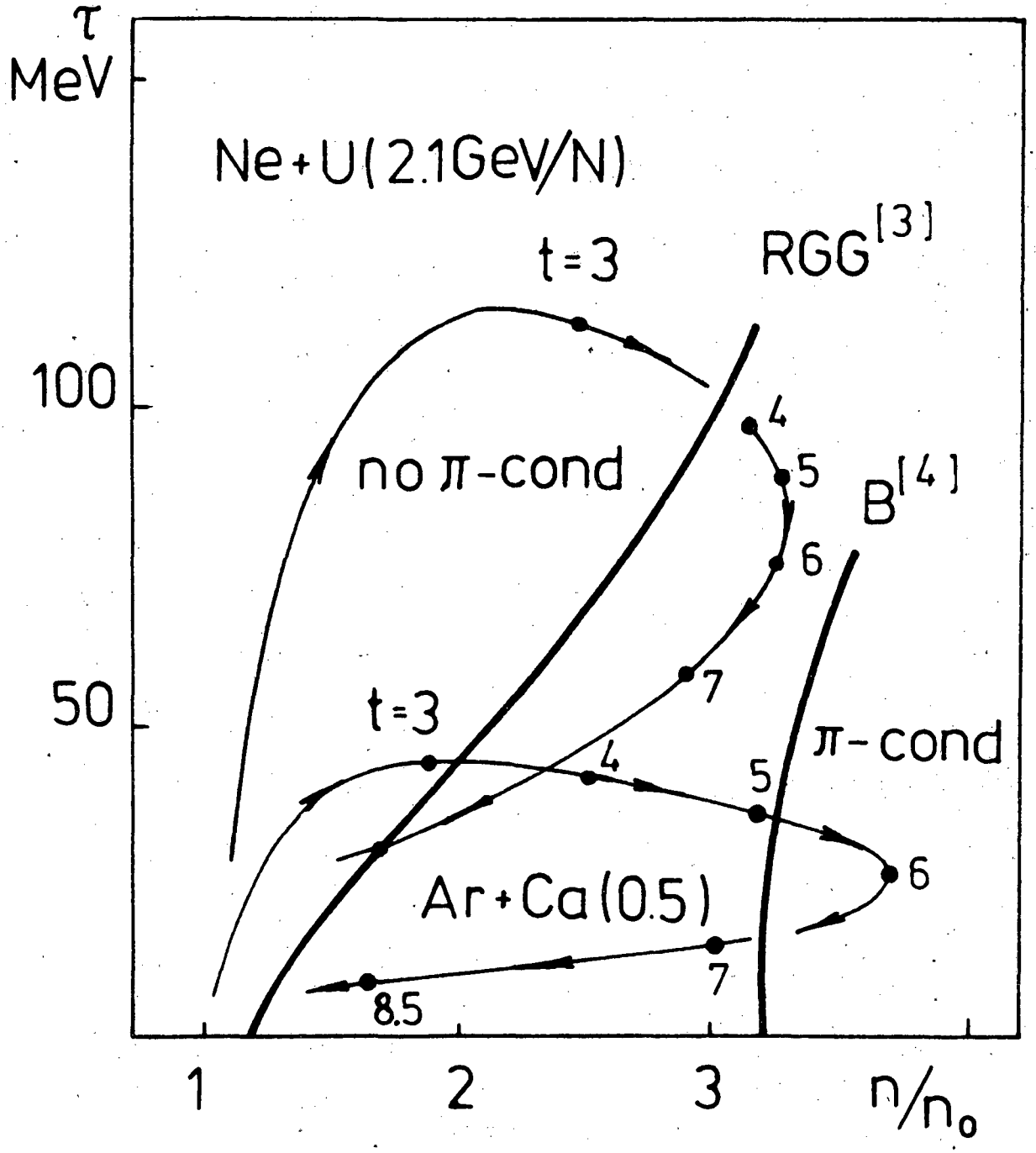
τ
MeV
Ne+U(2.1GeV/N)
t=3
RGG[3]
100
4
5
no π-cond
B[4]
6
7
50
t=3
π-cond
4
5
6
Ar+Ca(0.5)
7
8.5
1
2
3
n/n0
XBL 805-9542

Fig. 4

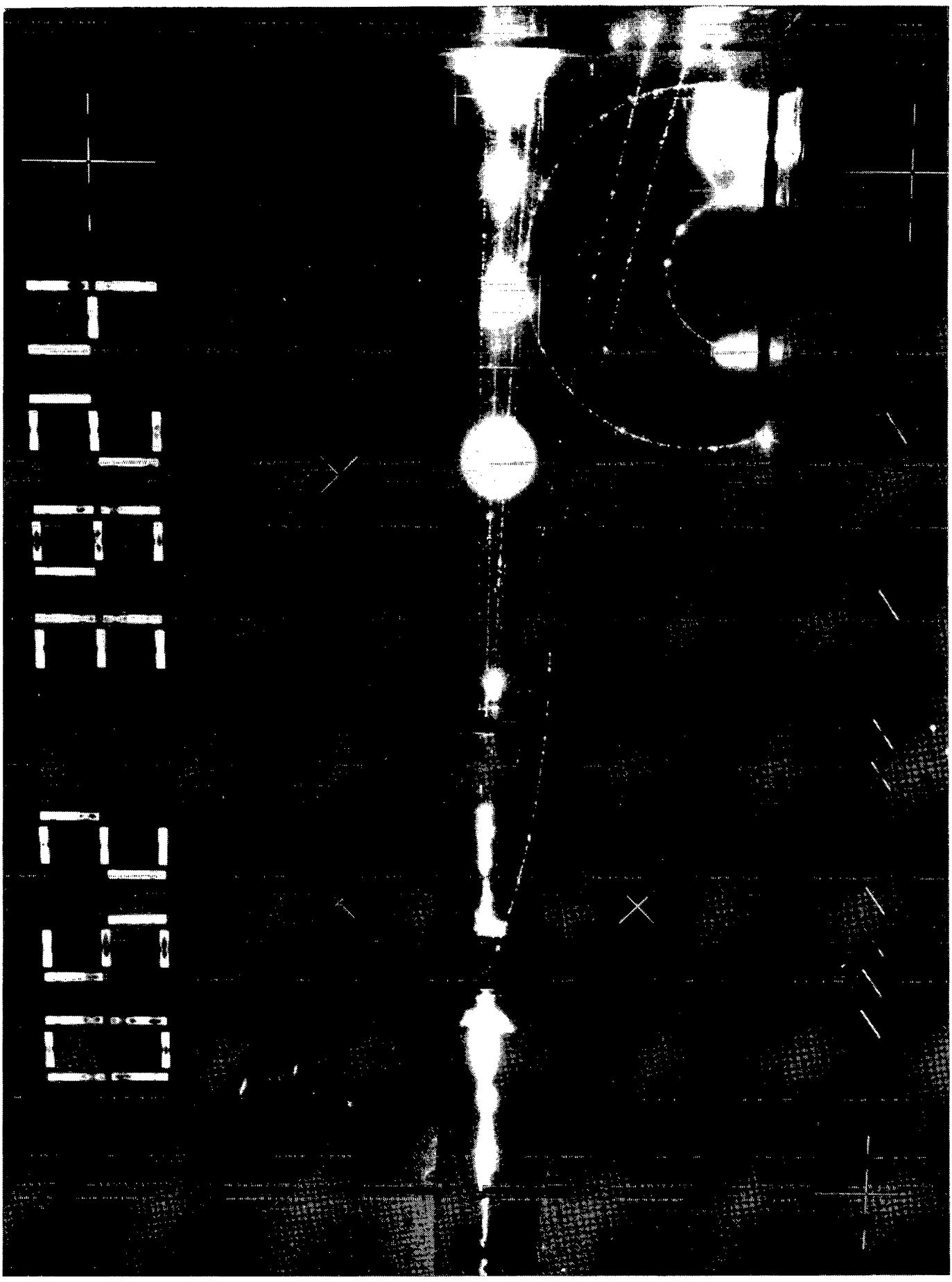

XBB 817-6600

Fig. 5 (a)

XBB 817-6599

Fig. 5 (b)

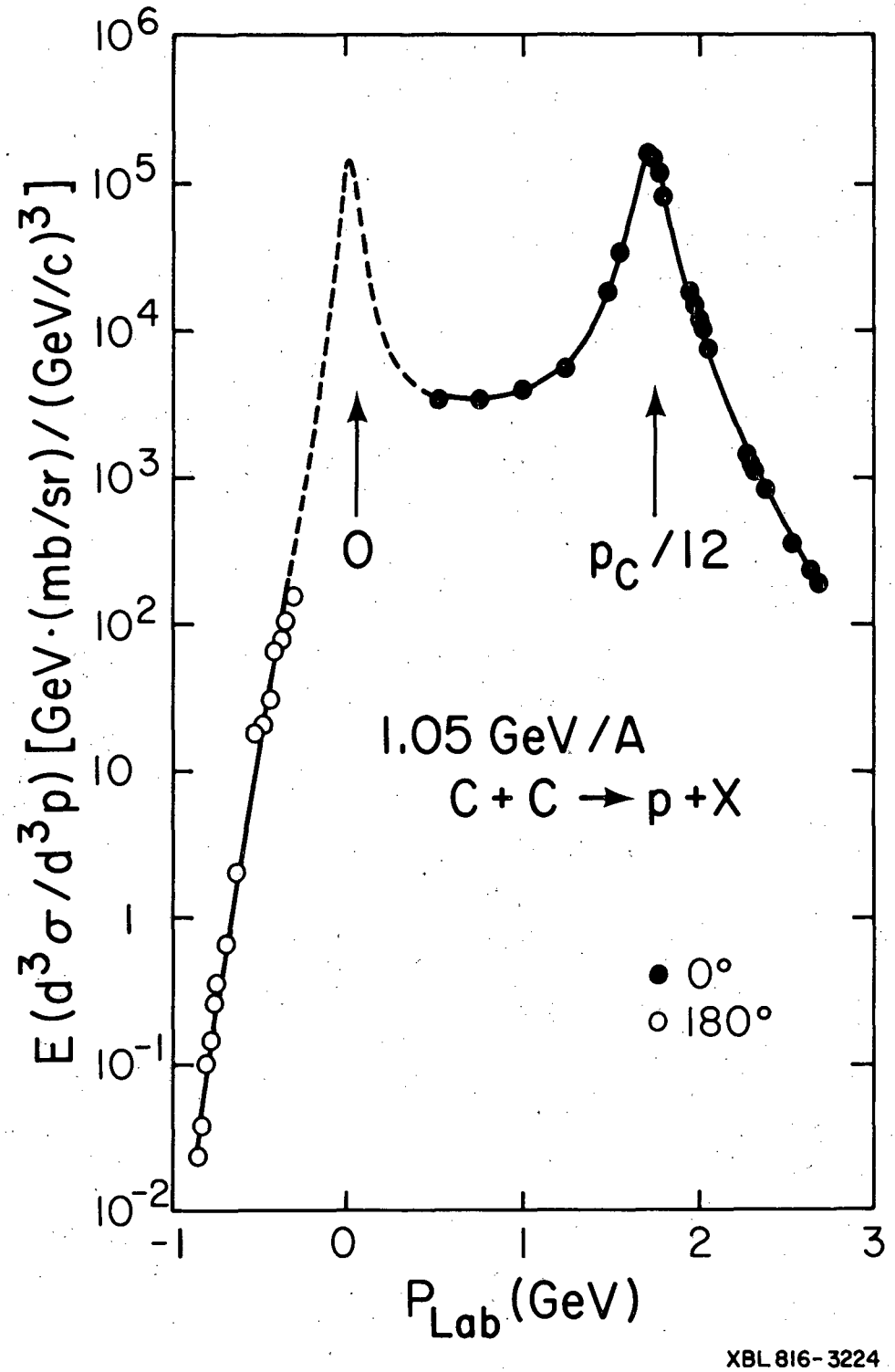
10^6
10^5
10^4
10^3
10^2
10
1
10^{-1}
10^{-2}
$E(d^3\sigma/d^3p)$ [GeV·(mb/sr)/(GeV/c)^3]
0
$p_C/12$
1.05 GeV/A
C + C → p + X
● 0°
○ 180°
-1
0
1
2
3
P_{Lab} (GeV)
XBL 816-3224

Fig. 6 (a)

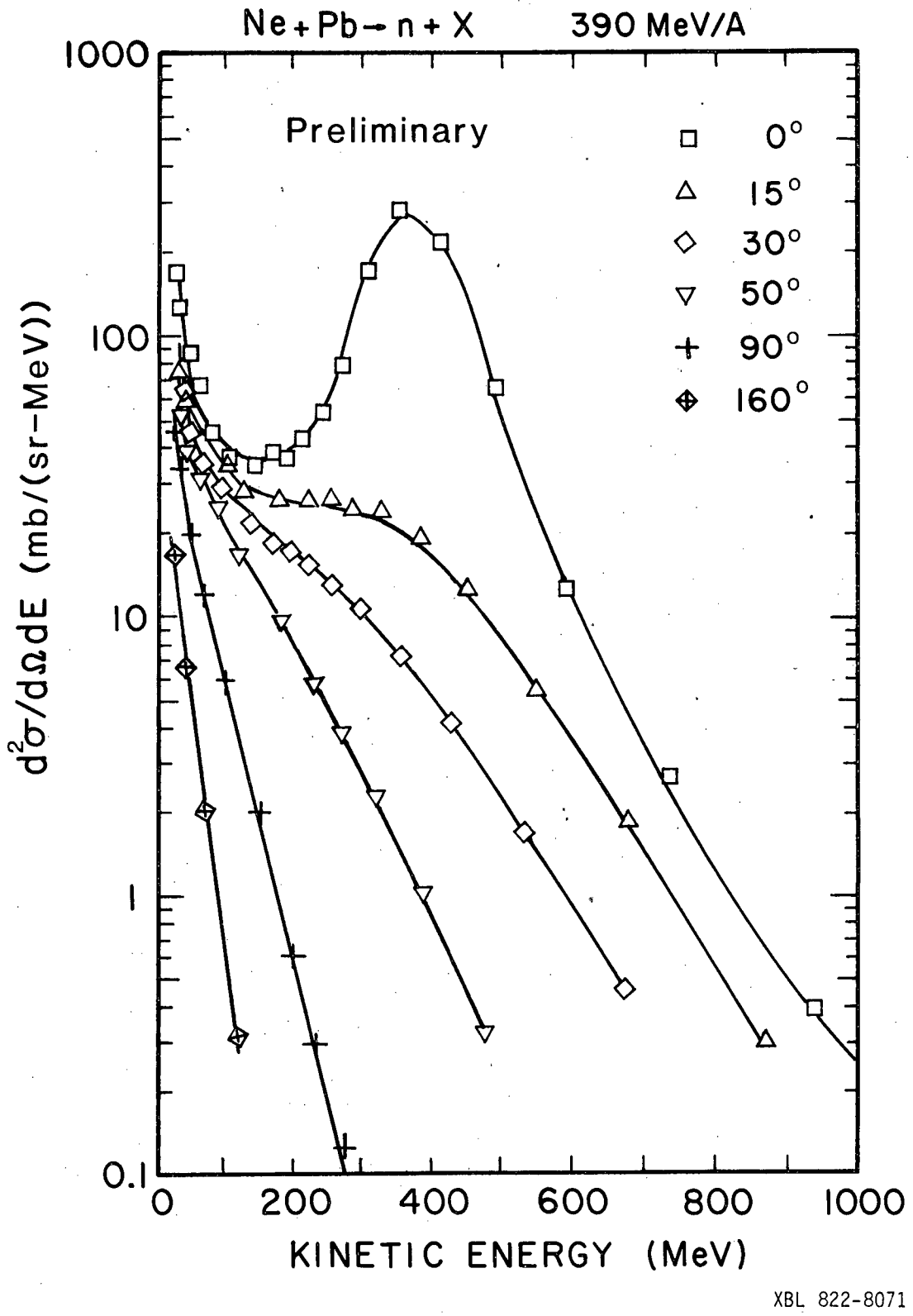
Ne + Pb → n + X
390 MeV/A
Preliminary
0°
15°
30°
50°
90°
160°
1000
100
10
1
0.1
0
200
400
600
800
1000
d²σ/dΩdE (mb/(sr-MeV))
KINETIC ENERGY (MeV)
XBL 822-8071

Fig. 6 (b)

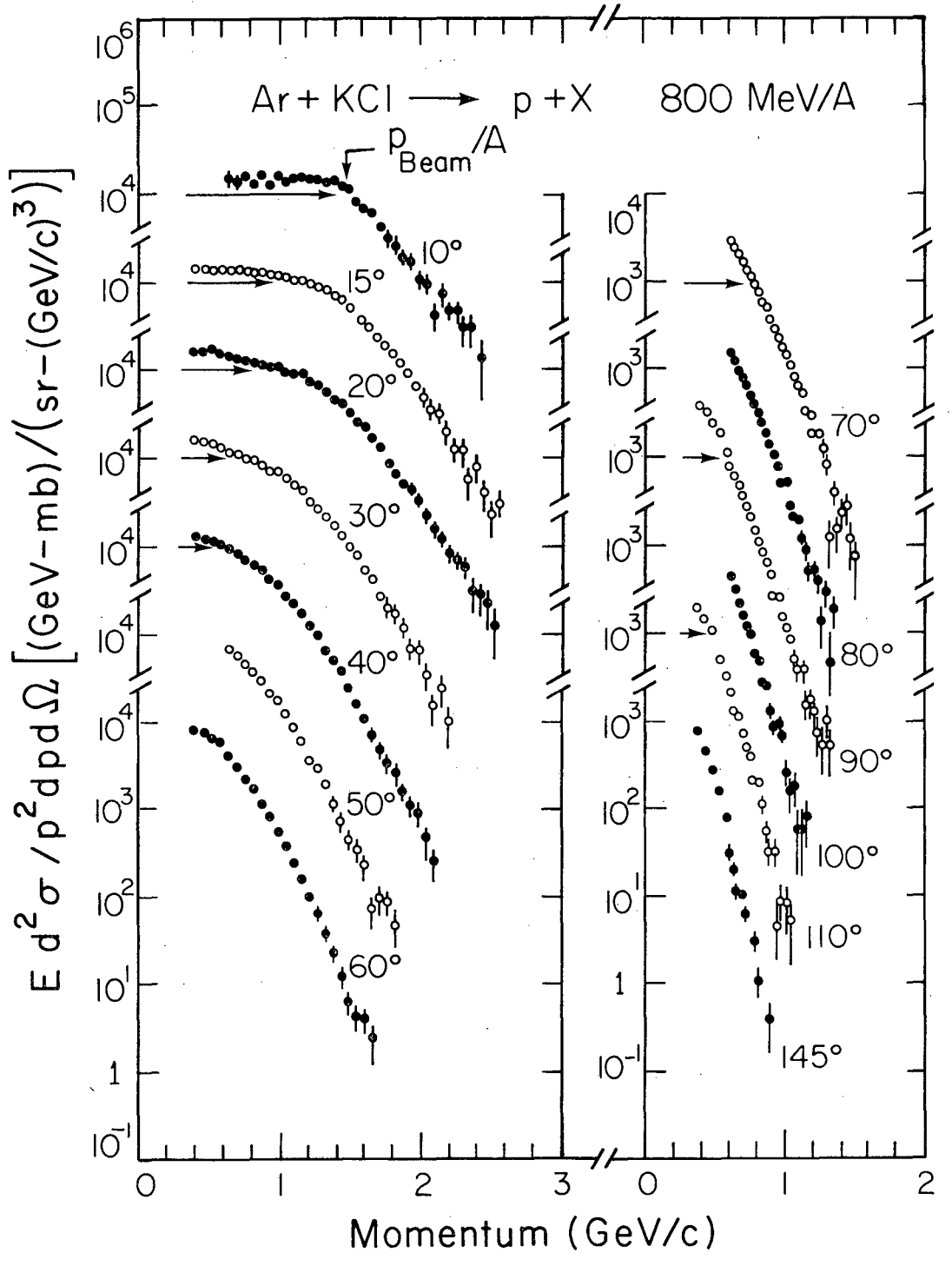

XBL 8011-2393

Fig. 7

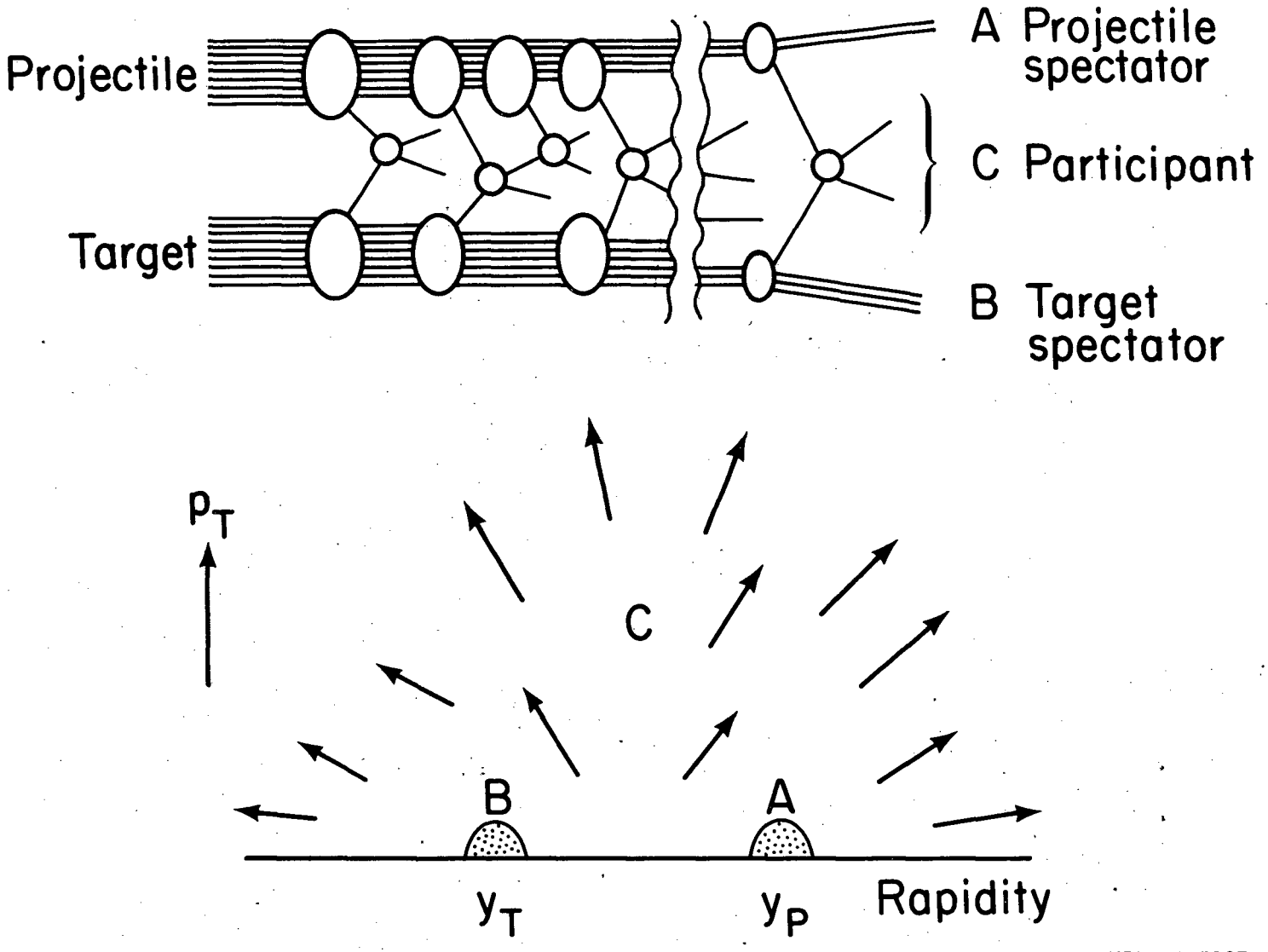
Projectile
Target
A Projectile spectator
C Participant
B Target spectator
p_T
C
B
A
y_T
y_P
Rapidity
XBL 816-3223

Fig. 8

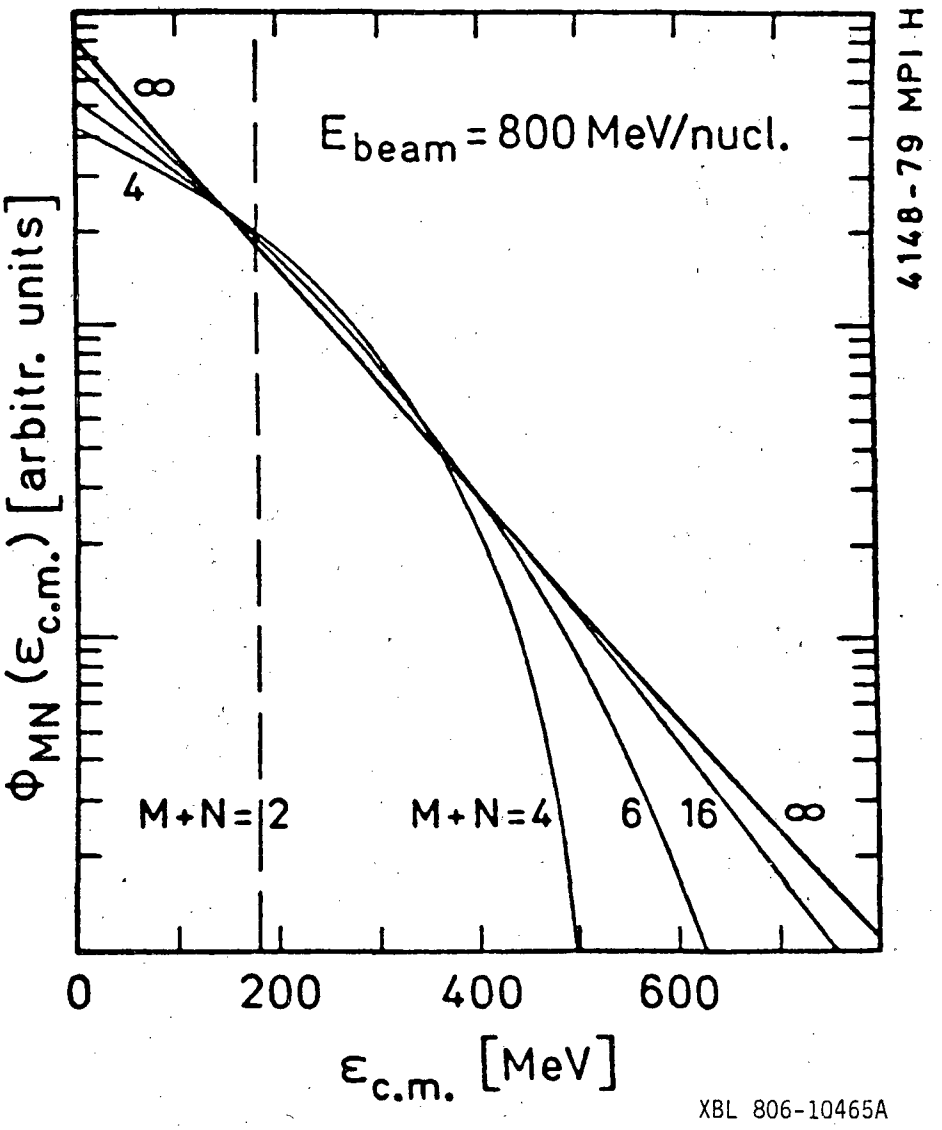
E_{beam} = 800 MeV/nucl.
$\Phi_{MN}(\varepsilon_{c.m.})$ [arbitr. units]
$\varepsilon_{c.m.}$ [MeV]
M+N=2
M+N=4
4
6
8
16
8
0
200
400
600
4148-79 MPI H
XBL 806-10465A

Fig. 9

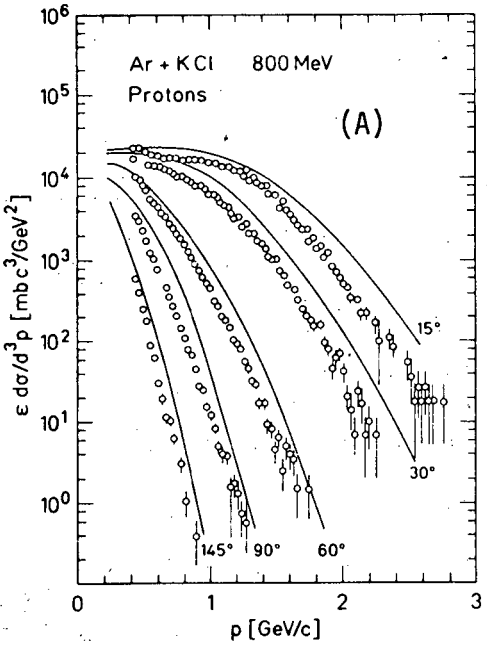

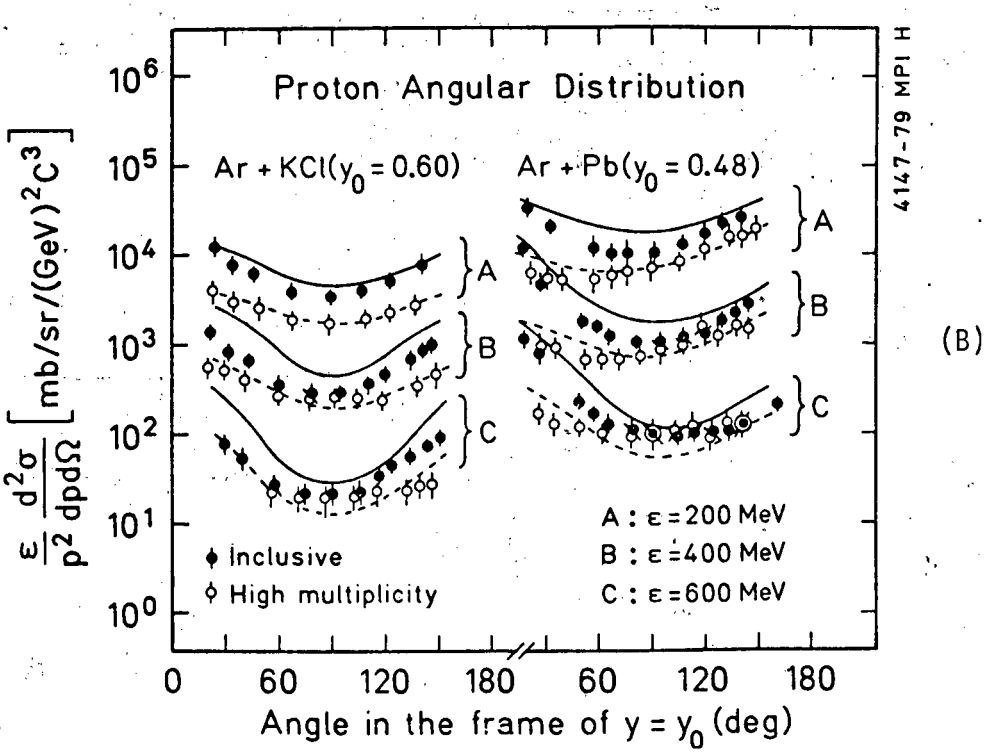

(B)

XBL 806-10464A

Fig. 10

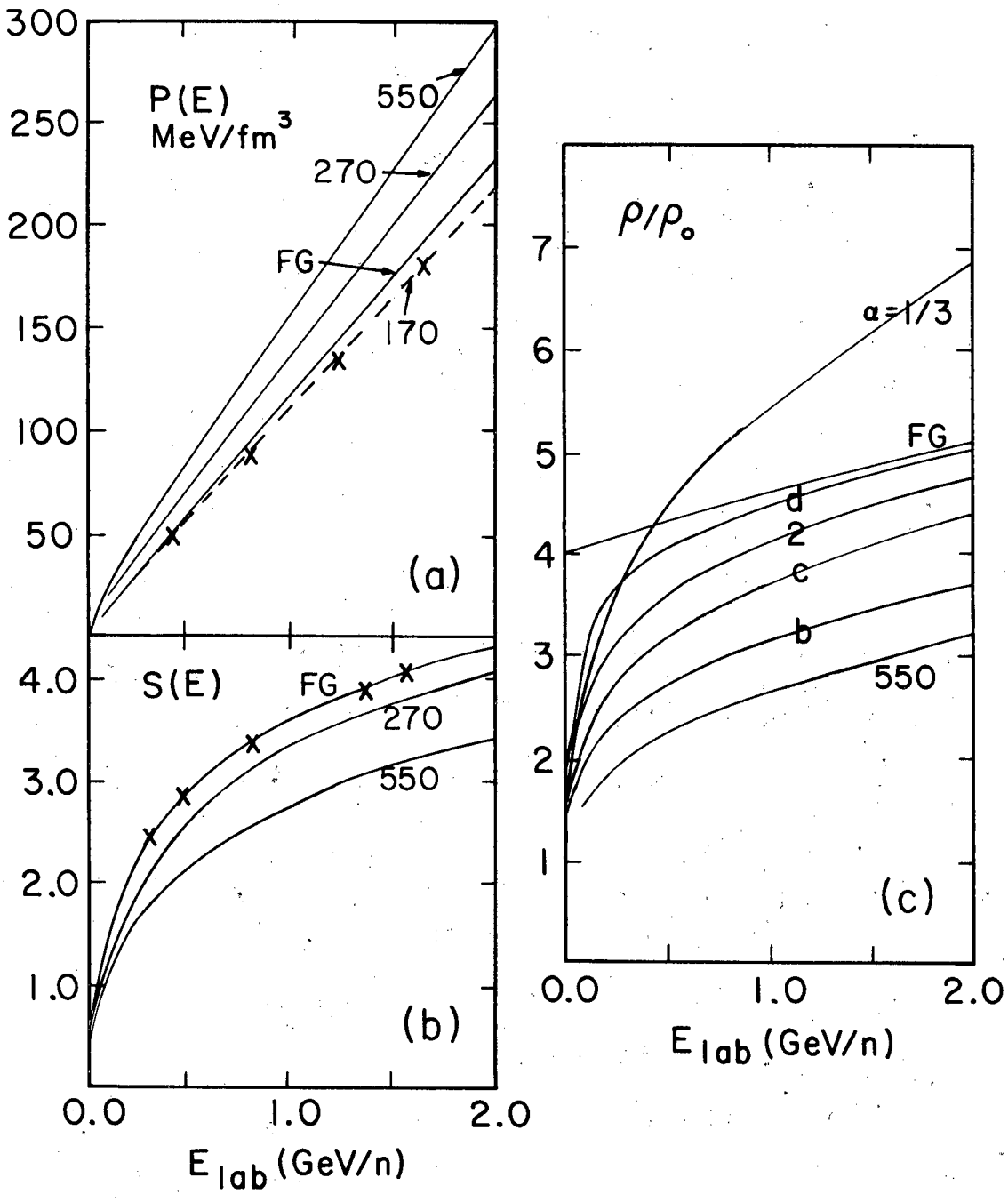
P(E)
MeV/fm³
550
270
FG
170
(a)
S(E)
FG
270
550
(b)
ρ/ρ₀
α=1/3
FG
d
2
c
b
550
(c)
E lab (GeV/n)
E lab (GeV/n)
XBL 813-8436

Fig. 11

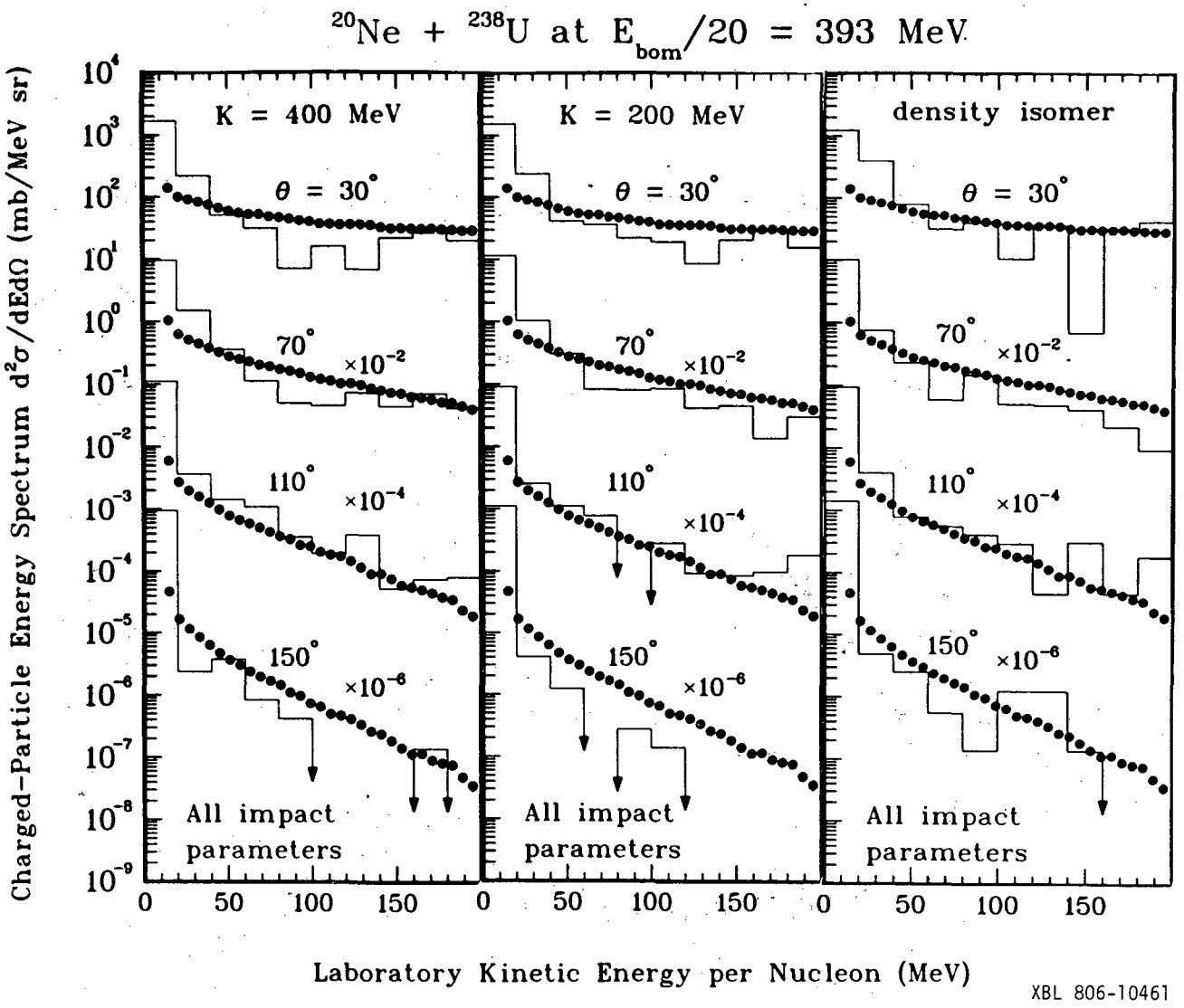
$^{20}Ne + ^{238}U$ at $E_{bom}/20 = 393$ MeV
K = 400 MeV
K = 200 MeV
density isomer
θ = 30°
70°
×10⁻²
110°
×10⁻⁴
150°
×10⁻⁶
All impact parameters
Charged-Particle Energy Spectrum d²σ/dEdΩ (mb/MeV sr)
Laboratory Kinetic Energy per Nucleon (MeV)
XBL 806-10461

Fig. 12

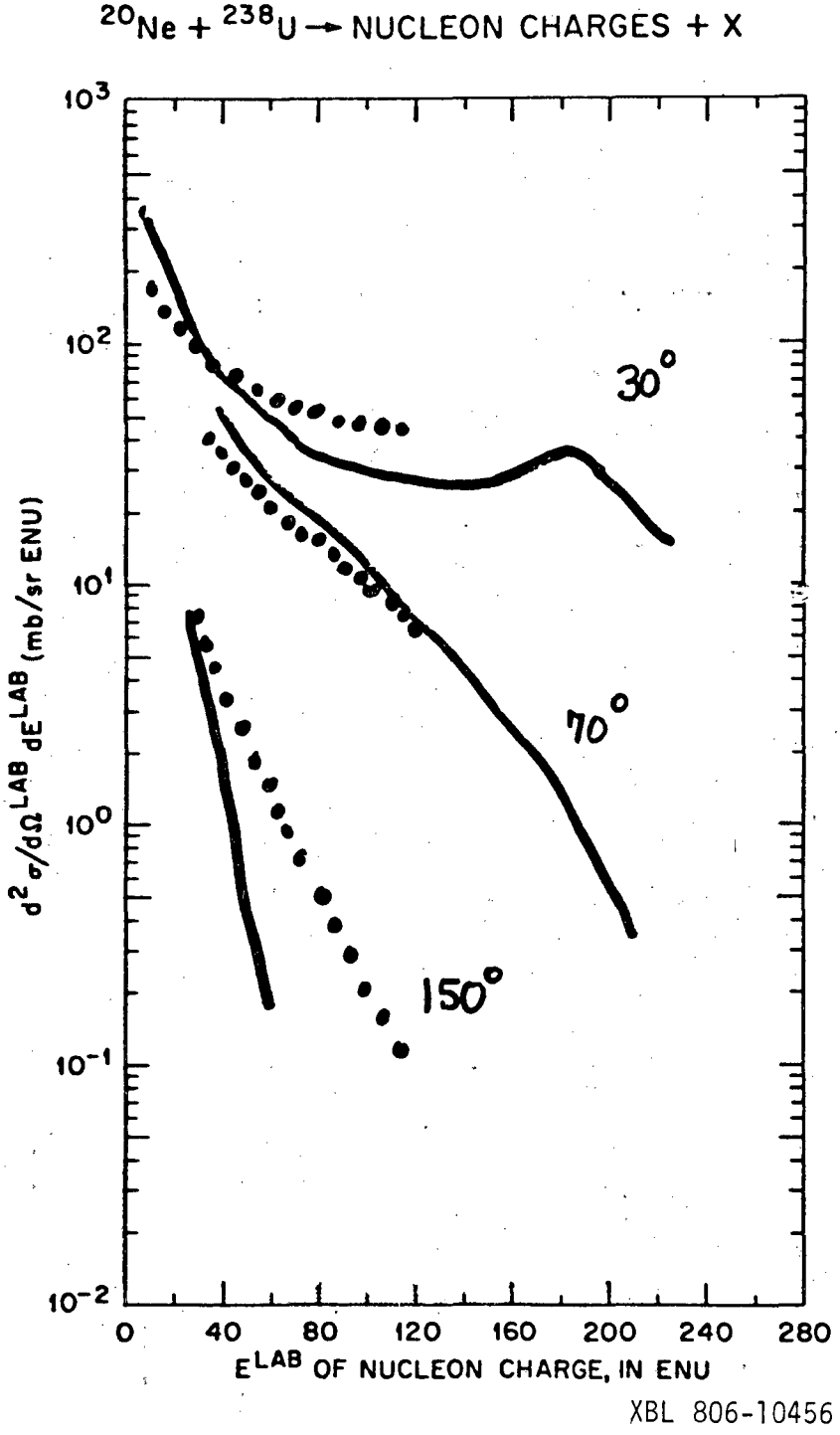
$^{20}Ne + ^{238}U \rightarrow$ NUCLEON CHARGES + X
$d^2\sigma/d\Omega^{LAB} dE^{LAB}$ (mb/sr ENU)
10^3
10^2
10^1
10^0
10^{-1}
10^{-2}
30°
70°
150°
0
40
80
120
160
200
240
280
E^{LAB} OF NUCLEON CHARGE, IN ENU
XBL 806-10456

Fig. 13

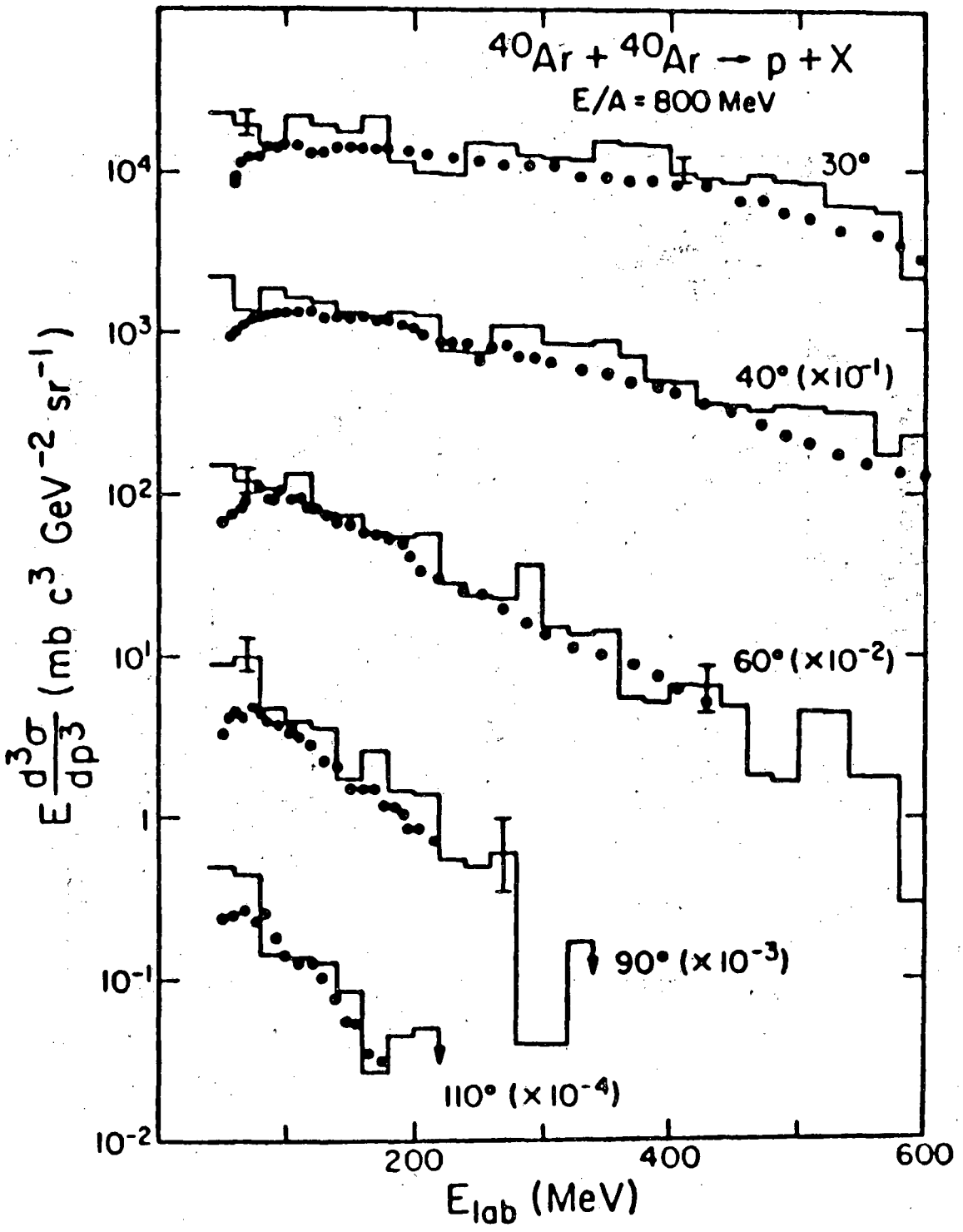

XBL 806-10454A

Fig. 14

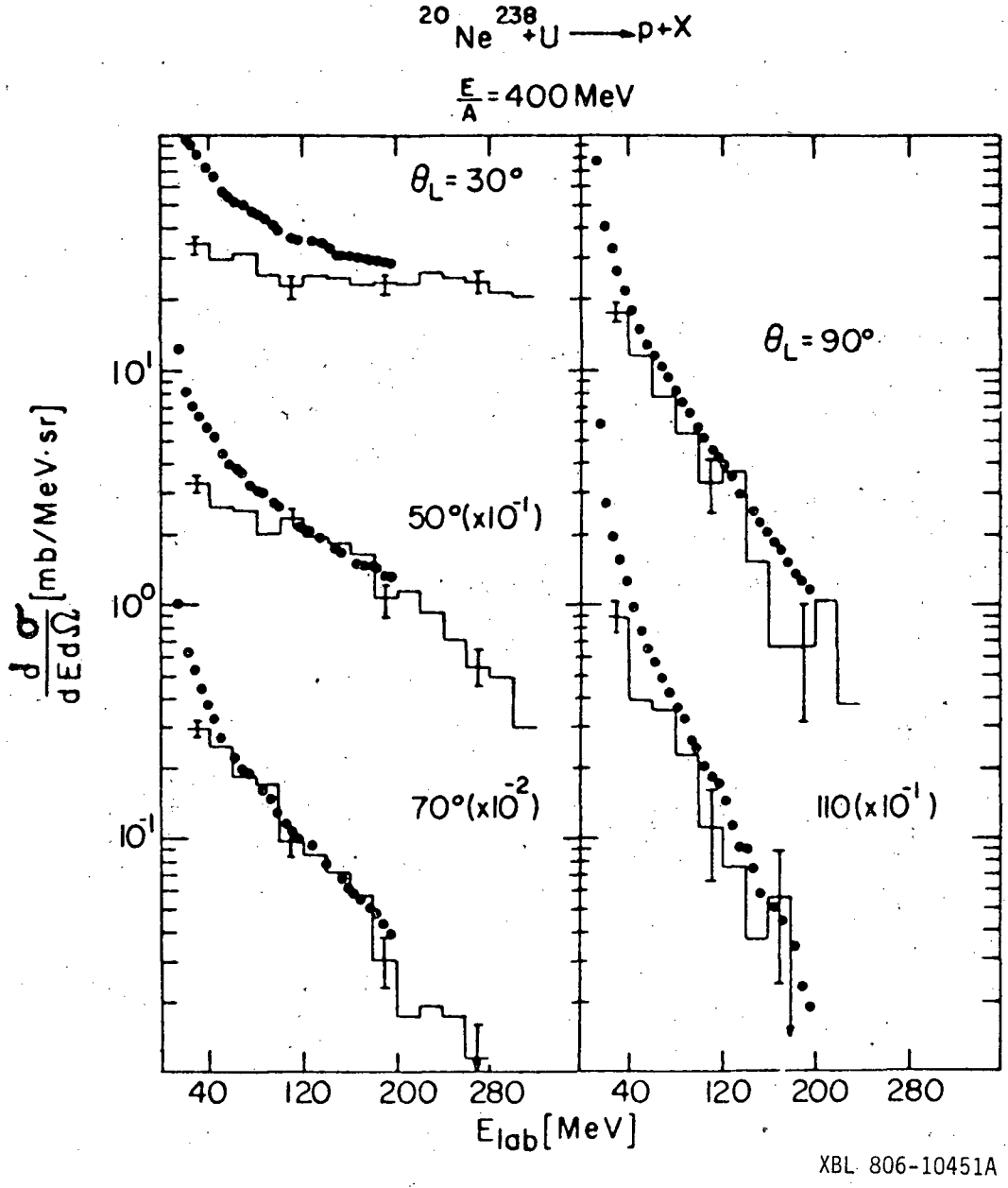
$^{20}Ne^{238}+U \longrightarrow p+X$
$\frac{E}{A}$ = 400 MeV
θ_L = 30°
θ_L = 90°
50°(x10^{-1})
70°(x10^{-2})
110(x10^{-1})
$\frac{d\sigma}{dEd\Omega}$ [mb/MeV·sr]
10^1
10^0
10^{-1}
40
120
200
280
E_{lab} [MeV]
XBL 806-10451A

Fig. 15

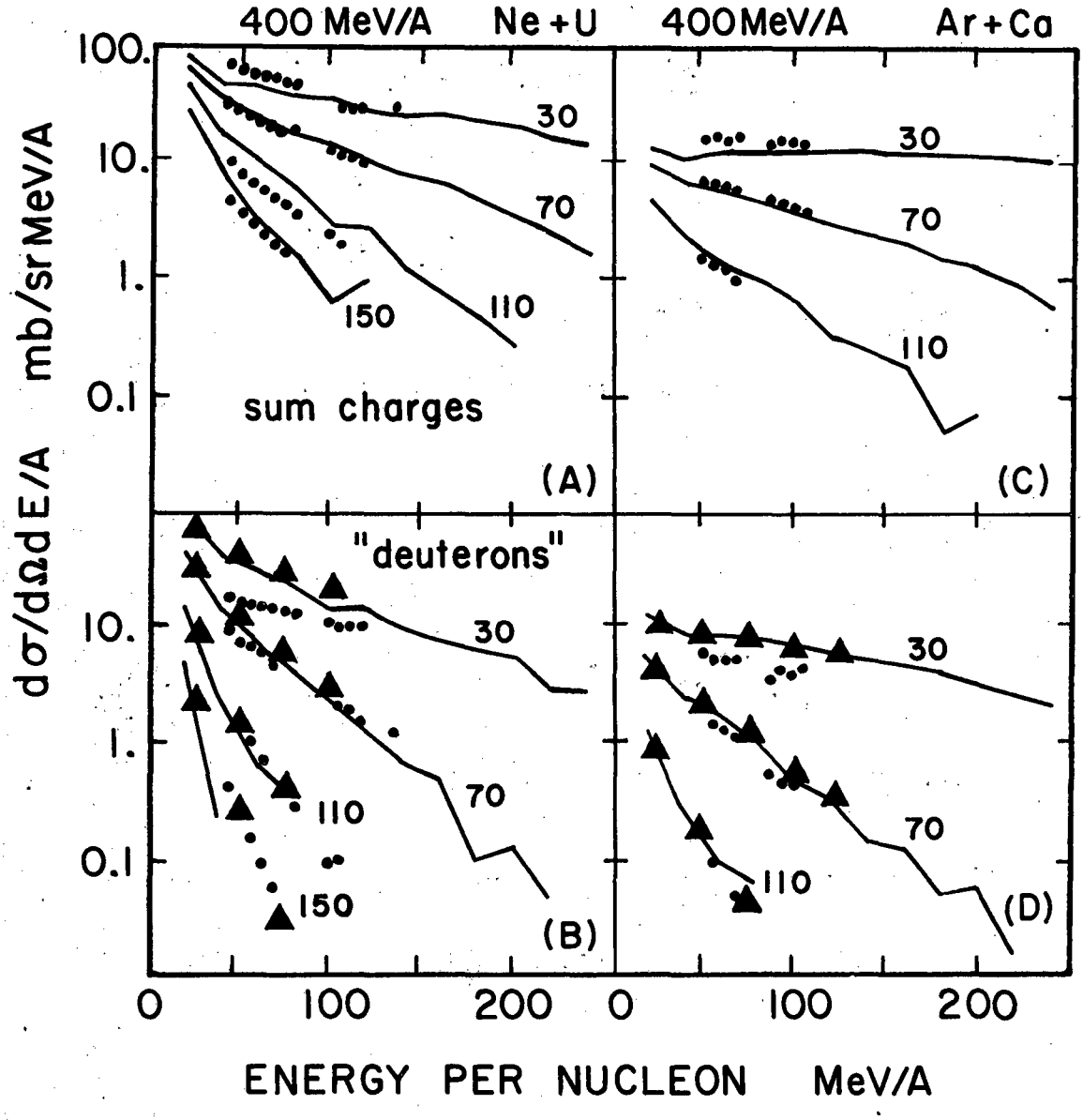

XBL 822-7955

Fig. 16

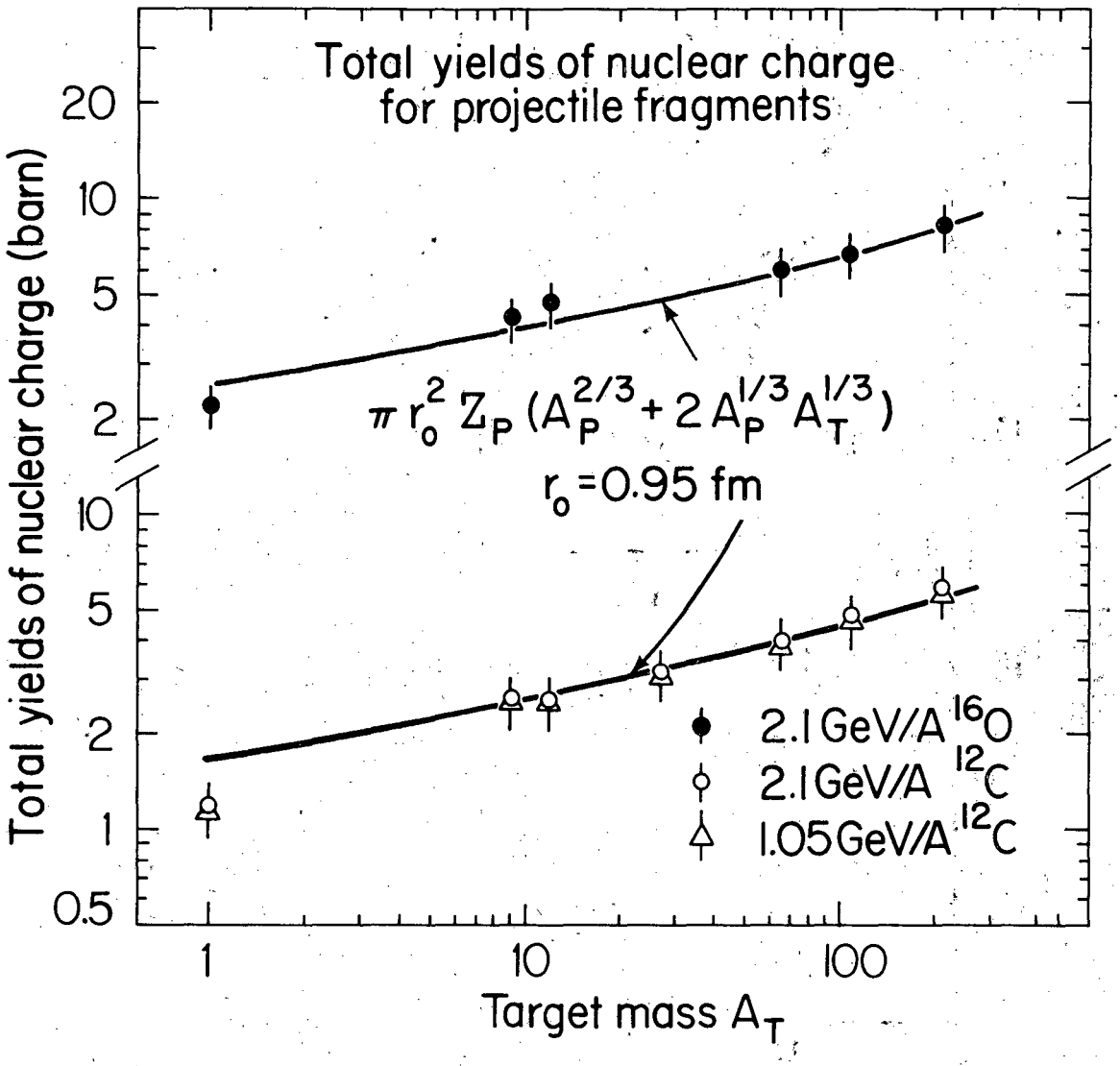

XBL 797 - 2083

Fig. 17 (a)

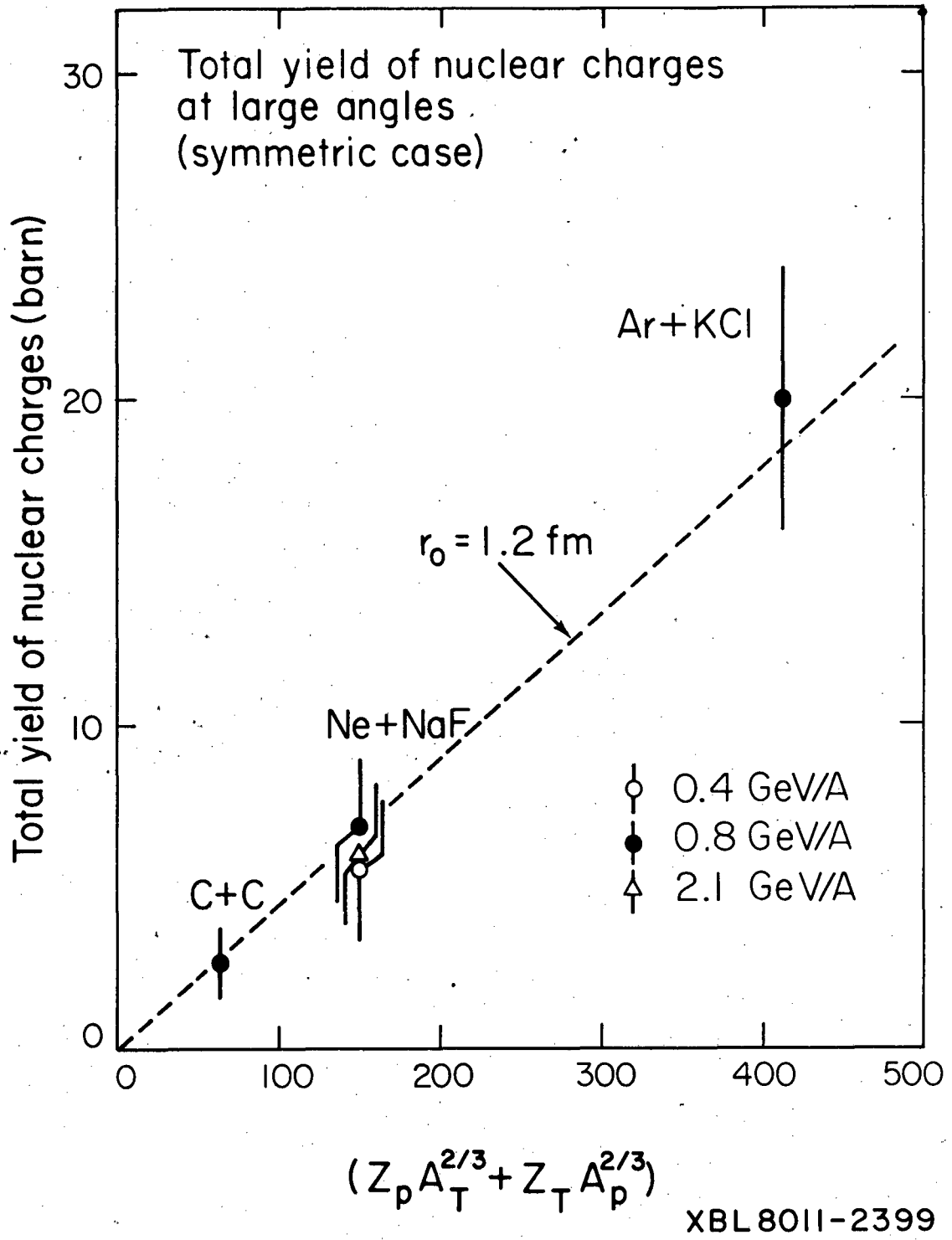
Total yield of nuclear charges
at large angles
(symmetric case)
Total yield of nuclear charges (barn)
30
20
10
0
0
100
200
300
400
500
Ar+KCl
$r_0 = 1.2$ fm
Ne+NaF
C+C
0.4 GeV/A
0.8 GeV/A
2.1 GeV/A
$(Z_p A_T^{2/3} + Z_T A_p^{2/3})$
XBL8011-2399

Fig. 17 (b)

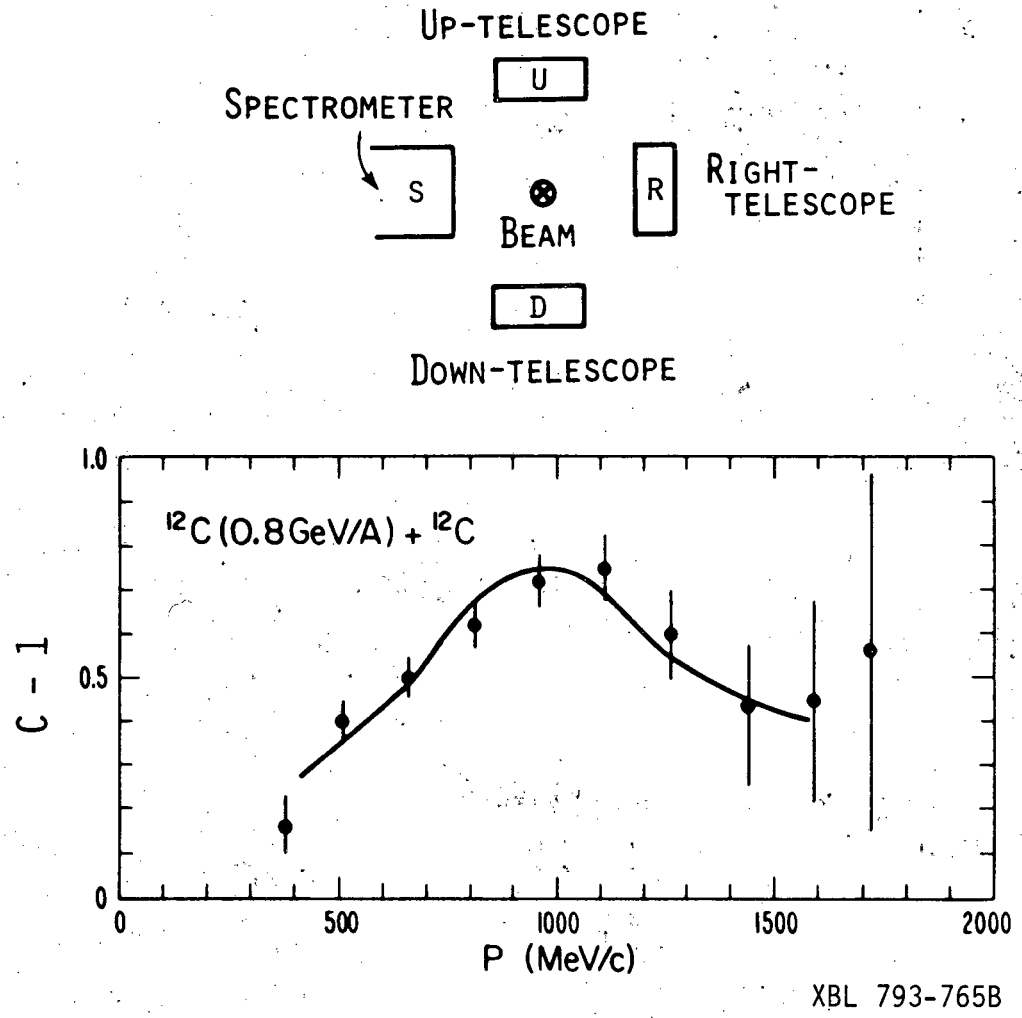
UP-TELESCOPE
U
SPECTROMETER
S
BEAM
R
RIGHT-
TELESCOPE
D
DOWN-TELESCOPE
^{12}C (0.8GeV/A) + ^{12}C
C - 1
1.0
0.5
0
0
500
1000
1500
2000
P (MeV/c)
XBL 793-765B

Fig. 18

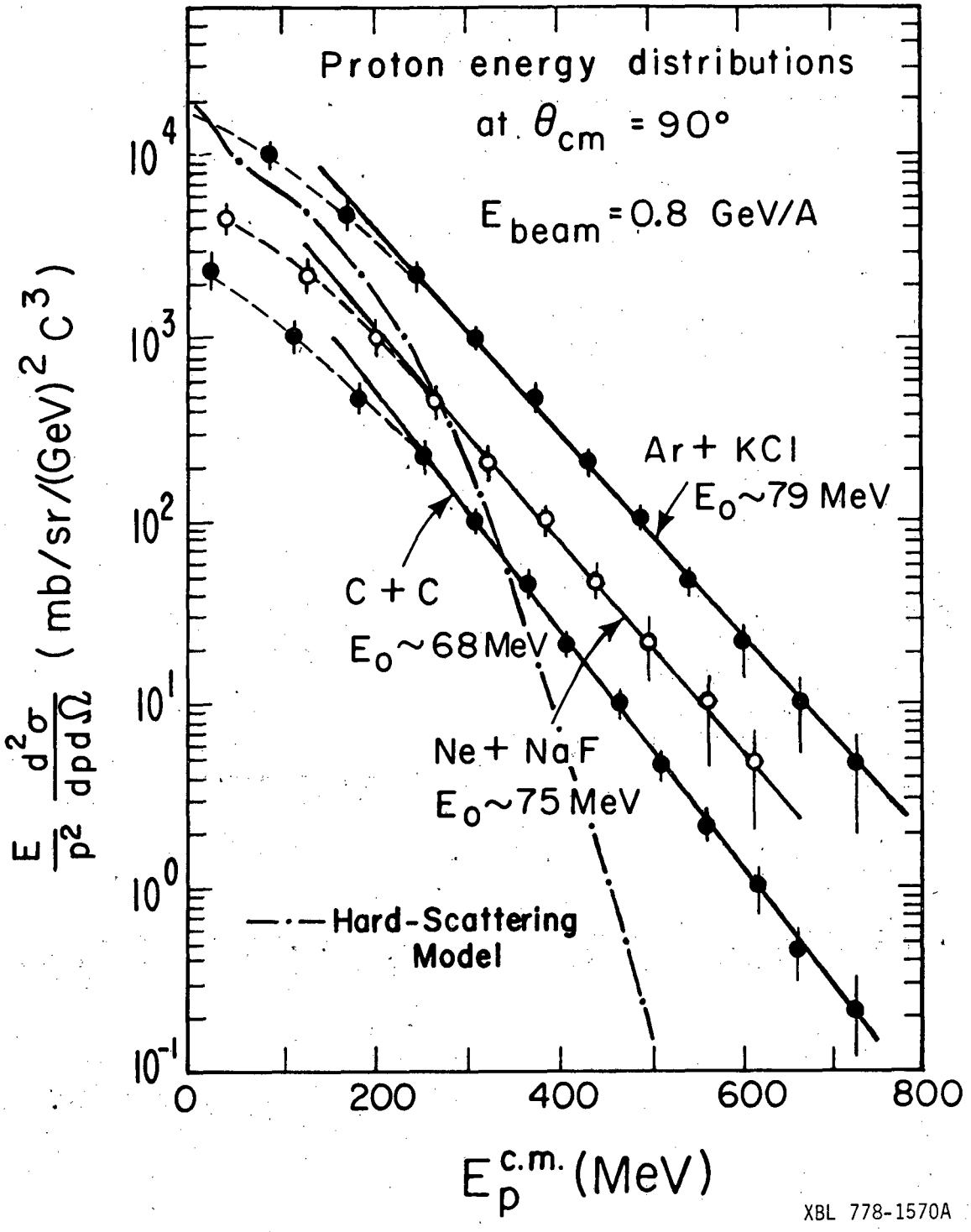
Proton energy distributions
at θ_{cm} = 90°
E_{beam} = 0.8 GeV/A
Ar + KCl
E_o ~ 79 MeV
C + C
E_o ~ 68 MeV
Ne + NaF
E_o ~ 75 MeV
Hard-Scattering Model
$E \frac{d^2\sigma}{p^2 dp d\Omega}$ (mb/sr/(GeV)^2 C^3)
10^4
10^3
10^2
10^1
10^0
10^{-1}
0
200
400
600
800
$E_p^{c.m.}$ (MeV)
XBL 778-1570A

Fig. 19

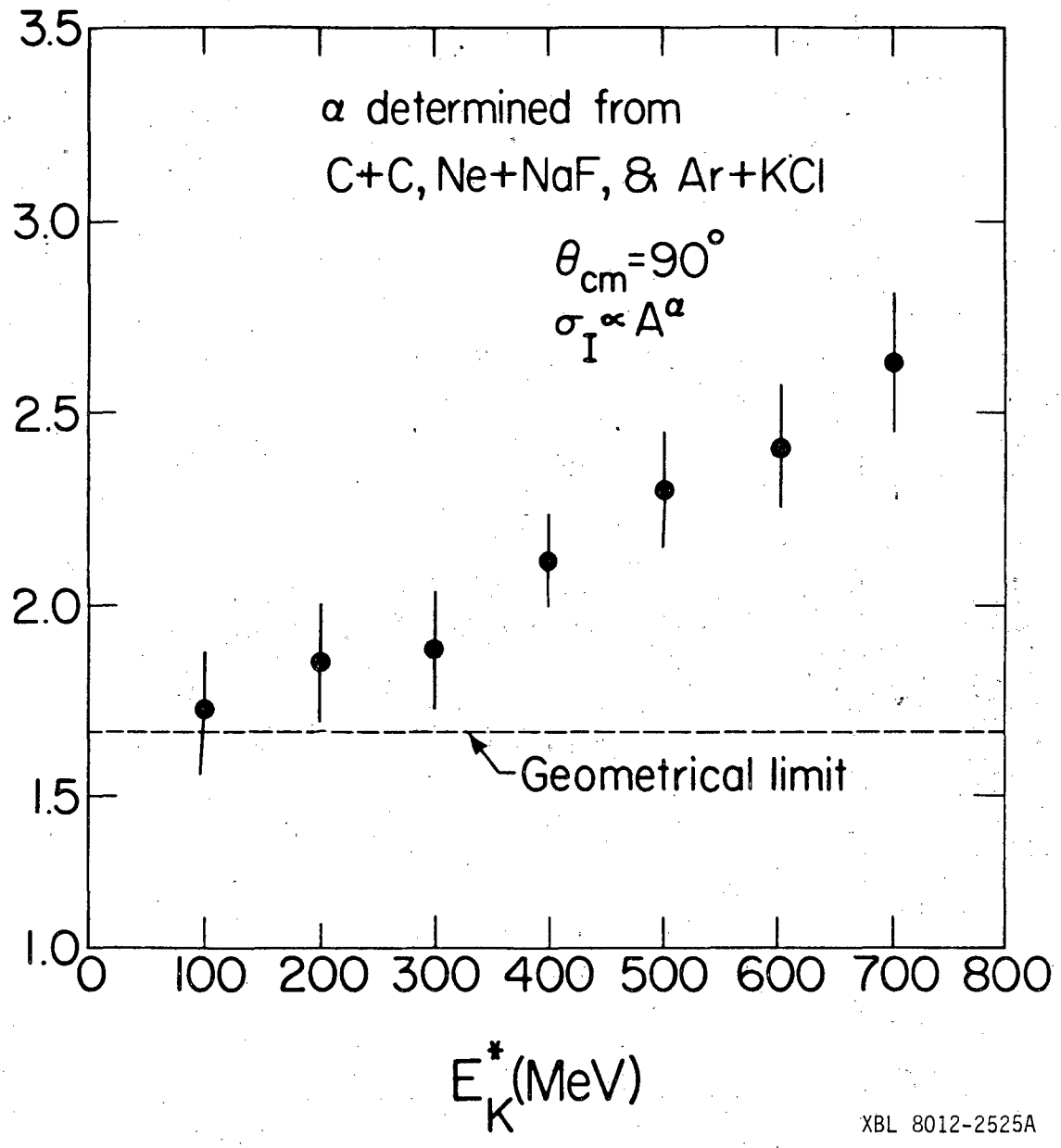
α determined from
C+C, Ne+NaF, & Ar+KCl
$\theta_{cm}=90°$
$\sigma_I \propto A^{\alpha}$
Geometrical limit
3.5
3.0
2.5
2.0
1.5
1.0
0
100
200
300
400
500
600
700
800
E_K^*(MeV)
XBL 8012-2525A

Fig. 20

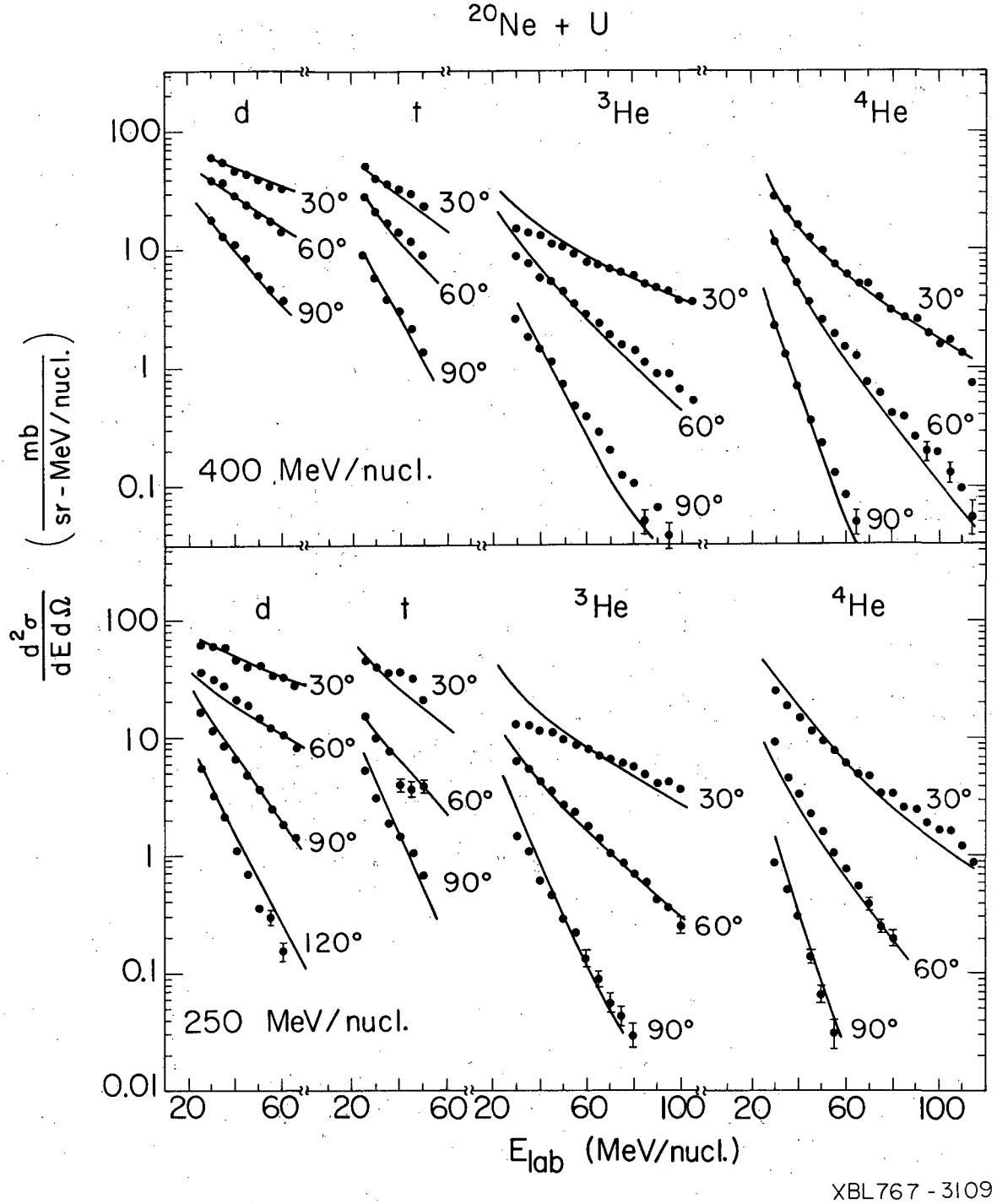
^{20}Ne + U
d
t
^{3}He
^{4}He
400 MeV/nucl.
250 MeV/nucl.
30°
60°
90°
120°
$\frac{d^2\sigma}{dE\,d\Omega}$ $\left(\frac{mb}{sr\text{-}MeV/nucl.}\right)$
E_{lab} (MeV/nucl.)
XBL767-3109

Fig. 21

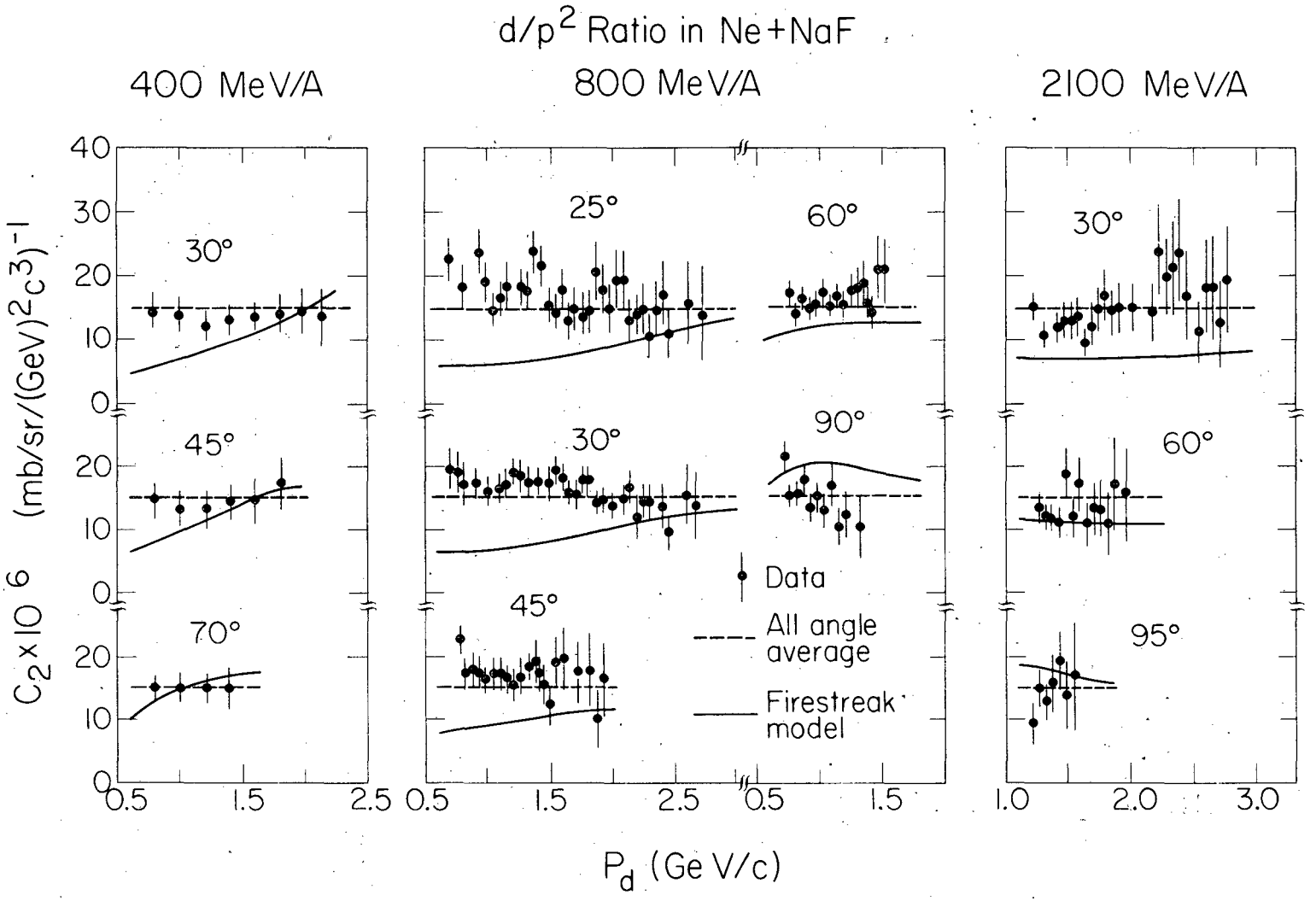
d/p² Ratio in Ne+NaF
400 MeV/A
800 MeV/A
2100 MeV/A
30°
45°
70°
25°
60°
30°
90°
45°
30°
60°
95°
Data
All angle average
Firestreak model
C₂×10⁶ (mb/sr/(GeV)²c³)⁻¹
P_d (GeV/c)
XBL 8012-2517

Fig. 22

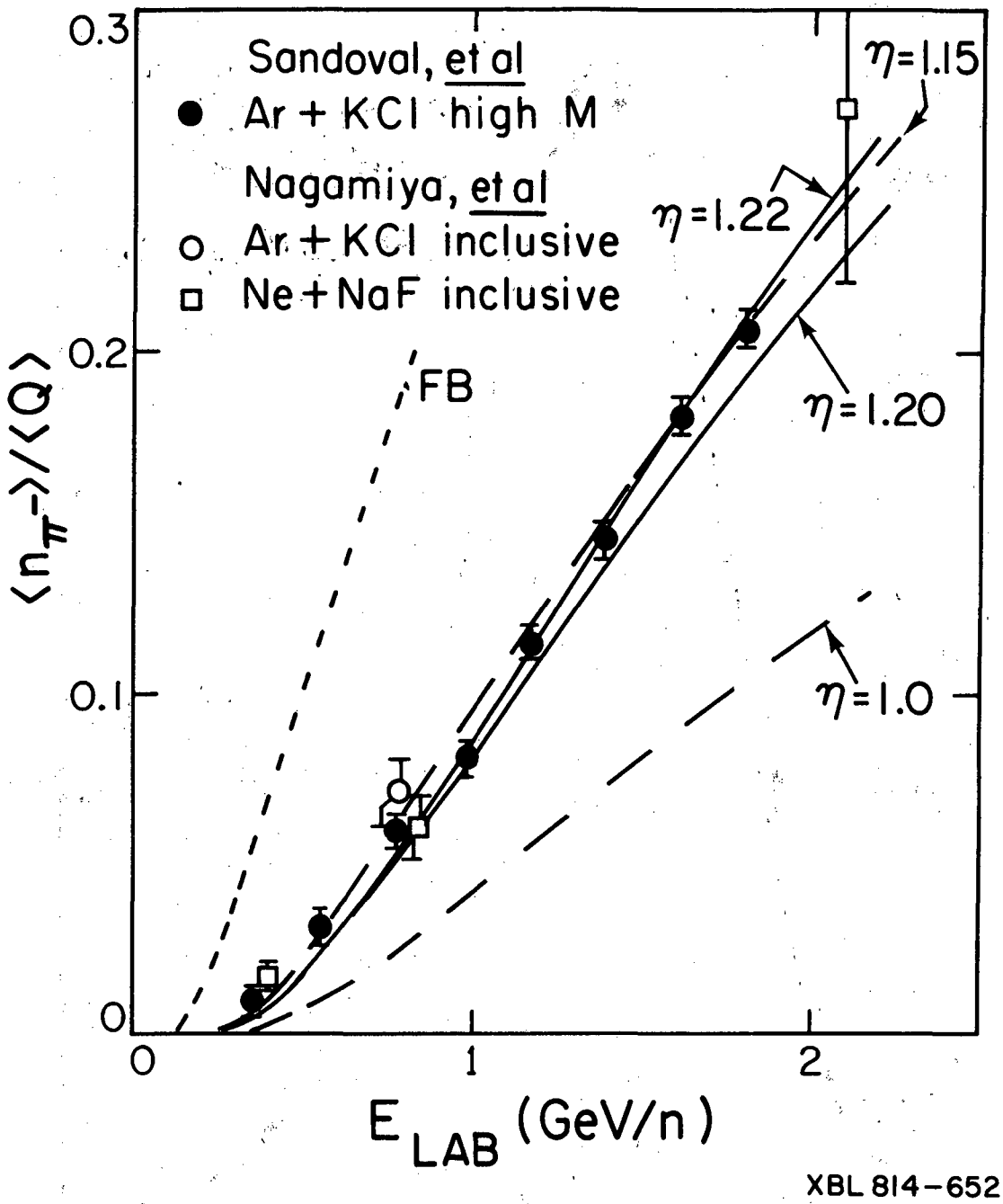
Sandoval, et al
Ar + KCl high M
Nagamiya, et al
Ar + KCl inclusive
Ne + NaF inclusive
FB
η=1.15
η=1.22
η=1.20
η=1.0
0.3
0.2
0.1
0
0
1
2
⟨nπ⁻⟩/⟨Q⟩
E LAB (GeV/n)
XBL 814-652

Fig. 23

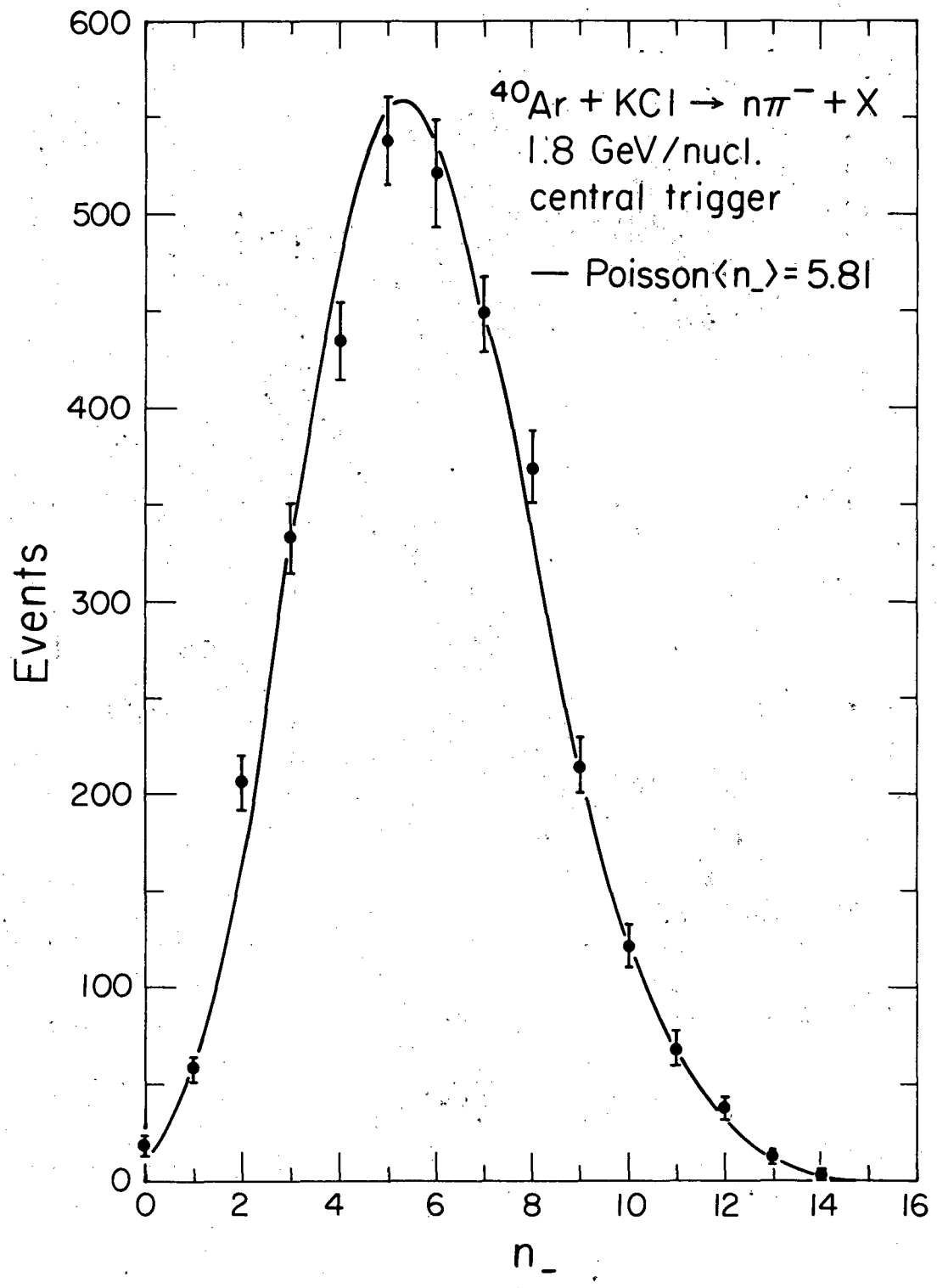
$^{40}Ar + KCl \rightarrow n\pi^- + X$
1.8 GeV/nucl.
central trigger
— Poisson⟨n_⟩= 5.81
Events
n_
0
100
200
300
400
500
600
0
2
4
6
8
10
12
14
16
XBL 822-4454

Fig. 24

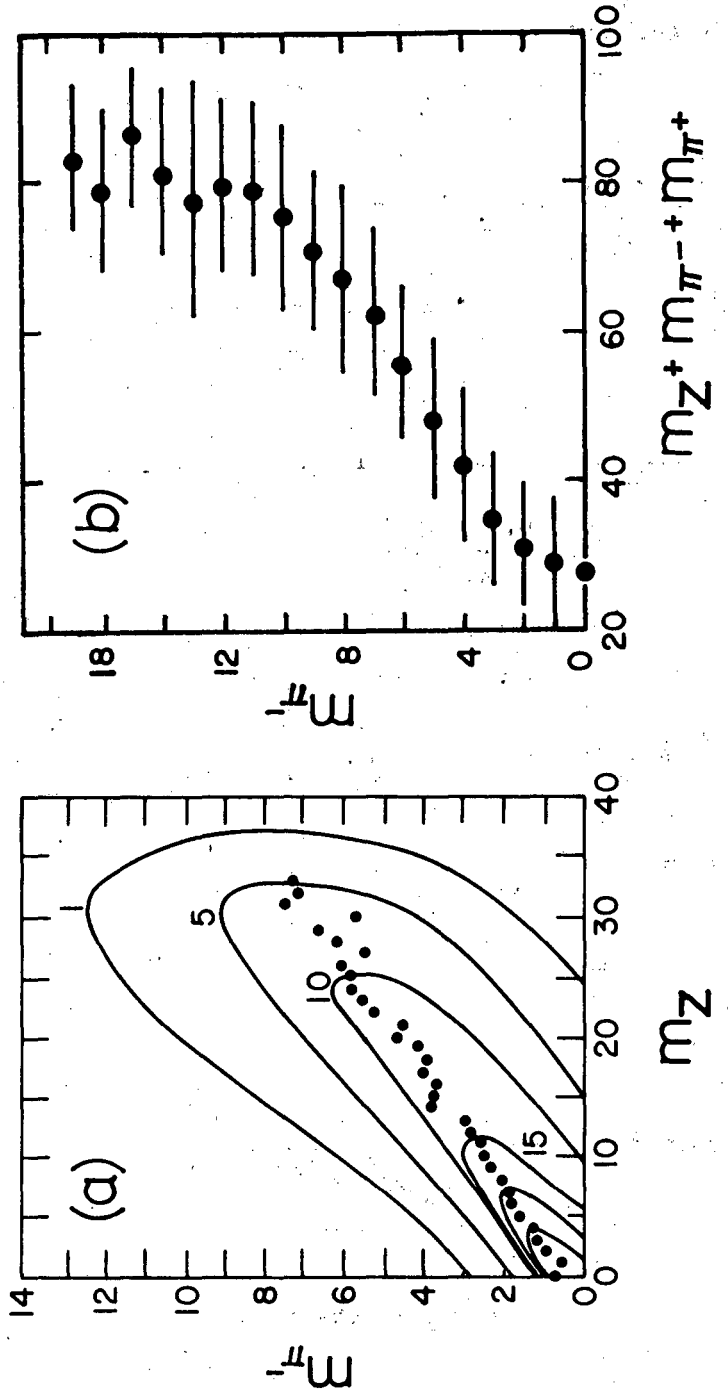

Fig. 25

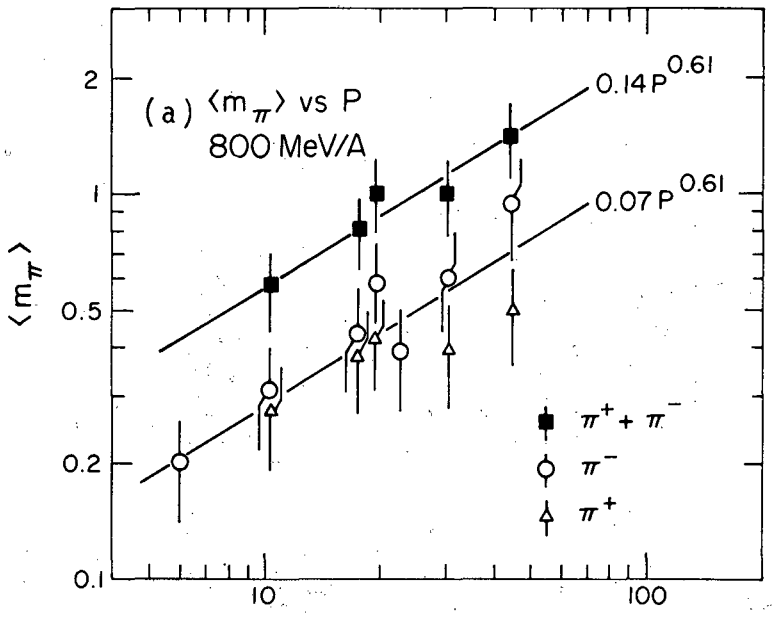

$$P \equiv \frac{A_P A_T^{2/3} + A_T A_P^{2/3}}{(A_P^{1/3} + A_T^{1/3})^2}$$

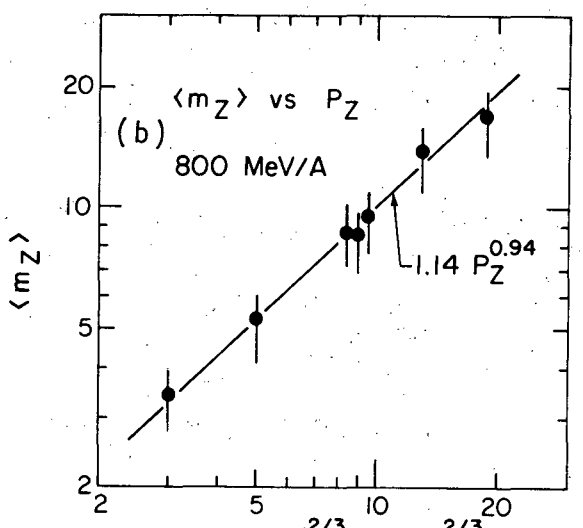

$$P_Z \equiv \frac{Z_P A_T^{2/3} + Z_T A_P^{2/3}}{(A_P^{1/3} + A_T^{1/3})^2}$$

XBL 816-2354A

Fig. 26

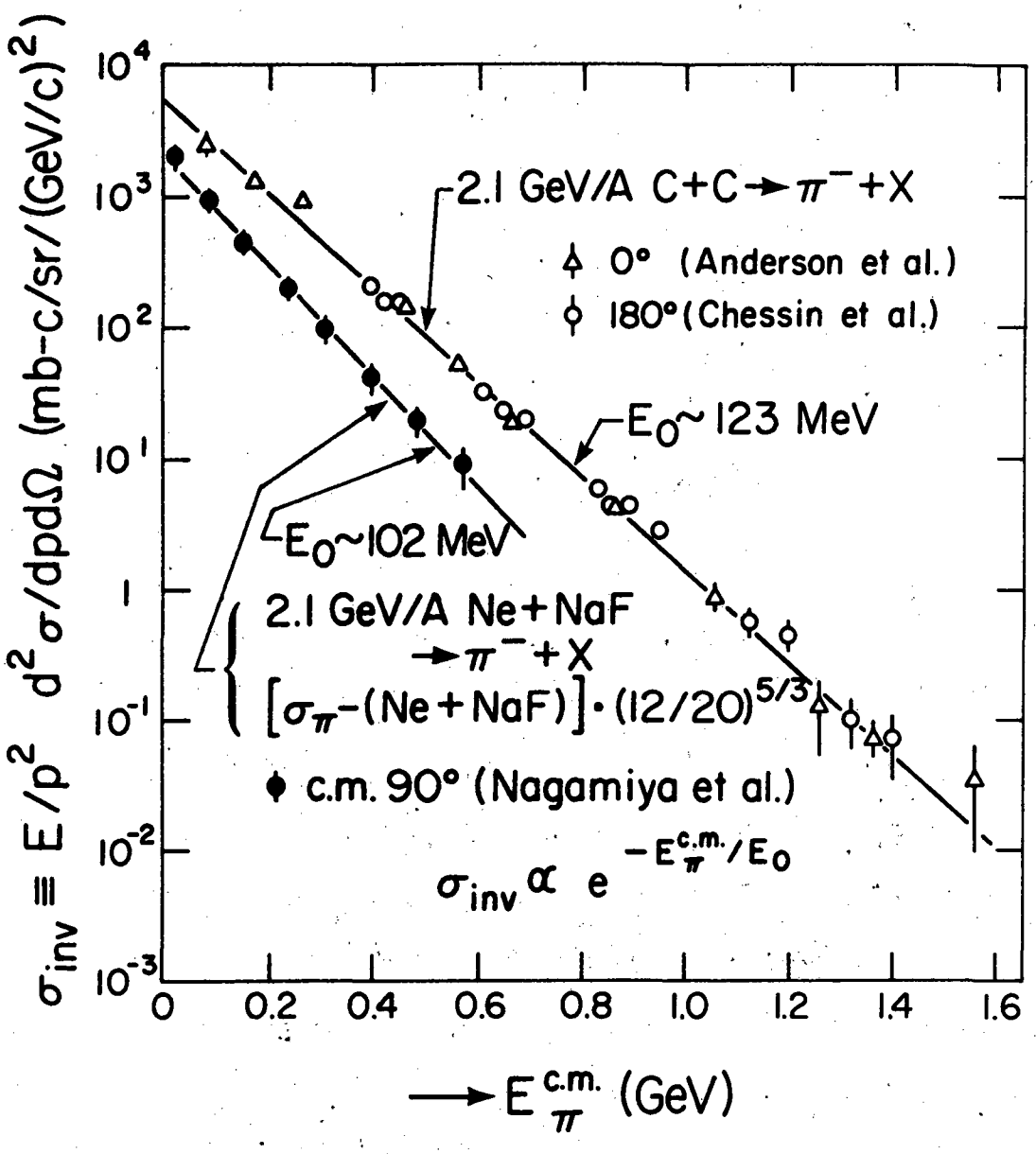

XBL 816-2359

Fig. 27

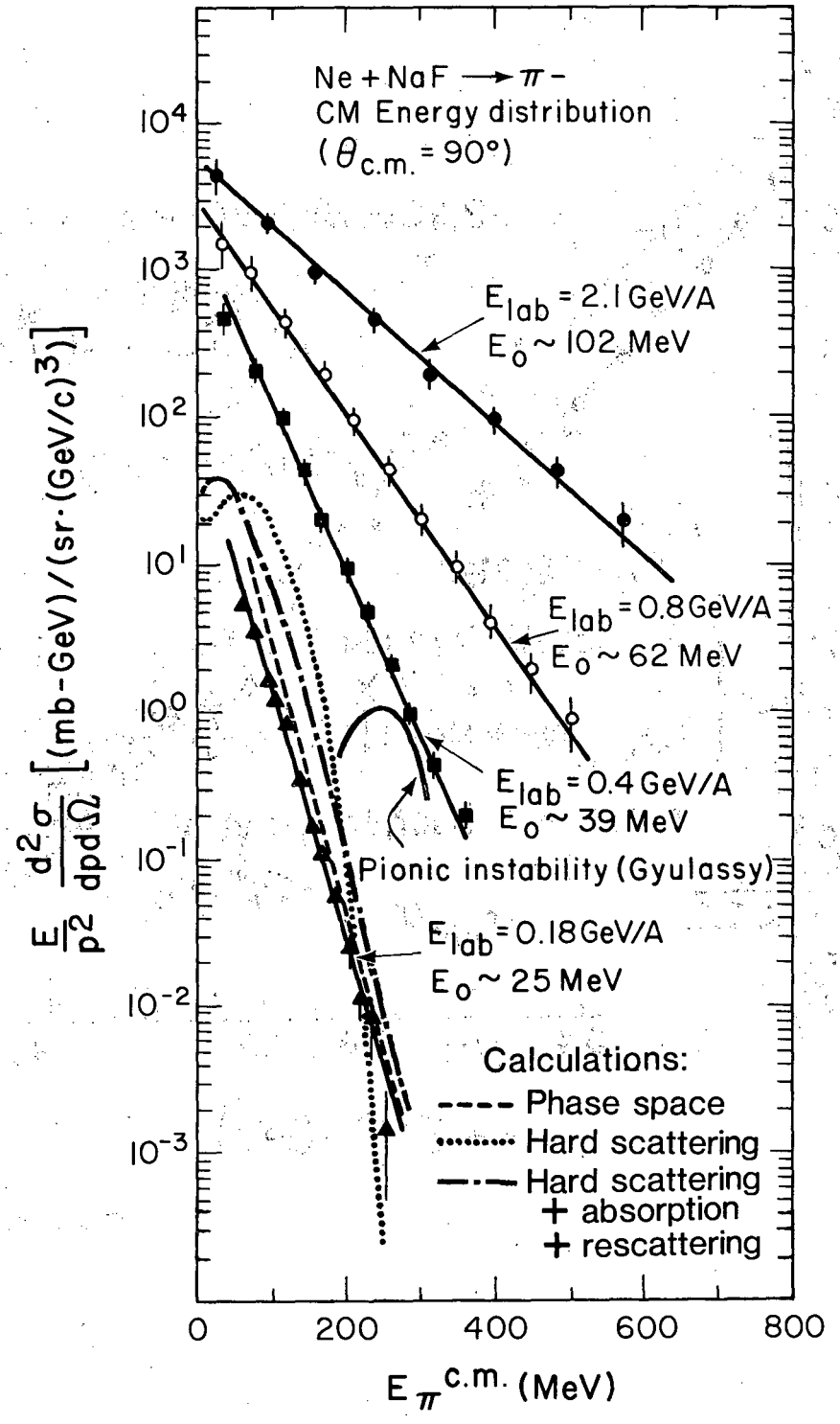
Ne + NaF → π⁻
CM Energy distribution
(θc.m. = 90°)
Elab = 2.1 GeV/A
E0 ~ 102 MeV
Elab = 0.8 GeV/A
E0 ~ 62 MeV
Elab = 0.4 GeV/A
E0 ~ 39 MeV
Pionic instability (Gyulassy)
Elab = 0.18 GeV/A
E0 ~ 25 MeV
Calculations:
Phase space
Hard scattering
Hard scattering + absorption + rescattering
E d²σ/p² dpdΩ [(mb-GeV)/(sr·(GeV/c)³)]
Eπ c.m. (MeV)
XBL 8112-13235

Fig. 23

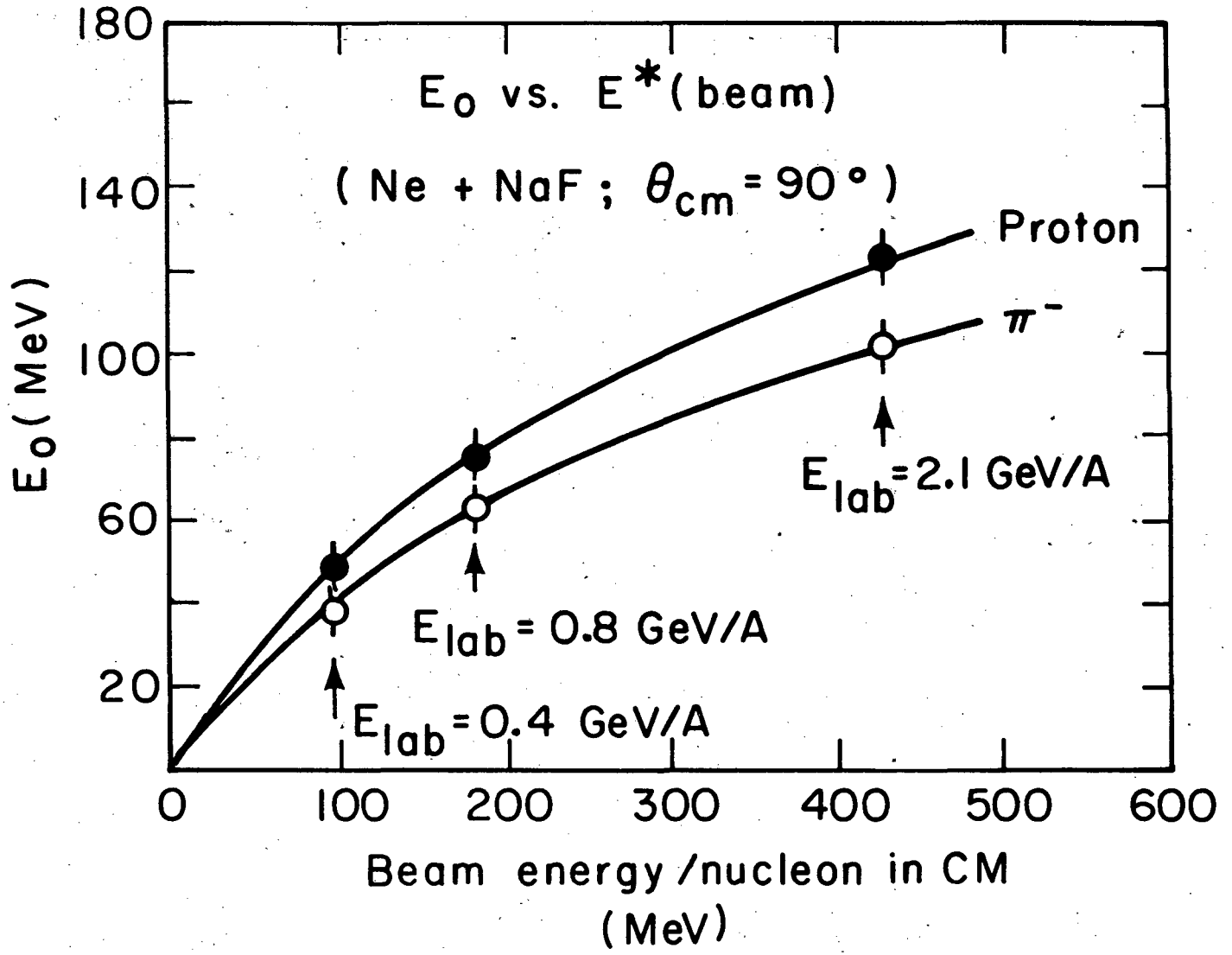

XBL788-1495B

Fig. 29

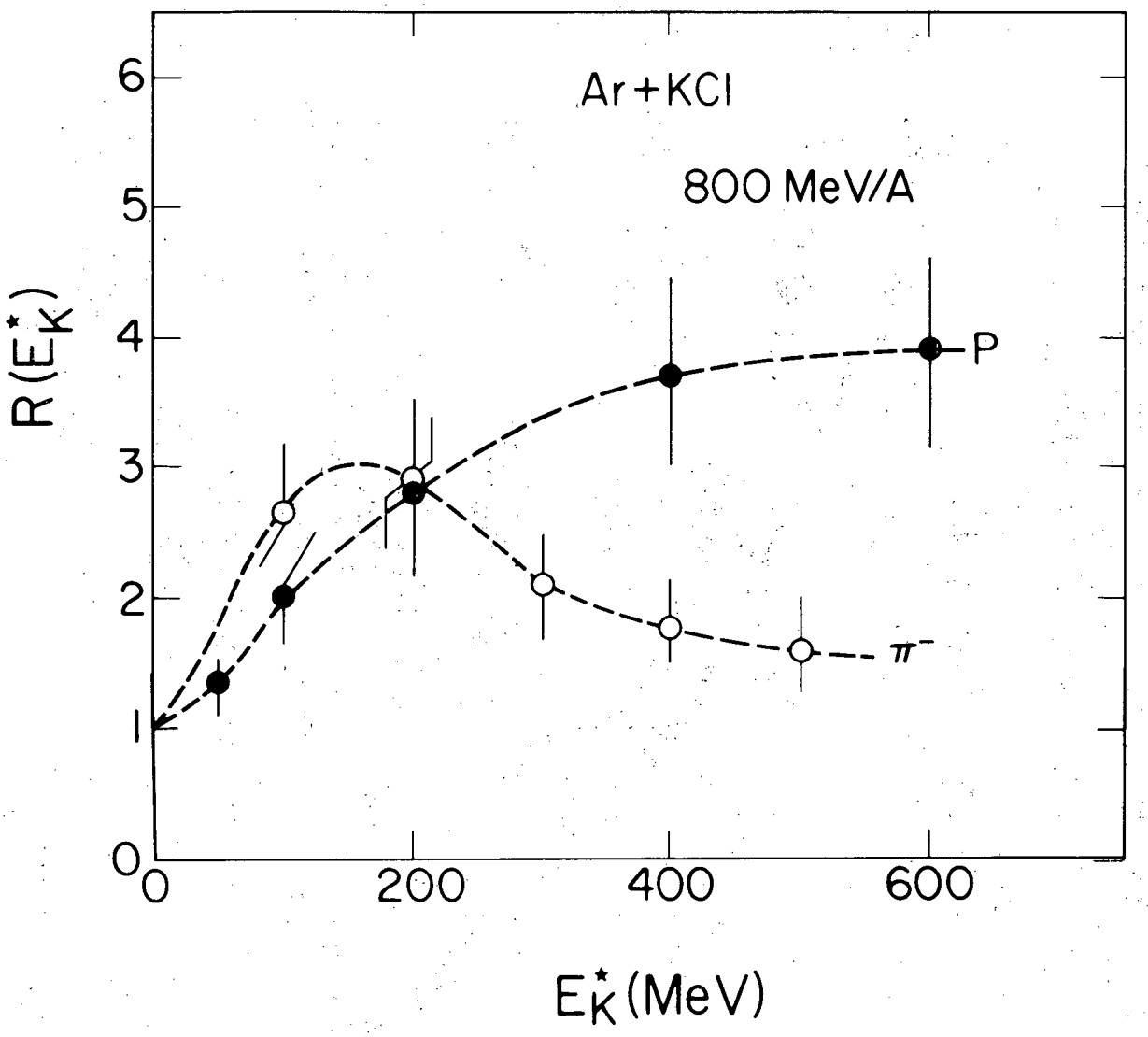

XBL 8012-2522 A

Fig. 30

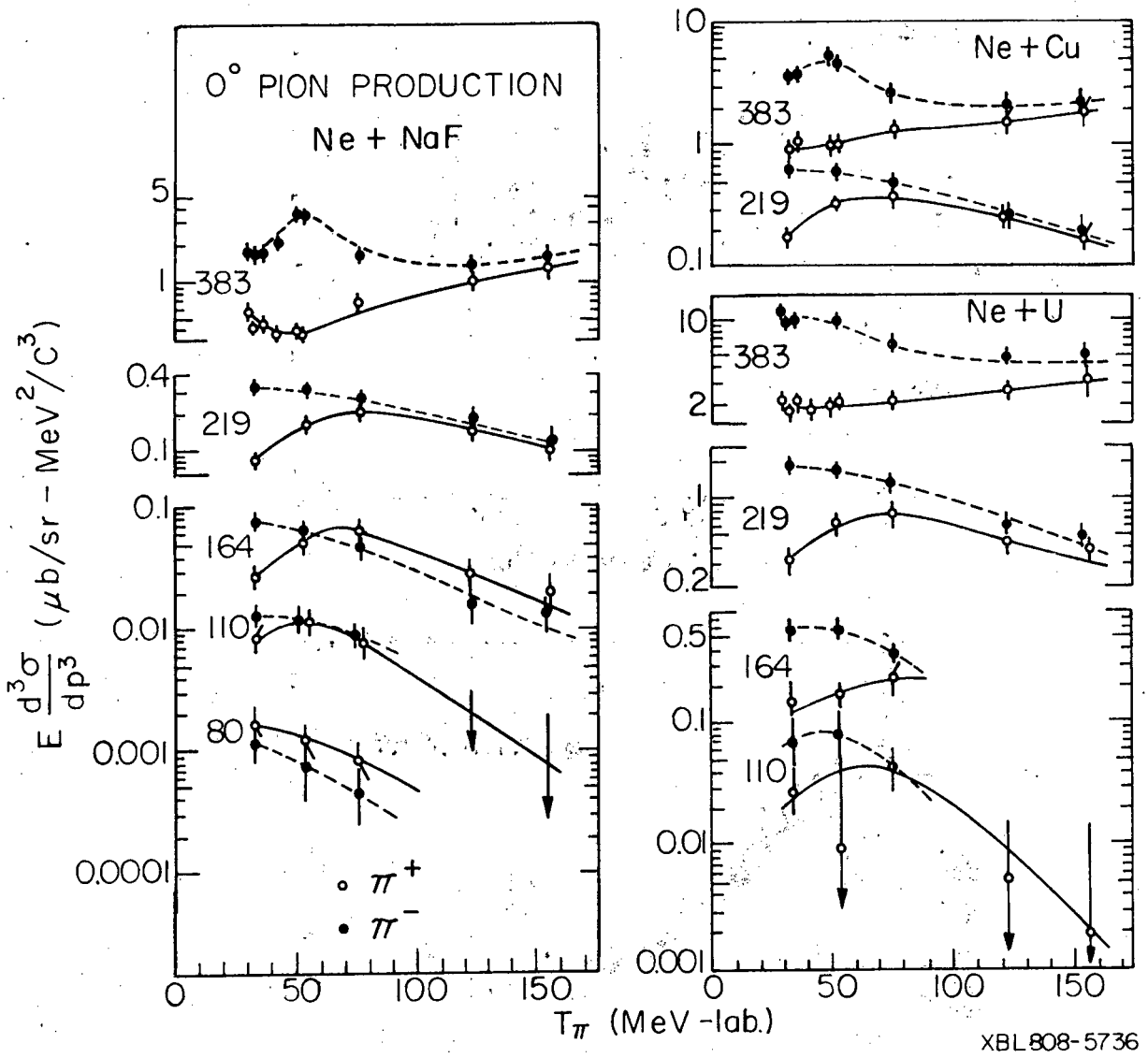
0° PION PRODUCTION
Ne + NaF
Ne + Cu
Ne + U
383
219
164
110
80
π^+
π^-
$E\frac{d^3\sigma}{dp^3}$ (μb/sr - MeV^2/C^3)
T_π (MeV -lab.)
XBL808-5736

Fig. 31

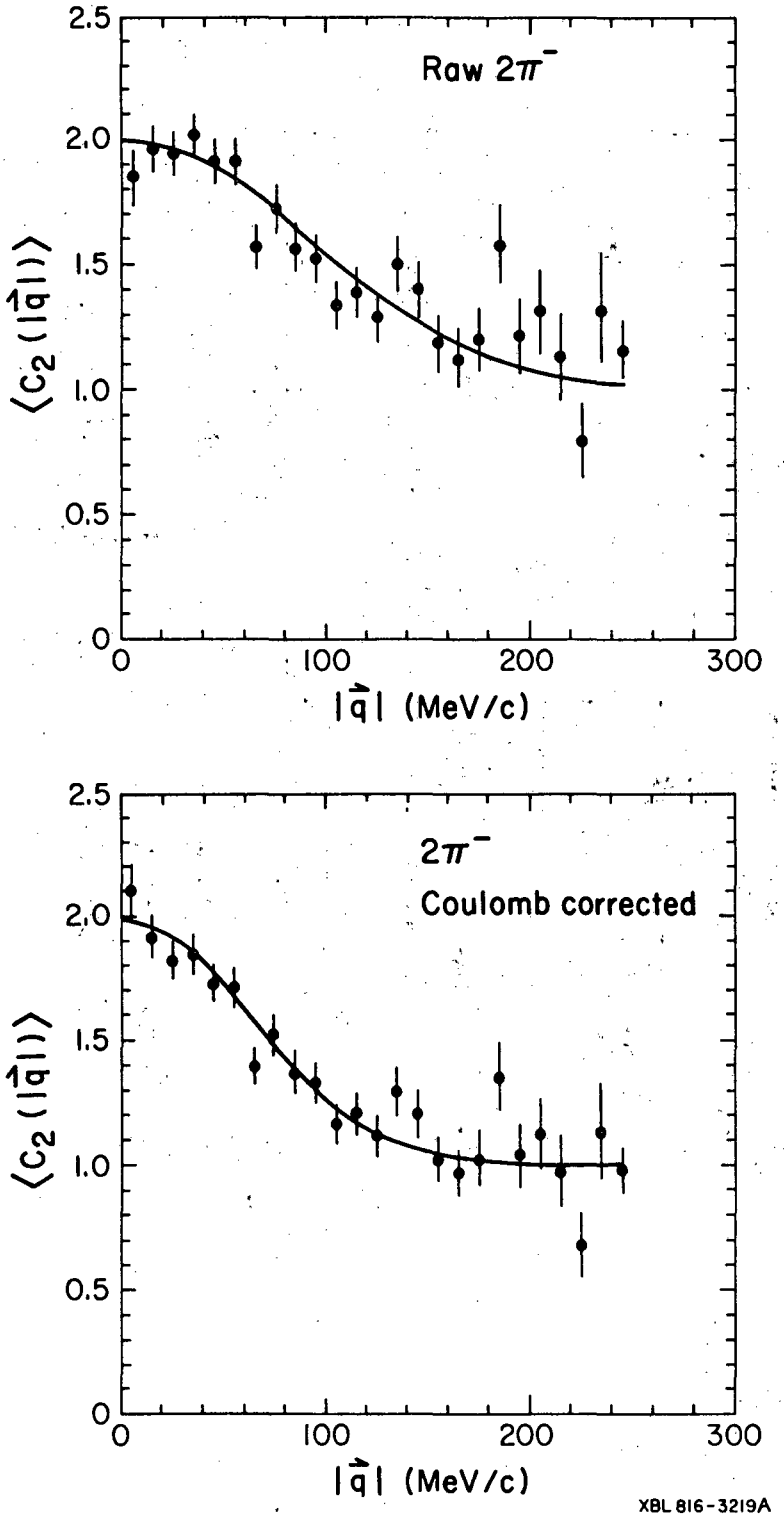
Raw $2\pi^-$
$\langle C_2(|\vec{q}|)\rangle$
$|\vec{q}|$ (MeV/c)
$2\pi^-$
Coulomb corrected
$\langle C_2(|\vec{q}|)\rangle$
$|\vec{q}|$ (MeV/c)
XBL 816-3219A

Fig. 32

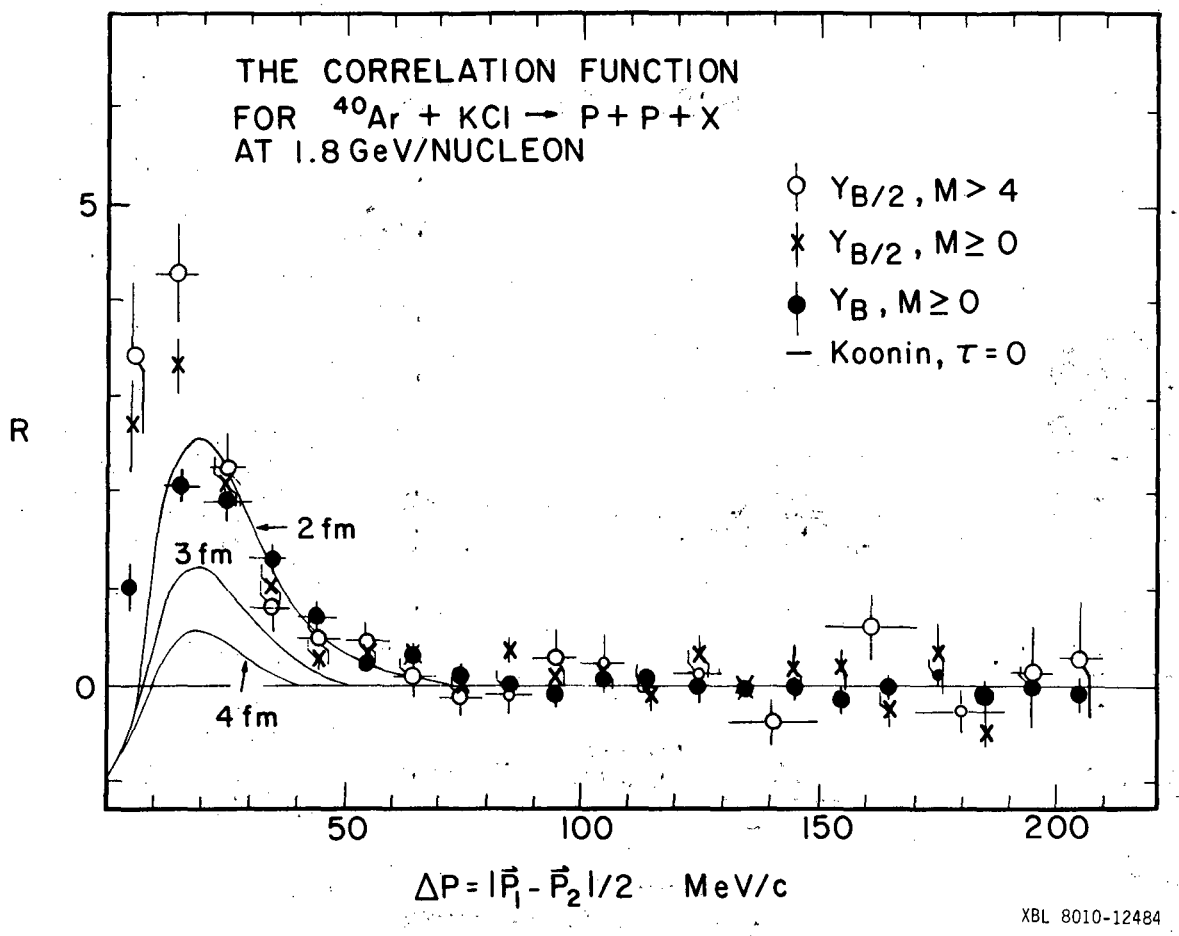
THE CORRELATION FUNCTION
FOR $^{40}Ar + KCl \rightarrow P + P + X$
AT 1.8 GeV/NUCLEON
$Y_{B/2}$, M > 4
$Y_{B/2}$, M ≥ 0
Y_B, M ≥ 0
Koonin, τ = 0
R
5
0
2 fm
3 fm
4 fm
50
100
150
200
$\Delta P = |\vec{P}_1 - \vec{P}_2|/2$ MeV/c
XBL 8010-12484

Fig. 33

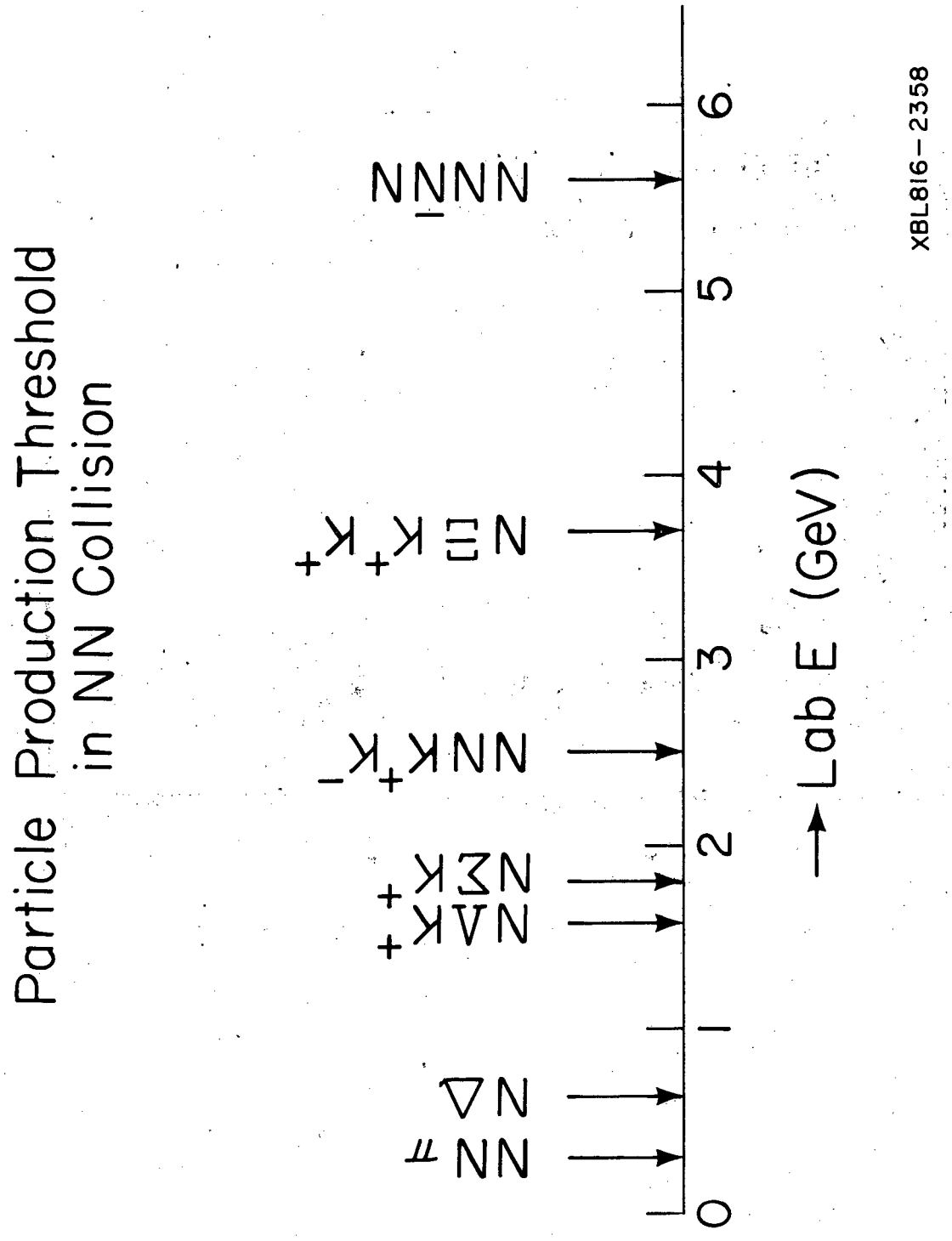
Particle Production Threshold
in NN Collision
NNπ
NΔ
NΛK+
NΣK+
NNK+K-
NΞK+K+
NNN̄N
0
1
2
3
4
5
6
→Lab E (GeV)
XBL816-2358

Fig. 34

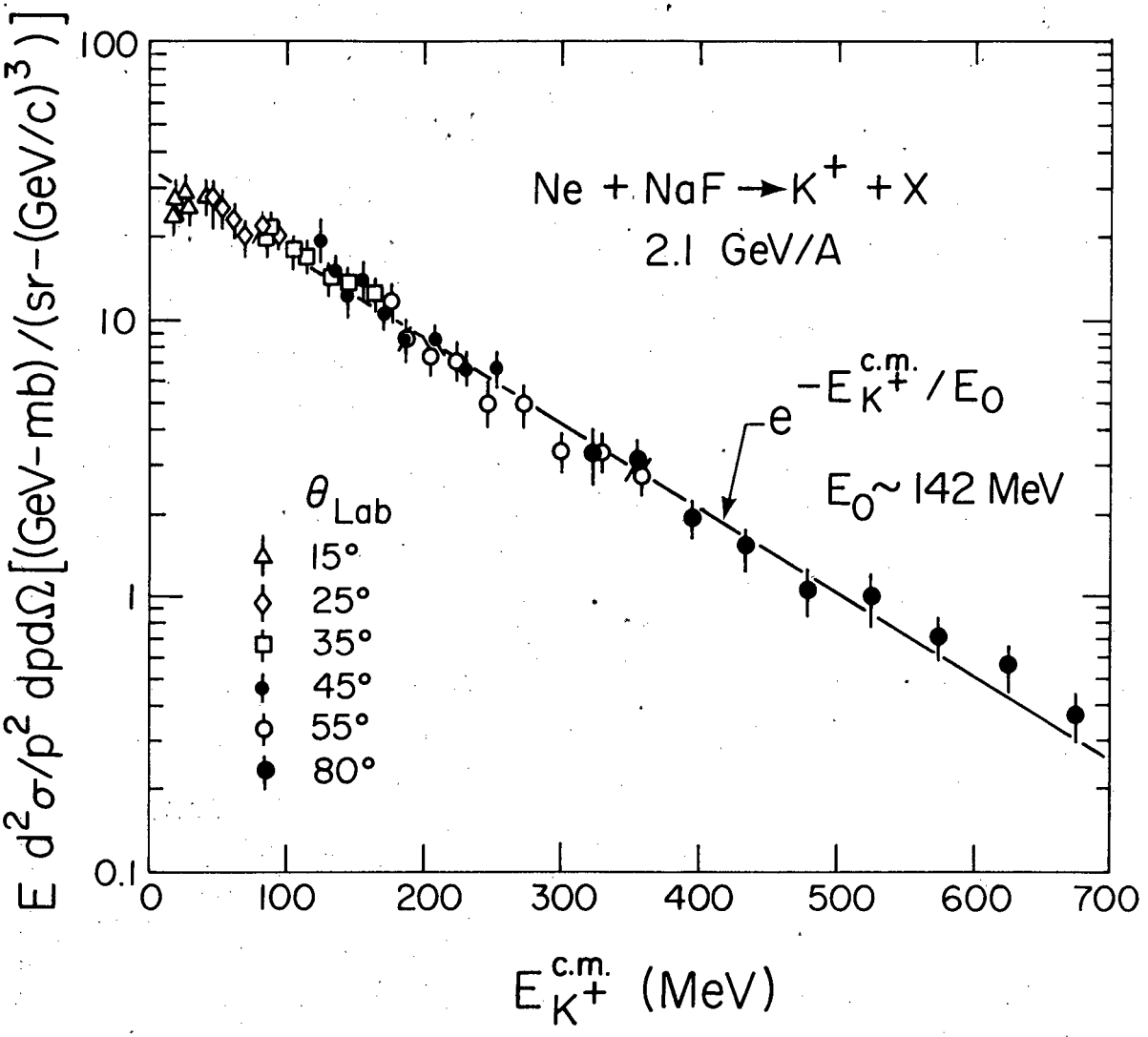

XBL 816-2361

Fig. 35

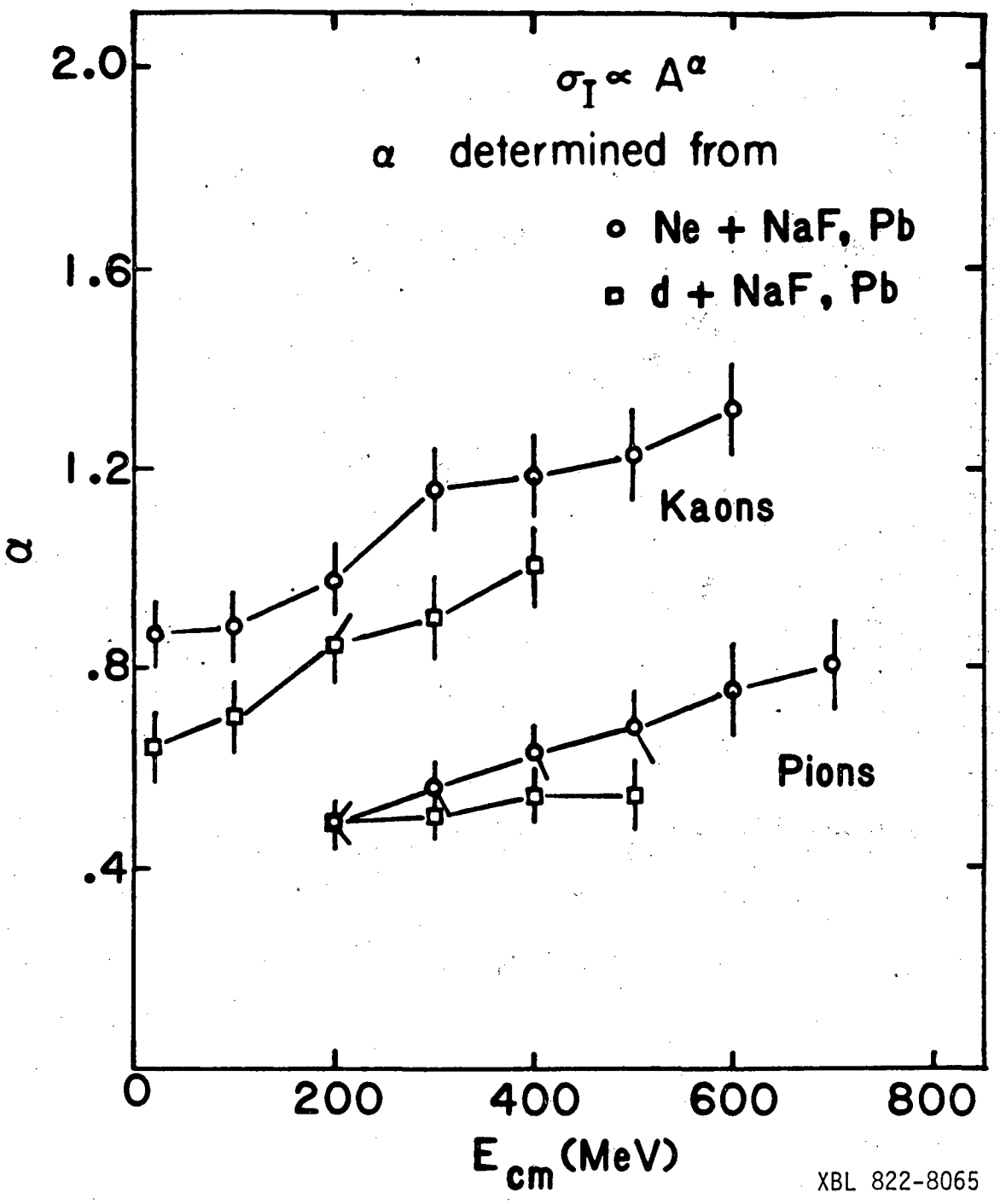
$\sigma_I \propto A^\alpha$
α determined from
Ne + NaF, Pb
d + NaF, Pb
Kaons
Pions
α
2.0
1.6
1.2
.8
.4
0
200
400
600
800
E_{cm} (MeV)
XBL 822-8065

Fig. 36

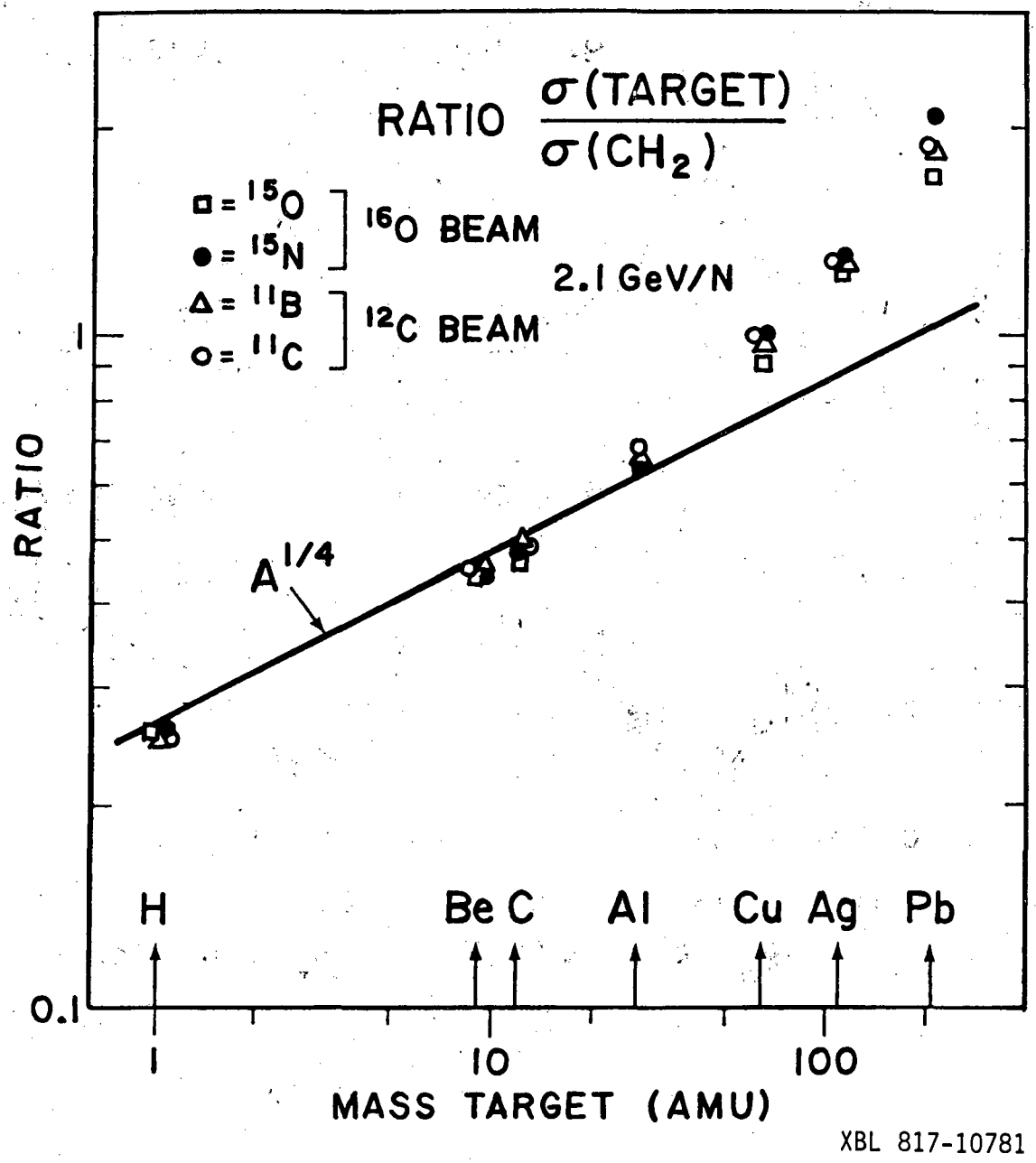
RATIO σ(TARGET)/σ(CH2)
□ = 15O
● = 15N
16O BEAM
Δ = 11B
○ = 11C
12C BEAM
2.1 GeV/N
RATIO
A1/4
1
0.1
H
Be C
Al
Cu Ag
Pb
1
10
100
MASS TARGET (AMU)
XBL 817-10781

Fig. 37

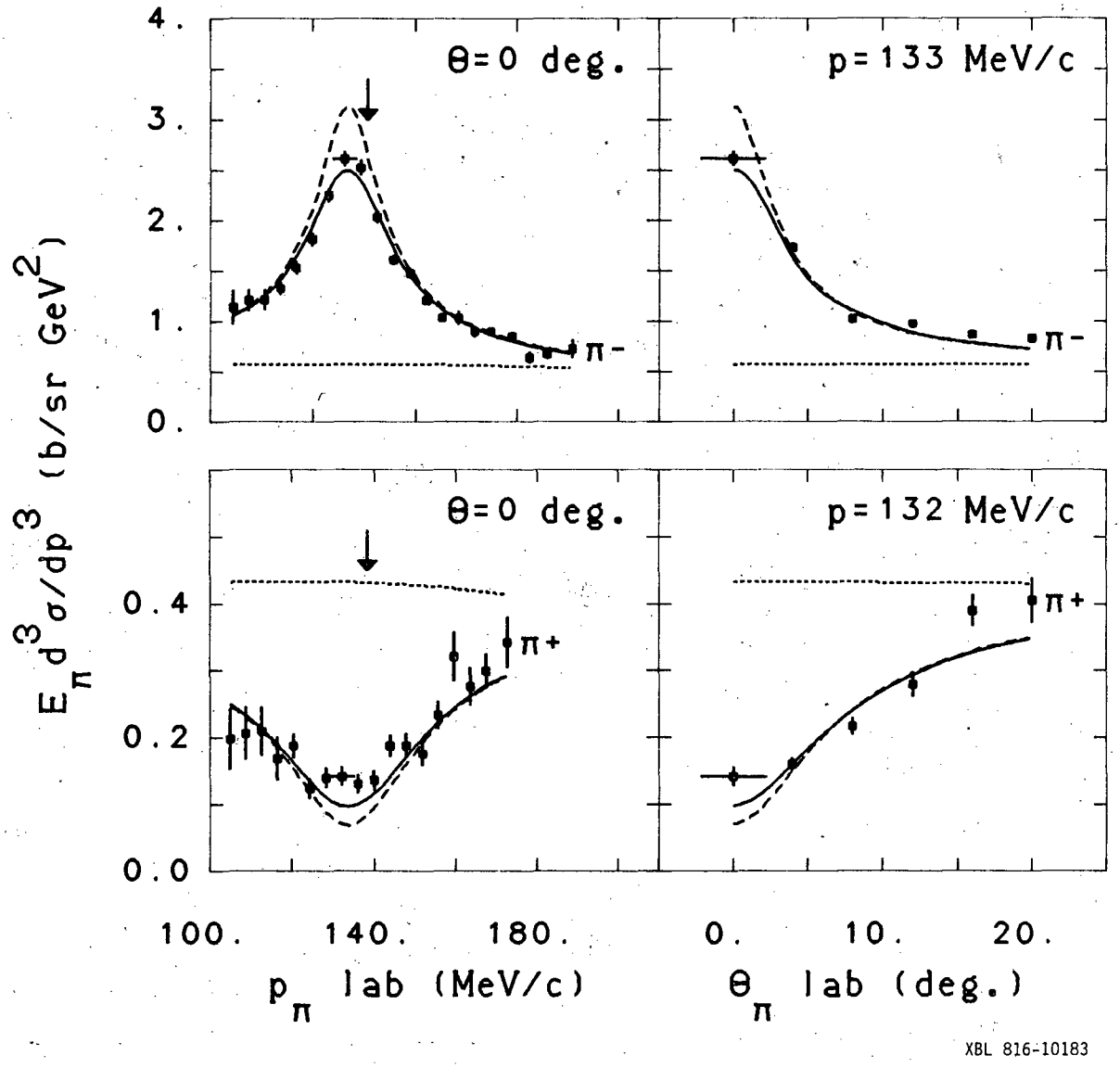
θ=0 deg.
p=133 MeV/c
π-
θ=0 deg.
p=132 MeV/c
π+
4.
3.
2.
1.
0.
0.4
0.2
0.0
100.
140.
180.
0.
10.
20.
$E_\pi d^3\sigma/dp^3$ (b/sr GeV^2)
p_π lab (MeV/c)
θ_π lab (deg.)
XBL 816-10183

Fig. 38

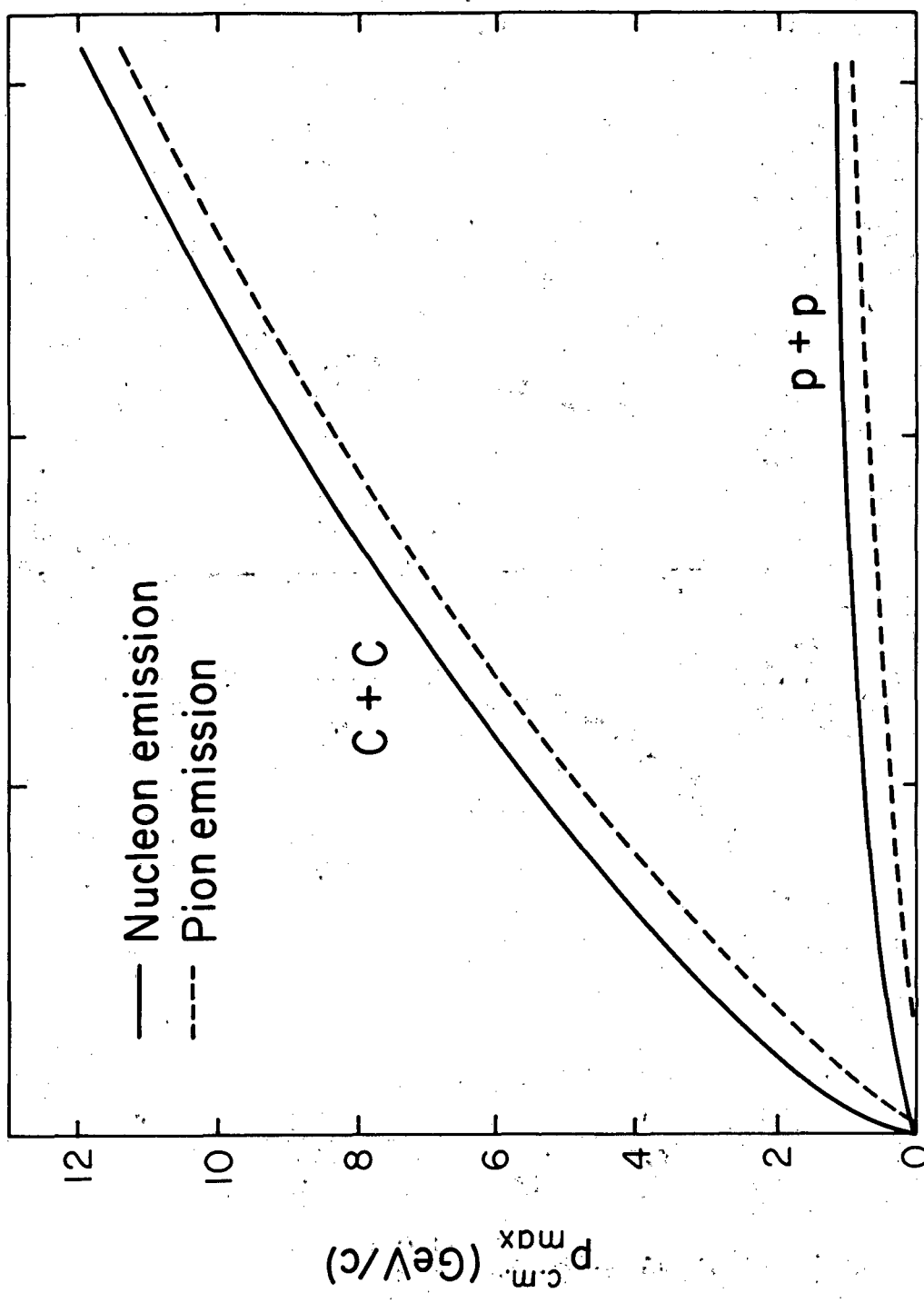
Nucleon emission
Pion emission
C + C
p + p
$p^{c.m.}_{max}$ (GeV/c)
E^{Lab}_{Beam}/A (GeV)
0
2
4
6
8
10
12
1
2
3
XBL 816-3225

Fig. 39

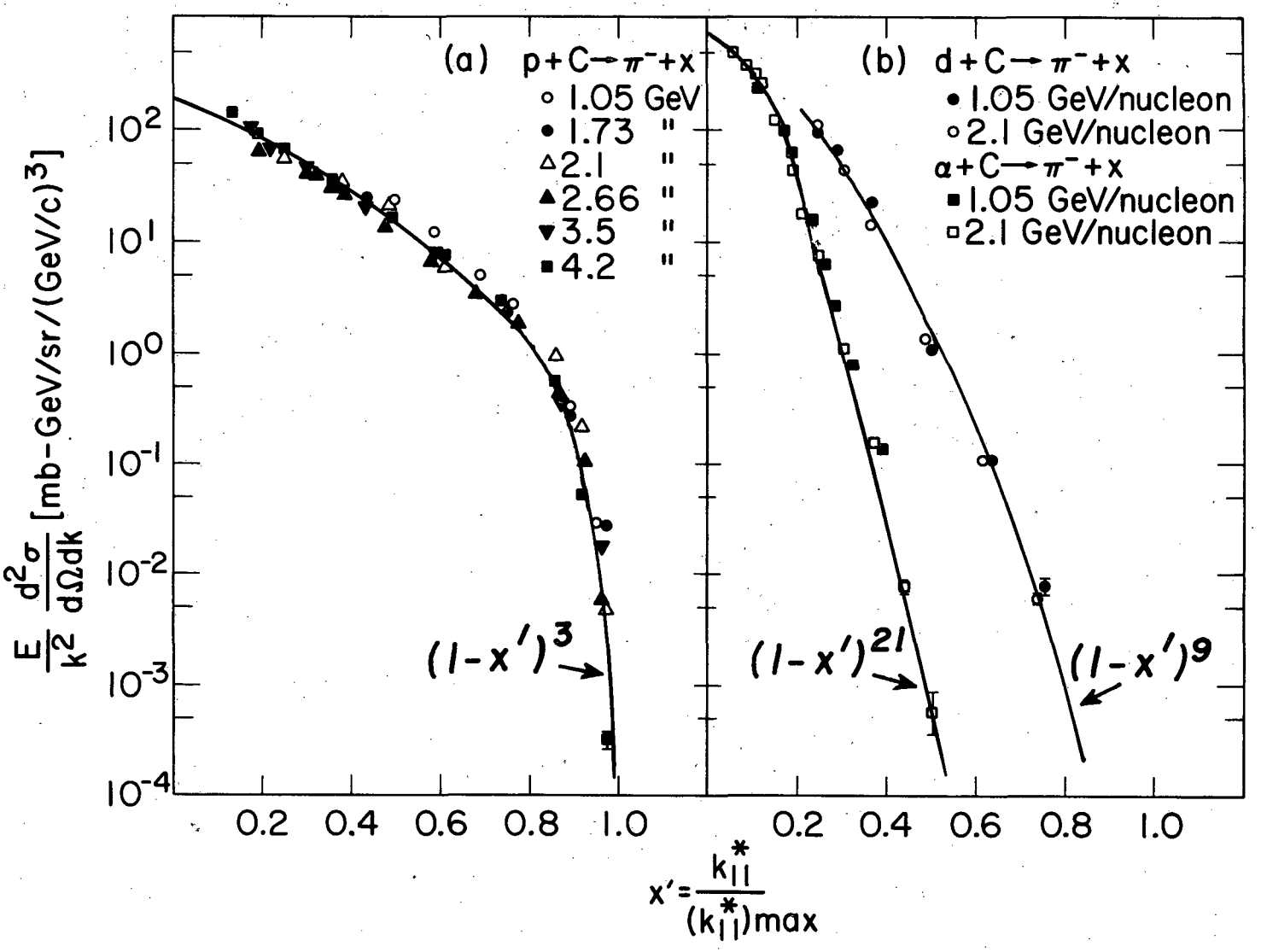

XBL 748-3896 A

Fig. 40

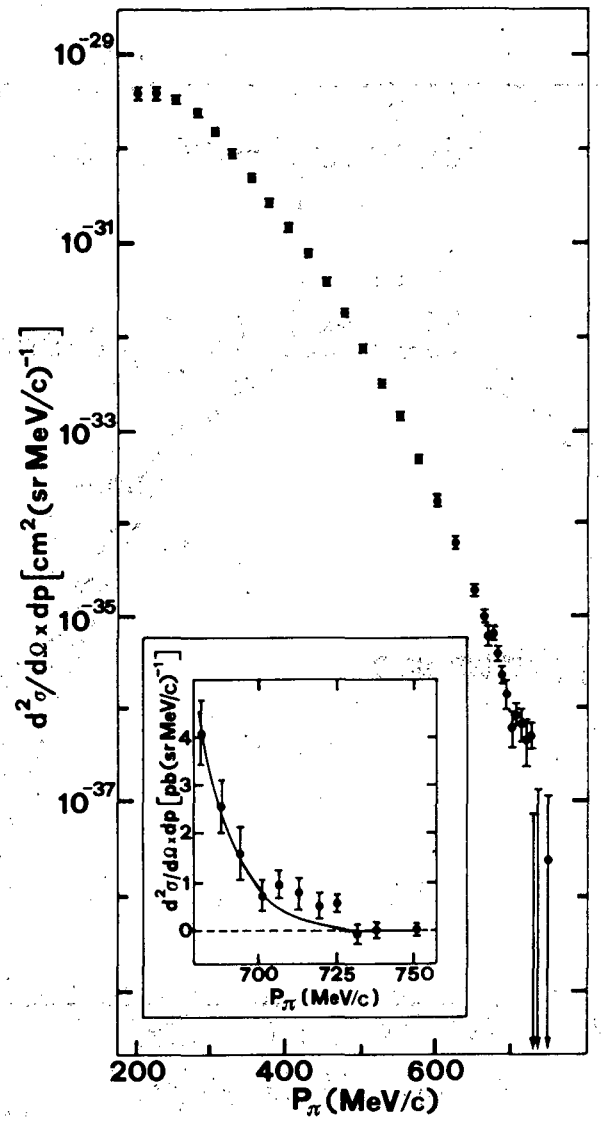
10^{-29}
10^{-31}
10^{-33}
10^{-35}
10^{-37}
$d^2\sigma/d\Omega \times dp\,[cm^2(sr\,MeV/c)^{-1}]$
200
400
600
P_π (MeV/c)
$d^2\sigma/d\Omega \times dp\,[pb(sr\,MeV/c)^{-1}]$
4
3
2
1
0
700
725
750
P_π (MeV/c)

Fig. 41

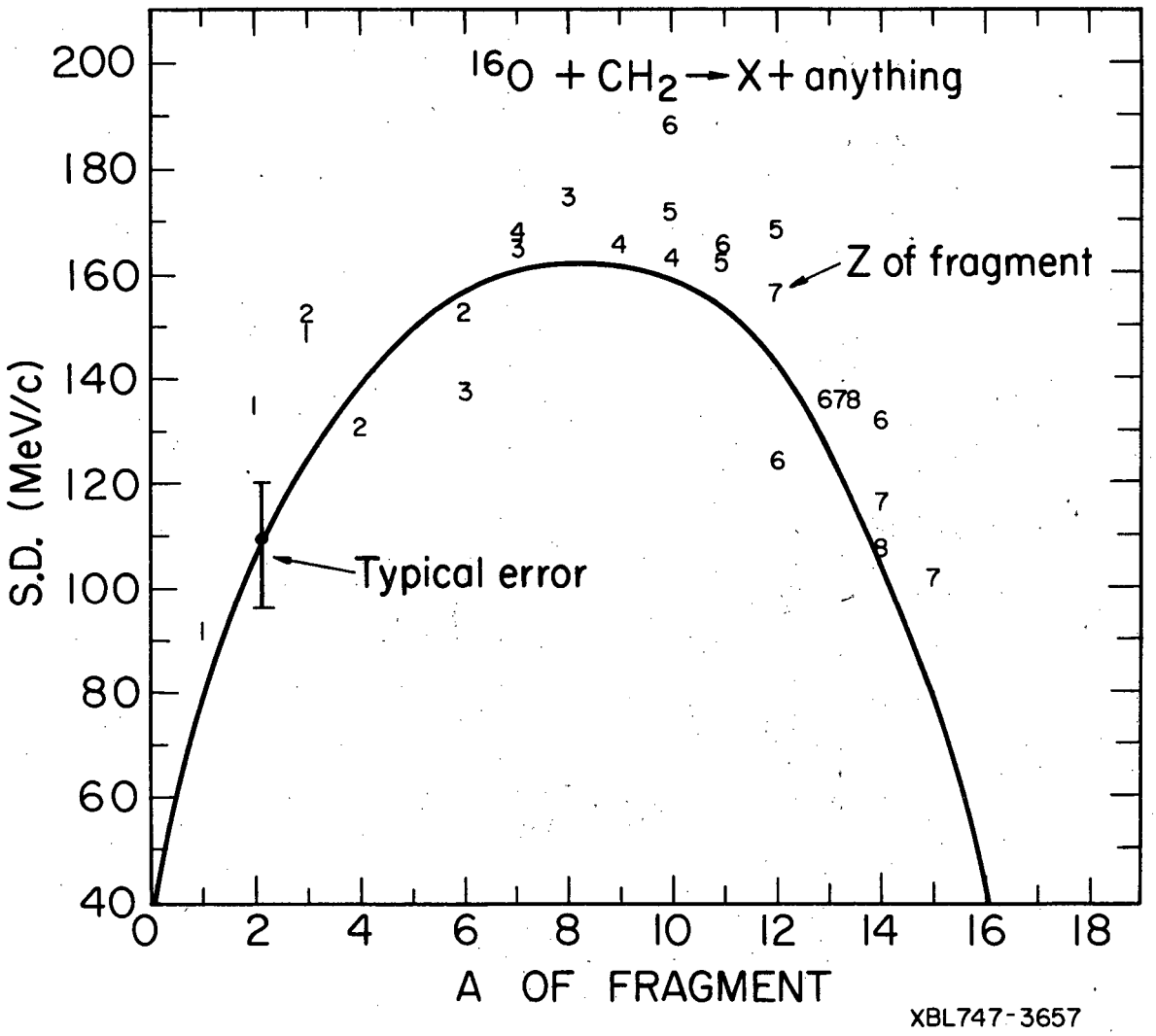
$^{16}O + CH_2 \rightarrow X +$ anything
Z of fragment
Typical error
S.D. (MeV/c)
A OF FRAGMENT
XBL747-3657

Fig. 42

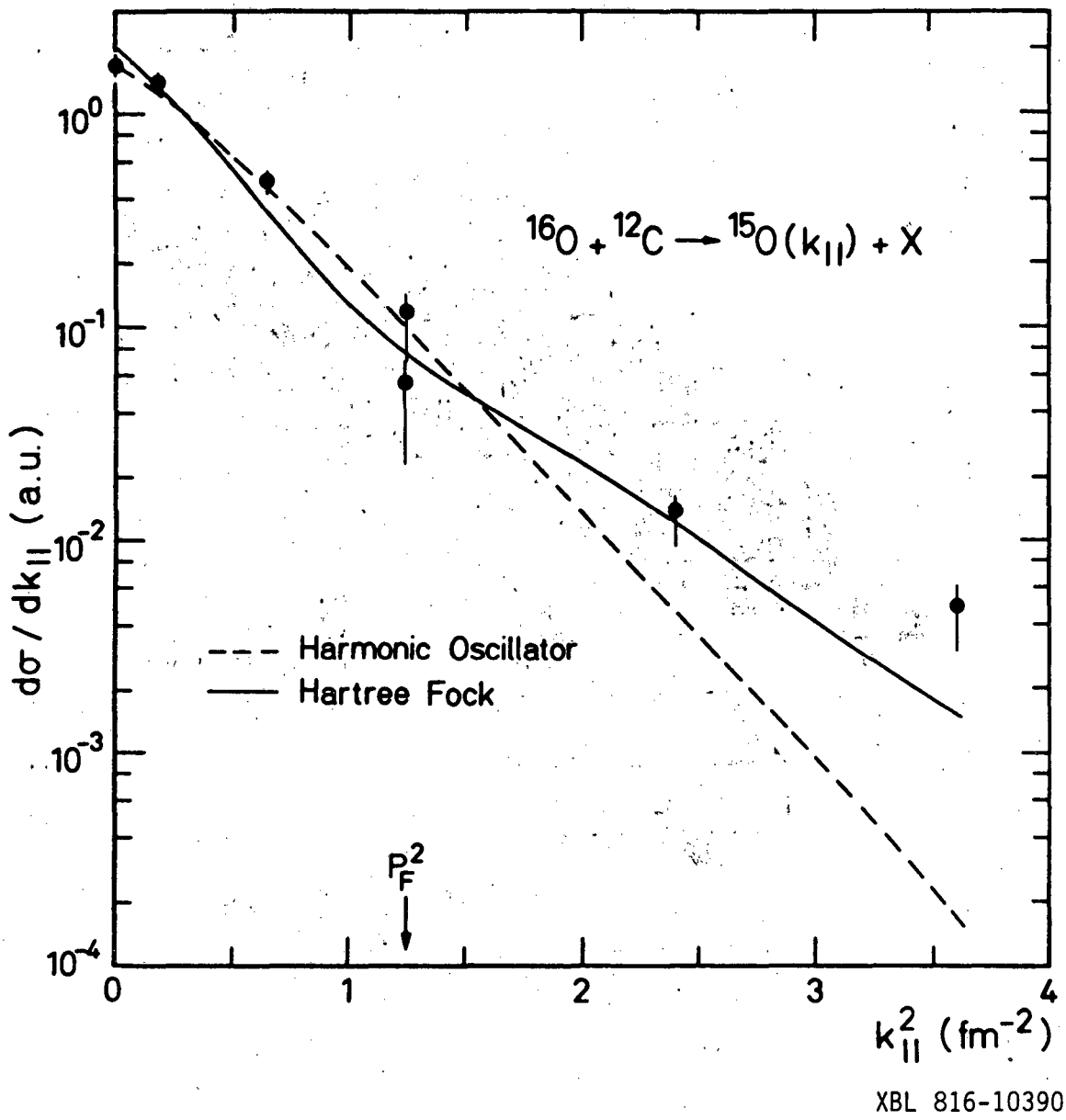
$^{16}O + ^{12}C \rightarrow ^{15}O(k_{||}) + X$
$d\sigma / dk_{||}$ (a.u.)
10^0
10^{-1}
10^{-2}
10^{-3}
10^{-4}
Harmonic Oscillator
Hartree Fock
P_F^2
0
1
2
3
4
$k_{||}^2$ (fm^{-2})
XBL 816-10390

Fig. 43

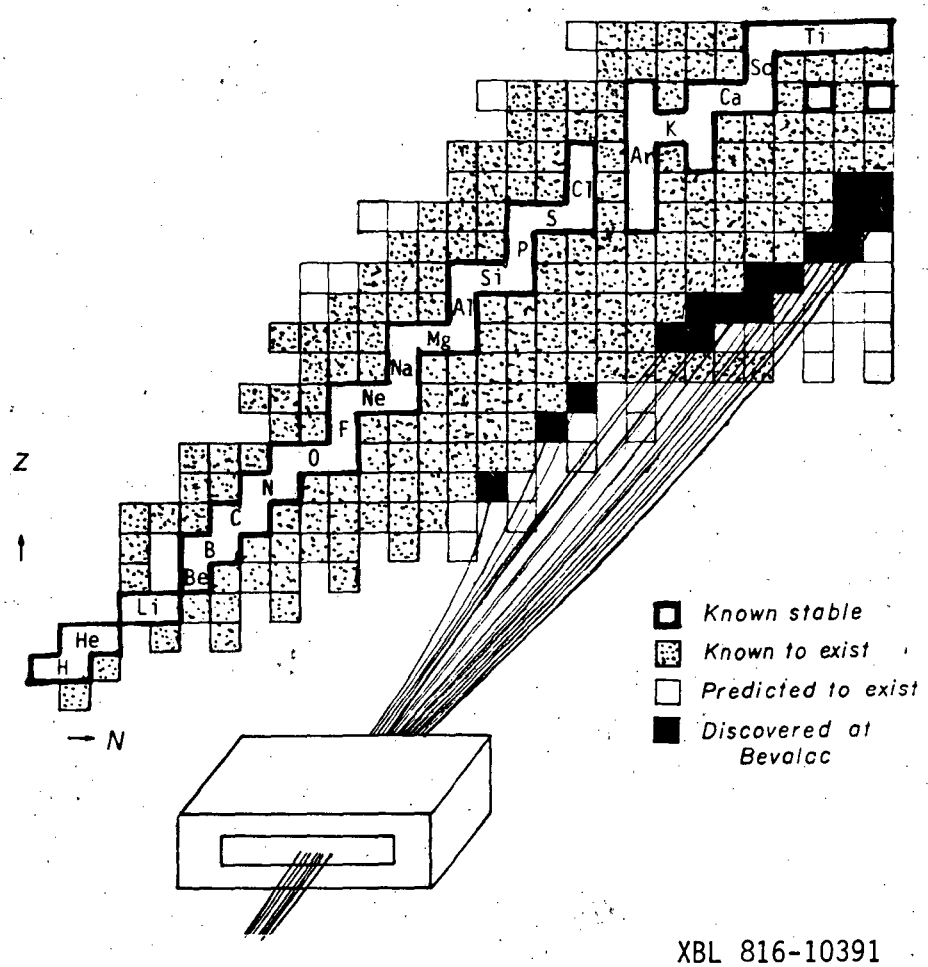

XBL 816-10391

Fig. 44

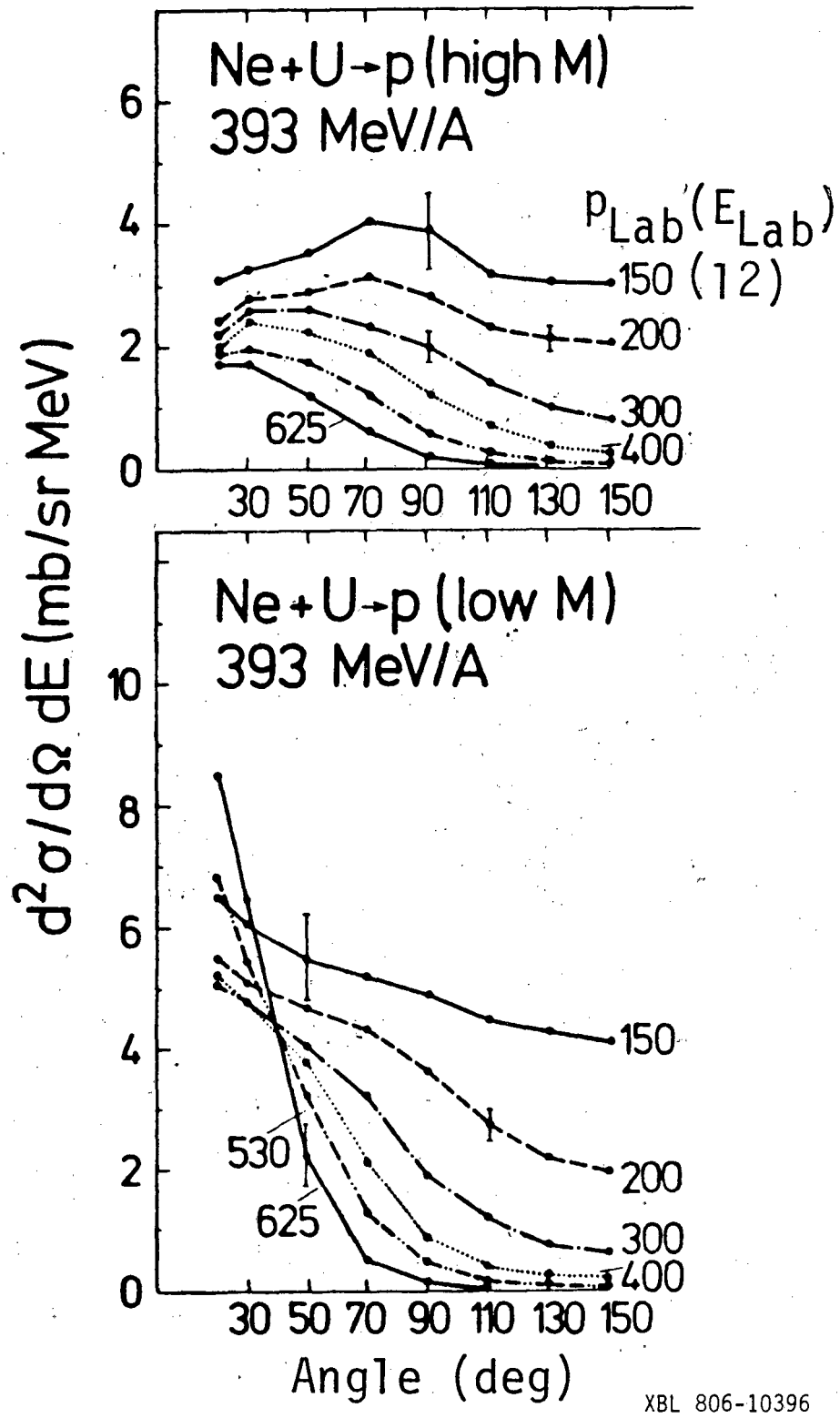
Ne+U→p (high M)
393 MeV/A
p_{Lab} (E_{Lab})
150 (12)
200
300
400
625
Ne+U→p (low M)
393 MeV/A
150
200
300
400
530
625
$d^2\sigma/d\Omega\, dE$ (mb/sr MeV)
Angle (deg)
XBL 806-10396

Fig. 45

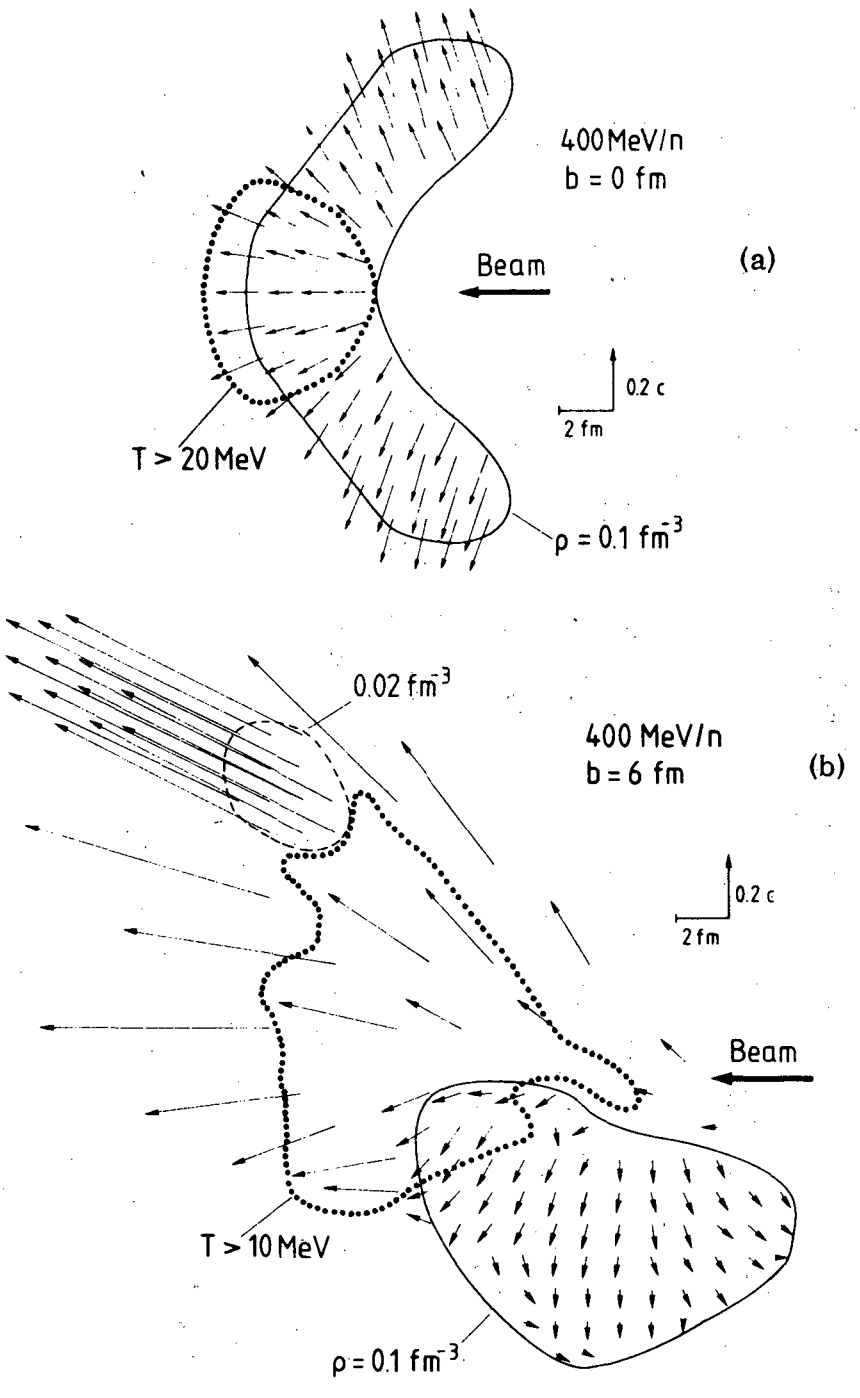
400 MeV/n
b = 0 fm
Beam
(a)
0.2 c
2 fm
T > 20 MeV
ρ = 0.1 fm⁻³
0.02 fm⁻³
400 MeV/n
b = 6 fm
(b)
0.2 c
2 fm
Beam
T > 10 MeV
ρ = 0.1 fm⁻³
XBL 821-7777

Fig. 46

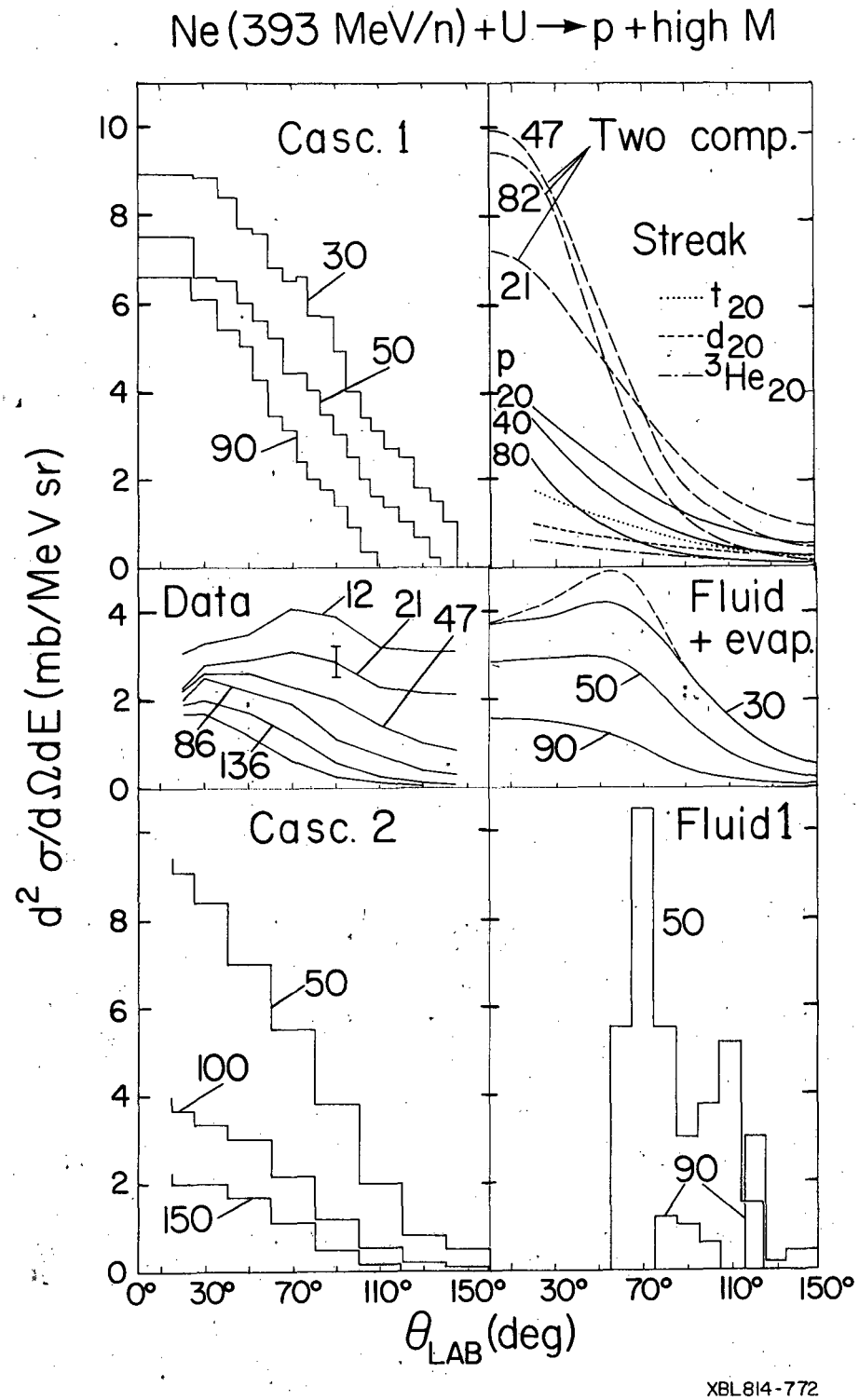
Ne(393 MeV/n)+U → p+high M
Casc. 1
30
50
90
47 Two comp.
82
Streak
21
t_{20}
d_{20}
$^3He_{20}$
p
20
40
80
Data
12
21
47
86
136
Fluid
+ evap.
50
30
90
Casc. 2
50
100
150
Fluid1
50
90
$d^2\sigma/d\Omega dE$ (mb/MeV sr)
0° 30° 70° 110° 150° 30° 70° 110° 150°
θ_{LAB} (deg)
XBL814-772

Fig. 47 (a)

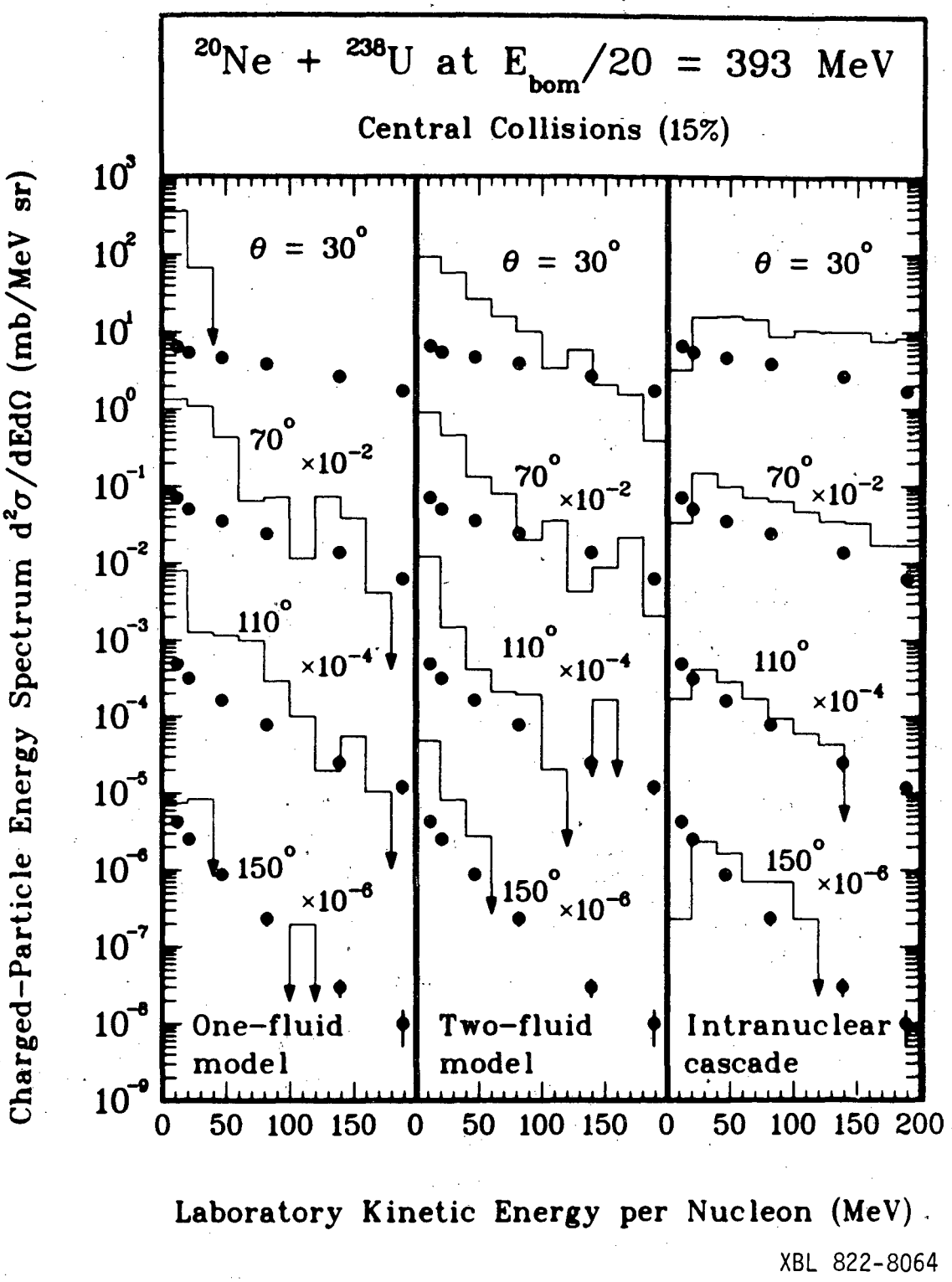
$^{20}Ne + ^{238}U$ at $E_{bom}/20$ = 393 MeV
Central Collisions (15%)
Charged-Particle Energy Spectrum $d^2\sigma/dEd\Omega$ (mb/MeV sr)
θ = 30°
70° ×10⁻²
110° ×10⁻⁴
150° ×10⁻⁶
One-fluid model
Two-fluid model
Intranuclear cascade
Laboratory Kinetic Energy per Nucleon (MeV)
XBL 822-8064

Fig. 47 (b)

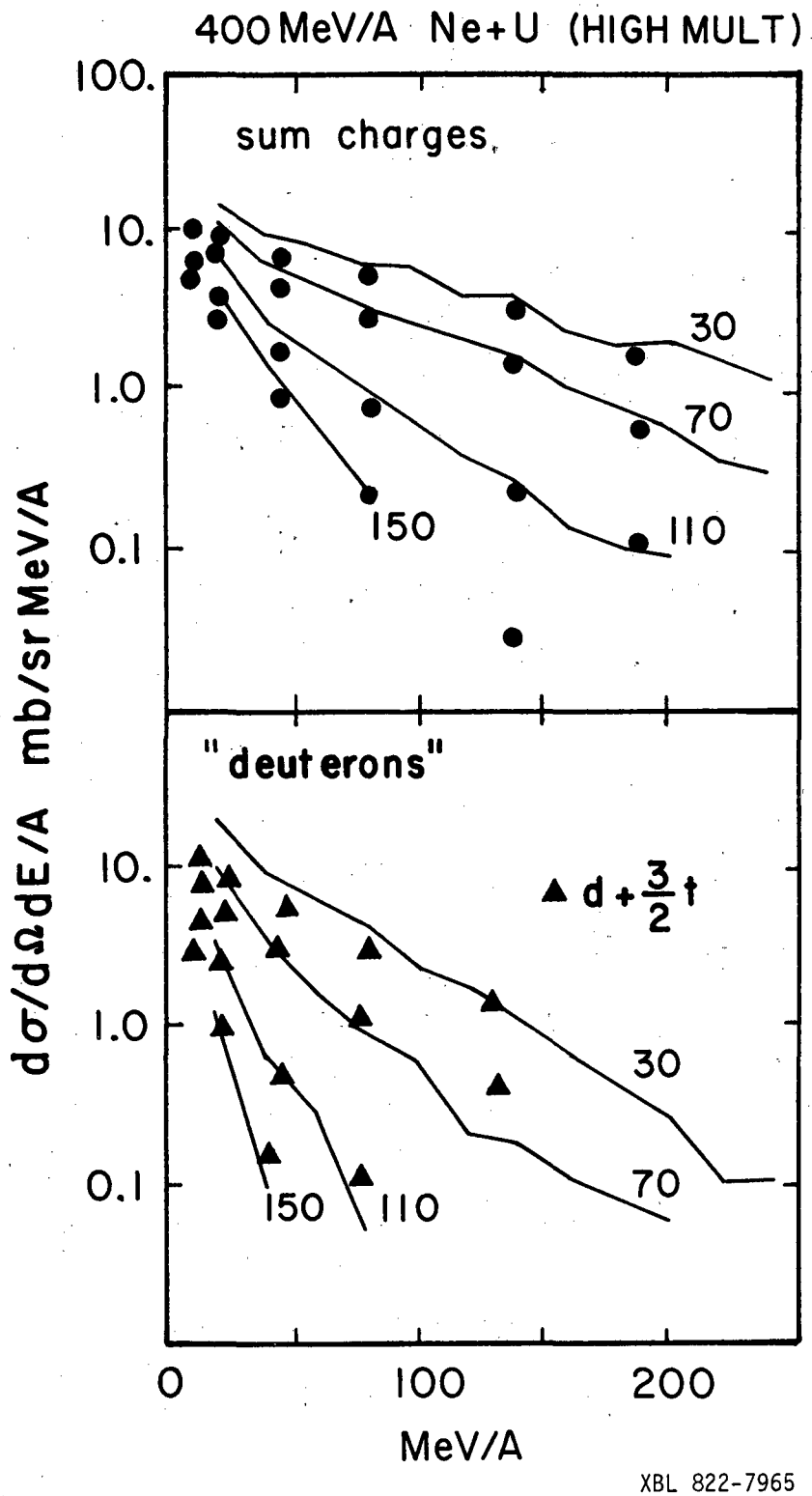
400 MeV/A Ne+U (HIGH MULT)
sum charges
"deuterons"
$d\sigma/d\Omega dE/A$ mb/sr MeV/A
30
70
110
150
$d + \frac{3}{2}t$
100.
10.
1.0
0.1
0
100
200
MeV/A
XBL 822-7965

Fig. 47 (c)

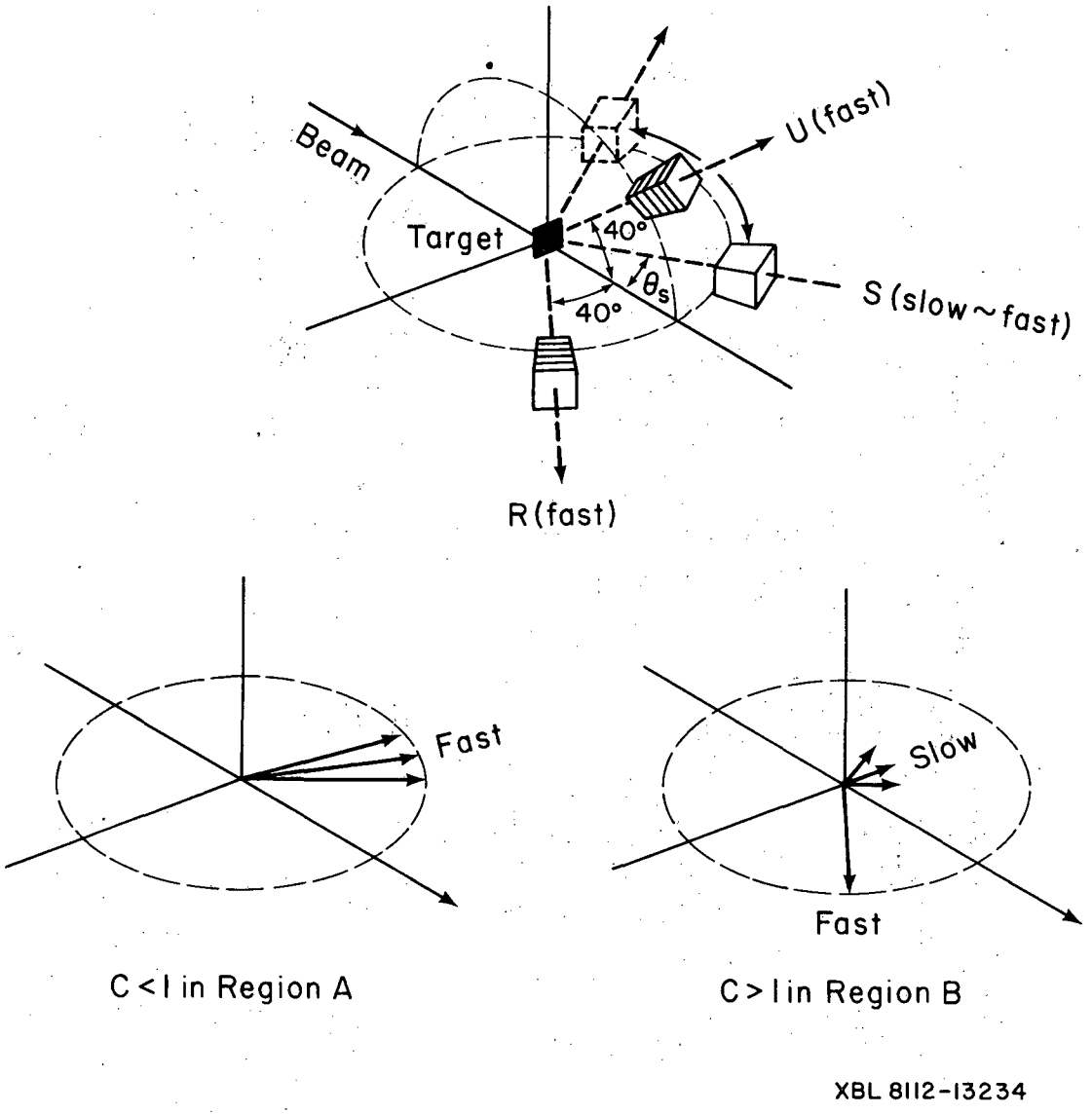
Beam
Target
U(fast)
40°
θ_s
40°
S (slow ~ fast)
R(fast)
Fast
C < I in Region A
Slow
Fast
C > I in Region B
XBL 8112-13234

Fig. 48

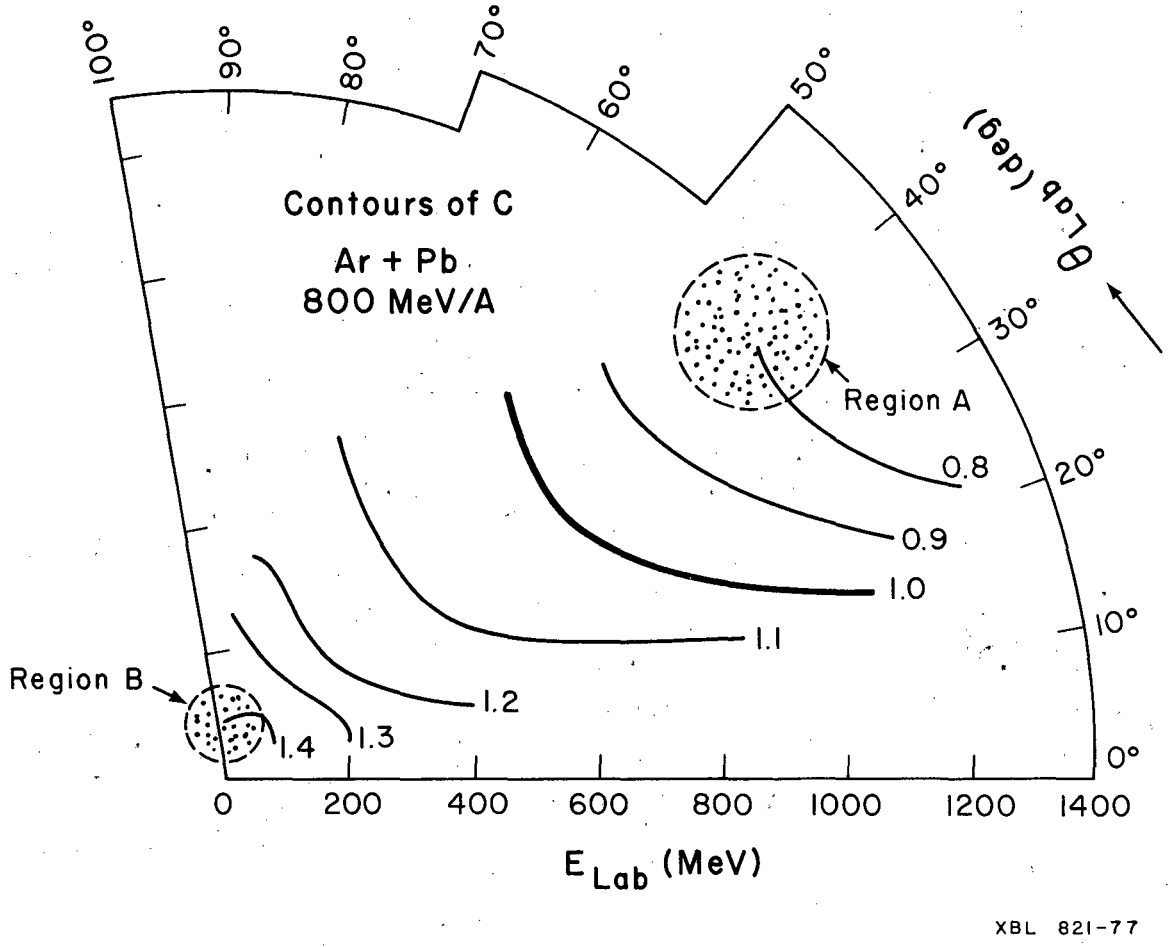

XBL 821-77

Fig. 49

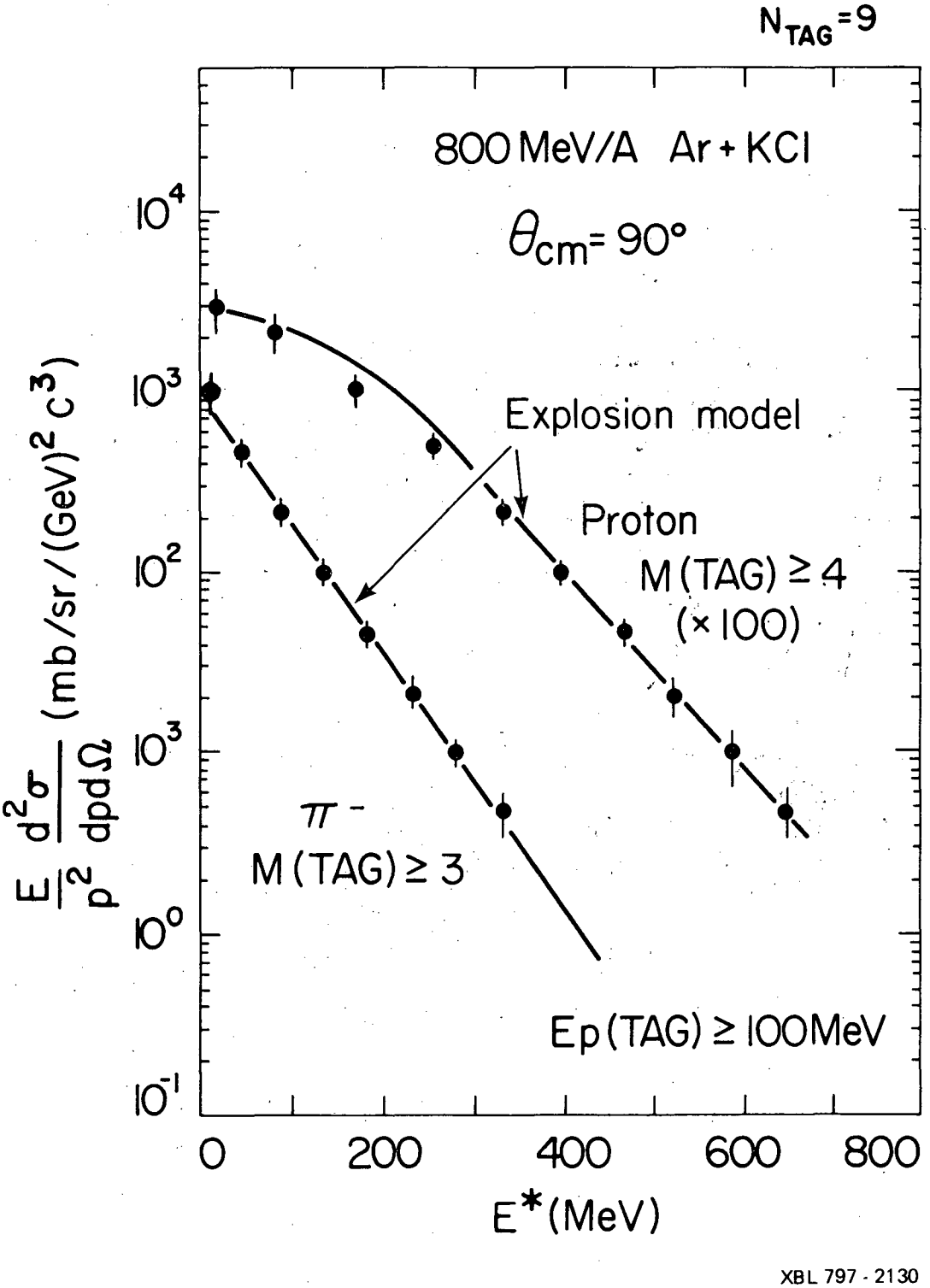
N_TAG=9
800 MeV/A Ar + KCl
θcm= 90°
Explosion model
Proton
M(TAG) ≥ 4
(×100)
π⁻
M(TAG) ≥ 3
Ep(TAG) ≥ 100MeV
E d²σ/p² dpdΩ (mb/sr/(GeV)² c³)
E*(MeV)
XBL 797-2130

Fig. 50

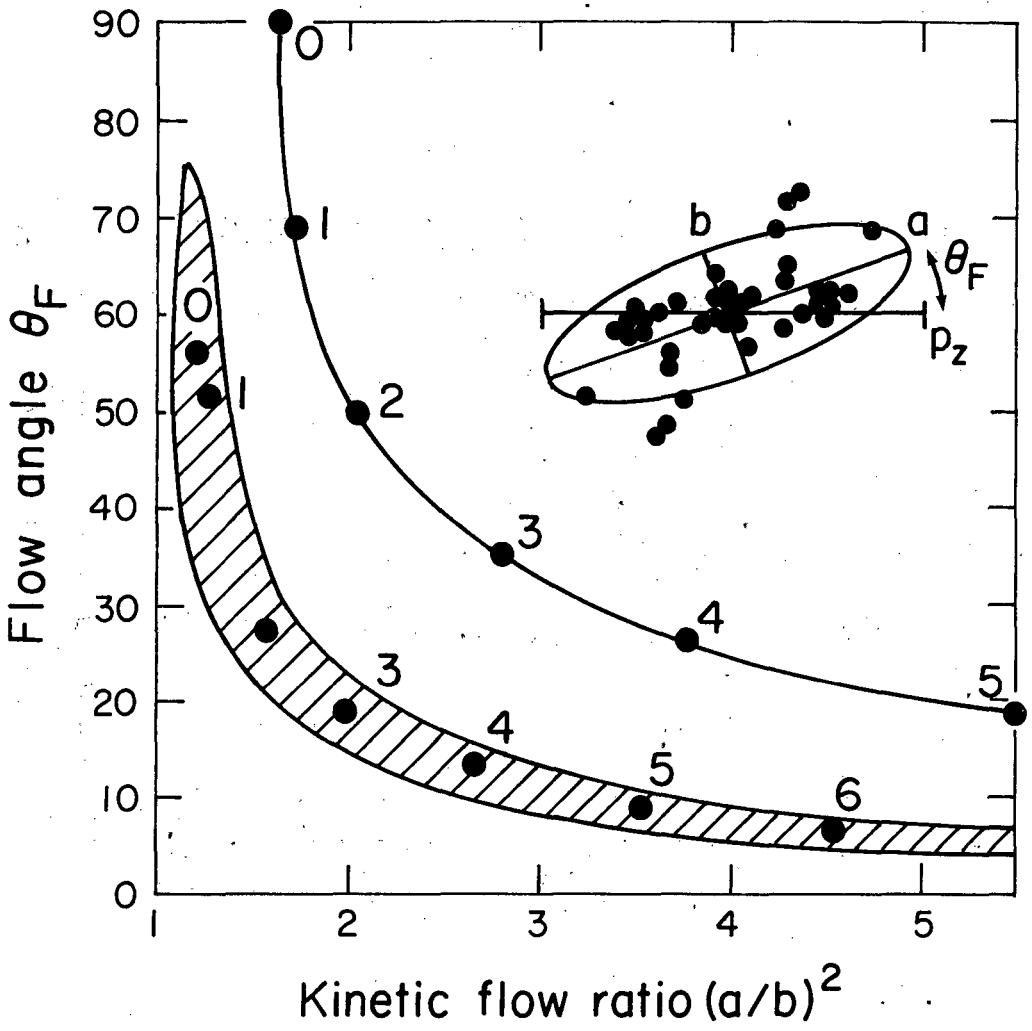

XBL 822 - 4485

Fig. 51

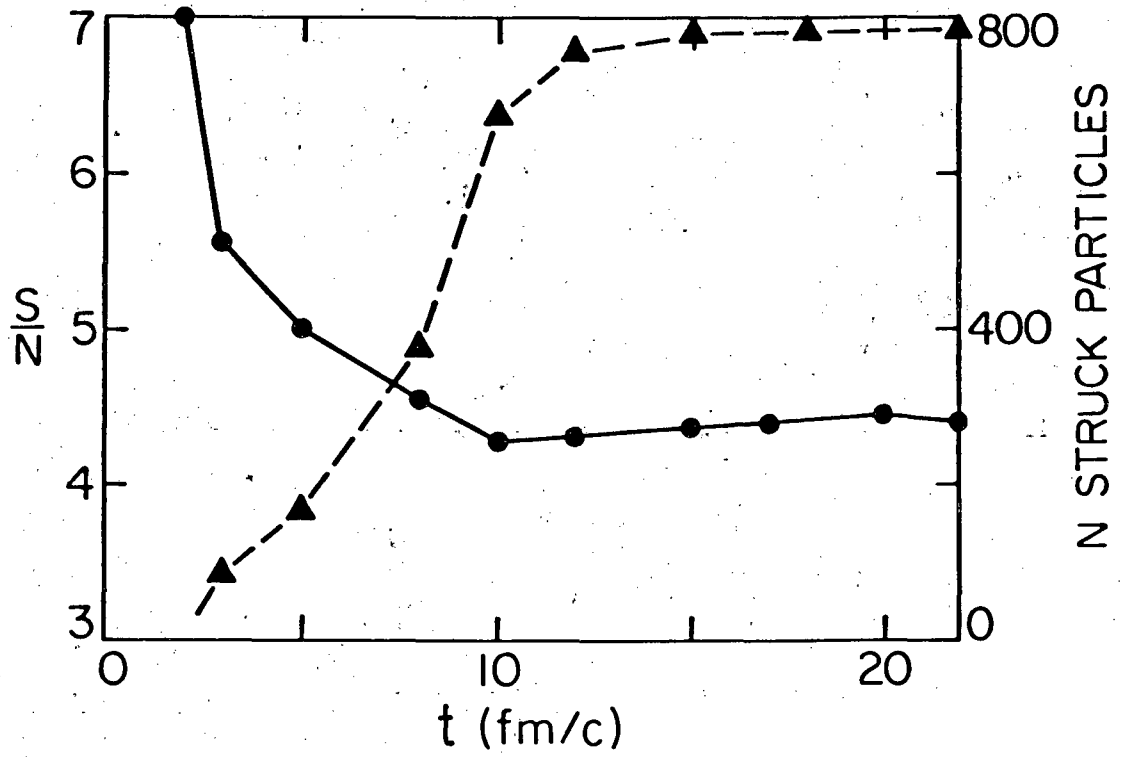

XBL 817-10510

Fig. 52

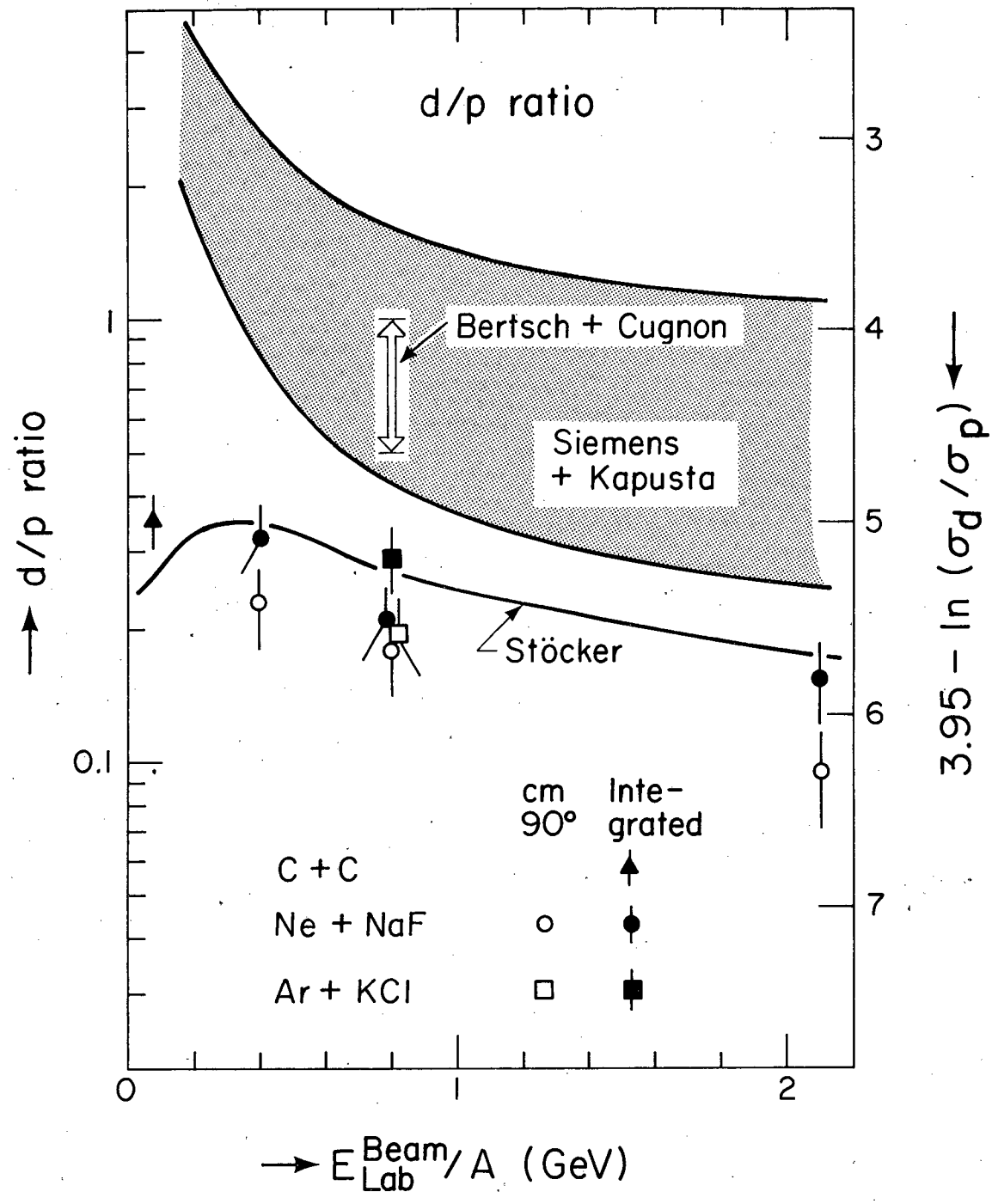

XBL 822-4484

Fig. 53

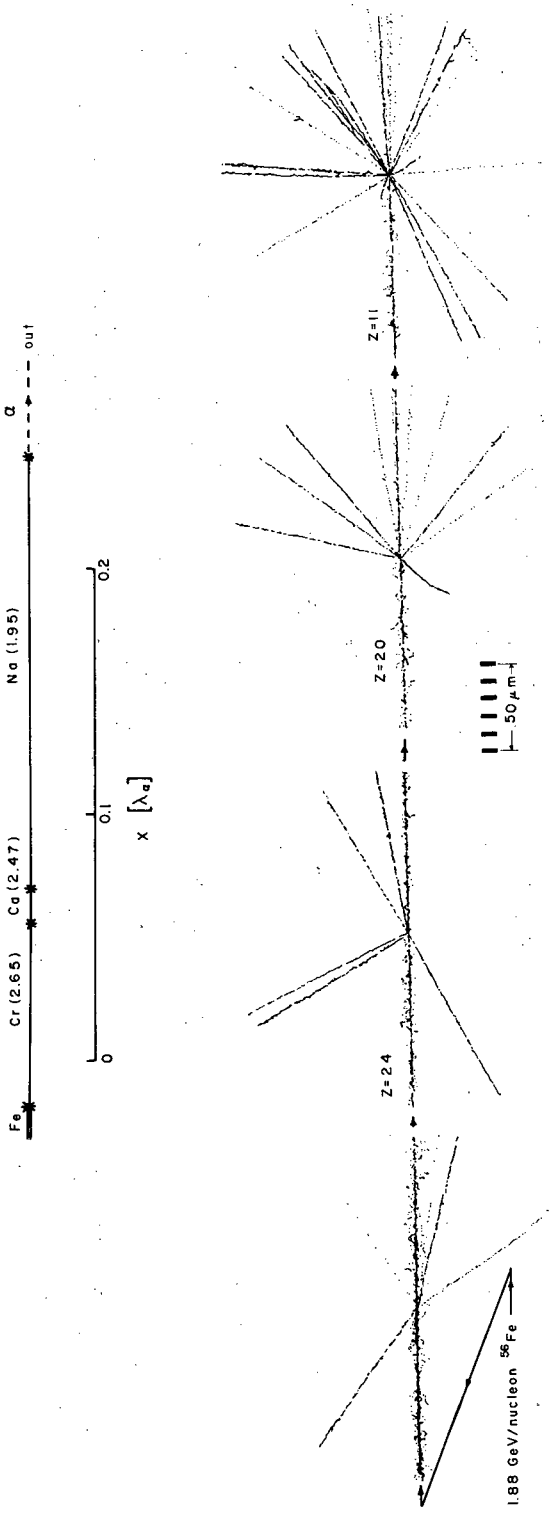

XBL 794-9277

Fig. 54

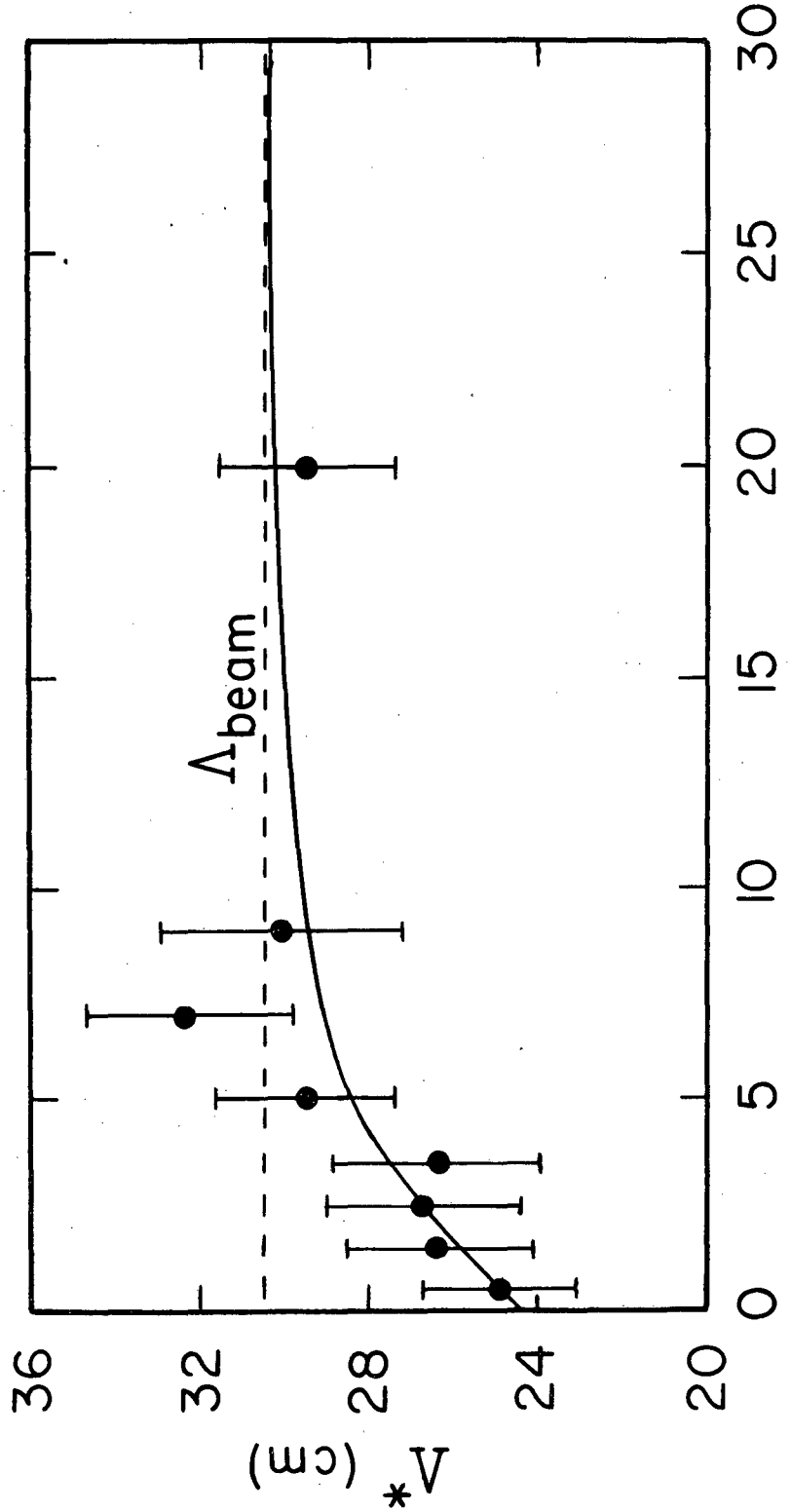

XBL 808-11485

Fig. 55

This report was done with support from the Department of Energy. Any conclusions or opinions expressed in this report represent solely those of the author(s) and not necessarily those of The Regents of the University of California, the Lawrence Berkeley Laboratory or the Department of Energy.

Reference to a company or product name does not imply approval or recommendation of the product by the University of California or the U.S. Department of Energy to the exclusion of others that may be suitable.

TECHNICAL INFORMATION DEPARTMENT
LAWRENCE BERKELEY LABORATORY
UNIVERSITY OF CALIFORNIA
BERKELEY, CALIFORNIA 94720